Structure and Properties Interrelationships of $SrBi_2(Ta_{1-x}Nb_x)_2O_9$
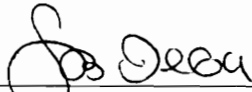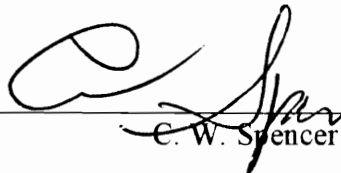
by

Tze-Chiun Chen

Dissertation submitted to the Faculty of the

Virginia Polytechnic Institute and State University

in Partial fulfillment of the requirement for the degree of

DOCTOR OF PHILOSOPHY
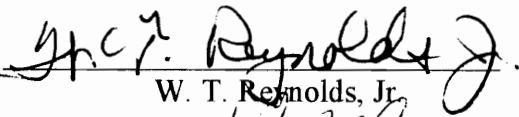
in

Materials Engineering Science

APPROVED:

_____
S. B. Desu, Chairman

_____   _____
C. W. Spencer   W. T. Reynolds, Jr.
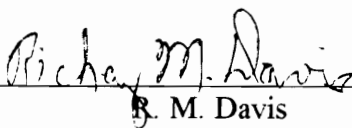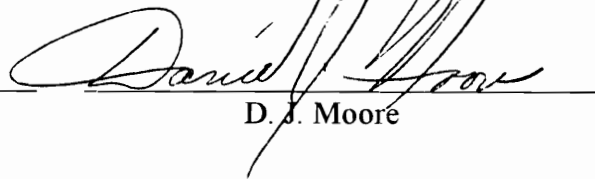
_____   _____
R. M. Davis   D. F. Moore

December 1995

Blacksburg, Virginia

Key words: Ferroelectric, Hysteresis, Polarization, Fatigue, Ellipsometry, Impedance

C. 2

LD
5655
V856
1995
C447
C.2

C. 2

Structure and Properties Interrelationships of $SrBi_2(Ta_{1-x}Nb_x)_2O_9$

by

Tze-Chiun Chen

Committee Chairman: Seshu B. Desu

Materials Engineering Science

(ABSTRACT)

In recent years, the ferroelectric oxides belonging to the family of layered perovskite, e.g., $SrBi_2(Ta_{1-x}Nb_x)_2O_9$ (or SBTN), were identified as promising candidates for nonvolatile memory applications. $SrBi_2Ta_2O_9$ (or SBT) thin films were found to exhibit no fatigue up to 10^{12} switching cycles, very good retention properties and low leakage current densities on Pt electrodes. However, high temperature processing, i.e. 750 - 800°C, is needed for SBT to exhibit ferroelectric properties. Moreover, the fundamental properties of SBTN have not been fully characterized. In this research, SBTN solid solutions were studied from two aspects: the technical aspect and scientific aspect.

From the technical point of view, low temperature processing of SBTN ferroelectric thin films was developed. In this part of study, SBTN thin films were made by metalorganic decomposition method (MOD) and were deposited on Pt-electrodes. The structure development study by a non-destructive optical method, spectroscopic ellipsometry, was proposed to determine nucleation and grain growth temperatures. The information on structure development can be obtained by observing how the refractive indices and film thicknesses change as functions of annealing temperature. The results of structure development study for SBT thin films suggest that the ferroelectric properties are controlled by grain growth process rather than nucleation process. The critical factor for ferroelectric properties was to have grain size exceeding a critical value, i.e., 0.1 μm.

Applying this concept, low temperature processing can be achieved by growing larger grains at lower temperature. The processing temperature of SBTN thin films was reduced by 50 - 100°C by adding excess Bi or increasing Nb/Ta ratio. The optimum excess Bi content in SBT was 30 - 50% ; within this range, limited solid solution of Bi_2O_3 and SBT was formed.

From the scientific aspect of view, optical properties and ionic transport phenomena of SBTN bulk ceramics were investigated for the first time. The reason of using bulk ceramics is to exclude the difficulties associated with thin film technology, e.g., grain size effect and electrode-ferroelectric interface effect. These bulk property studies provide fundamental understanding of SBTN materials and provide a guideline for process development in device applications. The optical dispersion functions of bulk SBTN were obtained by using various angle spectroscopic ellipsometry with a surface layer correction. The values of refractive indices were found to vary with composition, which are possibly associated with crystallographic orientation. Using the Lorentz Oscillator model, the approximate energy band gaps of SBTN solid solutions were estimated to be about 5 eV.

The ionic transport phenomena of SBT and $SrBi_2Nb_2O_9$ (or SBN) were investigated by using impedance spectroscopy. This technique allows to separate the effect of ion transport in grain, grain boundary and electrode-ferroelectric interface. In this study, the fatigue model of bismuth layered oxides was discussed through ionic conductivity and interface absorption effect. One conducting species, oxygen vacancies with positive charges, was assumed in the model. High ionic conductivities of SBT and SBN ($\sim 10^{-7}$ S/cm) comparing to $Pb(Zr_{1-x}Ti_x)O_3$ ($\sim 10^{-11}\text{-}10^{-10}$ S/cm) suggests high defect concentration and high charge mobility in bismuth layered oxide materials. As a result, the most possible model to explain high resistance to fatigue of SBT/SBN was the easy recovery of oxygen vacancies from the entrapment at electrode-ferroelectric interfaces.

Acknowledgments

I would like to express my sincere appreciation to my advisor Dr. Seshu B. Desu for his advice, patience and support throughout the course of this work. Not only did he guide me in the research with his endless enthusiasm, but he and his wife, Mallika, also offered countless support for my family. Through him, I have learned how to discover and organized a new idea and how to present my work effectively. These skills will continue to contribute well in my future career.

I would like to thank my committee members for their invaluable conversations: to Prof. William T. Reynolds for his invaluable discussion on the phase transformation of SBTN thin films; to Prof. Chester W. Spencer and Prof. Richey M. Davis for reviewing this thesis and providing me versatile suggestions and comments; to Prof. Daniel J. Moore, although he left Virginia Tech for Indiana, his willingness to stay in the committee made me out of speech to express his kindness; to Dr. Carlos Suchicital for representing Prof. Moore during the dissertation meeting.

My special thanks are due to Dr. Tingkai Li and Prof. Xubai Zhang for being a helpful partner, especially for preparing samples during my pregnancy, to Dr. BaoPing He for collecting XRD data, to Steve for invaluable discussion on ESCA data, to Dr. Chien-Hsiung Peng for invaluable discussion on optical properties of thin films, to Dr. Chein-Chia Chiu for his advise on bulk sample preparation, to Greg Menk, Dr. Hemanshu Bhatt, Dr. Justin Gaynor, Dr. Dillip Vijay and Dr. Sasanga for worthful review of this manuscript.

Last but not the least, I acknowledge my indeptness to all the members of the Thin films group - the wise Prof. Chen, the honest Zhu, the daddy Wei Pan, the versatile Wei Tao, the lovely neighbor Masaya, the naughty and strong Song, the chef Jay, the tall

Bryan, the quite Nikhil, and the forever young Prof. Gu - each of whom have, in their unique way, contributed to making my stay at the lab joyfully and memorable.

Finally, I wish to express my deepest love and appreciation to my husband and my new born baby, Chai-Liang Thio and Vibert. Without Thio's total support, love and sacrifices I could not have finished this work.

This work is dedicated to my parents.

Table of Contents

List of Figures

List of Tables

Chapter 1. Introduction

Since 1920 the Rochelle salts ($NaKC_4H_4O_6 \cdot 4H_2O$) were discovered with ferroelectric properties by Valasek [1], a large number of new ferroelectric materials have been discovered and investigated. These materials have received continued attention for device applications using the dielectric, piezoelectric and pyroelectric properties of ferroelectrics, e.g., multilayer capacitors, modulators, gas ignitors and intruder alarms, etc.. Recently, ferroelectric materials have received attention for their application in nonvolatile memory devices in ultra-large scale integration (ULSI).

1.1 Ferroelectric Properties

Ferroelectricity is defined as the spontaneous alignment of electric dipoles by their mutual interaction. A crystal is said to be ferroelectric when it has two orientation states in the absence of an electric field and can be switched from one to another of these states by an electric field. Ferroelectric properties occur below a critical temperature, so called Curie temperature. Below Curie temperature, the perovskite cubic lattices are distorted by stretching along one side (e.g., the c-axis) and shrinking along the other two sides (e.g., a- and b-axis) so that the small anions are shifted from the center position of the oxygen octahedral structure. It is because of this asymmetric lattice structure that dipoles occur along the c-axis. A net macroscopic polarization arises because of the constructive alignment of these dipoles occurring in the regions called domains. For the tetragonal structure as shown in Figure 1-1, a typical c to a axis ratio is about 1.02 to 1.06. In the $Pb(Zr_{1-x}Ti_x)O_3$ (PZT) system, the B site ion is displaced roughly 0.1 Å from the center of
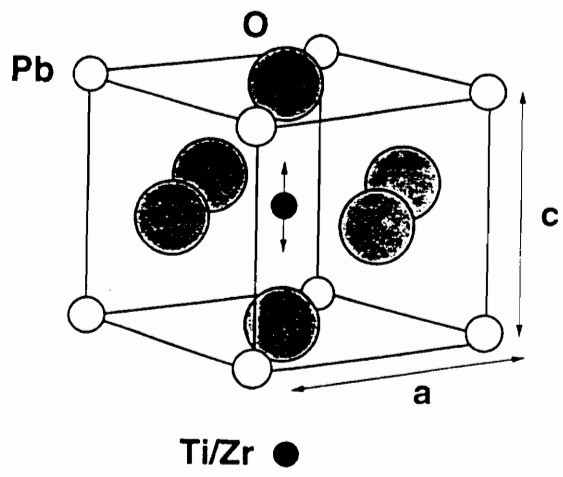
Figure 1-1   The tetragonal structure of PZT unit cell. The tetragonal distortion is about 2-6% depending on the Zr/Ti ratio.

the oxygen octahedron (the lattice constant is approximately 4 Å). In a polycrystalline PZT thin film, the grain size is typically less than 1000 Å and each grain may consist of many domains [2].

On the other hand, when temperature increases to above Curie temperature, the lattice becomes center symmetry and the spontaneous polarization disappears. At this temperature region, ferroelectricity vanishes and the materials make a structural phase change from polar phases to non-polar phases, typically called the paraelectric phase.

The result of spontaneous polarization below Curie temperature is the appearance of a hysteresis loop for polarization in an alternating field as shown in Figure 1-2. This is similar to the hysteresis loop observed for ferromagnetic materials. The hysteresis results from the presence of different domains in which there is complete alignment of electric dipoles. At low fields and at very high fields a ferroelectric behaves like an ordinary dielectric, however, at the so-called coercive field, E_c, polarization reversal occurs giving a large dielectric non-linearity. The area within the loop is a measurement of the energy required to twice reverse the polarization. At high field strength, the polarization becomes saturated and have most of the domains of like orientation aligned in the direction of the electric field. Extrapolation of this curve back to the $E=0$ gives P_S, the saturation polarization corresponding to the spontaneous polarization with most of the dipoles aligned in parallel. When the electric field is cut off, the polarization does not go to zero but remains at a finite value, P_r, the remnant polarization. This is because the oriented domains are unable to return to their original random state without an additional energy input by an opposite electric field. That is, the coercive field E_c is the field required to change domain orientation.

It is because of these nonvolatile and switchable polarization states that make ferroelectric materials suitable for ferroelectric RAM (FRAM) devices. With such a device

3
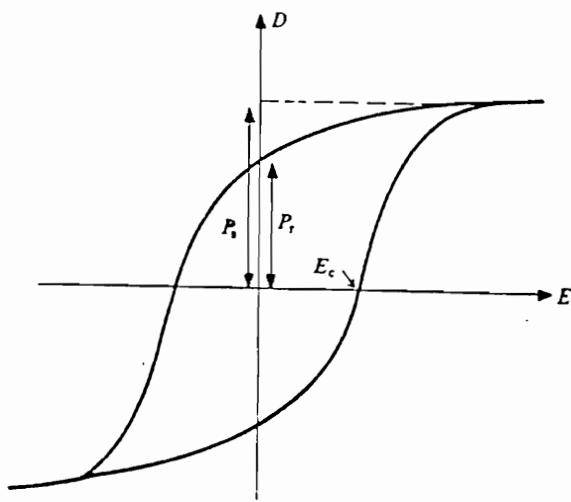
Figure 1-2.   Ferroelectric hysteresis loop.

one could encode the 1 and 0 states, which corresponds to $+P_r$ and $-P_r$ at zero applied electric field, required for the Boolean algebra of binary computer memories. Their high speed, nonvolatility, light weight, combined with low power requirements, physical robustness, radiation hardness and high density, suggest that they may replace DRAM as core memories for computation applications [3].

1.2 Background of Memory Devices

Let us begin by summarizing the overall situation with regard to digital memories in the United States at present. The memories in use at present range from the slow, inexpensive devices (tape or disk) used for archival storage to the fast but expensive SRAM and the slightly slower DRAMs, whose availability in high-density chips (up to 1 Mbit) has permitted them to become dominant in the $8 billion per year computer memory market. The more expensive devices, e.g., plated wire, CMOS with battery backup, magnetic bubble memory, EEPROMs, and core, generally have some combination of attributes required for specific applications, particularly including nonvolatility (retention of memory when power is interrupted) and radiation hardness. The projected U.S. memory market will be greatly simplified in a few years, however, if ferroelectric RAMs become commercially available in high-density (for example, 256-kbit) devices with satisfactory operating characteristics and lifetimes. The intrinsic nonvolatility and radiation hardness of ferroelectric RAMs may greatly simplify the existing collections of computer memories, which will still include tape and disk systems for archival storage, as well as inexpensive high-density DRAMs and ultrafast SRAMs; however, most of the other memory devices now in use may be rendered obsolete by ferroelectric RAMs. The radiation hardness of ferroelectric memories depends on this ability to function and retain

5

information when the memories are subjected to intense X-ray, particle fluxes of charged ions, and neutrons, for both total integrated dosage and dose rates. A typical ferroelectric will withstand more than 5 Mrad of high-energy X-rays per square centimeter and an intensity of 10^{11} rad-cm^{-2}s^{-1}, or 10^{14} 1-MeV neutrons per square centimeter, and will exhibit no single event upset and very little degradation in performance. These properties may permit wide use of ferroelectrics in military aircraft as higher speed replacement for EEPROMs, magnetic bubble memory, and disk. But radiation hardness is of interest not only to the military. Many civilian applications in space require radiation hardness; for example, a 1992 launch of a NASA satellite that must pass repeatedly through the Van Allen belt over several years of operation is at present likely to have core memory in its on-board computers. Replacement of core with ferroelectric RAMs could permit a significant improvement in weight, space, and power supply requirements while at the same time improving speed [4].

When one considers all the selection requirements for a nonvolatile memory, namely fast read/write, radiation hardness, cost effectiveness via compatibility with currently used IC processing technology, high endurance and retention, and nondestructive readout (NDRO) capability, the ferroelectric memory stands out as a logical choice for all applications where submicrosecond programming is needed.

1.3 Memory Application

1.3.1 Memory Operation

The major advantage of ferroelectric devices in the memory world is their nonvolatility. Nonvolatile literally means that the stored information cannot "evaporate" --

if the power is interrupted. In the case of DRAM, it loses the information stored in it. In contrast, a nonvolatile memory, such as magnetic core, retains information if the power is cut off. The initial idea using ferroelectric nonvolatility was to use a ferroelectric thin film, which can be permanently polarized by an electric voltage pulse, as the gate dielectric of a transistor. However, read errors might occur in such a memory cell due to the absence of a well defined threshold voltage for polarization. In 1987, a new concept of ferroelectric memory was introduced. The key idea was to use a ferroelectric thin film as the dielectric in the capacitor of a DRAM cell. Due to the fact that such a cell is refreshed every time it is read, READ disturbance could be avoided. If extreme endurance (10^{16} read/write cycles) and good data retention could be achieved, this could be the ideal memory. FRAM can potentially match DRAM in WRITE and READ speed and beat DRAM in cell size, with nonvolatility offered as a bonus.

A ferroelectric memory cell is a one-transistor DRAM cell where the conventional DRAM capacitor is replaced by a ferroelectric capacitor, as shown in Figure 1-3. For DRAM applications, the memory operates identically to conventional DRAMs. For non-volatile memory applications, the polarization state of the ferroelectric film corresponds to the logic state of the memory cell. Writing is accomplished by biasing the bit line at V_{DD} or 0 V and pulsing the bottom capacitor plate as shown in Figure 1-4(a). The cell contents are read by precharging the bit line and pulsing the bottom capacitor plate as shown in Figure 1-4(b). If sensing is performed during this pulse, the logic 0 and 1 voltages on the bit line will be proportional to the polarization values in Figure 1-4(c). If sensing occurs after the pulse, net charge transfer to the bit line will occur for only one logic state as shown in Figure 1-4(d). The latter case improves the logic 1 to logic 0 signal ratio. Because of the destructive nature of the read, the cell contents have to be restored as in a DRAM. Since the bottom capacitor plate is pulsed for non-volatile memory operation, this

7

Word Line

Bit Line

Storage
Node

Ferroelectric
Capacitor
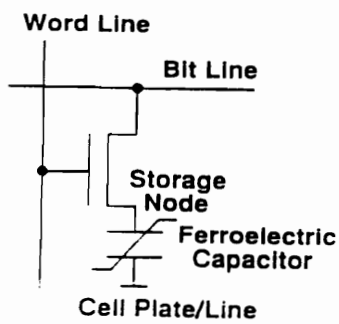
Cell Plate/Line

Figure 1-3   A ferroelectric memory cell is a DRAM cell with a ferroelectric capacitor.
               For non-volatile memory applications, the DRAM cell plate is replaced
               with a drive line running parallel to the word line [67].
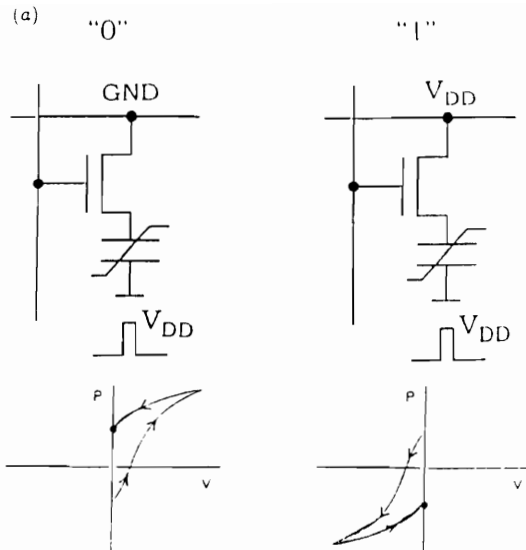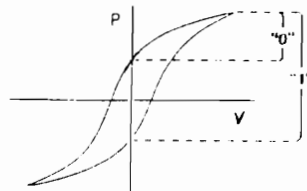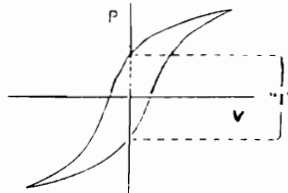
Figure 1-4   (a) Writing to a ferroelectric non-volatile memory is accomplished by pulsing the drive line while holding the bit line at either 0 V or V$_{DD}$. For a logic ONE, the polarization reversal corresponding to the hysteresis excursion in the figure occurs before the pulse on the drive line. (b) A read is performed by precharging the bit line and pulsing the drive line. Sensing can be performed either (c) during or (d) after the drive-line pulse. [67]

plate is typically separated into drive lines running parallel to the word lines to reduce memory access time and to avoid potential disturb conditions [5].

A third application for this memory cell is a DRAM with non-volatile store/recall [6]. In this scheme, the memory normally operates as a DRAM. Upon receiving a power-down signal, the memory contents are converted from the DRAM voltage levels to one of the two polarization states of the ferroelectric capacitor. Similarly, upon power-up, the contents are restored to the original DRAM levels. In this manner, the endurance requirements for non-volatile operation are reduced significantly, allowing more reliable memory operation.

1.3.2 Ferroelectric Thin Film Process And Integration

The properties of ferroelectric thin films are strongly dependent on the fabrication process, especially the electrode technology, ferroelectric deposition method and damage cased by subsequent process steps. Ferroelectric films are commonly deposited via sputtering [7], metalorganic chemical vapor deposition (MOCVD) [8,9], or a spin-on processes like sol-gel process and metalorganic decomposition (MOD) [10,11]. Because of the complex multicomponent nature of ferroelectric materials, precise microscopic control of stoichiometry is essential for obtaining uniform single-phase films. Furthermore, the deposition method should have a low cost per wafer and use existing process equipment. Sputtering uses conventional equipment; however, stoichiometry control using either a single composite target or co-sputtering is difficult. The spin-on technique satisfies all the above requirements and produce good quality films with less than 2% thickness and refractive index variations across a 125 mm wafer [12]. However, the disadvantage of the spin-on technique is poor step coverage and cannot be applied on the substrates with

complicate shapes. MOCVD is a very promising technique which is still in the exploratory stage. The progress in MOCVD has been slow because of lack of volatile precursors which satisfy environmental and safety requirements. However, this technique which offers advantages such as good step coverage, high deposition rate and low temperature deposition could be a very suitable way to increase the ferroelectric memory density and its performance.

The integration of a ferroelectric capacitor into a standard silicon IC process is designed as a module which can be integrated with CMOS technology as illustrated in Figure 1-5 [13]. The module is inserted in the CMOS process flow immediately prior to contact hole formation. In the typical process flow shown in Figure 1-5, the capacitor module consists of deposition and patterning of a buffer layer (e.g., 1000 - 1500Å TiO_2), a bottom electrode (e.g., 1000 Å Pt), the ferroelectric film (e.g., 1500Å PZT), a top electrode (e.g., 1000Å Pt) and an interlevel dielectric layer (either CVD SiO_2 or an SiO_2/Si_3N_4 stack). Finally, the back-end processing which includes the deposition of an isolation layer surrounding the capacitor is again done by standard process. Since ferroelectric processing involves reactive materials that are not common in silicon processing, special precautions have to be taken to prevent the ferroelectric processing from influencing the standard devices as well as to avoid the back-end processing destroying the ferroelectric characteristics. Solutions to these problems can range from the addition of suitable barrier layers, e.g., TiO_2, and adaptations in the ferroelectric capacitor processing to modifications in the back-end processing.

11
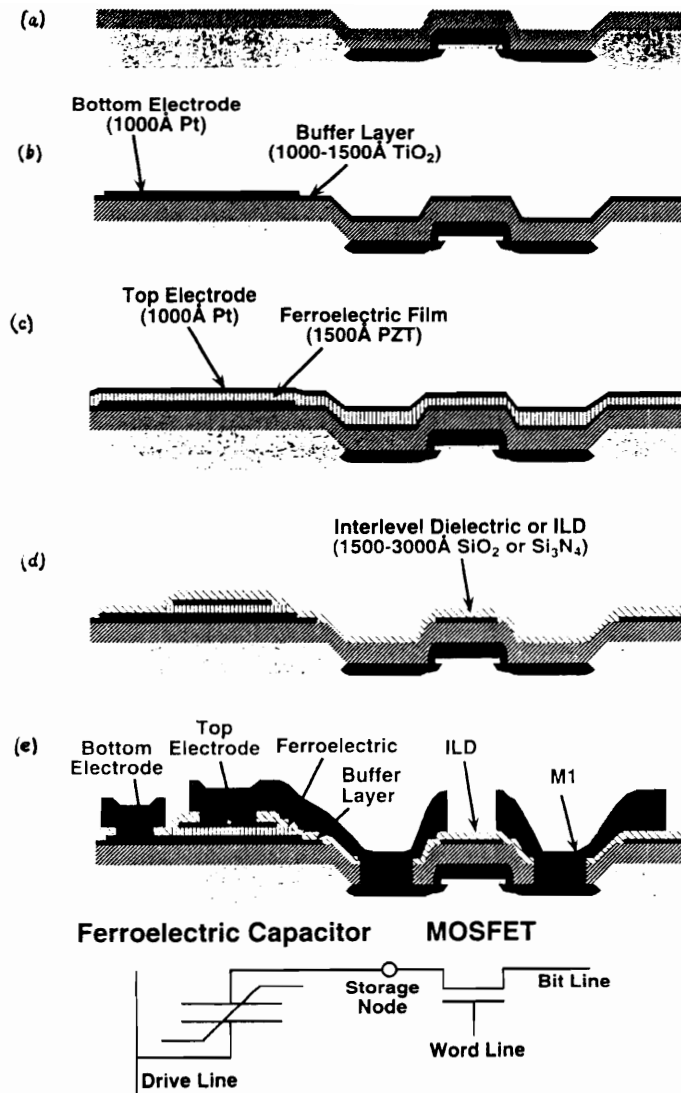
Figure 1-5   (a) The ferroelectric capacitor process module is inserted in the CMOS
              process flow immediately prior to contact hole formation and consists of
              (b) the deposition of a buffer layer and deposition and patterning of a
              bottom electrode, (c) the deposition and crystallization of a ferroelectric
              film followed by the deposition of a top electrode and (d) patterning of the
              top electrode, ferroelectric film and buffer layer followed by the deposition
              of an interlevel dielectric. (e) After contact hole definition and
              metallization, memory cell fabrication is complete. [67]

1.4 Ferroelectric Materials

Ferroelectric materials can be classified into four structure types: (1) perovskite ABO_3 (e.g. $BaTiO_3$, $PbTiO_3$ etc.), (2) pyrochlore (e.g. $Cd_2Nb_2O_7$), (3) tungsten bronze (e.g. $PbNb_2O_6$ and $PbTa_2O_6$) and (4) layered bismuth oxides (e.g. $SrBi_2Ta_2O_9$). A feature common to these four structures is the presence of ions of small size and large charge (e.g. Ti^{4+}, Nb^{5+}, Ta^{5+} etc.), which are linked through corners forming continuous chains of oxygen-metal-oxygen. This kind of structural arrangement was discovered to be favorable for the occurrence of ferroelectricity in oxides[14,15].

An ideal ferroelectric should have an adequate dielectric constant, reasonable spontaneous polarization, high Curie temperature, low voltage operation, high dielectric breakdown strength, and should be chemically stable. In addition, the ferroelectric capacitor should have good retention and endurance. $Pb(Zr_xTi_{1-x})O_3$ (PZT) has been a well-known material having perovskite structure for all major FRAM development programs currently in progress [16-18]. The choice of PZT is supported by the fact that optimization of hysteresis properties is readily possible by choosing a composition close to the morphotropic phase boundary (between the tetragonal and rhombohedral phases). Sanchez et al. [19] have demonstrated the feasibility of growing films of composition $Zr/Ti = 50/50$, displaying good dielectric integrity and switching properties at thicknesses down to 42.5 nm.

In recent decade, good quality thin films of PZT have been deposited by a number of techniques such as sol-gel [10,19-25], sputtering [26-28], metal-organic deposition (MOD) and chemical vapor deposition (CVD) [29-36]. However, there are still some problems existed with PZT materials for nonvolatile memory device applications, e.g., leakage current and degradation of ferroelectricity such as aging, fatigue, retention and

13

imprint [31,37,38]. Among them, fatigue, a decrease in switchable polarization with increasing number of polarization reversals, is an important reliability issue for FRAM devices which use a destructive readout operation, (switching of polarization at each read/write operation). To improve the fatigue characteristics of PZT-based capacitors, different techniques such as doping and use of oxide electrodes have been proposed [31,32,39-46]. Even though the fatigue rate of PZT-based thin films is improved by the above techniques, high leakage current density is still observed in conjunction with retention and imprint [47]. Unfortunately, there is still no unified process or method that can thoroughly satisfy all the requirements, i.e., low leakage current density and low fatigue rate, in the applications of nonvolatile memory devices.

Recently, alternative materials such as bismuth layered oxides, e.g., $SrBi_2(Ta_{1-x}Nb_x)_2O_9$ (SBTN) which have perovskite-like layer-type structure, were identified as promising candidates for nonvolatile memory applications [48-56]. The bulk bismuth layer-type ferroelectric compounds were discovered in 1959 [57-62]. The family of bismuth layered oxides has the formula

$$(Bi_2O_2)^{2+}(Me_{m-1}R_mO_{3m+1})^{2-}$$
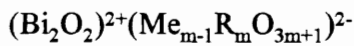
where

Me = mono-, di-, or trivalent ions,

R = Ti^{4+}, Nb^{5+}, Ta^{5+} etc., single or in combination,

m = 2, 3, 4 etc.

These compounds have a structure comprised of a stacking of m perovskite-like units of O-R-O chains between Bi_2O_2 layers along pseudo-tetrahedral c-axis as shown in Figure 1-6. The perovskite-like units are continuous only in the planes perpendicular to the c-axis; along c-axis, the continuous extension of O-R-O chains is interrupted not only by the presence of Bi_2O_2 layers but also by the translation of the perovskite-like units in the

14
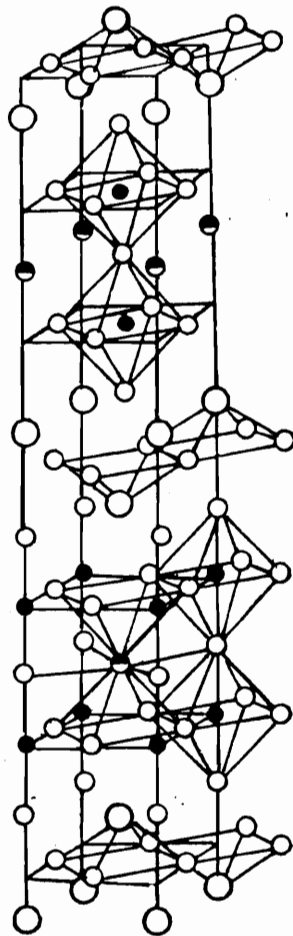
⊖ : Me (Sr, Ba, or Pb),　　　○ : Bi,　　　● : R (Ta or Nb),　　　○ : O

Figure 1-6　　Pseudo-tetrahedral unit cell of $MeBi_2R_2O_9$.

planes perpendicular to the c-axis. Because the presence of RO_6 octahedrons in perovskite-like layers, spontaneous polarization can occur in the planes of these layers.

. $SrBi_2Ta_2O_9$ (SBT) thin films belonging to the family of bismuth layered oxide were found to exhibit no fatigue up to 10^{12} switching cycles, very good retention properties and low leakage current density on Pt electrodes. Figure 1-7 shows a comparison of remnant polarization changes for PZT and SBT with applied fatigue cycles. It is believed that the degradation problems of PZT thin films is due to a surface space-charge layer formed by oxygen vacancies accumulated at electrode-ferroelectric interface [63-66]. On the other hand, SBT is thought to be able to compensate in some way for space-charge and/or oxygen gradient near the electrode, thus increasing the resistance to fatigue. Because of the characteristics of fatigue resistance, these bismuth layered oxides are now being considered as the proper ferroelectric materials to replace PZT for the nonvolatile memory applications.

1.5 Objectives

To be a good ferroelectric thin film for the application of memory devices, a low processing temperature is necessary to avoid the interdiffusion problems between ferroelectric material, electrodes and substrate material, which usually result in degradation problems such as fatigue, retention and imprint, etc. Also a reliable process has to be developed to provide good stoichiometry control, smooth surface morphology, high packing density, and good ferroelectric properties. Although the ferroelectric properties of bismuth layered oxide ceramics were discovered in the past few decades, there was no research on their thin film forms until recently. It was found that high temperature annealing (e.g. $800^{\circ}C$) was required to obtain good ferroelectric properties
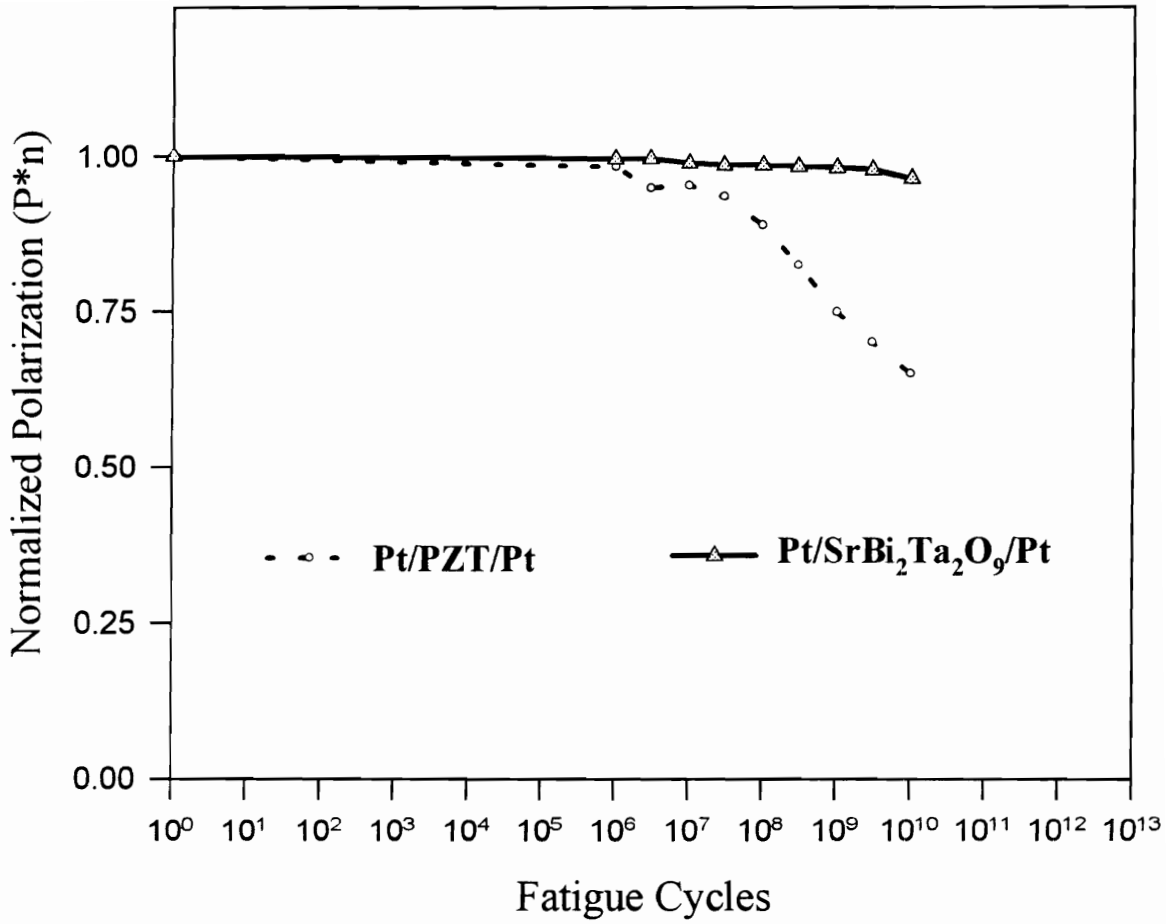
Figure 1-7   Normalized polarization (P*n) comparison of PZT and bismuth
layered oxides (SBT) with applied fatigue cycles.

for SBT thin films [48]. However, such high temperature annealing is unfavorable for thin film fabrication. It was also found that non-stoichiometric compounds (e.g., additional 50% of excess bismuth was added into SBT) were favorable for the occurrence of ferroelectric properties. Until now, it is still not very clear why high temperature annealing and non-stoichiometric compounds are required for the occurrence of ferroelectric properties. Additionally, it is still not clear why bismuth layered oxides have high resistance to electrical degradation.

In order to improve the thin film fabrication process and quality, it is necessary to have well understanding about the fundamental properties of the materials. Therefore, the questions mentioned before have to be answered for successful development of thin film applications in nonvolatile memory devices. This induces the motivation of this research. The primary focus of this research is to study the fundamental properties of bismuth layered oxides, i.e., $SrBi_2(Ta_{1-x}Nb_x)_2O_9$, so that it can provide a guideline for fabricating high quality ferroelectric thin films with adequate high P_r, low E_c, low leakage current density and high resistance to degradation.

In this research, the bismuth layered oxides, $SrBi_2(Ta_{1-x}Nb_x)_2O_9$ (SBTN), were investigated in both bulk and thin film forms. The objectives of this research were:

(I) lower the thin film process temperatures by reducing nucleation and grain growth temperatures, and

(II) provide a guideline for thin film applications on nonvolatile memory devices by investigating the structures and properties of bulk materials.

By accomplishing objective (I), low temperature processes of thin film fabrication can be established, which may reduce the process difficulties and cost. The objective (II) provides the fundamental understanding of the bulk ceramics which can help to optimize the

composition and process conditions for thin films to have better performance on the applications.

In the first objective, low temperature processes of thin film fabrications are pursued. To achieve this, it is necessary to know where the characteristic temperatures (i.e., nucleation and grain growth temperatures) are. To learn this, a study of structure development by the spectroscopic ellipsometry for SBTN thin films made by metalorganic decomposition (MOD) is proposed. By learning the phase formation mechanism, low temperature processes can be achieved by reducing either the nucleation or grain growth temperatures. The structure development study and low temperature processing of SBTN thin films are discussed in detail in Chapter 3, after the introduction and samples preparation description of the whole research in Chapter 1 and 2 respectively.

Via the structure development study, it was found that post-top-electrode-deposition annealing and additional amount of Bi in SBTN thin films were required to exhibit good ferroelectric hysteresis properties. Therefore, further studies for the effects of Bi concentration on ferroelectric properties were shown in Chapter 4.

To achieve the second objective, it is necessary to have better understanding about the structure and property relationship of SBT ceramics. The advantage for studying bulk ceramics is to overcome the difficulties that are associated with thin film technology, e.g., electrode-ferroelectric interfaces, grain size effect and packing density of the films. The optical properties of SBTN bulk ceramics were studied in Chapter 5 for fundamental understandings. The conduction mechanism was studied in terms of ion transportation phenomenon in the bulk materials. To learn this, an unique technique of impedance spectroscopy was proposed in Chapter 6 for electrical properties characterization.

Chapter 2.   Sample Preparation

This chapter describes the preparation procedures of SBTN samples in both bulk and thin film forms. The sample preparation procedure of SBTN thin films by metalorganic decomposition method (MOD) is applied in Chapter 3 and 4 for thin film characterization. While the preparation procedure for bulk SBTN ceramics by solid state reaction is applied in Chapter 5 and 6 for bulk properties characterization. The experimental procedures of each subject are described in the individual chapter.

2.1 Thin Film Preparation

2.1.1 Preparation of MOD Precursor Solutions

SBTN ferroelectric thin films were fabricated by the MOD method. Strontium 2-ethylhexanoate ($Sr(C_7H_{15}COO)_2$, 99.8%, from Alfa Chemicals (Alfa)), Bismuth 2-ethylhexanoate ($Bi(C_7H_{15}COO)_3$, 99%, (Alfa)), Tantalum ethoxide ($Ta(OC_2H_5)_5$, Assay, Gelest Inc. (GI)), Niobium (V) ethoxide ($Nb(OC_2H_5)_5$, 99.95%, Aldrich Chemical Company (ACC)), and 2-ethylhexanoic acid ($C_7H_{15}COOH$, 99%, ACC) were used as the starting materials with xylene (A.C.S. Aldrich) as the solvent. A flow chart of SBTN precursor solution preparation by MOD method is shown in Figure 2-1. Initially, tantalum ethoxide and niobium ethoxide were added to 2-ethylhexanoic acid. The solution was stirred and heated to a maximum temperature of 100 - 120°C to distill out the alcohol and water and increase the reaction rate. After the reaction was complete, the solution was cooled to room temperature and a measured quantity of strontium 2-ethylhexanoate with
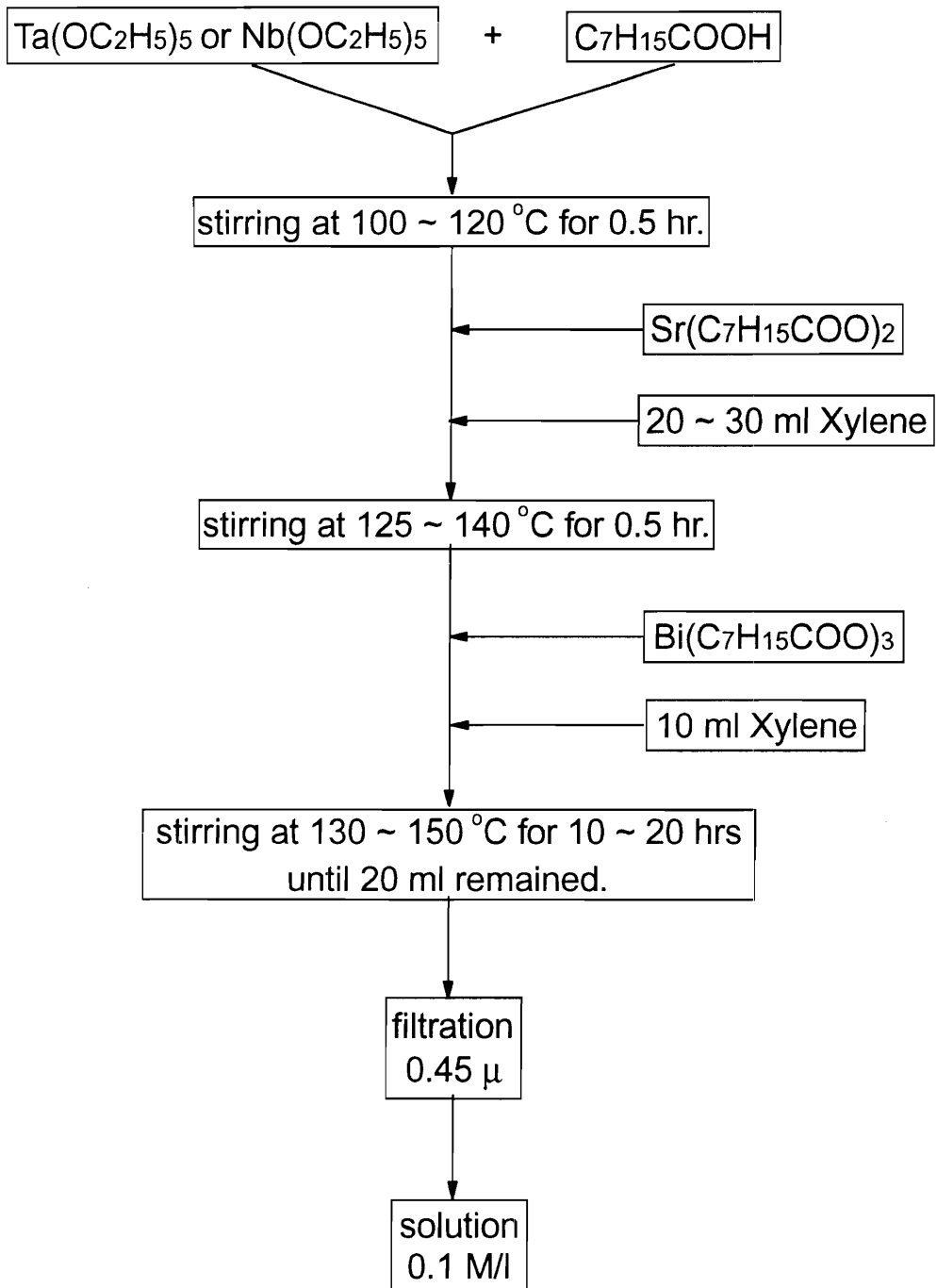
Figure 2-1. The preparation procedure of SBTN precursor solutions by MOD.

20 - 30 ml of xylene was added to the solution. The resulting solution was stirred and heated to a maximum temperature of 125 - 140°C until a clear solution was formed. Subsequently, bismuth 2-ethylhexanoate with 10 ml xylene was added to the above solution with continued stirring. The temperature was maintained at 130 - 150°C to distill out all the light hydrocarbon fraction, water and some xylene until 20 ml of solution remained. The final concentration of the solutions were 0.1 moles of $SrBi_2Ta_2O_9$ per liter. Finally, the solutions were passed through a filter with 0.45 micron pore size to remove dust and other particles.

2.1.2 SBTN Thin Film Preparation

The precursor solution was then dispensed onto $Si/SiO_2/Ti/Pt$ or sapphire substrates for spin coating. A flow chart of MOD thin film prepared by a Headway Research Photo-Resist Spinner is shown in Figure 2-2. The substrates were spun at approximately two thousand revolutions per minute for 30-40 s in air during which the excess fluids were removed and the solvents were driven off leaving the substrate surface with a uniform coating of the organic film. The coated substrates were then baked at 210 - 230°C for 3 minutes in air to remove all the excess solvents. The spin-bake cycle was repeated several times to obtain the desired thickness (1000 - 3000Å) of the final films. The soft metalorganic films were then pyrolyzed to convert the metalorganic precursors to their constituent oxides, or other compounds. The annealing treatments were typically carried out in a tube furnace at temperatures ranging from 450 - 750°C for 3 hours in oxygen atmosphere. The heat treatment removed all the solvent and organic components and resulted in a dense, single-phase thin film. For electrical properties measurement, a top

substrate baking at 130 ~ 150°C for 0.5 hr.

few drops of SBTN precursor solution on substrate

spin coating with 2000 rpm / 30 sec.

3 cycles

baking at 210 ~ 230°C for 3 mins

baking in oxygen atmosphere at 450°C for 3 hrs

1st annealing in oxygen atmosphere at 500 ~ 750°C for 3 hrs

structure development study

top Pt electrode deposition (sputtering)

2nd annealing at 700°C for 1 hr.

Ferroelectric properties characterization

Figure 2-2. The preparation procedure of SBTN MOD thin films.

Pt-electrode was sputtered onto the films followed by a post-top-electrode-deposition annealing.

2.2 Preparation of SBTN Bulk Ceramics

The bulk of samples were made by solid state reaction method starting from mixing the metal oxide powders, $SrCO_3$, Bi_2O_3, Ta_2O_5 and Nb_2O_5 (from Alfa with purity greater than 99.9%), with desired quantities. A flow chart of bulk sample preparation is shown in Figure 2-3. The SBT and SBN powders were obtained by calcinating the mixing powders for $1050^{\circ}C$ in 3 hours. With the calcinated powders a pellet form of sample can be made. The pellets were sintered at $1280^{\circ}C$ for 3 hours. In order to have an external contact, the platinum electrodes were sputtered onto both sides of SBN pellet. Then it had a platinum lead attached on the electrodes with platinum paste. Whereas, for SBT sample, a platinum lead was directly attached on each side of the pellet with platinum paste.
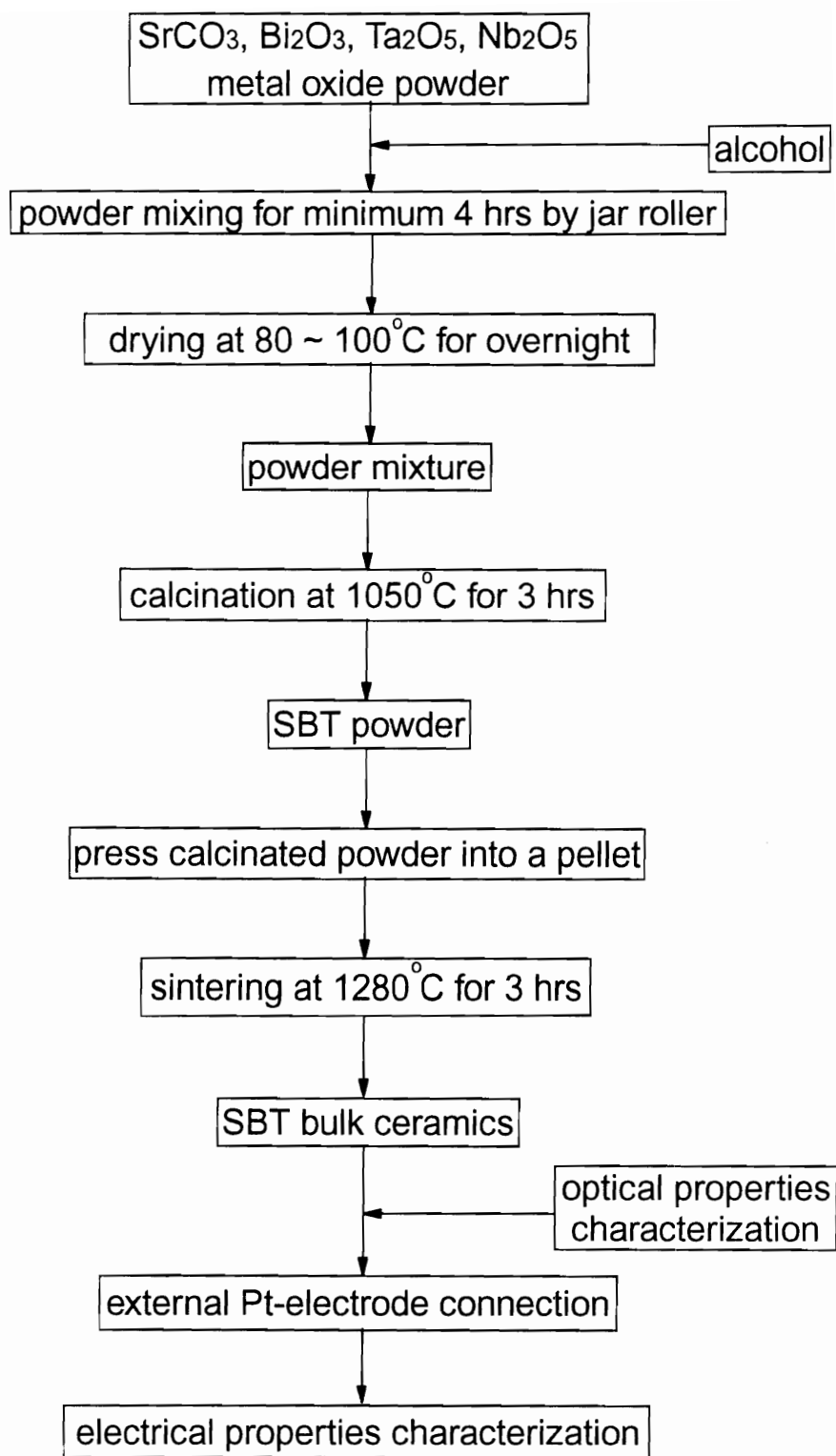
Figure 2-3. The preparation procedure of SBT bulk ceramics.

Chapter 3. Structure Development Studies of $SrBi_2(Ta_{1-x}Nb_x)_2O_9$ Thin Films

In this research, two tasks were pursued: (1) determination of the onset temperature of ferroelectric hysteresis properties of $SrBi_2Ta_2O_9$ thin films by structure development study, and (2) low temperature processing for thin film fabrication. For task (1), a non-destructive optical method using spectroscopic ellipsometry was proposed for characterizing the structure development of $SrBi_2Ta_2O_9$ thin films. By comparing the results of the structure development study and ferroelectric hysteresis properties investigation, the onset temperature of hysteresis curve of $SrBi_2Ta_2O_9$ with 50% excess Bi was determined. For task (2), the effects of excess Bi content and Nb/Ta ratio of $SrBi_2(Ta_{1-x}Nb_x)_2O_9$ on ferroelectric hysteresis properties were studied.

3.1 Introduction

Although the SBT ferroelectric thin films were fabricated successfully in our laboratory[50-52,55,68,69], there are still some processing difficulties that need to be overcome. One of these problems is the processing temperature of the thin films. Recent studies on the structure and ferroelectric properties of SBT thin films [50-52,55,68,69] showed that good ferroelectric hysteresis properties in SBT thin films can only be obtained with annealing temperatures around 700 - 800°C. However, for FRAM applications, low temperature processing (*e.g.*, lower than 650°C) of the ferroelectric thin films is necessary to avoid interlayer diffusion and other problems.

For the case of PZT thin films, the ferroelectric hysteresis properties with high remanant polarization (P_r) can be obtained at temperature range of 600 - 650°C. Previous studies by Kwok and Desu [23,24,70,71] show that, for PZT thin films, the critical process to obtain well-defined hysteresis curve is the nucleation of the perovskite phase. Once the perovskite phase is formed, the hysteresis curves of PZT thin films can be obtained at relatively low temperatures (*e.g.* about 600°C). For SBT thin films, the phase formation of layer-type structure occurs at temperatures as low as 550 - 650°C. However, very poorly-defined hysteresis properties were detected for these SBT films at such low temperatures. The critical factors that control the onset of well-defined hysteresis curve of SBT is obviously not simply the nucleation process as in the PZT case.

In order to reduce the processing temperature, the needs for high temperature annealing of SBT thin film have to be understood. One way to do this is to study the structure development of bismuth layered oxides. Understanding the various aspects of structure development in these thin films is the key for developing possible alternative low temperature processes.

A structure development study of PZT thin films by an non-destructive optical envelop method using UV-VIS spectrum data was proposed by Peng and Desu [72,73]. This technique was very effective in identifying various characteristic temperatures and the kinetics of phase transformation in PZT films. It is expected that the optical properties will be different for different structure phases (*e.g.*, amorphous, pyroclore and perovskite phases) Using the nature of structure change during phase transformation, one can obtain information on structure development by following the changes of refractive index and film thickness as functions of annealing temperature. By observing these changes, the initiation and completion temperatures of phase formation can be identified. This optical

method was suggested to be more effective than conventional nondestructive techniques such as x-ray diffraction.

In this research, the study of structure development was employed to determine the onset temperature of ferroelectric hysteresis curves in SBT thin films. A new non-destructive optical method using spectroscopic ellipsometry was proposed for characterizing the structure development of the thin films. Spectroscopic ellipsometry is a branch of reflection techniques using polarized incident light. One of the advantage of this technique is that the thin films can be deposited directly on a reflective Pt-substrate rather than a transparent substrate. Another advantage is that the thickness and the optical properties of the films can be obtained simultaneously. Thus information on structure development can be obtained by observing the refractive indices and film thicknesses changes as a function of annealing temperature. Moreover, the effects of excess Bi in SBT thin film and Nb/Ta ratio of $SrBi_2(Ta_{1-x}Nb_x)_2O_9$ (or SBTN) solid solutions on the onset of hysteresis curves were investigated with an aim to reduce the processing temperature. The phase transformation of the polycrystalline bismuth layered oxide from the amorphous phase was identified by XRD.

3.2 Experimental Procedure

The SBTN thin films were prepared by the metal-organic decomposition (MOD) method as described in Section 2.1. Precursors were prepared for the compositions of $SrBi_2Ta_2O_9$, $SrBi_2(Ta_{0.4}Nb_{0.6})_2O_9$ and $SrBi_2Nb_2O_9$ with 0% and 50% excess Bi. For structure development study, a thin film was spin coated on a Pt coated silicon substrate. For phase identification by XRD, a film was spin coated on a sapphire substrate. The films were then annealed at 400°C in oxygen atmosphere for 3 hours and then characterized by

28

spectroscopic ellipsometry, XRD and SEM. The anneal and characterization steps were repeated for incremental temperature increases of 50°C until the maximum anneal temperature of 800°C was reached. In other words, all of the anneal cycles and measurements were done on one sample excluding the samples for ferroelectrics characterization. For ferroelectrics characterization, several SBTN films of the same composition were deposited by the same method. These films were each annealed at different temperatures from 600°C to 800°C at 50°C intervals. After the heat treatment, a Pt-electrode was sputtered on top of the film for external connection. A second annealing was done after top electrode deposition. The ferroelectrics characterization was then done before and after this post top-electrode-deposition annealing.

3.3 Optical Method: Spectroscopic Ellipsometry

Spectroscopic ellipsometry is a branch of reflection spectroscopy using linearly polarized incident light, which yields information about the optical constants of materials, the thickness of overlayers, and the roughness and porosity of thin films. In this research, the ellipsometry parameters, Δ and Ψ, were analyzed by the software developed by J.A. Woollam Company. The analysis consists of building a nominal optical model for the sample, choosing fit parameters such as film thickness and optical constants, and initiating a regression algorithm. In order to obtain the accurate results, the appropriate optical model has to be built up according to the natural of thin films. In general, most deposition techniques produce thin films with a relative density less than unity. Therefore, porosity in the film has to be considered as a separate single phase. Figure 3-1 shows the optical model for a SBT MOD thin film grown on a Pt substrate. In this model, it is assumed that the film with a thickness d is a two phase mixture consisting of a bulk SBT phase and
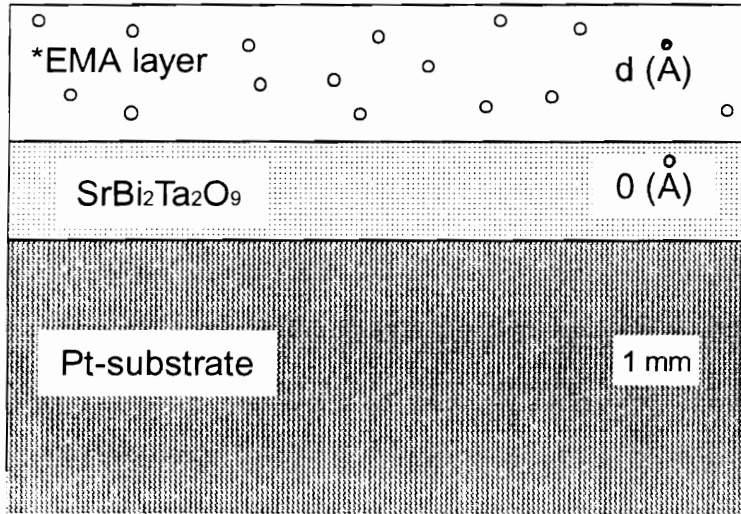
Figure 3-1   The optical model for SBT MOD thin film.
(*EMA layer = SBT bulk phase + porosity)

porosity. The Bruggeman effective medium approximation (EMA)[74] was used to describe this effective layer of two phases mixture, which can be expressed by

$$f \frac{n_b^2 - n^2}{n_b^2 + 2n^2} + (1-f) \frac{1-n^2}{1+n^2} = 0 \tag{3-1}$$

where f is the volume fraction of material, n_b is the refractive index of the bulk material and n is the effective refractive index of the heterogeneous medium.

A dummy layer representing void-free SBT with zero thickness is inserted in-between the Pt-substrate and the film. The optical constants obtained from this dummy layer represent the actual optical constants of SBT bulk phase excluding the porosity. Change in the parameters for this dummy layer will reflect the optical constants change in the real SBT film (*i.e.*, the top layer with the mixture of SBT and voids). On the other hand, the thickness of the effective EMA layer, which includes SBT and porosity, represents the actual overlayer thickness of deposited SBT film. This optical model was also applied on the other SBTN MOD films.

3.4 Results And Discussion

3.4.1 Structure Development Study of SBT with 50% Excess Bi Content

3.4.1.1 Structure Development Model of MOD SBT Thin Films

In general, the phase transformation of an MOD thin film usually starts from an amorphous phase because the starting material is a metal-organic precursor. In the case of

PZT, an intermediate phase, *i.e.* the pyrochlore phase, is always found during phase transformation from the amorphous to the perovskite phase. By comparison, the phase transformation of bismuth layered oxide SBT is simpler than that of PZT. The structure development of MOD SBT thin films from the initial as-deposited state to the final layer structure phase involves phase transformation of three different phases, i.e., the metalorganic compounds (MO), the amorphous phase (A), and the crystalline layer structure phase (C). The model of structure development for the materials is illustrated as Figure 3-2. In this model, it is assumed that the film has three single-phase states and one two-phase-mixture at certain temperature intervals. After solvent removal at about 220°C, the film is constituted of a mixture of metalorganic compounds. As temperature increases to T^A, the amorphous phase is formed. In this research, T^A is typically set at 450°C at which all the films are pyrolyzed. When the annealing temperature increases to T_i^C, the SBT crystalline phase is initiated from the amorphous phase. As temperature increases to T_c^C, the crystalline phase is completely formed. When the annealing temperature increases further, grain growth takes place.

It is well known that ferroelectric hysteresis properties can only occur in SBT crystalline phase rather than amorphous phase. Thus, according to the structure development model, the onset temperature for obtaining well-defined hysteresis curves for SBT, T_0^H, may occur either during amorphous-crystalline phase transformation or during the grain growth process.

3.4.1.2 XRD Results

In Figure 3-3, the XRD patterns of SBT with 50% excess Bi were plotted as a function of annealing temperature. For SBT MOD thin films, the perovskite-like layer
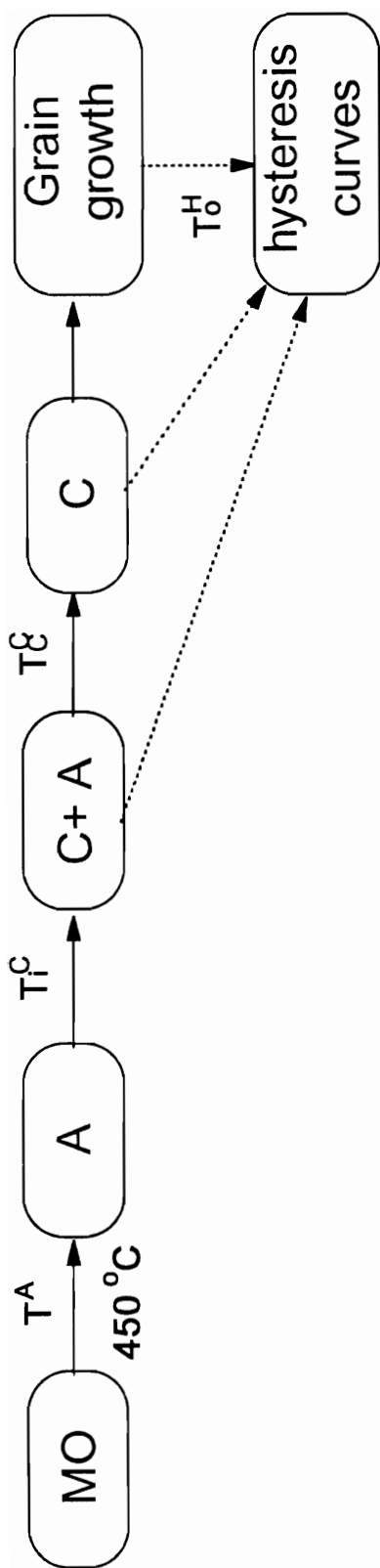
Figure 3-2   Structure development model of SBT MOD thin film.

Figure 3-3   Temperature dependence X-ray diffraction patterns of SBT thin films with 50% excess Bi. (deposited on saphirre substrates)

structure phase was nucleated directly from the amorphous phase without exhibiting any intermediate phase as shown in Figure 3-3. For temperatures below 500°C, a small but very broad peak around 2θ angle of 28 -30° indicates that the SBT film was amorphous. When the annealing temperature was increased to 550°C, this major peak increased in intensity and FWHM of the peak also decrased. At the same time, three other small and broad peaks began to show up at 2θ = 33°, 48° and 56°. The presence of all these peaks indicate that the SBT crystalline phase with very fine grain size had formed. This suggests that the initiation of amorphous-crystalline phase transformation (i.e., T_i^C) occurs at about 500 - 550°C. As temperature was increased further, peaks showed a small shift in 2θ and became sharp with high intensity. Finally, for anneal temperatures above 700°C, the diffraction lines were consistent with the major peaks of polycrystalline SBT, and this is a sign of complete crystallization of SBT. In other words, the temperature of complete crystallization of the film, T_c^C, was observed at about 650 - 700°C. It can be seen that, within whole temperature range, no intermediate phases at moderate temperatures and no second phase at high temperatures were observed.

From XRD data, we have learned that the T_i^C and T_c^C of SBT occurred at temperatures as low as 500 - 550°C and 650 - 700°C, however, no ferroelectric hysteresis curves were detected for annealing temperatures below 700°C. This implies that the onset temperature of well-defined hysteresis curve for SBT, T_O^H, is not simply controlled by the formation of crystalline phase. According to the proposed structure development model, the T_O^H possibly occurred during grain growth process. Although the X-ray diffraction method is a direct technique for investigating phase transformation, for studying grain growth it is not a very effective technique. Compared to the XRD method, optical method, which is discussed in the next section, provided more detailed information on the grain growth process.

3.4.1.3 Optical Method

The optical properties and the thicknesses of SBT thin films were measured using spectroscopic ellipsometry. The optical model for the sample has been discussed in Section 3.3 above. Figure 3-4 shows the changes in refractive index and overall thickness of SBT thin films as a function of annealing temperature. Additionally, the relative grain sizes and the ferroelectric hysteresis curves as a function of temperature are also illustrated in Figure 3-4. In general, the overall thickness of the film decreased with increasing annealing temperature, whereas the refractive index increased. Basically, the curves in Figure 3-4 can be divided into three regions, *i.e.*, amorphous phase (I), amorphous-crystalline phase transformation (II) and grain growth (III) regions. In region I, the organic component of the precursor was burnt off and the film structure was amorphous with a low refractive index of about 1.8 - 1.9. In this region, the refractive index and film thickness were almost constant and no ferroelectric hysteresis curves were observed. According to the XRD data, the initiation temperature of phase transformation, T_i^C, occurred towards the end of this region (*i.e.*, 500 - 550°C).

In region II, gradual changes of refractive index and film thickness were observed. As the annealing temperature was increased, the film thickness decreased while the refractive index increased. Although the slopes of the curves obtained in this region are small, it still suggests that these gradual changes are responsible for the amorphous to crystalline phase transformation of SBT films as confirmed by the above XRD data. Complete crystallization, T_c^C, occurred at the end of this region according to the XRD data (*i.e.*, 650 - 700°C). However, the films exposed to temperatures of region II did not exhibit any ferroelectric hysteresis properties.

Figure 3-4   Temperature dependence refractive index (at wavelength of 640 nm) and film thickness for SBT with 50% excess bismuth (deposited on Pt substrate).

*Longitudinal grain: only length of the grain is shown here.

37

In the region III of Figure 3-4, abrupt changes of refractive index and film thickness were observed, which were associated with the grain growth process. Figure 3-5 presents the typical example of surface morphology of the films annealed at 650°C and 700°C. As annealing temperature increased from 650°C to 700°C, the grain size increased by about 2 times in width and almost 4 times in length. Complete crystallization and large grain size led to a dramatic decrease in film thickness and increase in refractive index.

Comparison of ferroelectric properties of the films exposed to regions I, II and III (Figure 3-4) indicates that well-defined hysteresis curves could only be obtained for SBT films annealed at temperatures above 700°C. At an annealing temperature of 650°C, the hysteresis loop was only open a little with a small value of $2P_r$ as shown in Table 3-1. However, higher annealing temperatures, e.g. above 700°C, substantially improved the hysteresis curves of SBT thin films. For annealing temperatures above 700°C, saturated ferroelectric hysteresis loops were observed with a larger value of $2P_r$.

While MOD SBT films with $2P_r$ values greater than 20 μC/cm² have been successfully fabricated in our laboratory [53], the $2P_r$ values presented in Table 3-1 are significantly lower (< 7 μC/cm²) and the hysteresis curves obtained are asymmetric to $E = 0$ at origin. This is because the process parameters for film fabrication were not optimized in the present study. The asymmetric loop is due to the asymmetry of top and bottom electrode-ferroelectric interfaces, which is discussed in a seperate paper [68]. This electrode interface asymmetry can be improved by a post-top-electrode-deposition heat treatment.

(a) 650°C
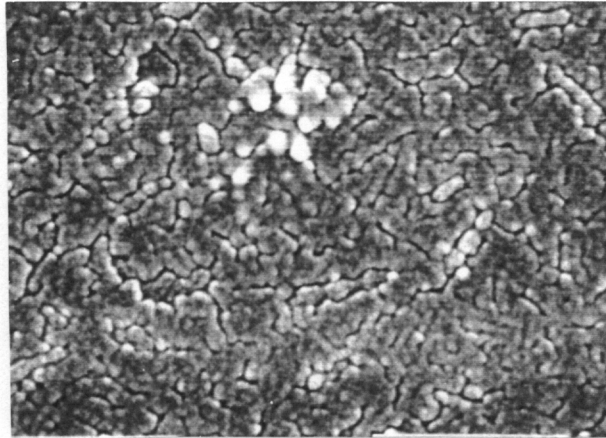
(b) 700°C
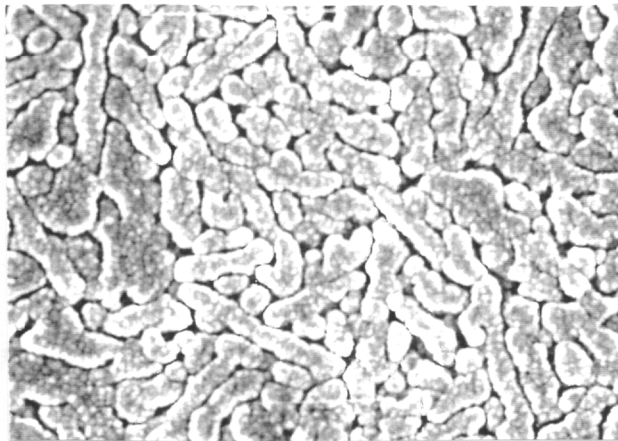
0.2 μm

Figure 3-5   Surface morphology of SBT thin film with 50% excess Bi
annealed at temperatures of (a) 650°C and (b) 700°C. (SEM
photos with 50000X magnification) (deposited on Pt substrate)

Table 3-1.   The remnant polarization ($2P_r$) and grain size (G.S.) of $SrBi_2Ta_2O_9$ with 0% and 50% excess Bi at different annealing temperatures. ($2P_r$ was measured by RT66 Ferroelectricity Characterizer, and grain size was measured by SEM morphology)

exc. Bi %		Annealing Temperature				
		600°C	650°C	700°C	750°C	800°C
50%	$2P_r$ (μC/cm^2)	0.2	3.23	6.17	4.10*	--**
	G.S.‡ (L/W) (µm)	0.04/0.04	0.07/0.04	0.27/0.10	0.39/0.11	0.40/0.14
0%	G.S.† (µm)	0.03	0.04	0.05	0.07	0.08

* Low $2P_r$ value is due to asymmetry of hysteresis loop.

** At annealing temperature above 800°C, electrical breakdown was occurred.

‡ The longitudinal grains were observed for 50% excess Bi.

† The grains are uniaxial (width = length) for 0% excess Bi.

Several interesting phenomena were observed by comparing the results of the structure development and ferroelectric properties investigations. For temperatures below 650°C, grain sizes were smaller and no ferroelectric hysteresis properties were detected. However, for temperatures above 700°C, larger grain size and better hysteresis curves were observed. These evidence suggest that, for SBT thin films, the onset temperature of well-defined ferroelectric hysteresis curves, T_O^H, is dominated by grain growth process rather than phase transformation process. The critical factor that controls T_O^H was found to be the grain size. In order to obtain well-defined hysteresis curves, the grain size of the film has to be above a critical value. Unlike PZT, where the ferroelectric axis can be one of the three axes, the ferroelectric axis of SBT layer-type structure is restricted to a-b plane [50,51]. Due to the constriction of ferroelectric axis and the layered structure, it is expected that larger grain size is required for SBT thin film to have enough dipoles line-up to exhibit ferroelectric hysteresis curves. In the case of SBT thin film with 50% excess Bi, the T_O^H is at about 700°C, and the critical grain size is about 0.1 μm in width and 0.27 μm in length.

3.4.2 Low Processing Temperature of SBT MOD Thin Films

3.4.2.1 The Effect of Excess Bi in SBT Thin Films

It is clear from the previous section that the critical factor controlling the hysteresis curves was the grain growth process. In order to exhibit ferroelectric hysteresis curves, the grain size of the film has to be larger than a critical value. However, the requirement of the additional amount of Bi to show hysteresis curves needs to be investigated. In this section, the effect of excess Bi in SBT thin films is presented.

Figure 3-6 shows the XRD patterns of SBT thin film with 0% excess Bi. The T_i^C of the compound was found to be around 600 - 650°C, whereas the T_c^C was about 750°C. The initiation and completion temperatures of amorphous to crystalline phase transformation for SBT with 0% excess Bi was found to be about 100°C higher than that for SBT with 50% excess Bi. However, no ferroelectric hysteresis curves were detected even at annealing temperature as high as 750 - 800°C for the compound with 0% excess Bi.

Figure 3-7 shows the structure development of SBT with 0% excess Bi by optical method. In this figure, the region of phase transformation at lower temperatures was not significant. However, the grain growth region was observed for temperatures above 650°C. By comparing, although the temperature region for grain growth were similar for both 0% and 50% excess Bi (Figure 3-4), the slopes of the curves obtained in this region for 0% excess Bi were smaller than that of 50% excess Bi. The values of refractive indices increased with increasing excess Bi content. At 700°C, higher value of refractive index (n ~ 2.10) for SBT with 50% excess Bi was observed than for the SBT with 0% excess Bi (n ~ 1.89). The higher value of refractive index and smaller slopes in grain growth region suggest larger grain and denser film formation for the compound with 50% excess Bi. Figure 3-8 shows the thin film surface morphology of SBT with 0% excess Bi at 700°C and the calculated grain sizes at various annealing temperatures are listed in Table 3-1. A dramatic increase of grain size was observed by the addition of excess 50% of Bi.

The grain size effect may explain the absence of hysteresis curves for SBT with 0% excess Bi. Even though the temperature region of grain growth occurred at about 650 - 750°C, the value of grain size was far beyond the critical grain size. In other words, the onset temperature of hysteresis curve, T_0^H, could be much higher than T_c^C. In conclusion, the structure development studies of SBT thin films indicates that the excess Bi in SBT
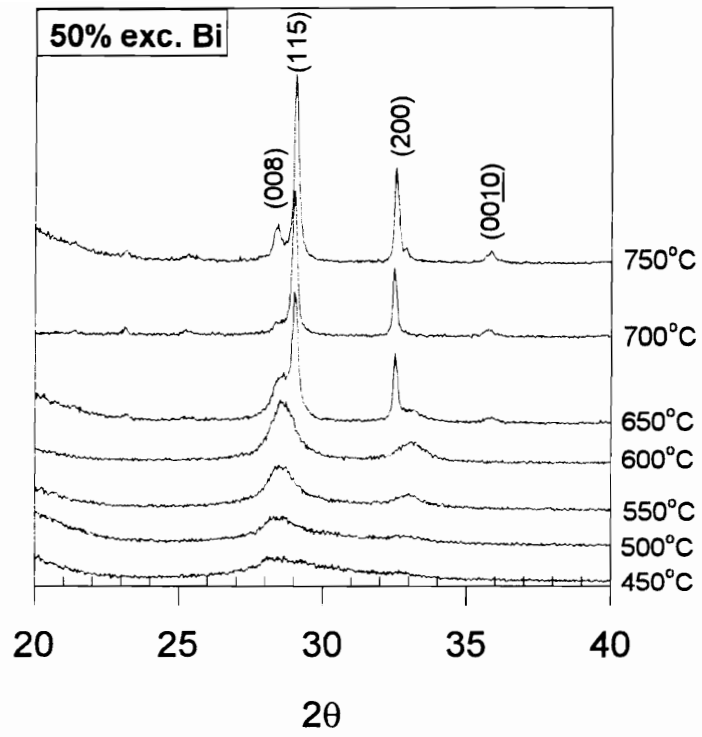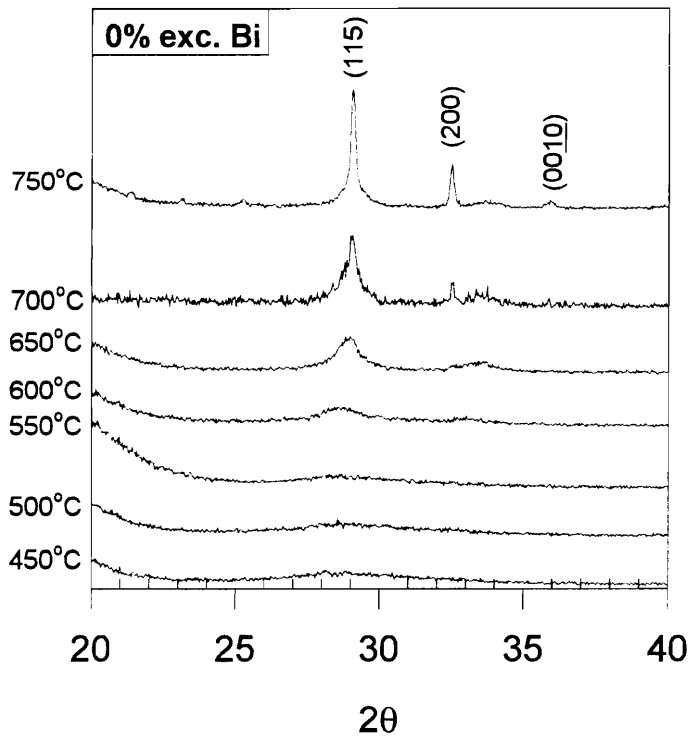
Figure 3-6   Temperature dependence X-ray diffraction patterns of SBT thin films with 0% excess Bi. (deposited on saphirre substrates)
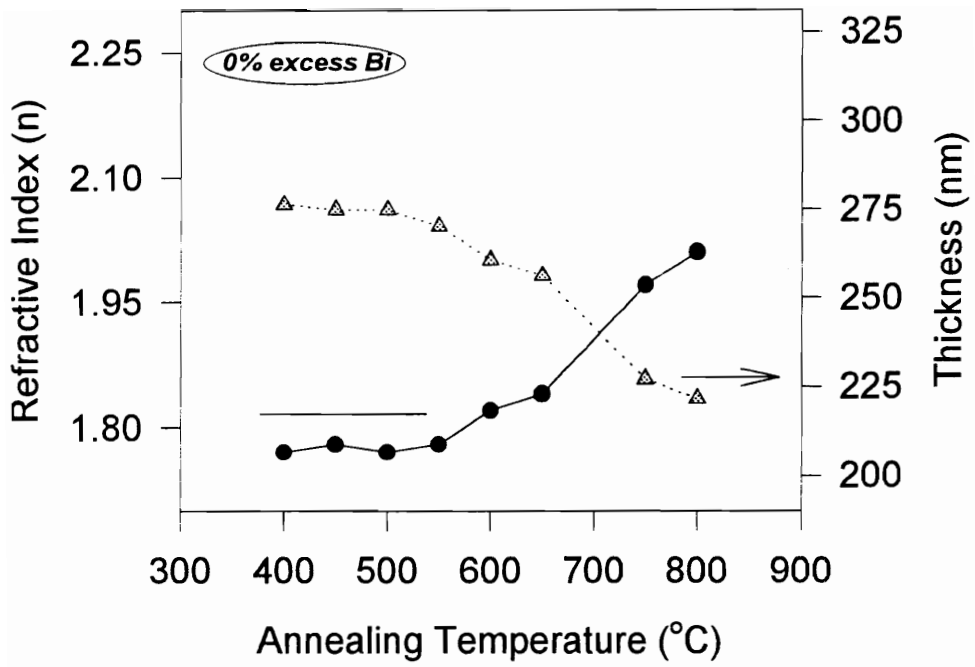
Figure 3-7   Temperature dependence refractive index (at wavelength of 640 nm) and film thickness for SBT with 0% excess Bi.
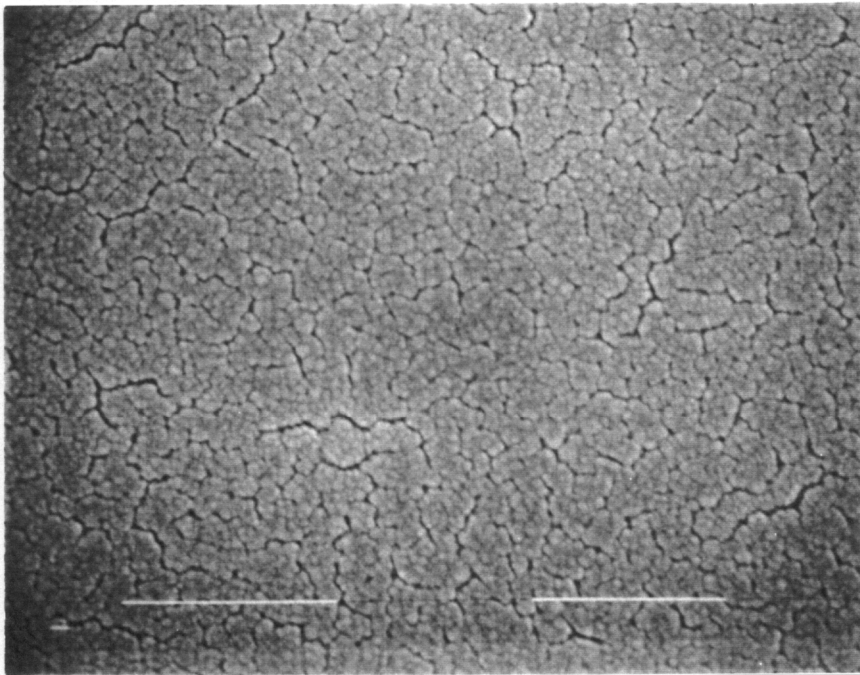
0.2 µm

Figure 3-8   Surface morphology of SBT thin film with 0% excess Bi
              annealed at 700°C. (SEM photos with 50000X magnification)
              (deposited on Pt substrate)

thin films has the effects of reducing the phase transformation temperature and also enhancing grain size at lower annealing temperature. Excess bismuth was required to lower the hysteresis onset temperature of SBT thin films, which was eventually lowered to 700°C by adding 50% excess Bi in the films.

3.4.2.2 The Effect of Nb/Ta Ratio for SBTN Solid Solutions

The results of the above studies suggest that, to approach lower processing temperature, larger grains have to be grown at lower temperature. In this section, the effect of Nb/Ta ratio on the T_0^H is presented. The structure development of stoichiometric $SrBi_2(Ta_{1-x}Nb_x)_2O_9$ solid solutions (with 0% excess Bi) was studied for compositions of x = 0.6 and 1. Figure 3-9 shows the X-ray diffraction patterns of SBTN as a function of annealing temperature. By comparing with the XRD data of SBT with 0% excess Bi (x =0) in Figure 3-6, it was found that the initiation temperature of phase transformation, T_i^C, decreased by about 50°C (from 600°C to 550°C) with increasing x values from 0 to 1. The temperature of complete crystallization of SBTN, T_C^C, was also found to be about 100°C lower (i.e., from 750°C to 650°C) with increasing x values from 0 to 1.

The results of structure development of SBTN by optical method were shown in Figure 3-10. By comparing to the data of SBT with 0% excess Bi in Figure 3-7, it was found that the temperature region of grain growth shifted to lower temperature with increasing Nb/Ta ratio. With increasing x value from 0 to 1, the grain growth region shifted from about 700°C to 550°C. In other words, the temperature of grain growth process is reduced by the substitution of Ta anion by Nb anion. Figure 3-11 shows the surface morphology of SBTN at 650°C. A significant increase in grain size was observed with increasing Nb/Ta ratio.

46
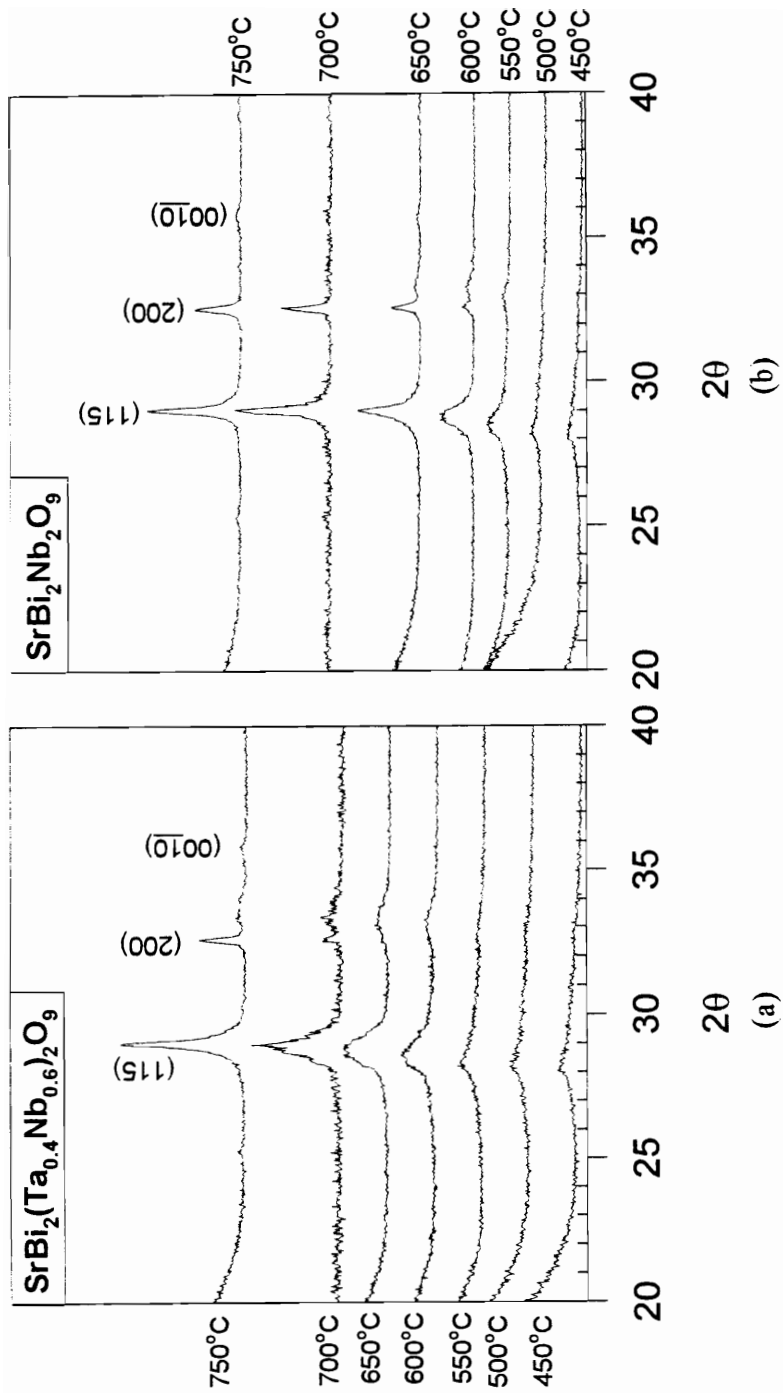
Figure 3-9   Temperature dependence X-ray diffraction patterns of (a) $SrBi_2(Ta_{0.4}Nb_{0.6})_2O_9$ and (b) $SrBi_2Nb_2O_9$ thin films with 0% excess Bi. (deposited on saphirre substrates)
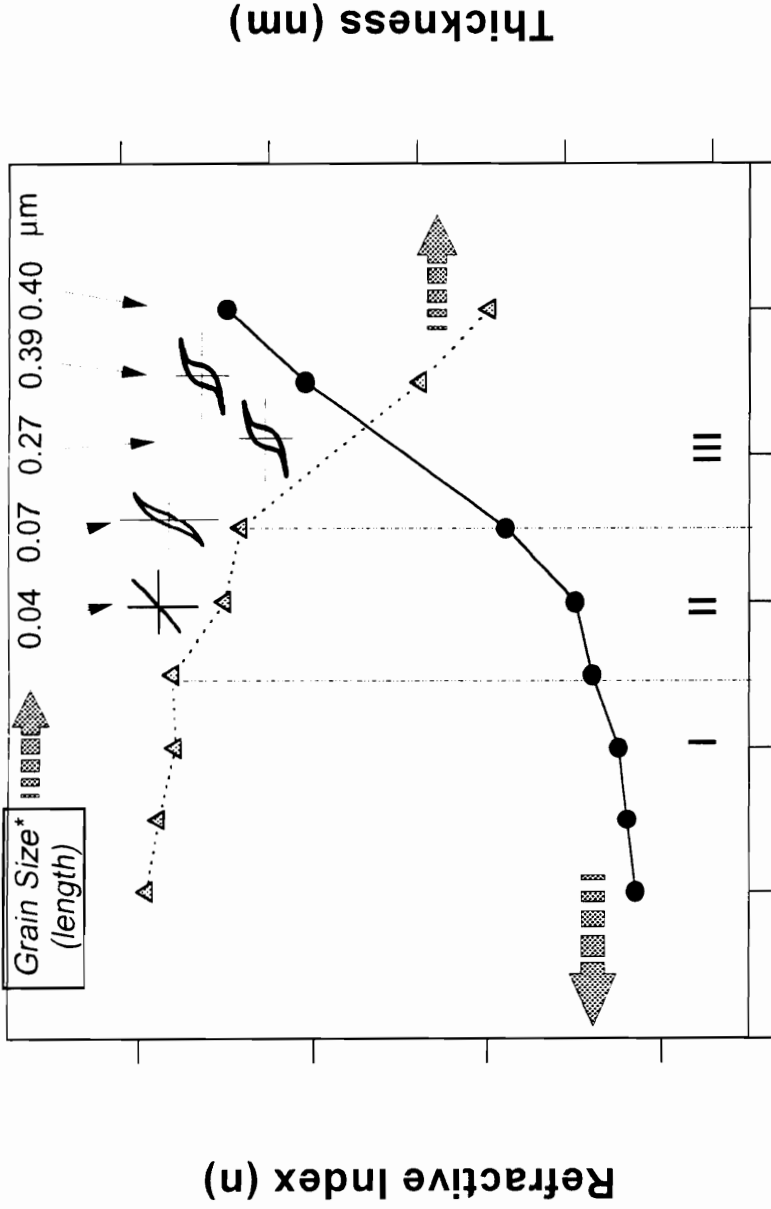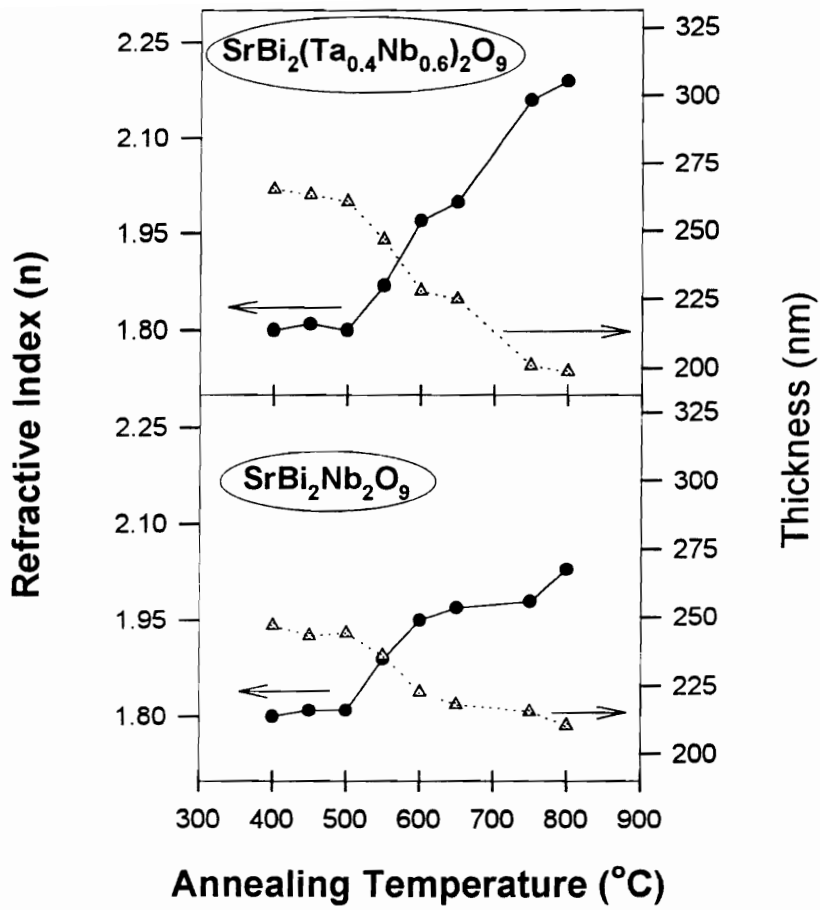
Figure 3-10   Temperature dependence refractive index (at wavelength
of 640 nm) and film thickness for SBTN with 0% excess Bi.

(a) $SrBi_2Ta_2O_9$
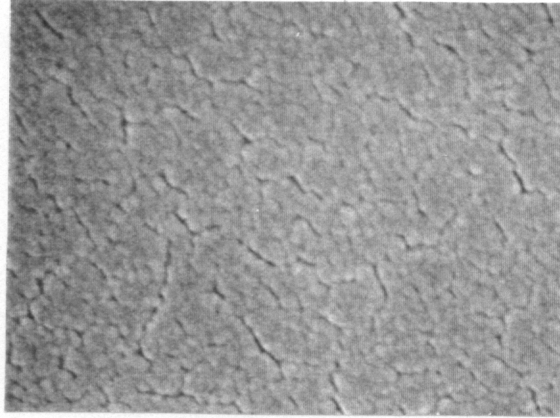
(b) $SrBi_2(Ta_{0.4}Nb_{0.6})_2O_9$
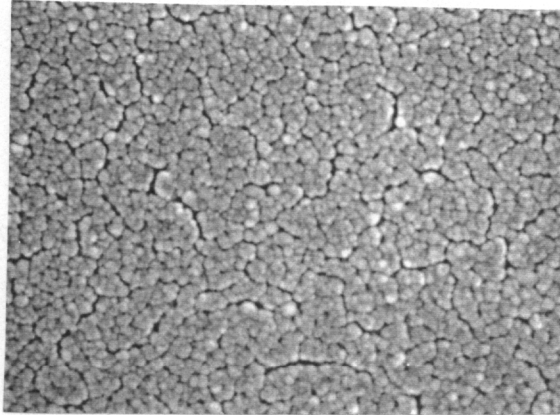
(c) $SrBi_2Nb_2O_9$
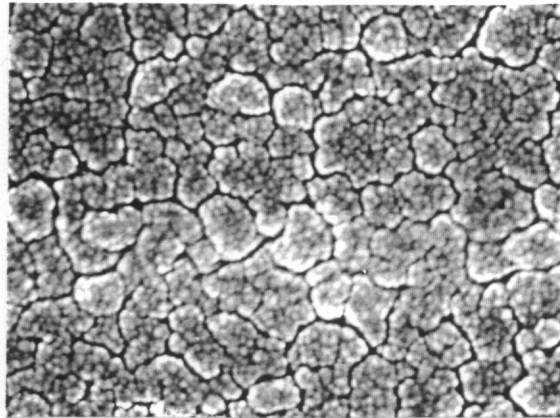
0.2 μm

Figure 3-11   Surface morphology of (a) $SrBi_2Ta_2O_9$, (b) $SrBi_2(Ta_{0.4}Nb_{0.6})_2O_9$, and (c) $SrBi_2Nb_2O_9$ thin films with 0% excess Bi annealed at 650°C. (SEM photos with 50000X magnification)(deposited on Pt substrate)

However, no ferroelectric hysteresis curves were detected for SBTN thin films with 0% excess Bi. Thus, in order to improve the hysteresis properties, additional 50% of Bi was added to SBTN thin films. The measured ferroelectric hysteresis curves are illustrated in Figure 3-12. For temperatures below 650°C, no hysteresis curve was detected for all the compositions. However, for annealing temperature of 650°C, the development of hysteresis curves was observed with increasing Nb/Ta ratio. At temperature as low as 650°C, the hysteresis curve of SBN showed low P_r and high E_c. As increased annealing temperature to about 700°C, the hysteresis curve of SBN became mature with higher P_r value and low E_c, whereas the hysteresis curve of SBT just started to show.

By comparing the results of structure development and ferroelectric properties characterization, it was found that Nb anion in SBTN has the effect of reducing grain growth temperature. The onset temperature of hysteresis curve was reduced with increasing Nb/Ta ratio.

3.5 Conclusion

In this research, we present for the first time the structure development study of SBTN thin films as revealed by spectroscopic ellipsometry. By this optical method, the temperatures at which grain growth dominates can be identified. Unlike PZT, for which nucleation of perovskite phase is the critical process to obtain ferroelectric properties, the critical process for SBTN to have ferroelectric properties is grain growth. In order to exhibit hysteresis curves, the grains of SBTN have to grow over a critical value, i.e., 0.1 μm in width and 0.27 μm in length. It was found that the additional Bi content in SBTN enhanced grain growth at low temperatures. For SBT with 50% excess Bi, the grain size
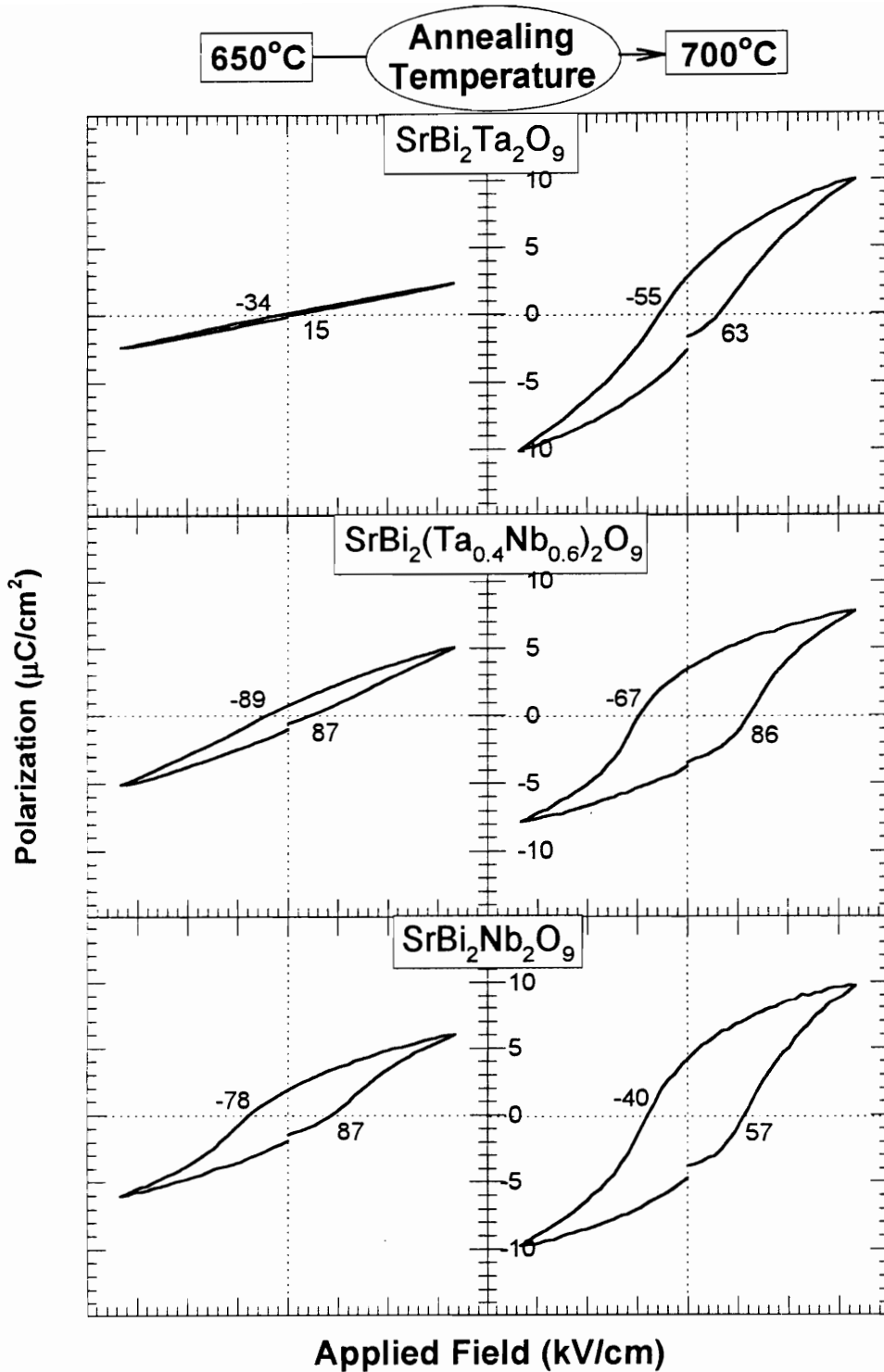
Figure 3-12 Ferroelectric hysteresis curves of SBTN thin films with 50% excess Bi measured at 650°C and 700°C. (to obtain symmetric curves, post top-electrode-deposition annealing was applied at the same temperature as pre top-electrode-deposition annealing).

was found to be over the critical value at temperature about 700°C at which the ferroelectric hysteresis properties were observed. This temperature was found to be 50 - 100°C lower than the published values (e.g., 750 - 800°C). In addition, Nb anion in SBTN was found to reduce T_O^H. Consequently, the temperature at which the films exhibited well-defined ferroelectric hysteresis properties was reduced by 50°C by choosing $SrBi_2Nb_2O_9$ thin film.

For the layer-type structure of SBT, the ferroelectric axis could be either in the a-b plane or along the c-axis. Recent research[50,51,75] has shown that, for SBT thin films, ferroelectric properties are observed in the a-b plane rather than along the c-axis. The results of Desu et. al. [46,48] showed that $2P_r$ values increased to a saturated value as the lattice orientation ratio of $I_{(115)}/I_{(008)}$ increased. By comparison, very poor ferroelectric properties were obtained for completely c-axis oriented films (i.e. $I_{(115)}/I_{(008)} = 0$). In the present study, we show that critical grain size dominates the onset of ferroelectric properties. In conclusion, the lattice orientation and critical grain size are two important factors that affect the ferroelectric properties. However, it is hard to tell which one is dominant for good ferroelectric properties because the effects of grain size and orientation could not be separated in the present study. For instance, the (115) planes give a very strong XRD peak for annealing temperatures of about 650 - 700°C. At the same time, a dramatic increase in grain size as well as the onset of ferroelectric hysteresis loops were observed within this temperature range. Therefore, we hypothesize that, for the same orientation ratio of $I_{(115)}/I_{(008)}$, larger grain sizes will give higher P_r values.

Chapter 4. The Effect of Excess Bismuth on The Ferroelectric Properties of $SrBi_2Ta_2O_9$ Thin Films

In this chapter, the effect of excess bismuth on the microstructure and ferroelectric properties of SBT thin films having perovskite-like layer-type structure was investigated for a wide range of excess bismuth content ranging from 0% to 100%. For the first time, the limited solid solution of $SrBi_2Ta_2O_9$ (SBT) and Bi_2O_3 was shown when the excess amount of Bi was less than 50%. The formation of solid solution enhanced the grain size and *a-b* plane orientation of the films; resulting in substantially improvement for ferroelectric hysteresis properties of the films. The optimum range of bismuth concentration showing reliable ferroelectric hysteresis properties was also investigated.

4.1 Introduction

Previous studies[53,76] have shown that the excess amount of Bi in SBT MOD thin film has the effect of enhancing the grain size, and it is required to exhibit ferroelectric hysteresis curves. The studies showed that it was necessary to have Bi excess in the films to obtain good ferroelectric hysteresis curves. However, the role of excess Bi content and the detailed understanding of its effect in determining the ferroelectric properties of layered structure oxides is still lacking.

Unlike PZT, where the ferroelectrics axis can be one of the three axes, the ferroelectric axis of bismuth layered oxides like SBT was restricted to *a-b* plane [50]. In this case, in layered oxides, the grain size and crystallographic orientation become the important factors in determining ferroelectric properties. In this research, the effect of

excess Bi in SBT thin films was studied with respect of grain size and crystallographic orientation. The optimum range of bismuth concentration showing reliable ferroelectric hysteresis properties was investigated.

Moreover, how the excess amount of Bi exists in the material was also investigated. There is a similarity between SBT and PZT: both of them have high volatile components in the materials, i.e., bismuth oxide in SBT and lead oxide in PZT. For the case of PZT, a certain amount of lead oxide evaporates during thin film fabrication because of their high volatility at relatively low temperatures. Commonly, a small amount of excess Pb (e.g., < 10%) is included in the films to control the stoichiometry of the film, so that prevents the formation of pyrochlore phase at high temperatures and increases the density of the films. However, the need for addition of excess Bi in SBT films is not clear yet. If the requirement of the excess Bi is to control stoichiometry of SBT film like PZT case, then the amount of 50% of excess Bi seems too much for this purpose. There is another possibility that these excess bismuth may remain in the films instead of evaporating away. For this case, the excess bismuth may stay in the materials either as a second phase or in the form of solid solution. If this is the case, the effect of the bismuth on the ferroelectric properties of SBT thin films becomes important for the applications.

In this research, the SBT ferroelectric thin films were fabricated by metalorganic decomposition (MOD) method. The effects of excess Bi were studied over a wide range of excess bismuth concentrations ranging from 0% to 100%. In order to investigate the thermal stability, powder mixtures of $SrCO_3$, Bi_2O_3 and Ta_2O_5 with 0 - 70% excess Bi was prepared by solid state synthesis method. The thermal stability of SBT was investigated by monitoring the weight loss of powder during heat treatment from room temperature to 1400°C. Standard X-ray diffraction technique was used for phase identification (Scintag XDS 2000). The composition was analyzed by energy dispersive X-ray analysis (EDX)

54

and X-ray photoelectron spectroscopy (XPS). The electrical properties were characterized by Keithley 617 programmable electrometer and the ferroelectric properties were measured by the standardized RT66A tester (Radiant Technologies, Inc.) under the Virtual-Ground mode.

4.2 Experimental Procedure

SBT ferroelectric thin films were fabricated by the MOD method as described in Section 2.1. Solutions with 0 - 100% excess bismuth were prepared for studying the effect of bismuth on the microstructure and ferroelectric properties of thin films. The films were deposited on sapphire substrates for phase identification. For ferroelectrics characterization and surface morphology investigation, the films were deposited on $Si/SiO_2/Ti/Pt$ substrates. The phase of the films were identified by XRD method after first annealing at $700^{\circ}C$. The surface morphology formed at $700^{\circ}C$ was observed by SEM. For ferroelectric characterization, the films were annealed at $750^{\circ}C$ for 3 hours followed by a post top-electrode-deposition annealing for $700^{\circ}C$ and 1 hour.

In addition to the thin film samples, the powder mixture of $SrCO_3$, Bi_2O_3 and Ta_2O_5 with 0 - 70% excess Bi, was also prepared for the thermal stability study of SBT. The powder preparation method was described in Section 2.2. The powder mixture was then heat treated for a temperature range from room temperature to $1400^{\circ}C$ for weight loss measurement.

55

4.3 Results And Discussion

4.3.1 Effect of Excess Bi on Ferroelectric Properties

The ferroelectric hysteresis properties were studied as functions of bismuth concentration. Figure 4-1 shows the hysteresis curve as a function of Bi concentration. For SBT films with excess Bi amount less than 10% and greater than 70%, skinny hysteresis curves with extremely low remanant polarization ($2P_r$) were observed. On the other hand, the mature hysteresis curves were only obtained for the films with 30 - 50% excess Bi. The values of $2P_r$ and coercive field (E_c) for each composition are shown in Figure 4-2. Within the range of 30 - 50% excess Bi, the films exhibited maximum values of $2P_r$.

Figure 4-3 shows the leakage current density as a function of Bi concentration. For excess Bi less than 10%, the leakage current density was extremely high. When the amount of excess Bi increased to about 10 - 50%, leakage current density was dramatically reduced. However, as the amount of excess Bi increased further, leakage current density increased again with increasing Bi concentration.

Although the SBT films with 10% excess Bi showed low leakage current density, poor hysteresis curves was obtained for this composition. From the results of hysteresis properties and leakage current density, the optimum composition for exhibiting good hysteresis properties is within 30 to 50% excess Bi.
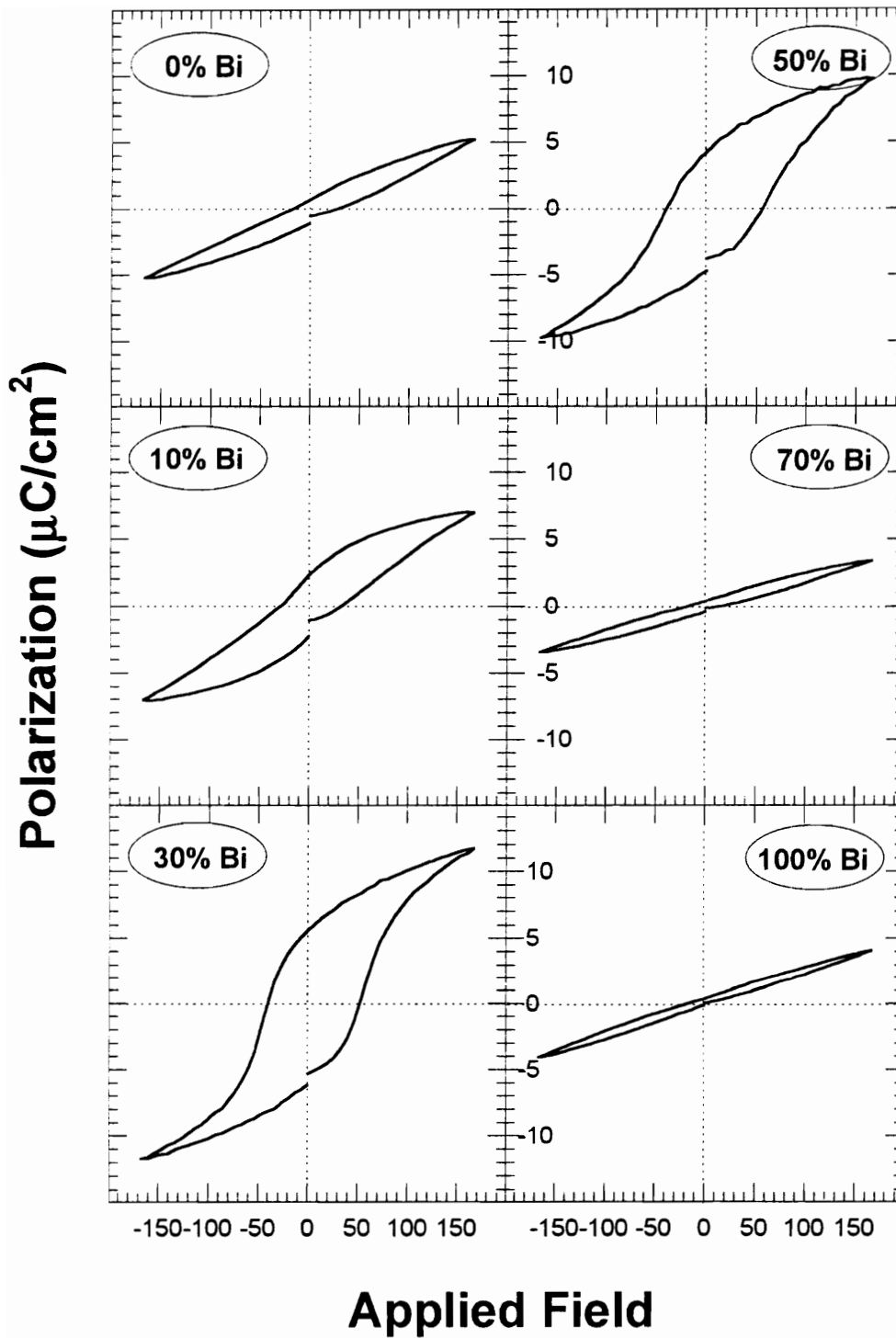
Figure 4-1 Ferroelectric hysteresis loops for SBT thin films with excess
Bi content from 0 to 100%. (films were annealed at 750°C for
3 hours followed by a post-top-electrode-deposition annealing
of 700°C for 1 hour)
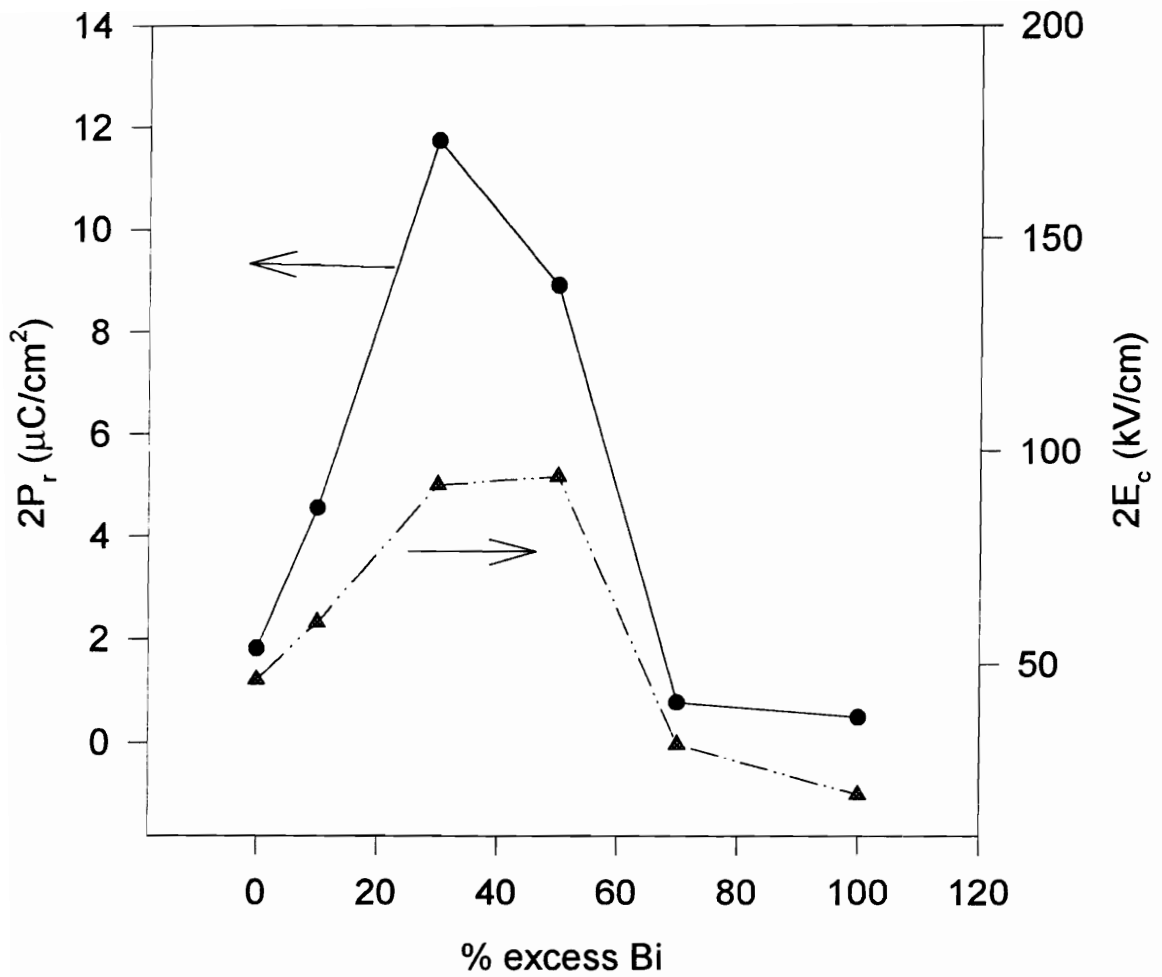
Figure 4-2   Bi concentration dependence ramanent polarization ($2P_r$) and coercive field ($2E_c$).
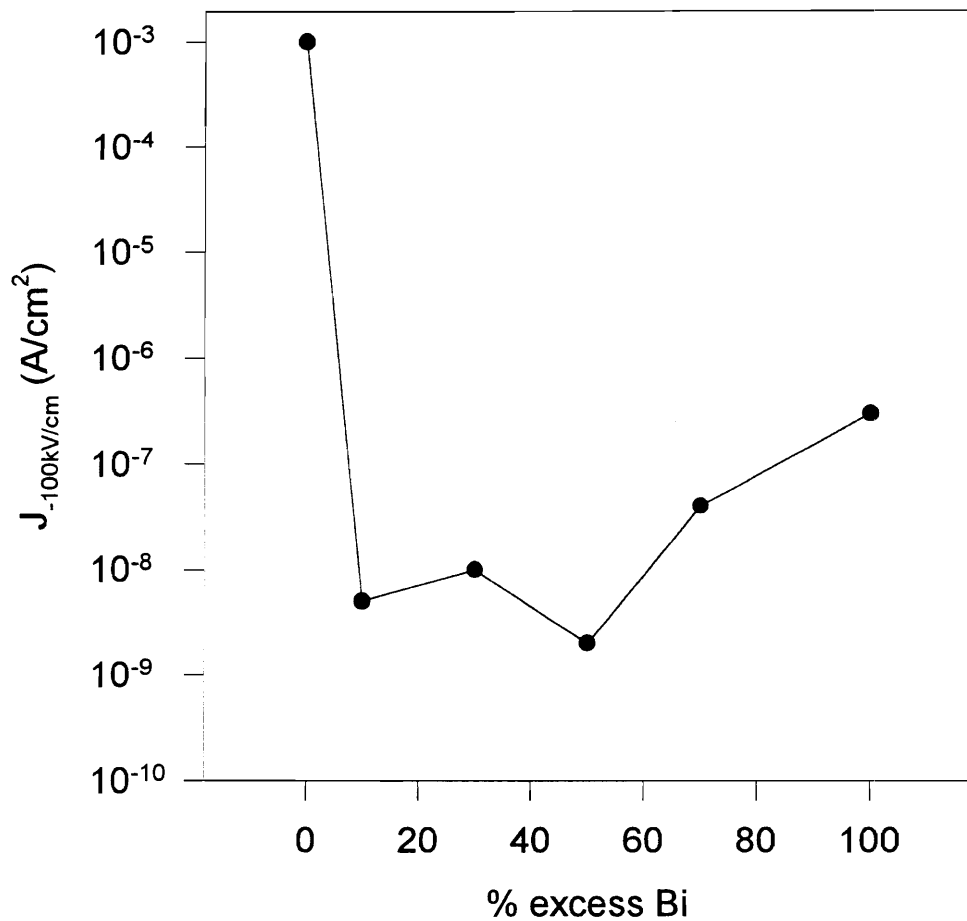
Figure 4-3   Bi concentration dependence leakage currents of SBT thin films. (films were annealed at 750°C for 3 hours followed by a post-top-electrode-deposition annealing of 700°C for 1 hour and measured at 100 kV/cm)

4.3.2 Effect of Excess Bi on SBT Microstructure

The phases of SBT thin films with varied excess Bi content were investigated by XRD and are illustrated in Figure 4-4. XRD results clearly show that, for excess Bi content in the range of 10 - 50%, the films show a single phase of SBT layer-type structure. For the film with 0% excess Bi, the broader peaks indicate very fine grained microstructure of SBT thin films. However, for excess bismuth content greater than 50%, Bi_2O_3 appears as a second phase along with the SBT phase. This indicates that there is a possibility that the solid solution was formed between SBT and Bi_2O_3. However, due to the high volatility of Bi_2O_3 (melting point is about 723°C) during high temperature annealing, the evaporation of Bi_2O_3 might occur.

In order to understand the evaporation behavior of bismuth oxide as a function of annealing temperature, the thermal stability of SBT powders made by solid state reaction were studied by the weight loss measurements during heat treatment. The reason for using powder is to overcome the difficulty of weight loss analysis in thin film form. Figure 4-5 shows the result of the weight loss measured as a function of annealing temperature for SBT powders having 0 - 70% excess amount of Bi. The curves of Figure 4-5 can be divided into four regions. In region I, at temperatures below 600°C, no weight loss was observed for all the compositions. In region II of temperature range between 600 - 800°C, about 4% weight loss was observed. This small amount of weight loss is due to the decomposition of $SrCO_3$ leading to the loss of CO_2 gas. In this region, the structure of the powders are still mixed phases of starting powders. As temperature increased further to region III, *i.e.*, 800 - 1200°C, almost no weight loss was observed. However, in this region, the SBT layer-type structure phase was formed. Table 4-1 shows the structure of the $SrBi_2Ta_2O_9$ powders with various amount of excess Bi detected by XRD. Between

60
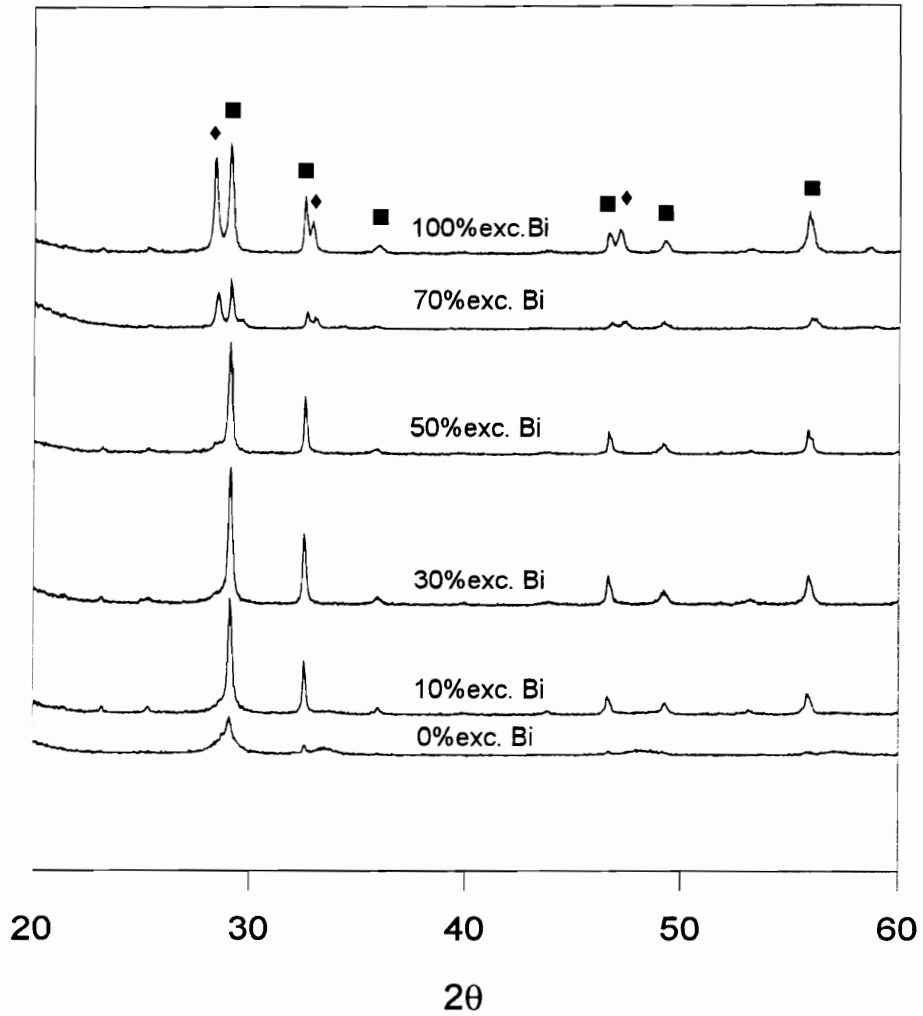
Figure 4-4   Bi concentration dependence X-ray diffraction patterns of SBT
thin films. (■) and (♦) denote SBT phase and Bi_2O_3 phase,
respectively. (Films were annealed at $700^{\circ}C$ for 1 hour.)
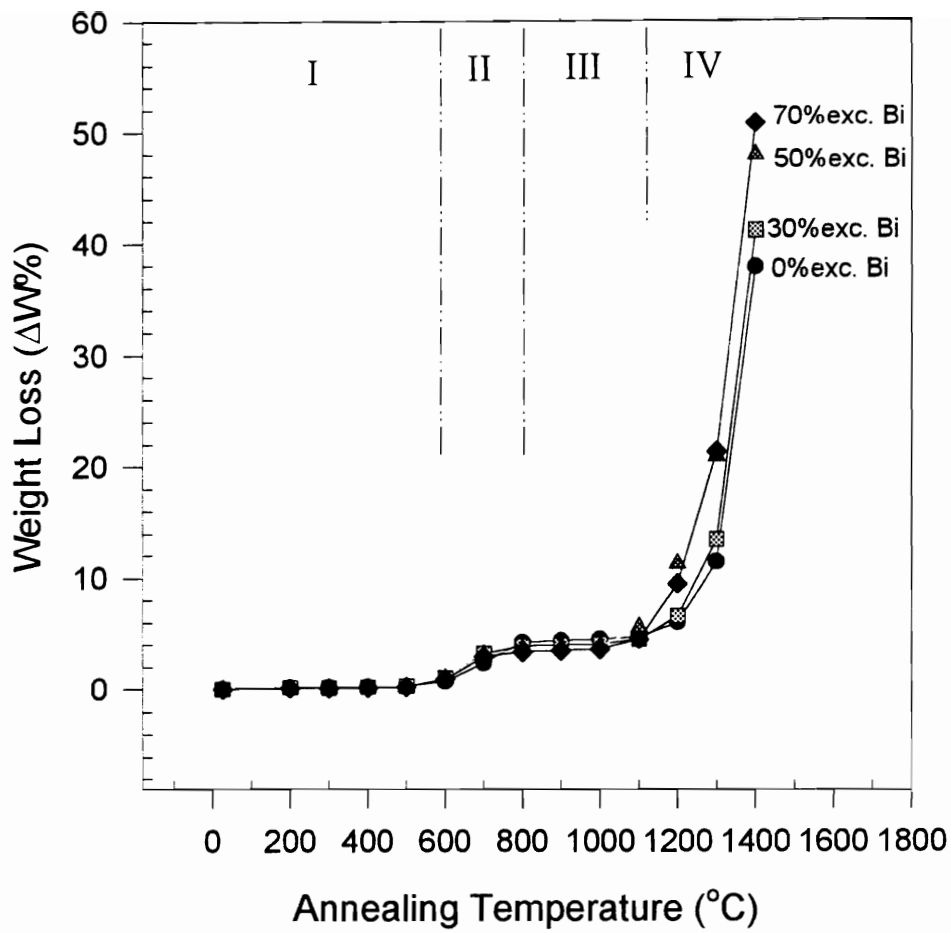
Figure 4-5 The weight losses of powder mixtures ($SrCO_3$, Bi_2O_3 and Ta_2O_5) with 0 - 70% excess Bi are plotted as a function of annealing temperatures.

Regions (I), (II): mixture phases, (III): SBT phase, and (IV): decomposition.

Table 4-1   Structures of SBT powders with varied excess Bi contents made by solid state synthesis and MOD methods.

The structures were detected by XRD.

Tempe-rature	Solid state reaction $SrBi_2Ta_2O_9 + x\%$ exc. Bi				MOD method $SrBi_2Ta_2O_9$ (50% exc. Bi)
	x = 0	x = 30	x = 50	x = 70	
700°C	--	--	--	--	SBT
950°C	SBT	SBT	$SBT+Bi_2O_3$*	$SBT+Bi_2O_3$	SBT
1200°C	SBT	SBT	$SBT+Bi_2O_3$*	$SBT+Bi_2O_3$	SBT
1400°C	$SBT+SrTa_4O_{11}+SrO$	$SBT+SrTa_4O_{11}+SrO$	$SBT+SrTa_4O_{11}+SrO$	$SBT+SrTa_4O_{11}+SrO$	$SBT+SrTa_4O_{11}+SrO$

*Note: very small amount of bismuth oxide.

950 - 1200°C and for the compounds with excess bismuth less than 50%, single phase of SBT layer-type structure was detected. On the other hand, for the compounds having excess bismuth oxide greater than 50%, a mixture of SBT and Bi_2O_3 phases was observed.

In the region IV of Figure 4-5, about 40 - 50% of weight loss was measured at temperatures up to 1400°C. The weight loss increased with increasing Bi content. Meanwhile, the film structure shown in Table 4-1 shows that secondary phases of $SrTa_4O_{11}$ and SrO are formed for all the compositions and for both the fabrication methods (solid state and MOD) in this temperature range. The dramatic weight loss in the region IV is the result of the evaporation of bismuth oxide leading to the appearance of the second phase. The evaporation of Bi_2O_3 was confirmed by EDX composition analysis. Table 4-2 shows an example of EDX analysis for SBT powders with 0% excess bismuth oxide. For temperatures below 1200°C, the SBT powders had stoichiometric composition. However, a over 50% loss of Bi concentration was observed at 1400°C. This indicates that the volatilization of Bi_2O_3 and the decomposition of SBT occurs in region III. The chemical reaction of SBT decomposition can be expressed by

$$2 \ SrBi_2Ta_2O_9 = 2 \ Bi_2O_{3\,(g)} \uparrow + \ SrTa_4O_{11} + SrO$$
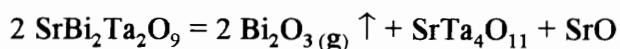
All the evidence shown above suggest that SBT and Bi_2O_3 can form limited solid solution while still maintaining perovskite-like layer-type structure. This implies the possibility of ion substitution between Bi, Sr and Ta anions. According to the studies of Smolenskii, et. al.[58], and Araujo, et. al.[48], Bi^{3+} anions can occupy anion sites in the perovskite-like layers, i.e., Sr^{2+} and Ta^{5+} sites. The limited solid solutions of SBT and Bi_2O_3 may have the form of $(Sr_{1-x}Bi_x)Bi_2(Ta_{2-x/2}Bi_{x/2})O_9$ ($0 \leq x \leq 0.6$). For x values greater

Table 4-2   EDX composition analysis for SBT with 0% excess Bi solid state
              synthesized powder at various annealing temperatures. (The theoretical
              atomic ratio of Sr:Bi:Ta is 1:2:2)

Annealing Temperature	25°C	950°C	1200°C	1400°C
Atomic ratio Sr : Bi : Ta	1.3 : 2 : 2	1.1 : 2.1 : 2	1.2 : 2 : 2	1.2 : 0.8 : 2

than 0.6 (i.e., the amount of excess Bi is greater than 50%), Bi_2O_3 occurs as a second phase (Figure 4-4).

The high leakage current and poor ferroelectric hysteresis properties for the films with high excess Bi content are possibly due to the formation of highly conductive Bi_2O_3 second phase. However, the reason of the absence of ferroelectric hysteresis properties of the films having low excess Bi content is possibly due to the fine grained microstructure of these compositions. According to our previous studies [76], there is a critical grain size (approximately 0.1μm in width and 0.27 in length) below which SBT films do not exhibit ferroelectric properties. Figure 4-6 and 4-7 show the SEM morphology and the grain size of SBT thin films with varied excess Bi content. It is observed that, the grain size of SBT films increases with increasing Bi content. On the other hand, grain shape is also changed with Bi content. With excess Bi less than 10%, fine uniaxial grains were observed with grain size smaller than the critical grain size. For excess Bi content within 10 - 50%, longitudinal grains were observed with a maximum shown at 30 - 50% excess Bi content. Within this range, the ratio of length to width of the grain is about 3. When excess Bi increases further to exceed 70%, uniaxial grains with constant grain size about 0.17 μm were observed. The change of grain shape for high excess Bi content is possibly associated with Bi_2O_3 second phase formation along with SBT phase.

In addition to the grain size effect, the ferroelectric properties are also affected by crystallographic orientation. For the perovskite-like layer-type structure, the continuous perovskite structure occurs in the a-b planes while the continuity of the perovskite is disturbed by bismuth oxide layers along the c-axis. Thus the ferroelectric axis could be either in the a-b planes or along the c-axis. In a previous study, the ferroelectric properties of SBT thin film capacitors have been characterized as a function of crystallographic orientation [46]. The results indicate that, SBT thin films oriented along c-axis exhibit

0% excess Bi
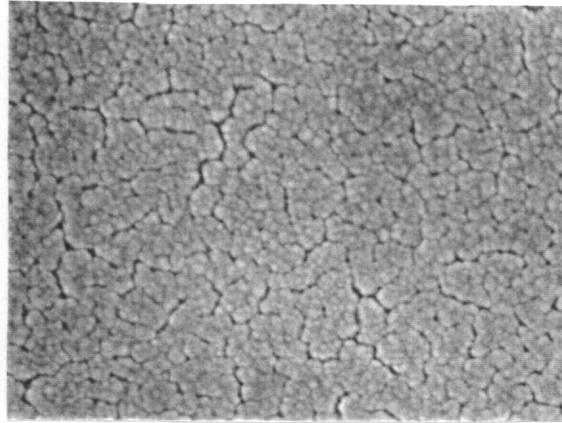
10% excess Bi
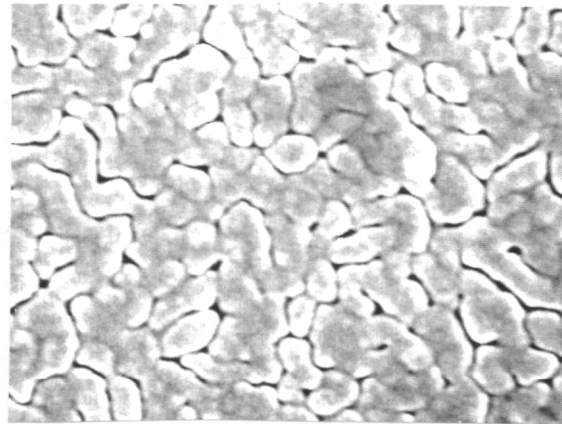
30% excess Bi
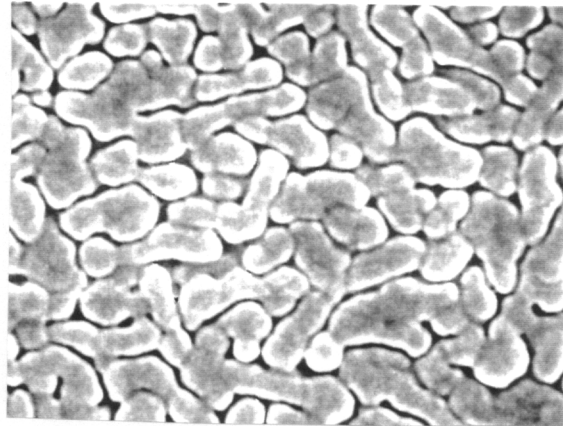
0.2 μm

Figure 4-6(a)   Surface morphology of SBT thin films with excess Bi content from
0% to 30% annealed at 700°C for 1 hour on Pt-substrate. (SEM
photos with 50000X magnification)

50% excess Bi
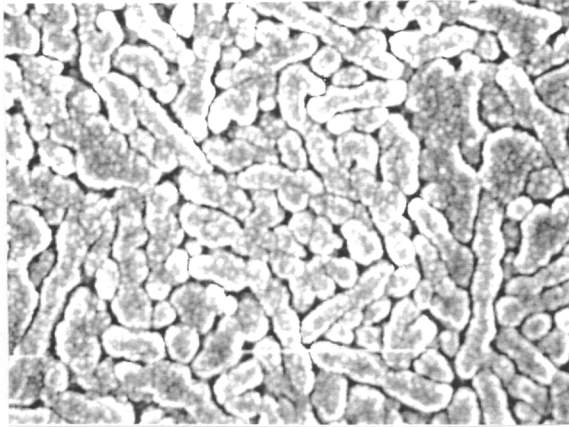
70% excess Bi
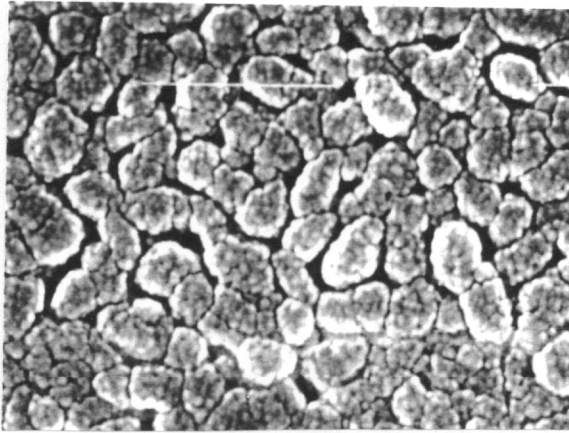
100% excess Bi
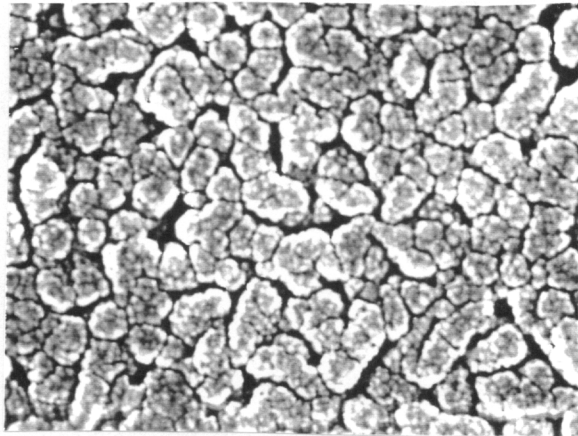
0.2 μm

Figure 4-6(b)   Surface morphology of SBT thin films with excess Bi content from
50% to 100% annealed at 700°C for 1 hour on Pt-substrate. (SEM
photos with 50000X magnification)
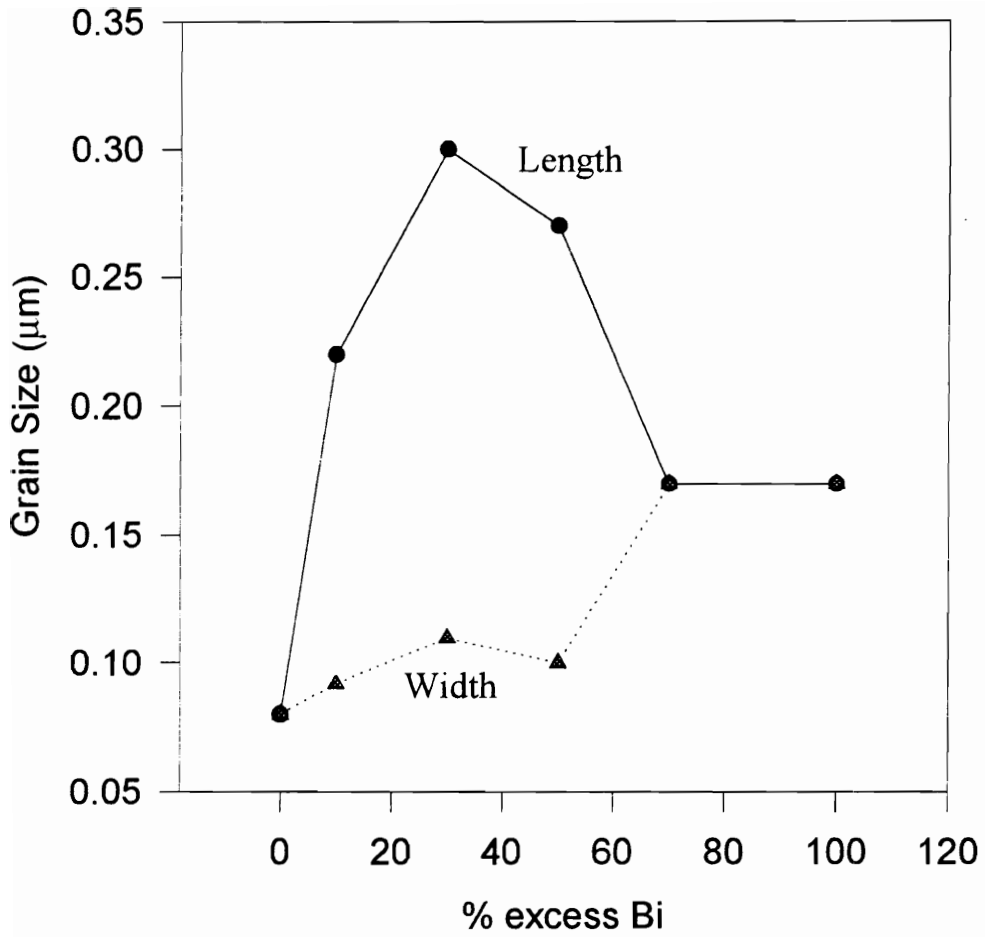
Figure 4-7   The grain sizes of SBT MOD thin films vary with excess Bi content. The films were annealed at 700°C for 1 hour on Pt-substrates.

almost no polarization, whereas the polarization and coercive field are high in the a-b plane. It has also been shown that the remanant polarization and coercivity decrease with increasing degree of c-axis orientation. This study suggests that the Bi_2O_2 layers intervening the perovskite-like units along the c-axis may not be participating in the cooperative phenomenon responsible for ferroelectricity in these materials.

In this study, the degree of a-b plane orientation of SBT thin films, R which is defined by the expression in equation (1), were roughly estimated by measuring the ratio of the (200) planes to the dominant (115) planes using polycrystalline powder as a standard reference,

$$R_{(200)} = \frac{[I_{(200)}/I_{(115)}]_F}{[I_{(200)}/I_{(115)}]_P} - 1 \qquad (4\text{-}1)$$

where F and P denote thin film and powder form, respectively. Figure 4-8 shows the calculated values of $R_{(200)}$ as a function of excess Bi content. From this figure, it is clear that the degree of a-b plane orientation increases with increasing excess bismuth content.

The above results indicate that the grain size and degree of a-b plane orientation both have a maximum at 30 -50% excess Bi content. By comparing to the results of ferroelectric properties obtained above, the combined effect of the grain size, crystallographic orientation and the formation of Bi_2O_3 second phase, leads to the optimum composition range of 30 - 50% excess Bi in which the SBT films have high remanant polarization and low leakage current density.

It is important to understand the role of excess bismuth content in the film for controlling the ferroelectric hysteresis properties of SBT thin films. The effect of excess Bi content on grain size, orientation and phase formation imply that the role of the excess Bi
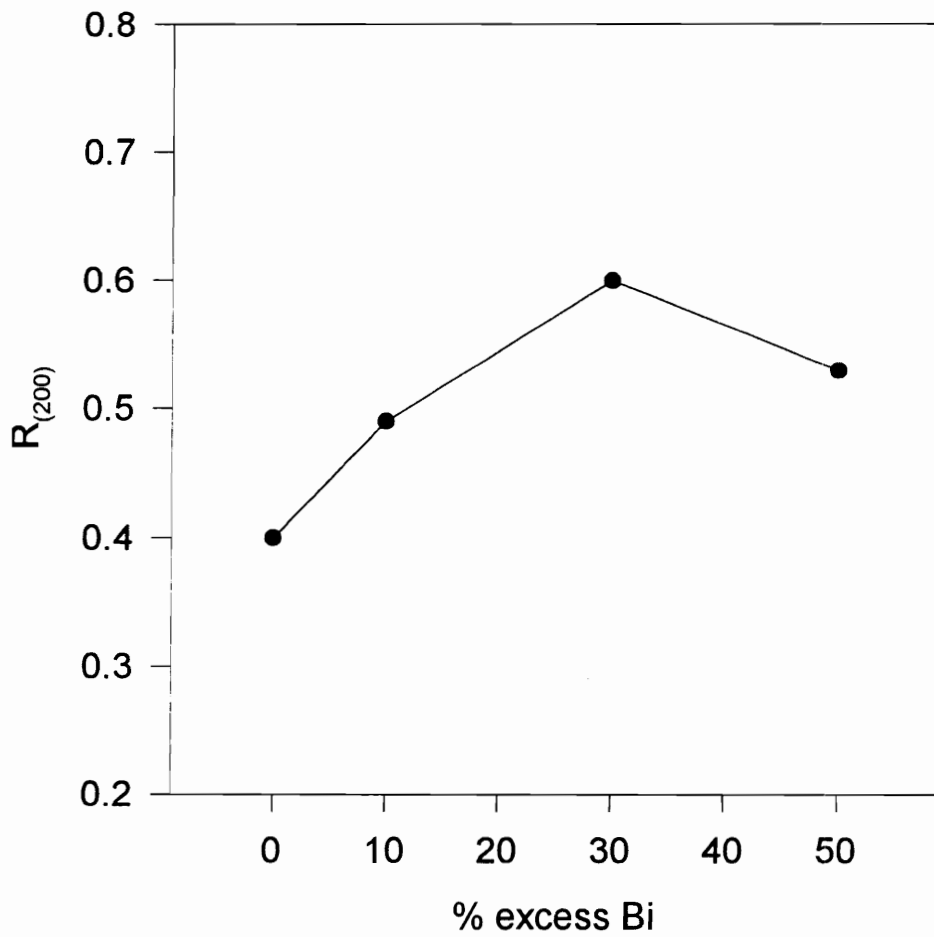
Figure 4-8 The crystallographic orientation changes are plotted as a function of excess Bi content. $R_{(200)} = \dfrac{[I_{(200)}/I_{(115)}]_F}{[I_{(200)}/I_{(115)}]_P} - 1$

in SBT film is not of simply controlling the stoichiometry of the film. This is unlike the case of PZT ferroelectric thin films, wherein Pb excess is included in the precursors to control the stoichiometry during heat treatment because of the high volatility of lead oxide at relatively low temperatures. As a result, the formation of limited solid solutions of SBT and Bi_2O_3 show significant changes in grain size and crystallographic orientation and substantially improvement on ferroelectric hysteresis curves.

4.4 Conclusion

For the first time, it was shown that the limited solid solutions can be formed for SBT and Bi_2O_3 when the excess amount of Bi in SBT was less than 50%. The formation of solid solutions enhanced the grain size and the degree of a-b plane orientation of SBT films, resulting in improved hysteresis properties of the films. With the combined effect of grain size and crystallographic orientation, the optimum excess amount of Bi in SBT film was found to be about 30 - 50%. Within this range, the hysteresis properties of the films showed maximum $2P_r$ values (around 12 μC/cm²) and low leakage current densities (about 10^{-9} A/cm²). On the other hand, when excess amount of Bi exceeded 50%, highly conductive Bi_2O_3 second phase was formed in SBT films, leading to poor hysteresis curves and high leakage current density.

Chapter 5. Optical Properties of $SrBi_2(Ta_{1-x}Nb_x)_2O_9$ Bulk Ceramics By Spectroscopic Ellipsometry

In this chapter, the fundamental understanding of the properties of bismuth layered oxides were acquired through the investigation of the optical properties. The optical properties of bulk ceramics SBTN were reported for the first time. A nondestructive method, variable angle spectroscopic ellipsometry, was employed in this research. The effective medium approximation (EMA) theory was used to account for surface roughness. The dispersion behavior of optical constants was examined by two models, Cauchy and Lorentz Oscillator. The Lorentz Oscillator model fitted the dispersion behavior more accurately than the Cauchy model, especially near the absorption region. In this research, it was shown that the refractive index at optical frequencies region could be correlated to SBTN lattice orientation. Moreover, by applying the Lorentz Oscillator model with a surface layer correction, we are roughly able to estimate the approximate energy band gap of SBTN from resonance frequency, $\hbar\omega_0$.

5.1 Introduction

For the first time, the optical properties of bismuth layered oxide, $SrBi_2(Ta_{1-x}Nb_x)_2O_9$ (or SBTN), are studied in bulk form by spectroscopic ellipsometry. In recent years, bismuth layered oxides have been receiving attention for ferroelectric memory device applications because of their high resistance to electrical degradation. However, the fundamental properties of these compounds are not widely investigated by researchers. In this chapter, the fundamental understanding of the properties of bismuth layered oxides are

acquired through the investigation of the optical properties by spectroscopic ellipsometry method.

Spectroscopic ellipsometry is a well-established technique for studying thin films and surfaces since the late 1800s[77]. It is a branch of reflection spectroscopy using linearly polarized incident light, which yields information about the optical constants of materials, the thickness of overlying layers, and the presence of roughness layers. It is also used extensively in integrated circuit (IC) manufacture and development, corrosion science, and the other areas. However, only few reports on bulk optical property characterization [78-80].

Determination of the optical properties of a material in its bulk form is a double challenge. It requires not only accurate instrumentation but also well-prepared samples. It has been shown that the UV-visible transmission is strongly affected by microstructure and surface conditions[81-84]. The importance of surface conditions can be appreciated by noting the penetration depth of light in opaque materials is typically 100 - 500 Å in the near UV, so even 1-Å surface films can affect the dielectric function (ε) and reflectance (R) of materials as much as several percentage points. There are several surface imperfection which always accompany with bulk sample preparation: (1) a contaminant or oxide layer, (2) a stressed layer due to mechanical forces involved in the preparation of sample (e.g., cleaning or polishing), and (3) surface roughness. All these should be considered potential sources of error in the determination of optical properties by a light-reflection technique such as ellipsometry. In this research, the imperfect surface layer was considered an individual thin film above the bulk ceramic sample. The theory of effective media approximation (EMA) was used to described this surface layer.

The ellipsometry parameters, Δ and Ψ, were analyzed by the software developed by J.A. Woollam Company. The analysis consists of building a nominal optical model for

the sample, choosing fit parameters such as film thickness or optical constants, and initiating a regression algorithm. In order to obtain the accurate results, the proper optical model has to be built up according to the nature of the samples. For instance, a heterogeneous surface overlayer need to be included in the optical model for bulk ceramics. Once the model is built up, a proper optical dispersion function has to be selected to fit the experimental data. In this study, two dispersion models, Cauchy and Lorentz Oscillator, were attempted. By selecting the proper dispersion function, not only can the optical constants in the optical frequency region be obtained, but the approximate energy band gap can also be estimated.

5.2 Experimental Procedure

The polycrystalline compounds of SBTN were made by solid state synthesis as described in Section 2.2. A 17 mm diameter disk with 2 mm thickness was obtained after sintering. The phase of SBTN layer-type structure was identified by X-ray diffraction. The sample surfaces were polished to mirror-like surfaces so the reflected light could be collected during ellipsometric measurement.

5.3 The Optical Model And The Effective Medium Approximation Theory (EMA)

The dielectric response of a heterogeneous medium can be described in terms of the dielectric properties of its components[84]. The effective dielectric response of a heterogeneous medium can be described by the Bruggeman Effective Medium Approximation (EMA)[74] and is represented as

.

$$\sum_{i=1}^{n} f_i \frac{\varepsilon_i - \varepsilon}{\varepsilon_i + 2\varepsilon} = 0 \qquad (5\text{-}1)$$

where n is the number of components in the heterogeneous medium, f_i is the volume fraction of each component, ε_i is the dielectric function of each component, and ε is the effective dielectric function of the heterogeneous medium. For most oxides, the extinction coefficients are much smaller than the refractive indices at visible wavelengths. Thus, the dielectric function in this region can be related to the refractive index by $\varepsilon = n^2$. Therefore, for a single phase material with voids in it, the EMA becomes

$$f \frac{n_b^2 - n^2}{n_b^2 + 2n^2} + (1-f) \frac{1-n^2}{1+n^2} = 0 \qquad (5\text{-}2)$$

where f is the volume fraction of material, n_b is the refractive index of the bulk material and n is the effective refractive index of the heterogeneous medium.

It is well known that grain boundaries, voids, disordered regions and other inhomogenieties on the microstructural length scale of 10-10000Å significantly affect the UV-visible optical properties of materials, even if they are macroscopically uniform. These imperfections exist everywhere in the material from the surface to the bulk and can not be ignored even after polishing. The existence of the surface heterogeneous overlayer has been proved by Thacher, et. al., for PZT ceramics. It shows[78-80] that the refractive index of surface layer is lower than the refractive index of the bulk due to the roughness and mechanical stress on the surface.

Basically, there are two ways to deal with this heterogeneous overlayer, one is to eliminate the overlayer, and another is to accept it as a necessary evil and have their effects identified by proper data acquisition and reduction. For the first approach, however, it is very difficult to eliminate the imperfect surface layer. Even though the surface oxidation layer and contamination can be taken off by processing in high vacuum system, the stress, voids and surface roughness are still there. Thus, the second approach becomes more practical in dealing with the overlayers.

Since several situations arise when a layer is not homogeneous, it is necessary to combine two or more different materials in this layer. For example, a rough surface has both mean height and correlation length of the irregularities less than the wavelength of light. Therefore, the combination of the material itself and the voids can be considered to make up an "effective layer" as suggested in Figure 5-1. Subsequently, the effective dielectric function and optical constants of this effective layer can be estimated by the EMA theory.

The sintered density of SBTN ceramics made for this research were about 90% of theoretical density, thus the voids were spread all over the materials. The mechanical stress was also induced in the sample surface during the polishing process. All these inhomogeneities need to be considered as the potential defects affecting the optical properties of SBT. However, it is difficult to distinguish the individual effects of each defect. Therefore, an alternative way to deal with this is using a void fraction to represent the total effect of all the possible inhomogeneities existed in the materials. The optical model of SBTN ceramics used in this study is schematic in Figure 5-2. It is assumed the infinite thickness of homogeneous bulk ceramics having a finite inhomogeneous surface layer above it. This inhomogeneous layer with thickness d results from the porosity, stress and roughness on the surface. It is also assumed that a portion of incident light is absorbed
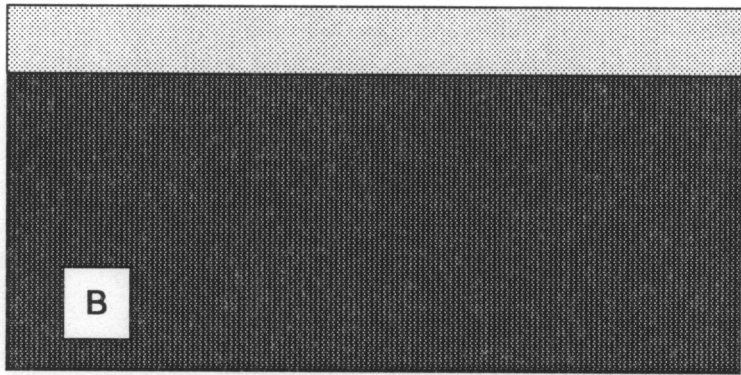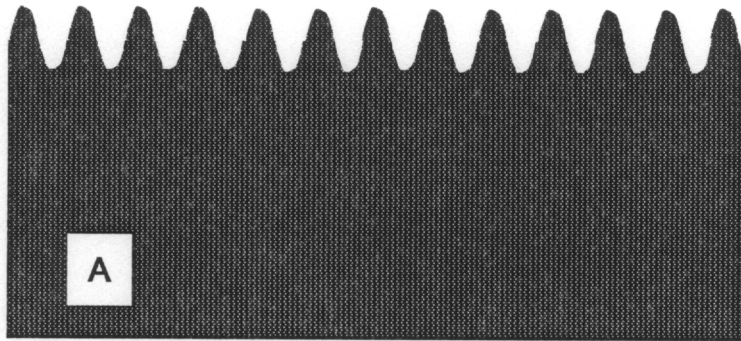
Figure 5-1. (A) A rough surface and (B) the equivalent effective layer on a substrate of the original material.
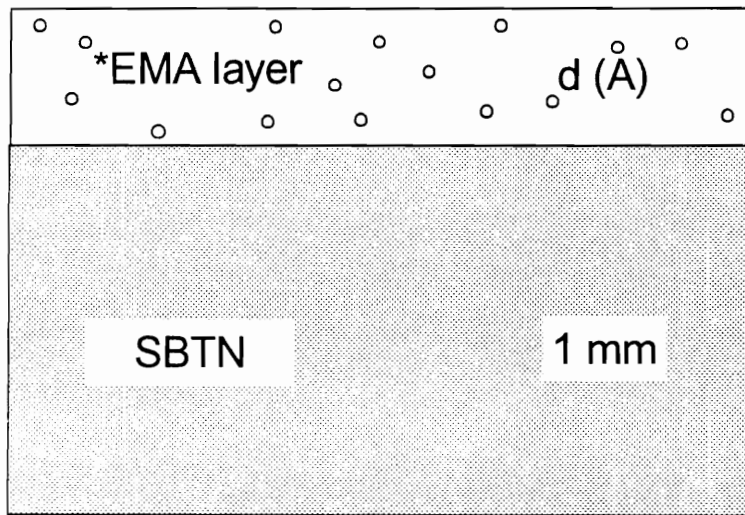
(*EMA layer = SBTN + voids)

Figure 5-2. The optical model of SBTN bulk ceramics.

by the bulk whereas another portion of incident light is reflected from the interface of the effective surface layer and the bulk. It is the reflected light that is collected for ellipsometric analysis. The optical properties of the effective surface layer is estimated on the basis of the bulk properties. In other words, any parameter change of the bulk consequently alters the properties of the effective surface layer.

5.4 Optical Dispersion Models

When a beam of light traverses a transparent liquid or solid, the velocity is a function of the wavelength, or frequency; usually the velocity is reduced for the higher frequencies. This means the index of refraction varies with wavelength, usually becoming greater as the wavelength becomes shorter. This phenomenon is called dispersion, since in optical devices it leads to the gradual separation of wavelengths in the direction of propagation.

When a large portion of the electromagnetic spectrum is considered, all materials have specific absorption bands, which occur at those frequencies where the atoms or molecules of the material absorb light quanta and undergo a change in state. Measurements of the index of refraction are difficult near the absorption bands since the light becomes almost completely absorbed. Most of the mathematical relationships for the treatment of dispersion have been developed empirically. A typical dispersion curve is shown in Figure 5-3. These curves are representative of normal dispersion, for which the following is noted:

1. The index of refraction increases as the wavelength decreases.
2. The rate of increase becomes greater at shorter wavelengths.
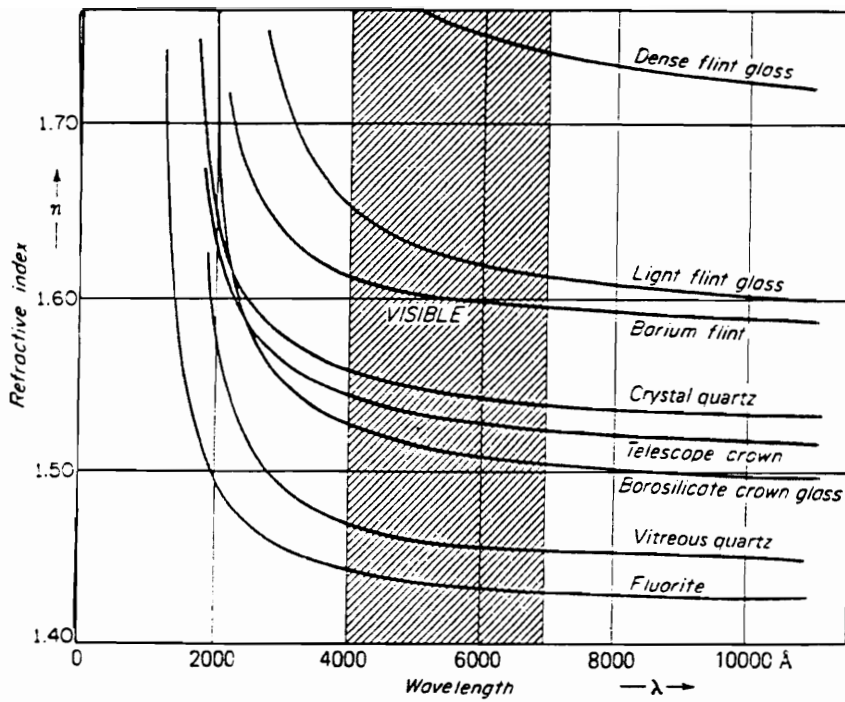
Figure 5-3.   Dispersion curves for several different materials commonly used for lenses and prisms [87].

3. For different substances the curve at a given wavelength is usually steeper for larger index of refraction.

4. The dispersion of one substance cannot in general be obtained from that of another substance by a mere change in the scale of ordinate.

The first successful attempt to represent the curve of normal dispersion by an equation was made by Cauchy in 1830 [85]. His equation may be written

$$n = A + \frac{B}{\lambda^2} + \frac{C}{\lambda^4} + \cdots \cdot \tag{5-3}$$

where A, B, and C are empirical constants. For dielectrics, this equation represents the curves in the visible region with considerable accuracy. However, if the measurements of refractive index of a transparent substance are extended into an absorption band, the dispersion curves begin to show marked deviations from the Cauchy equation. This equation predicts a very gradual decrease of n for long wavelength; the index approaches a limiting value as wavelength approaches infinity. This is not true for real dielectric materials. In contrary to the Cauchy's prediction, the measurement values of n decrease more and more rapidly as it approaches a region where light ceases to be transmitted at all. The behavior of the curves in the vicinity of absorption region is referred to as anomalous dispersion, because it does not correspond to relations like Cauchy formula. An typical example of anomalous dispersion is schematic as Figure 5-4. The region enclosed between dotted lines is found to be a continuous variation[86,87].

One of the first attempts at a theoretical treatment of dispersion was Sellmeier in 1871 [87]. The equation obtained by Sellmeier fits the experiments much better than
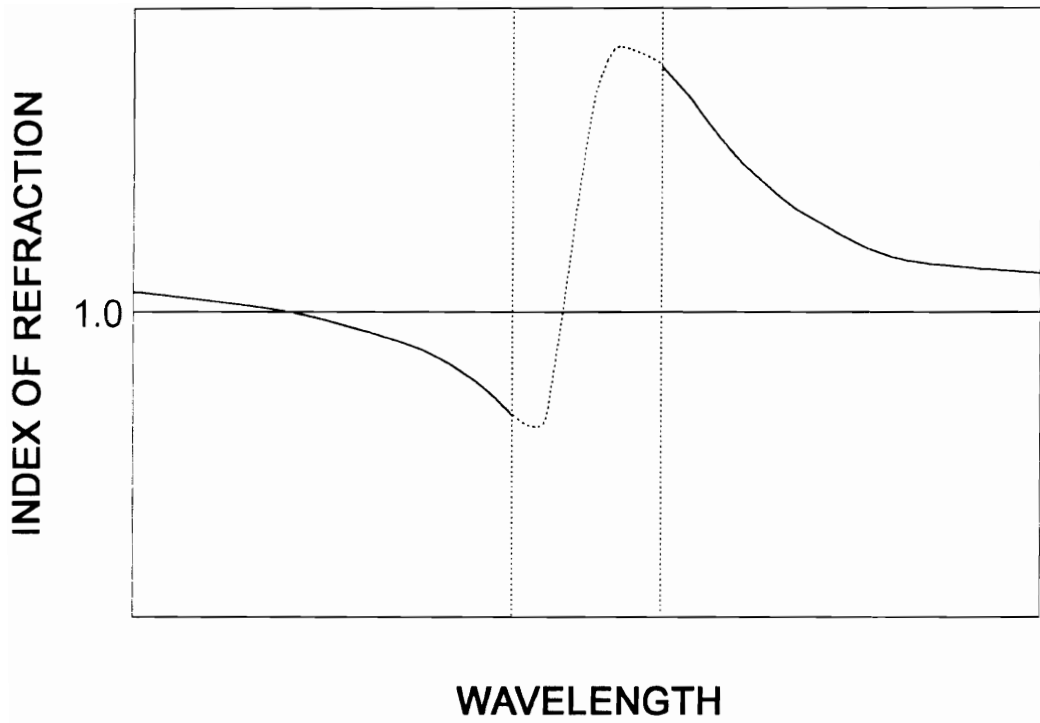
Figure 5-4.   Actual form of refractive index curve through an
absorption line [86].

Cauchy's formula and, in particular, shows a good fit near the absorption bands. However, Sellmeier's equation fails in the absorption bands; it goes to infinity at a resonant point and shows discontinuity in this absorption region. The discrepancy is because that Sellmeier's equation takes no account of the energy absorption of the wave. The dissipation of energy is due to the emission of electromagnetic waves by vibrating electrons. He neglected the effect of damping which has to be considered as an essential factor in the whole process.

By taking into account the damping effect, H.A. Lorentz[88,89] proposed a model which describe the motion of an electron bound to the nucleus:

$$m\frac{d^2\vec{r}}{dt^2}+m\Gamma\frac{d\vec{r}}{dt}+m\omega_0^2\vec{r} = -e\vec{E}_{loc} \qquad (5\text{-}4)$$

where m is the free electronic mass, ω_0 is the resonance frequency which is the frequency of incident field that the electron oscillates with, and Γ is the broadness. The field E_{loc} is the local field acting on the electron as a driving force and is taken to vary in time as $e^{-i\omega t}$. The term $m\Gamma(d\vec{r}/dt)$ represents viscous damping and provides for an energy loss mechanism. The term $m\omega_0^2\vec{r}$ is a Hook's law restoring force. Consequently, the complex dielectric function for nonmagnetic materials derived from Lorentz's model can be expressed by

$$\varepsilon^* = 1+\frac{4\pi e^2}{m}\sum_j\frac{N_j}{(\omega_j^2-\omega^2)-i\Gamma\omega} \quad , \text{ and} \qquad (5\text{-}5)$$

$$\sum_j N_j = N \qquad (5\text{-}6)$$

84

where N_j is the density of electrons bound with resonance frequencies ω_j. Since

$$\varepsilon^* = \varepsilon' + i\varepsilon'', \quad \text{and} \tag{5-7}$$

$$n^* = n - ik \tag{5-8}$$

According to Maxwell's relation, $\varepsilon = n^2$, the optical constants of dielectric materials can be related to the dielectric function by

$$\varepsilon' = n^2 - k^2 = 1 + \frac{4\pi Ne^2}{m} \sum_j \frac{(\omega_j^2 - \omega^2)}{(\omega_j^2 - \omega^2)^2 + \Gamma^2\omega^2}, \text{ and} \tag{5-9}$$

$$\varepsilon'' = 2nk = \frac{4\pi Ne^2}{m} \sum_j \frac{\Gamma\omega}{(\omega_j^2 - \omega^2)^2 + \Gamma^2\omega^2} \tag{5-10}$$

The Lorentz dispersion model shows much better fit to the actual behavior of dielectric materials, especially in the absorption region. In the anomalous dispersion region, continuous decrease of ε' function is derived with increasing frequency.

5.5 Results And Discussion

5.5.1 Homogeneous Bulk of $SrBi_2Ta_2O_9$ (or SBT)

If we assume a homogeneous bulk model with no overlayers, the optical constants can be directly inverted from the ellipsometric data and are so called pseudo-optical constants. In Figure 5-5 the solid circles represents the pseudo-n of SBT obtained from experimental data. Both normal and anomalous dispersions were observed from the data. In the visible region, a gradual increase in the refractive indices was observed. The rate of increase of pseudo-n increased with decreasing wavelength. This is the phenomenon for normal dispersion. A decrease of refractive index was then observed when the wavelength was decreased to the near ultra-violet region. This anomalous dispersion of refractive index indicates the absorption band associated with electronic oscillation. Two models, Cauchy dispersion and Lorentz Oscillators models, were applied to fit the experimental data. In Figure 5-5, the data obtained from Cauchy dispersion model is shown by dotted line. In the region of normal dispersion, the model showed very good fit with the experiment. However, the model began to show departure from the experimental values when it was close to anomalous dispersion region at the low wavelength end. The value of refractive index from the Cauchy model increased rapidly in the low wavelength region and almost reached infinity at the resonance point. This is in disagreement with the experimental values which show a decrease of refractive index when close to the resonance point.

On the other hand, the Lorentz Oscillator model, represented by solid line as shown in Figure 5-5, shows a better fit with the experimental data. Only one oscillator was
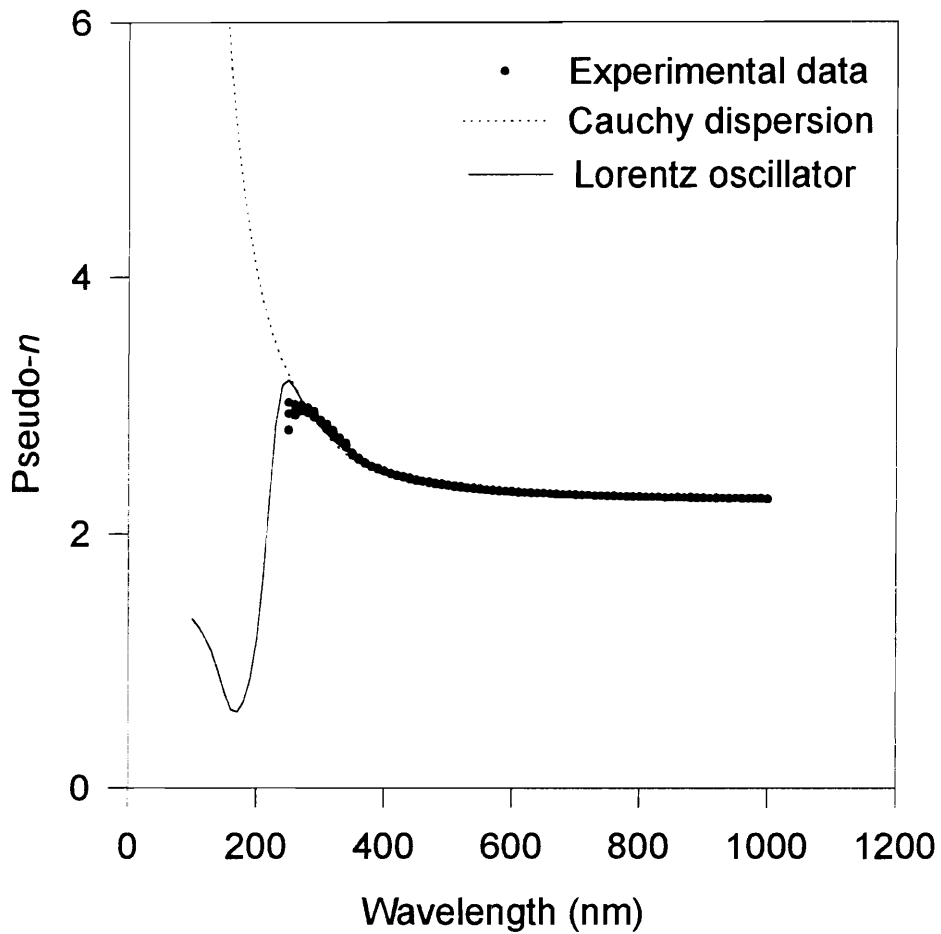
Figure 5-5   Wavelength dependence of pseudo-n for SBT obtained from:
(•) experimental data, (·····) Cauchy dispersion model, and
(——) Lorentz ocsillator.

assumed in the ultra-violet region. Therefore only one resonance frequency ω_0 (λ_0 for wavelength) is taken into account. Eq. (5-5) is then reduced to

$$\varepsilon^* = 1 + \frac{4\pi e^2}{m} \frac{N_0}{(\omega_0^2 - \omega^2) - i\Gamma\omega} \qquad (5\text{-}11)$$

From the data, it can be seen that the model shows very good fit to the experiment not only in the normal dispersion region but also in the anomalous dispersion region. The resonance frequency ω_0 is about 8.54×10^{15} s^{-1} (at wavelength about 221 nm). In the region of anomalous dispersion, the curve of the Lorentz Oscillator model has a maximum at a value of λ which is slightly greater than the resonance wavelength λ_0, and a minimum at a value slightly smaller than λ_0. Between the maximum and minimum the refractive index decreases continuously with decreasing wavelength.

Using the Lorentz oscillator model, we can analyze the wavelength-dependence behavior of SBT in terms of whether it is primarily reflection, absorption or transparent. The result is shown in Figure 5-6; the curves obtained were very similar to the case of KCl [88] which typically has a refractive index of about 1.5 in region I. Thus, the region I is characterized by high transparency without absorption, and probably a small reflection. The reflectivity arises from the induced polarization current corresponding to the valence electrons oscillating out of phase with the incident radiation. Region II of Figure 5-6 is characterized by strong absorption. However, there may also be appreciable reflectivity in this region because of high values of n and k. This simply means that, the light that is not reflected is strongly absorbed in the material. In region III where $\omega \gg \omega_0$, the electrons in the material respond as if they were free electrons. This is because the photon energy is much greater than the binding energy of electrons so that the material has a metallic
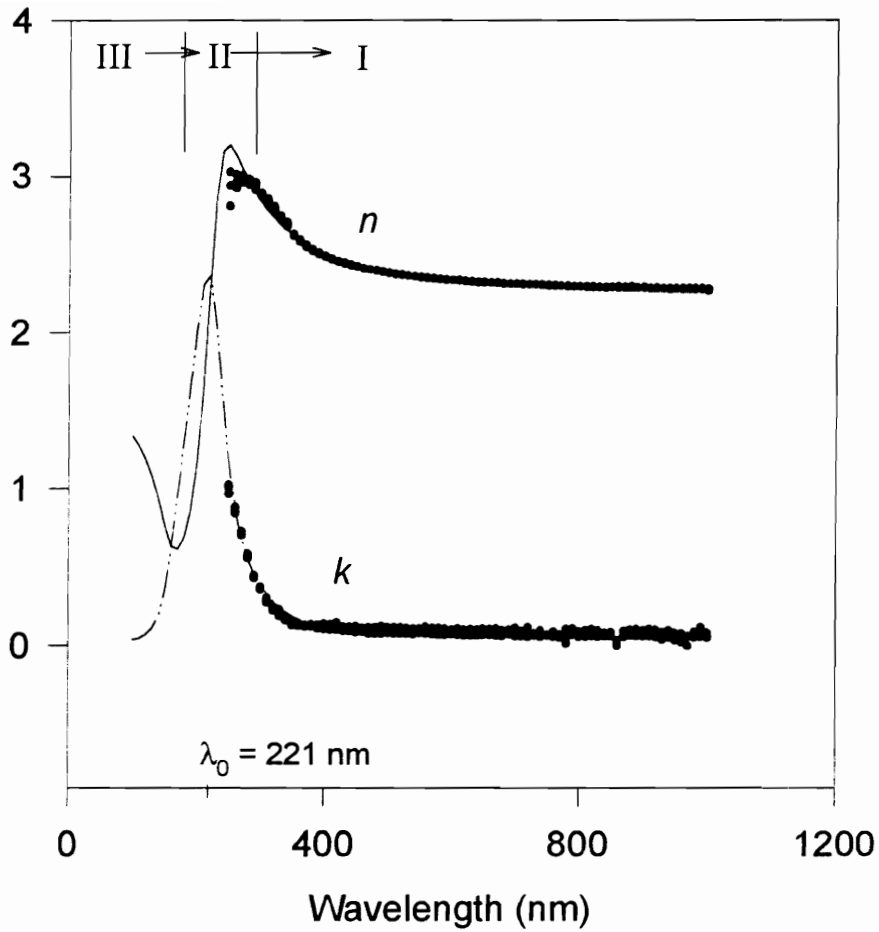
Figure 5-6 Wavelength dependence of pseud-n and pseudo-k for SBT according to the
Lorentz oscillator. The regions I, II, and III can be seen as primarily
transmitting, absorbing and reflecting.
Experimental data (•), and Lorentz oscillator model for pseudo-n (⸺)
and -k (—··—).

reflectance. For SBT ceramics, this region lies well into the ultraviolet and therefore it cannot be observed visually.

Although large deviation occurs in the absorption region for Cauchy dispersion, it still shows fairly good fit in the visible region which is far away from the absorption band. In fact, in the non-absorption region, the data obtained from the Cauchy dispersion model was very close to the data from the Lorentz Oscillator model; and both of them are in good agreement with the experimental data. Therefore, if only indices of refraction in the visible region are considered, a simple Cauchy model can describe the dispersion behavior very well.

5.5.2 Heterogeneous Surface Layer Correction for Bulk SBT

The index of refraction shown above was obtained directly from the experimental ellipsometric data assuming bulk without surface overlayers. However, this is not true for most of the bulk ceramics. There is always a heterogeneous surface layer as a result of the sample preparation process and it is very difficult to get rid of. According to the ellipsometry model illustrated in Figure 5-2, light was reflected at the interfaces between substrate-surface layer-ambient multilayer system. Here the ambient is air, the surface layer is the EMA layer which represents the effective inhomogeneous overlayer related to the surface roughness, stress and the other inhomogenieties; and the substrate is homogeneous SBT bulk ceramics. The optical constants obtained for the substrate phase were correlated to the bulk component of EMA layer. The optical properties of EMA layer can be changed by varying the parameters of SBT bulk substrate.

The effect of surface inhomogeniety on optical constants can be seen from Figure 5-7. It shows the dispersion relationship for the SBT bulk substrate and the surface layer.

Figure 5-7 The wavelength dependence of refractive indices for SBT ceramics and surface imperfection layer. (based on Cauchy dispersion model)

Since only the wavelengths in visible region were considered, the Cauchy dispersion model was applied to obtain the optical constants. For both the bulk phase and the surface layer, similar dispersion relations were observed. The refractive indices increased gradually at the moderate wavelength range, and increased more rapidly at low wavelength region. However, the refractive index for the surface layer was found to be lower than for the bulk substrate. For example, the index of refraction of bulk SBT is about 2.38 at wavelength 640 nm while it is only 2.32 for the surface layer at the same wavelength. The difference is a result of the voids that were introduced to model the surface layer to represent the effects of microscopic roughness present at the surface. The void fraction, f, in the surface layer is shown in Table 5-1. The fraction of voids indicates the degree of inhomogeniety of the surface layers. It was assumed that the inhomogeniety was mainly caused by surface roughness, porosity and residual stress as resulting from the sample surface preparation. According to the Bruggeman effective medium approximation, a large void fraction existing leads to a lower refractive index.

In addition to the refractive index, the extinction coefficient, k, was also determined. Figure 5-8 shows the extinction coefficient as a function of wavelength for SBT surface layer and substrate phase. In contrast to the refractive indices, the values of extinction coefficients obtained for both the surface layer and the bulk substrate were almost the same throughout the observed wavelength range. This is to be expected since in the optical model adopted, the void fraction was used to represent the inhomogenieties of the surface layer and these voids had air filled in them. There is almost no absorption of light for air within the UV-visible regime. Therefore, in the proposed effective surface layer, the absorption behavior is only the result of SBT component in the surface layer.

Because the effect of surface overlayer is excluded from the bulk sample in the EMA approximation, the optical constants obtained for the bulk substrate are the actual

Table 5-1   The void fractions* (f) and the thickness (d) of surface heterogeneous layer of SBTN estimated by EAM theory   and Cauchy dispersion model.

SrBi$_2$(Ta$_{1-x}$Nb$_x$)$_2$O$_9$		x = 0	x = 0.2	x = 0.4	x = 0.5	x = 0.7	x = 1
Cauchy	f (%)	4.4±0.1	2.1±0.9	6.9±0.2	4.9±0.2	3.5±0.3	13.9±1.7
	d (Å)	374±0.6	346±9.5	331±0.4	378±0.5	364±1.2	239±3.0
Lorentz	f (%)	2.3±0.3	0	2.9±0.2	4.0±0.4	0.8±0.2	1.5±0.7
Oscillator	d (Å)	583±1.8	0	533±1.2	581±1.4	596±3.7	435±12.9

*The void fractions and thicknesses here show the combining effect of surface inhomogeniety arising from the porosity, roughness and residual stress at the sample surface.
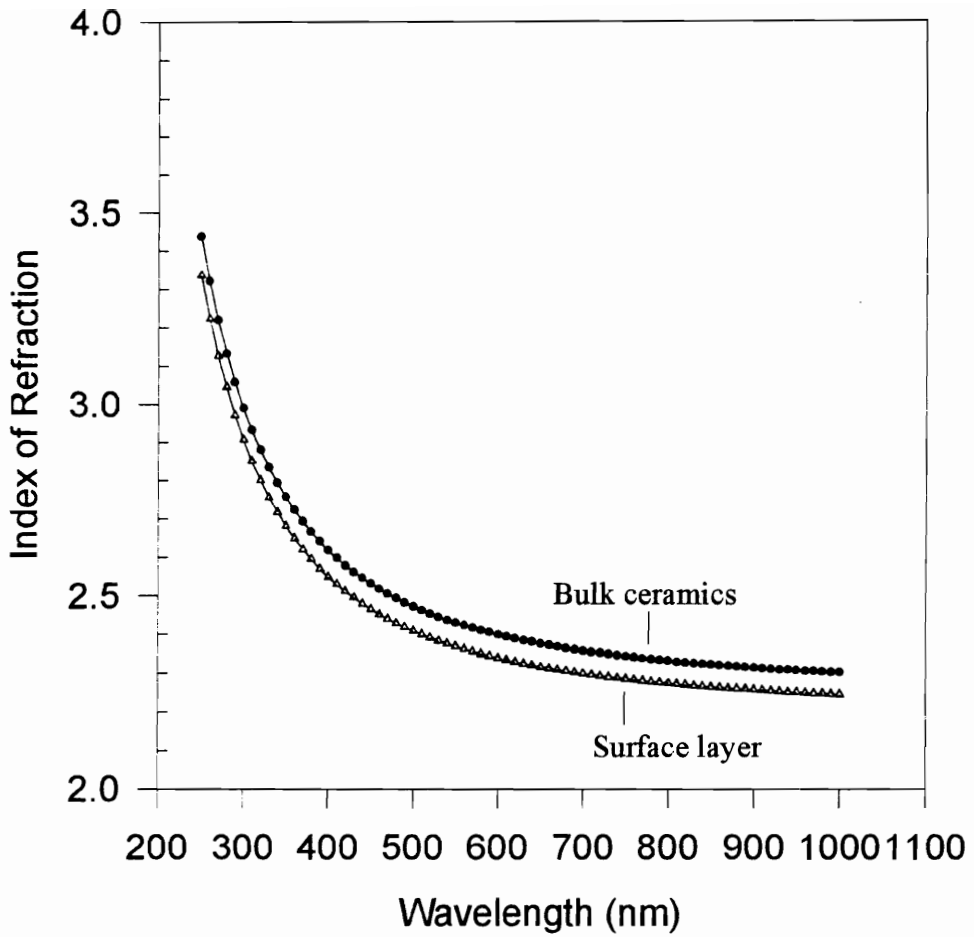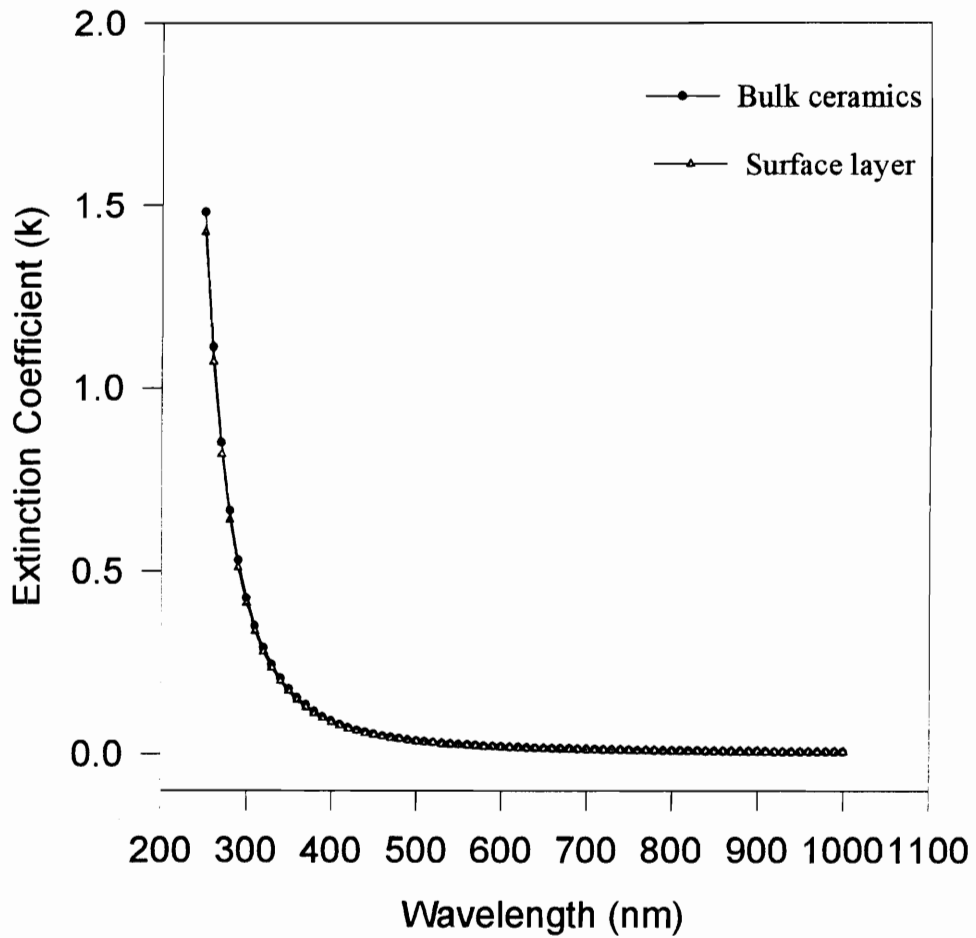
Figure 5-8　The wavelength dependence of extinction coefficient for SBT ceramics and surface imperfection layer. (based on Cauchy dispersion model)

values for SBT ceramics. By comparison with the result obtained from the assumption of bulk without surface overlayers (in Section 5.5.1), the actual index of refraction for SBT ceramics is higher than the pseudo-n (i.e., pseudo-n = 2.32 at 640 nm).

5.5.3 Optical Properties of SBTN Solid Solutions

Since only wavelengths in the visible region were concerned, Cauchy dispersion model was applied for SBTN solid solutions. The optical dispersion functions of the solid solutions were similar to the case of SBT as shown in Figure 5-7. In the SBTN solid solution system, the refractive indices were found to vary with Ta/Nb ratio. Figure 5-9 shows the composition dependence of refractive index (at wavelength 640 nm) for SBTN. Initially, the index of refraction increases with increasing Nb content reaching a maximum value when Nb content is about 50%, and then decreases with continuously increasing Nb content. In order to understand the relationship between optical properties and composition effects, it is convenient to discuss the polarizability of these materials.

It is known that dielectric materials react with and affect electromagnetic radiation because they contain charge carriers that can be displaced. The light waves are retarded because of the interaction of the electromagnetic radiation and the electronic systems of the atoms. According to the Lorentz-Lorentz equation, the polarizability α of the atoms of an elementary monatomic gas is related with the refractive index for waves of infinite wavelength through:

$$\alpha = \frac{3\varepsilon_0}{N_0}(\frac{n^2-1}{n^2+2})\frac{M}{\rho} = \frac{3\varepsilon_0}{N_0}R_\infty \qquad (5\text{-}19)$$
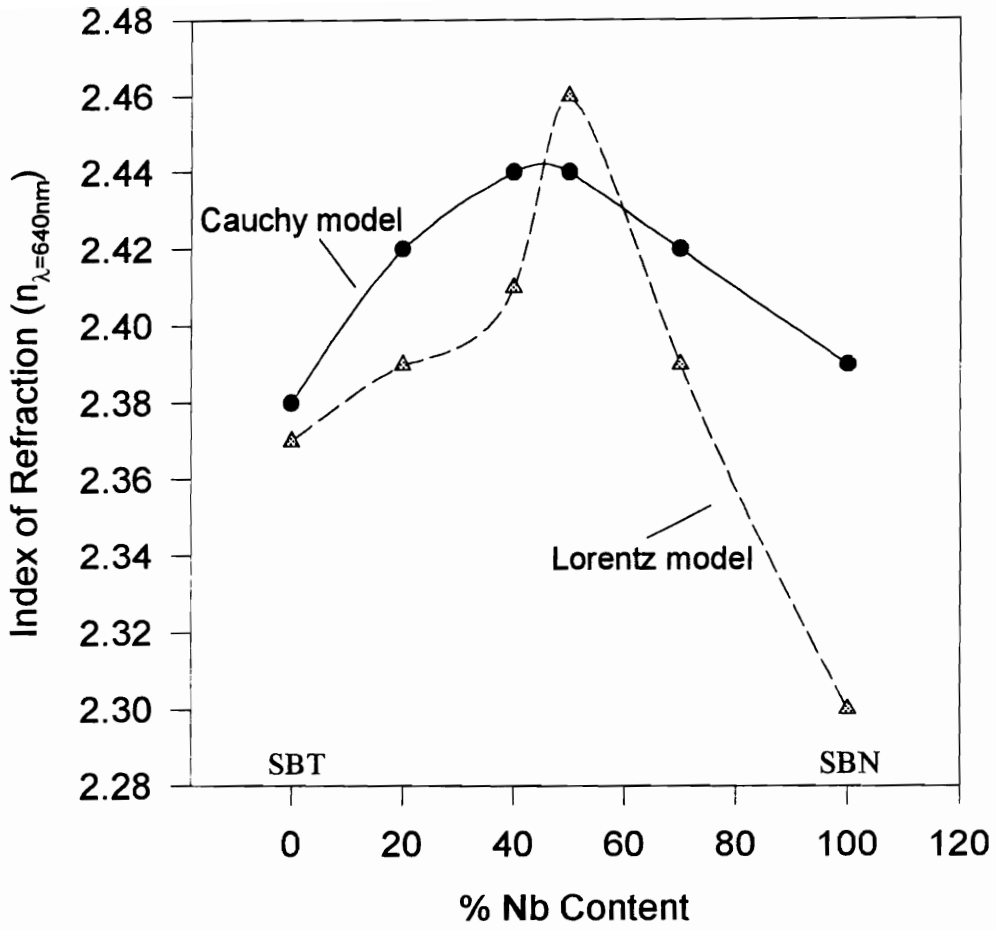
Figure 5-9 Composition dependence of refractive indices (at $\lambda = 640$ nm) for SBTN solid solutions.

where ε_0 is the dielectric constant of vacuum, N_0 is Avogadro's number, M is the molecular weight, ρ is the density, n is refractive index, and R_∞ is the molar refractivity which is directly proportional to the atomic polarizability.

In general, it is expected that the ionic polarizability increases with the size of the ion and with the degree of negative charge on isoelectric ions. As a result, the index of refraction increases with increasing atomic polarizability for large ions as indicated in the Lorentz-Lorentz equation. However, for SBTN solid solutions, both Ta^{5+} and Nb^{5+} ion sizes are almost the same (about 0.68Å). Therefore, the variation of refractive indices for SBTN is not because of the ion size. In addition to the ion size, the immediate surroundings and the arrangement of ions also affect the refractive index. In crystalline materials other than with cubic structure, the index of refraction is usually high in the directions that are close-packed in the structure. The more open structures lead to lower index of refraction. For SBTN solid solutions, since both Ta^{5+} and Nb^{5+} ions sizes are about the same, the variation of refractive indices of SBTN solid solutions could probably arise from the geometric arrangement of the atoms in the lattice. In bismuth layered-type structure, as illustrated in Figure 5-10, the loose packed planes are found between bismuth oxide layers and perovskite-like layers. If incident light is parallel to these layers (i.e., (00l) planes), the interaction between incident waves and atoms is expected to be less compared to the other directions. Thus the refractive index should be lower in the direction parallel to the (00l) planes, or perpendicular to the (hk0) planes. As a result, the variation of refractive indices for SBTN could be associated with the variation in lattice orientation. Figure 5-11 shows the lattice orientation ratio, $I_{(00\underline{10})}/I_{(200)}$, for SBTN calculated from XRD data. The data shows a maximum $I_{(00\underline{10})}/I_{(200)}$ ratio at about 50% Nb content. That is, at this composition, fewer (h00) planes are oriented parallel to the sample surface. This is
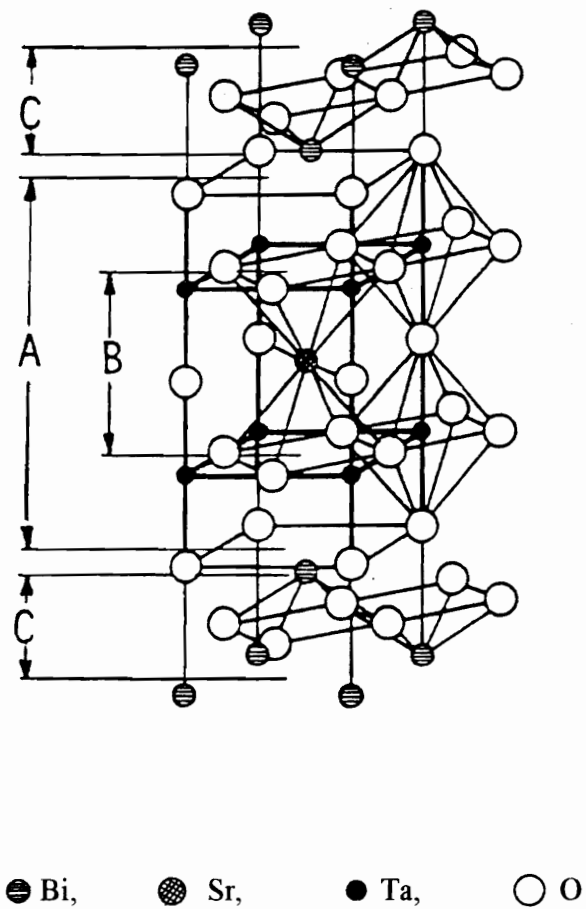
Figure 5-10 One half the pseudotetragonal unit cell of $SrBi_2Ta_2O_9$. "A" denotes the perovskite layer $SrTa_2O_7^{2-}$. "B" denotes units of hypothetical perovskite structure $SrTaO_3$. "C" denotes $(Bi_2O_2)^{2+}$ layers.
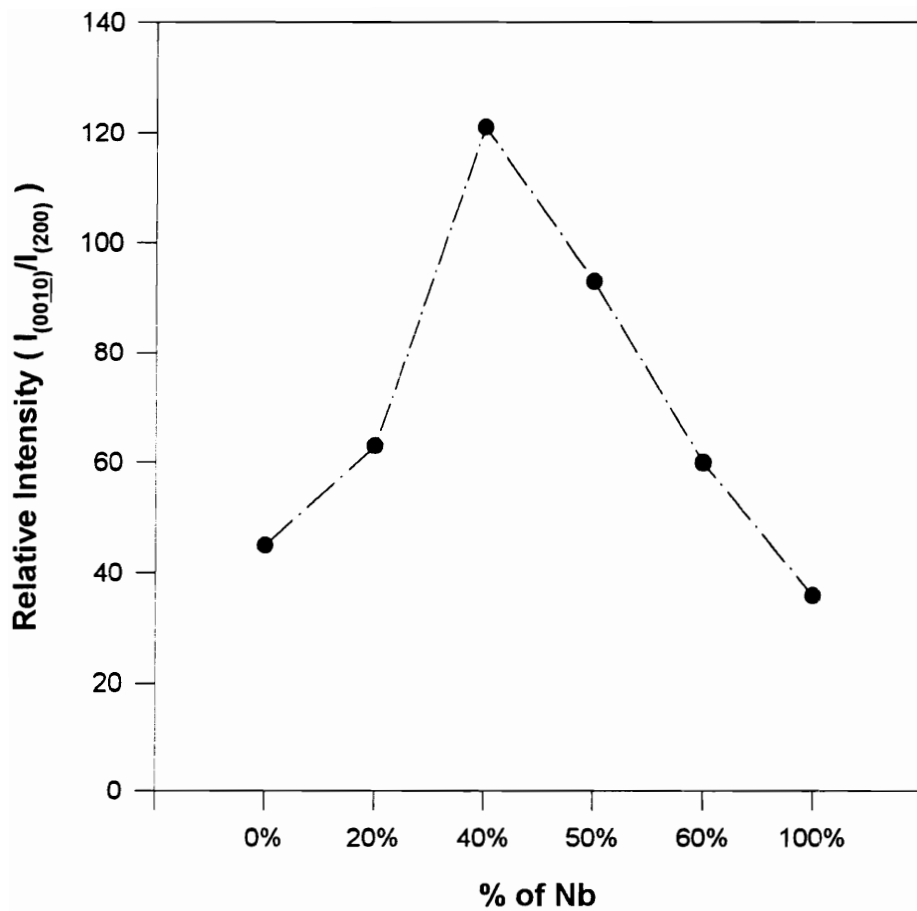
Figure 5-11   Lattice orientation ration $I_{(00\underline{10})}$ / $I_{(200)}$ varies with
Nb content in SBTN solid solutions.

in agreement with the result of refractive indices which also showed a maximum refractive index at about 50% Nb content.

5.6 Discussion

For frequencies within the visible region, both Cauchy and Lorentz Oscillator models can describe the normal dispersion behavior very well. However, in the anomalous dispersion region (i.e. absorption band), only the Lorentz Oscillator model can give the information accurately. By using the Lorentz Oscillator model with the surface layer correction, we are able to estimate the approximate energy band gap as well as the high-frequency dielectric constant, ε_∞.

In general, the total polarizability of the dielectric materials can be represented as the sum of electronic, ionic, dipolar and space charge polarizabilities. Among these, the dipoles and space charges only contribute to polarizability at frequencies lower than microwave. The contribution of ionic motions to the polarizability is mainly at infrared region and its contribution is rarely small at optical frequencies because the massive ions cannot follow such high frequencies. Thus, at visible and ultraviolet region, we shall only consider the electronic contribution to the dielectric constant. Consequently, the absorption band observed in visible-near ultraviolet region can be correlate to the band gap of the materials; and $\hbar\omega_0$ can be identified as corresponding approximately to the band gap. Additionally, the high-frequency dielectric constant can be obtained from the relation $\varepsilon_\infty = n^2$. The data of energy band gap and high-frequency dielectric constants are listed in Table 5-2. For SBTN solid solutions, according to Lorentz Oscillator model, all compositions have an energy band gap at about 5 ev, and ε_∞ with values at about 5 - 6.

Table 5-2   The energy band gap (E_g) and high frequency dielectric constants ($\varepsilon_r(\infty)$)

of SBTN.

SrBi$_2$(Ta$_{1-x}$Nb$_x$)$_2$O$_9$	Cauchy*		Lorentz Oscillator**	
	E_g (eV)	$\varepsilon_r(\infty) = n^2$ (at 640nm)	E_g (eV)	$\varepsilon_r(\infty) = n^2$ (at 640nm)
x = 0	4.55	5.66	5.47 ± 0.03	5.62 ± 0.10
x = 0.2	4.55	5.84	5.09 ± 0.06	5.71 ± 0.16
x = 0.4	4.55	5.96	5.30 ± 0.02	5.81 ± 0.05
x = 0.5	4.55	5.93	5.23 ± 0.02	6.05 ± 0.08
x = 0.7	4.55	5.85	5.11 ± 0.03	5.71 ± 0.08
x = 1	4.55	5.72	5.10 ± 0.06	5.29 ± 0.30

*E_g's of Cauchy model were estimated by the wavelength dependence absorption coefficients as shown in Appendix A.

**E_g's of Lorentz Oscillator model were obtained from ellipsometric simulation parameter.

According to the Debye equation, the real part of the complex dielectric constant can be expressed by

$$\varepsilon(\omega) = \varepsilon_\infty + \frac{\varepsilon_0 - \varepsilon_\infty}{1 - (\frac{\omega^i}{\omega_i})} \tag{5-20}$$

where ω_t is the transient frequency, and ε_0, ε_∞ are the static dielectric constant and the dielectric constant at high frequencies ($\omega \gg \omega_t$). In the first term on the right, ε_∞ contains only the contribution from the electronic polarizability. The second term on the right is the ac polarizability, and the ionic contribution is contained entirely in this term. As a matter of fact, the measured dielectric constants of SBTN [90] are within the range 100 - 300 (at frequencies 100 - 500 kHz). According to the previous result, for SBTN, the electronic contribution to the dielectric polarization is only 2-6%. Therefore, for SBTN, the contributions to the dielectric constant are mainly through ionic and dipolar polarizabilities in the low frequency range.

5.7 Conclusion

For the first time, the optical dispersion functions of $SrBi_2(Ta_{1-x}Nb_x)_2O_9$ ceramics were obtained by spectroscopic ellipsometry. The refractive indices of surface layer were found to be lower than the indices of the bulk. With lacking of surface layer correction in the optical model, the values of refractive index obtained for the bulk SBTN was found to be lower than the actual values because of the existing of the inhomogenieties in the materials. In the visible region, both Cauchy and Lorentz Oscillator models could describe the optical index dispersion behavior very well. However, in the absorption region, the

Cauchy model showed a large departure from the experimental data. In contrast, the Lorentz Oscillator provides a more accurate model in the absorption region. The approximate energy band gap for SBTN estimated by the Lorentz Oscillator model was about 5 ev. The results also indicated that the variation of refractive indices of SBTN was associated with the lattice orientation of the solid solution system.

Chapter 6. Fatigue Behavior of SrBi$_2$Ta$_2$O$_9$ And SrBi$_2$Nb$_2$O$_9$ By Impedance Spectroscopy Studies

In this chapter, the fatigue model of SBT and SBN is proposed for the first time. The model is built on the basis of the fatigue model proposed by Yoo and Desu [91-94]. The mechanism of less fatigue of SrBi$_2$Ta$_2$O$_9$ and SrBi$_2$Nb$_2$O$_9$ was discussed via the bulk ionic conductivities of the compounds. To obtain the bulk ionic conductivity, impedance spectroscopy study provides an effective method which allows to separate the individual contributions of bulk, grain boundaries and electrode-ferroelectric interfaces from the total cell impedance.

6.1 Introduction

Although SBTN thin films exhibit high potential for non-volatile memory applications, complete characterization of these material has not been done, yet. So far, we only know that the material has the property of fatigue resistance. However, the reasons for this fatigue behavior in these material is still unknown. Therefore, the objective of this study is to elucidate the reasons for fatigue resistance of these materials.

Fatigue in ferroelectric devices has been studied for several years and several mechanisms have been proposed to explain this degradation phenomenon [91-98]. A theoretical expression for the decrease in polarization was developed by Karan [95] based on space charge entrapment inside the ferroelectric that results in an increase in the interfacial resistance and decrease in the interfacial capacitance. Zheludev [96] proposed a planar model based on the formation of an inactive surface by space charge at the electrode-ferroelectric interfaces to produce a smaller amount of switched charge. Kudzin

[97] ascribed fatigue to the accumulation and resorption of space charge at the domain boundaries. Duiker [98] simulated fatigue by assuming dendritic growth of oxygen-deficient filaments. A quantitative fatigue model was proposed by Yoo and Desu [91-94] for PZT thin films. The model is on the basis of effective one-directional movement of defects due to asymmetric polarization under alternating pulses, and defects entrapment at electrode-ferroelectric interface (and/or grain and domain boundaries). The entrapment of defects creates space charges at electrode-ferroelectric interface.

In this research, the fatigue model of bismuth layered oxides, $SrBi_2Ta_2O_9$ (or SBT) and $SrBi_2Nb_2O_9$ (or SBN), was proposed on the basis of the concepts from Yoo and Desu [91-94]. The model was hypothesized by oxygen vacancies movement and was discussed via ionic transport phenomenon in the materials. In the present work, a new introduced complex impedance in the ferroelectric SBT and SBN bulk ceramics was employed to obtain the information about ionic transport phenomenon in the materials. The technique of complex impedance allows us to separate the individual contributions of grain interior, grain boundaries and electrode-ferroelectric interfaces to the total cell impedance. By using this technique, the ionic transport phenomenon in each component can be understand and can be used to explain the fatigue behavior in SBT/SBN.

6.2 Fatigue Model

As mentioned previously, fatigue in ferroelectric capacitors is manifested as a loss of switchable polarization and increase in coercive field with increasing number of polarization reversals. According to Yoo and Desu's fatigue model for Pt/PZT/Pt capacitors, defect movement under alternating pulses and defect entrapment at trapping sites (e.g., electrode-ferroelectric interface, domain boundaries and grain boundaries) has

been cited as the source of fatigue. These point defects could either be extrinsic or intrinsic. Extrinsic defects are impurities that are incorporated in the films during processing and can be controlled by controlling the processing environment. Intrinsic defects may include both defects that maintain the stoichiometry (Schottky defects) and defects that alter the stoichiometry in the materials.

When an ac field is applied to a ferroelectric capacitor, the ferroelectric material is polarized and an internal field is created by this polarization. The net local field is then expressed as [91-94]

$$E_L = E_A - E_i \qquad (6-1)$$

where E_A is the applied field and E_i the internal field. Although the externally applied field is symmetric, the net local field is asymmetric as a result of the internal field contribution. Under this asymmetric local field, there is an effective one-directional movement of the mobile defects towards the electrode-ferroelectric interfaces. In general, in polycrystalline thin films, the grain boundaries and the domain boundaries are usually coincident with the electrode-ferroelectric interfaces. The large interfacial energy at these boundaries/interfaces provides low potential energy sites for the defects and as a result causes their entrapment. Defects entrapment at the interfaces results in the development of space charge in these regions which in turn causes the domains to be pinned. The reduction in switchable polarization and increase in coercive field with increasing polarization reversals is a direct result of the domain pinning by the space charge.

There is sufficient experimental evidence to indicate that the defects accumulated at electrode-ferroelectric interfaces are mainly oxygen vacancies and it has a direct effect on the fatigue properties of the ferroelectric films. Scott et al. [99] have noticed a decrease

106

in the oxygen concentration (along with a loss of polarization) near the electrodes after fatigue cycling in Pt/PZT/Pt capacitors indicating increased accumulation of oxygen vacancies near the electrode-ferroelectric interface. Kwok and Desu [100] created near-surface oxygen depletion regions of different thickness in PZT films by processing the films under different partial pressures of oxygen. Higher fatigue rate was observed for the films processed under a low partial pressure of oxygen in the processing ambient (i.e., higher oxygen vacancy concentration in the films). Lee and Desu [101] have observed an increase in the interfacial capacitance (with no change in bulk permittivity) with increasing fatigue cycles in Pt/PZT/Pt capacitors. This observation has been attributed to the build up of space charge in the interface regions.

According to the above model, it is concluded that several requirements have to be satisfied for observing high fatigue rate. Generally, there should be enough high oxygen vacancy concentration in the materials; and these oxygen vacancies should have reasonable mobility to move under an applied electrical field. Additionally, there should be good trap sites existed in the cell. By applying an electric field, these oxygen vacancies will easily move in one direction towards the electrode. By changing the applied field direction, *i.e.*, ac electric field, those oxygen vacancies which have already reached the interface are trapped by some abnormal positions at the interface and are not able to move back to the bulk. As a result, these trapped oxygen vacancies create the space charges at the electrode-ferroelectric interface and fatigue happens. Referring this, the reason of less fatigue in the materials is possibly due to one of these factors, e.g., low defect concentration, low mobility and absence of good trap sites in the materials, or the combining effect of these factors.

The above concepts of fatigue are now applied to bismuth layered oxides SBT and SBN. The layer-type structure of SBT/SBN is comprised of a stacking of 2 perovskite-like

units of O-R-O (R denote Ta or Nb) chains between Bi_2O_2 layers along the pseudotetrahedral c-axis. As mentioned previously, oxygen vacancies are considered as the most mobile charges in perovskite ferroelectrics. Additionally, for highly conductive oxides like Bi_2O_3, the conducting species were also found to be oxygen vacancies. Considering these two structures, it is assumed that the most mobile charges in bismuth layered oxide are oxygen vacancies and they are responsible for the ionic conductivity in the materials [102,103]. The fatigue behavior in SBT/SBN is then discussed via bulk ionic conductivity in these materials.

The model of fatigue behavior in SBT and SBN is illustrated in Figure 6-1. This model is built on the basis of the assumptions of oxygen vacancy concentration, mobility, and the existence of trap sites in these materials. There are two hypothesises that lead to the characteristics of fatigue resistance for these materials. According to the model, the first hypothesis is that there is considerably low defect concentration in the materials. Therefore, the amount of defects accumulated at the trap sites (e.g., electrode-ferroelectric interfaces) is very little within a limited time. The space charges created in this case are not significant so that no fatigue properties is observed. According to this hypothesis, the bulk ionic conductivity in SBT/SBN should be considerably low, because of low defect concentration.

The second hypothesis to be considered is high defect concentration in these materials. In this case, the defect mobility can be either low or high. In the case of low defect mobility, high defect concentration may lead to a medium ionic conductivity in the bulk materials. On the other hand, the case of high defect mobility associated with high defect concentration may lead to a high ionic conductivity in the materials. For both cases, the defects could probably reach the electrode-ferroelectric interface in a limited time and are blocked by the electrode under an applied electric field. However, for the absence of
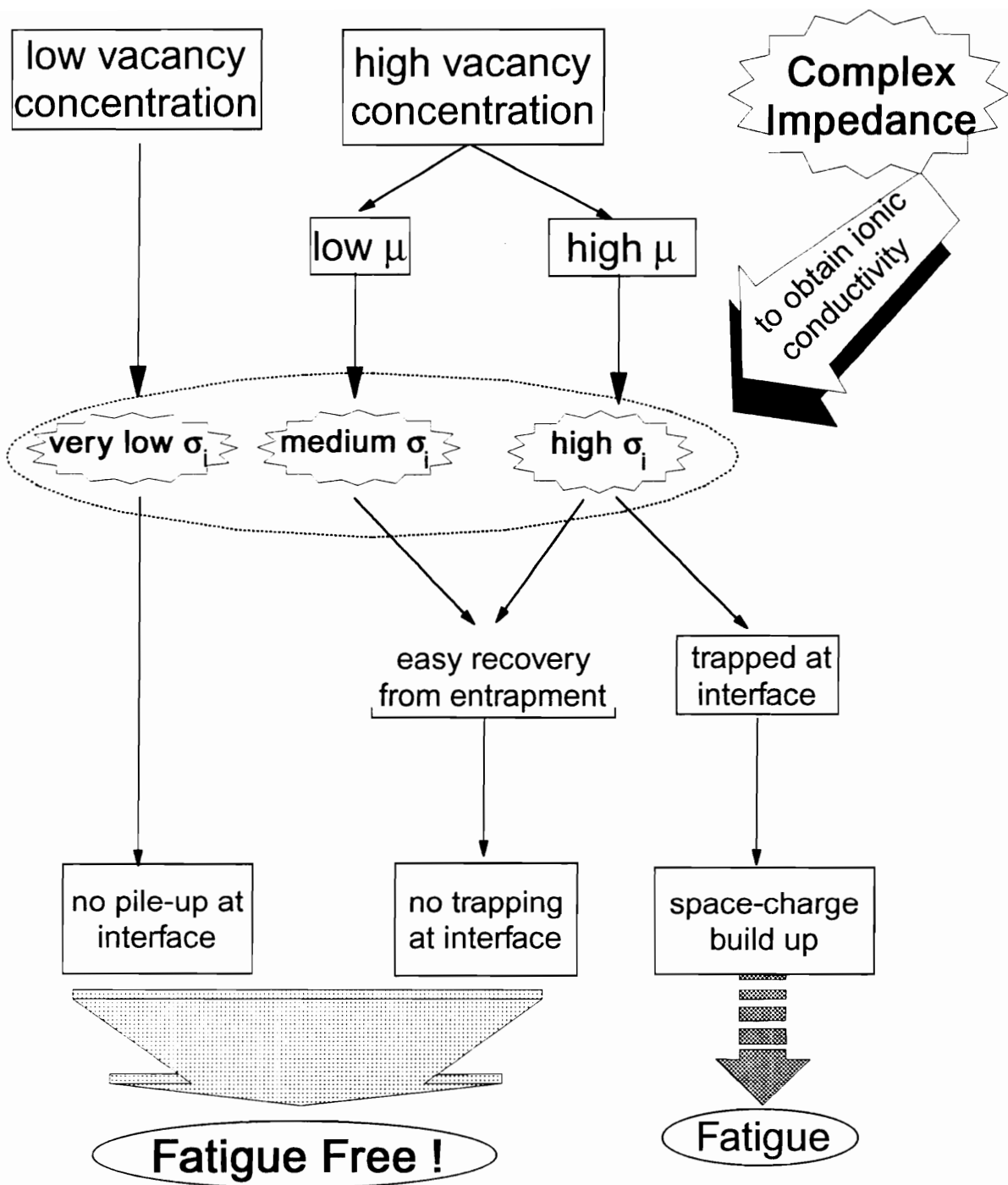
Figure 6-1. Fatigue model for SBT and SBN.

ferroelectric fatigue for SBT/SBN, the possible reason is that the easy recovery from the entrapment of these defects. Once the applied electrical field is switched, these defects can easily move back to the bulk from the trap sites. Because of no defects accumulation, there is no space charges created at the interface therefore the resistance to fatigue is increased.

According to this fatigue model, the mechanism of fatigue resistance in SBT and SBN is able to be identified by detecting the bulk ionic conductivity of these materials. To obtain the bulk ionic conductivity, the complex impedance was employed and it was shown to be a convenience technique which allowed to separate the contribution of the bulk from the total cell impedance.

6.3 Complex Impedance And The Equivalent Circuit Models

The use of complex impedance plane for the analysis of electrochemical reactions was introduced by Sluyters [104]. The complex impedance presentations represent the most basic form of information about the dielectric properties of a substance and they form the basis of most interpretational analysis on experimental data, i.e. the presence of inhomogenieties at separate regions characterized by different dielectric properties. The frequency-dependent complex impedance can be expressed by the combination of frequency-independent resistance and capacitance as shown below

$$Z^* = R - jX = R - j/\omega C \qquad (6\text{-}2)$$

where R is resistance, X is reactance and C is capacitance of the cell. As pointed out by Bauerle[105], this technique allows the separation of several contributions to the total cell

impedance, arising from bulk conduction and interfacial phenomena, as polarization effects at the electrode-electrolyte interfaces. Powers and Mitoff [106] have also achieved the experimental separation of electrode and grain boundary effects from bulk conductivities in β-alumina electrolyte.

The successful separation of intergranular from bulk phenomena depends ultimately on the choice of an appropriate equivalent circuit to represent the electrolyte properties. Armstrong et al. [107] have used equivalent circuit models in complex impedance planes to simulate the effects of blocking electrodes, grain boundaries, etc., and have shown that this method of circuit analysis can be applied to practical systems. There are several models of specific examples illustrated in Figure 6-2. In these models, the terms blocking , non-blocking and absorption have to be defined. These terms are applied to electrodes and they describe the degree to which the mobile ions in the electrolyte can penetrate the electrode material. A completely blocking electrode is the one which no penetration of the mobile ions can occur. The equivalent circuit and predicted complex impedance plane of this case are illustrated as Figure 6-2 (a), where C_g is a geometric capacitance of electrolyte, R_b is its bulk resistance, ω_1^* is equal to $(R_b C_g)^{-1}$, and C_{dl} is the capacitance which arises from the effect of mobile ions blocked by electrodes at electrode-electrolyte interfaces.

The opposite situation is that involving non-blocking electrodes which equivalent circuit model is shown in Figure 6-2 (c). Here, R_{ct} is a charge transfer resistance between the electrode and electrolyte and ω_2^* is equal to $(C_{dl} R_{ct})^{-1}$. For the case when charge transfer resistance for mobile ion transfer between the electrode and electrolyte is less than that between adjacent layers in the bulk of the electrolyte, the interfacial impedance becomes negligible and the equivalent circuit reduces to R_b in parallel with C_g.
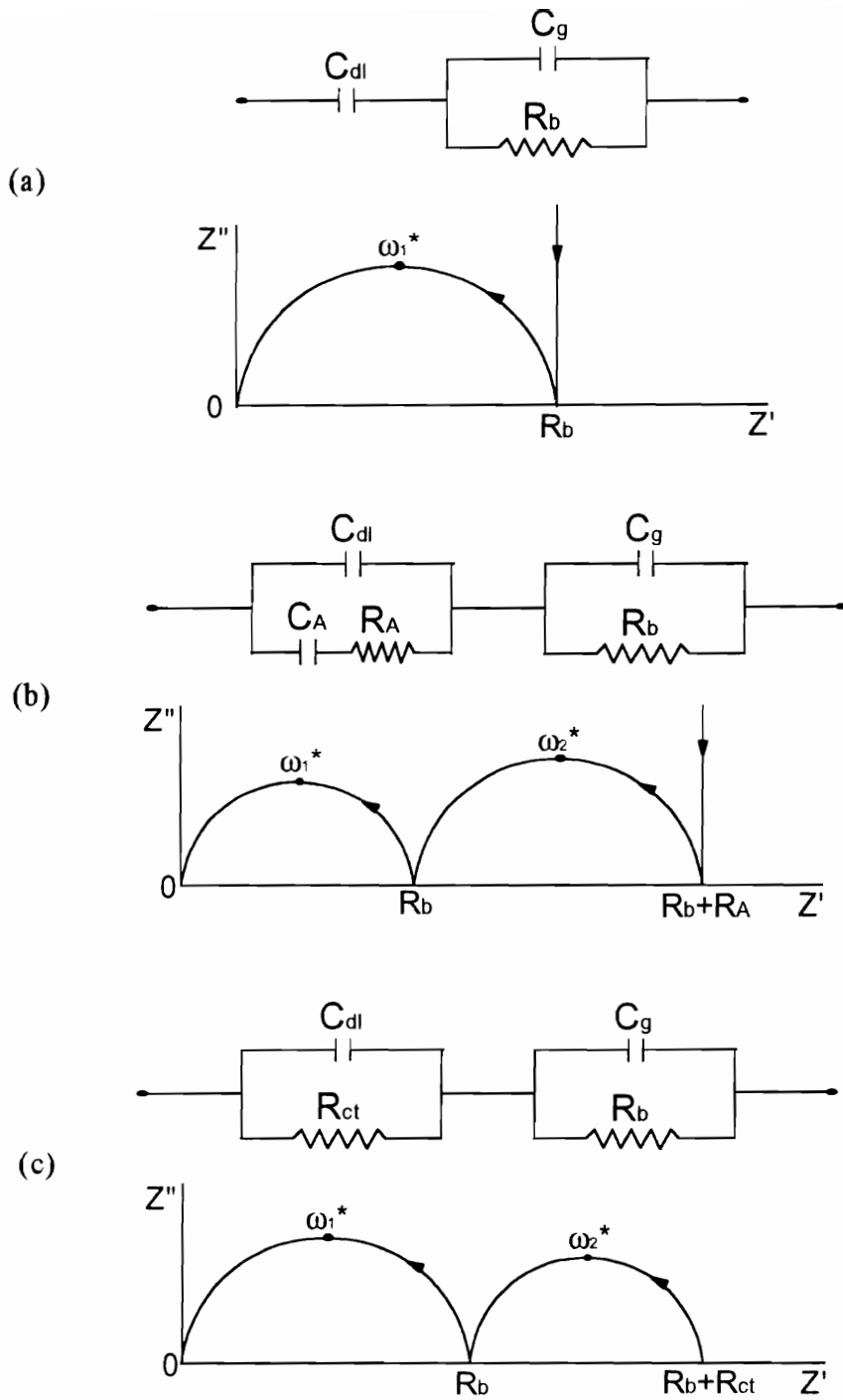
Figure 6-2. Equivalent circuits and predicted complex-plane impedance spectra for the cases of (a) blocking electrodes without specific absorption, (b) blocking electrodes with specific absorption, and (c) non-blocking electrodes [107].

112

The case of absorption, as shows in Figure 6-2 (b), is because some abnormal positions of the proximity of electrode surface become possible for the mobile ions and lead to the entrapment of these mobile ions. In this case, C_A is a capacitance which arises from the specific adsorption of the mobile ions and ω_2^* here is equal to $(C_{dl}R_A)^{-1}$.

6.4 Experimental Procedure

From our previous studies [50,51,53,108,109], good ferroelectric hysteresis properties were obtained for $SrBi_2(Ta_{1-x}Nb_x)_2O_9$ solid solution system. In this research, $SrBi_2Ta_2O_9$ (or SBT) and $SrBi_2Nb_2O_9$ (or SBN) were selected so that the properties may be extrapolated to the solid solution system. The reason for using bulk materials is to avoid the difficulties rising from thin film measurement. The bulk of samples were prepared by solid state reaction as described in Section 2.2. In order to have an external contact, the platinum electrodes were sputtered onto both sides of SBN pellet. Then it had a platinum lead attached on the electrodes with platinum paste. Whereas, for SBT sample, a platinum lead was directly attached on each side of the pellet with platinum paste.

The complex impedance of each sample were then measured by HP4192A impedance analyzer with a four terminal-shielded two terminal extension configuration. The applied frequency was scanned from 10 Hz to 1M Hz with no bias voltage applied. A very small oscillating amplitude (50 mV) was applied for each measurement. During the measurement, the heat treatment was carried out in a stand-alone oven controlled by OMEGA mode CN9000 temperature controller through a temperature range from room temperature to 700°C. The applicability of the impedance spectroscopy is limited only by the accuracy and range of the laboratory impedance analyzer. HP4192A can measure impedance in the frequency range of 5 Hz to 13 MHz. The upper limit of the measured

impedance value is approximately 1.3 MΩ. This value was shown to be the important limitation in the application of impedance spectroscopy.

6.5 Experimental Results

6.5.1 Complex Impedance of SrBi$_2$Ta$_2$O$_9$

The complex impedance of the samples was measured with temperature ranging from room temperature to 650°C, and across a frequency range from 10 Hz to 1 MHz. Because the resistance limitation of the instrument is only about 1.3 MΩ, the elevated temperatures are required to bring sample resistance below the limitation. Figure 6-3 (a), (b) and (c) show the typical examples of complex impedance planes for SBT ceramics at 108°C, 400°C, and 575°C. To a first approximation, these complex impedance planes can be represented by the equivalent circuit models shown in these Figures. Each semi-circle is represented by a parallel *RC* circuit which is corresponding to the individual component of the material, i.e., grain , grain boundary and electrode-ferroelectric interface. The resistances of each component can be obtained from the intersections of the arcs with *x*-axis; the capacitance can be calculated from the equation, $\omega_i R_i C_i = 1$, where ω_i is the frequency at the maximum of the semi-circle for *i* component. The calculated *R* and *C* values for each component at elevated temperatures are shown in these figures.

For temperatures below 400°C, similar complex impedance planes were observed with only one semicircle representing the bulk behavior as shown in Figure 6-3 (a). The bulk behavior of SBT ceramics is described in terms of the grain resistance R_g and the grain capacitance C_g in parallel, as illustrated in Figure 6-3 (a). The model of a parallel *RC* circuit was verified by a straight line observed in the admittance spectrum as shown in the
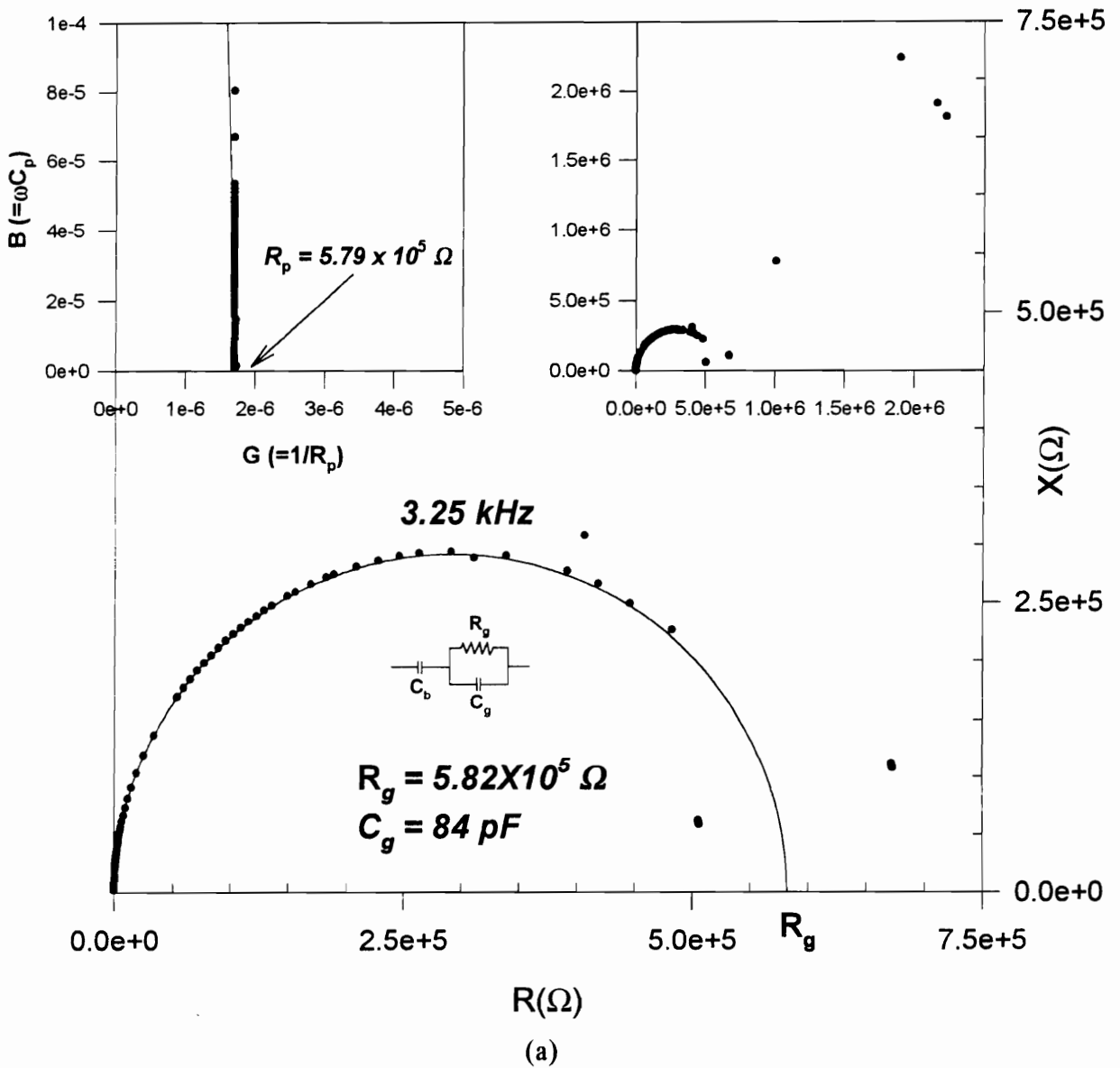
Figure 6-3(a). Complex impedance plane of SBT ceramics (with Pt-electrodes) measured at 108°C. (Sintering temperature: 1280°C/3 hrs; sample area = 1.1759 cm^2; sample thickness = 0.1498 cm)
- Right upper figure: complete spectrum of the complex impedance.
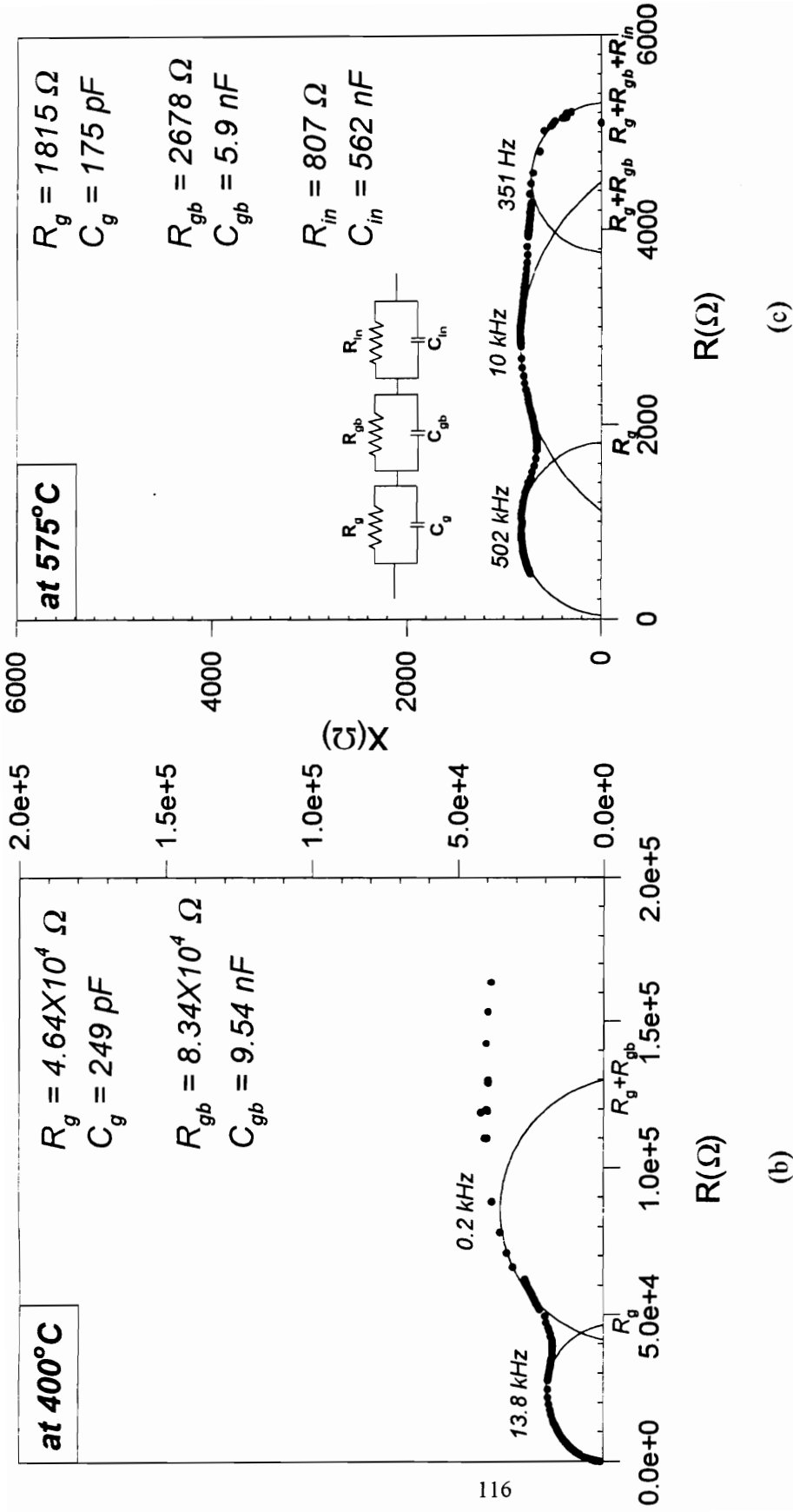- Left upper figure: complex adimittance plane at 108°C.

at 400°C

$R_g = 4.64 \times 10^4 \ \Omega$
$C_g = 249 \ pF$

$R_{gb} = 8.34 \times 10^4 \ \Omega$
$C_{gb} = 9.54 \ nF$

at 575°C

$R_g = 1815 \ \Omega$
$C_g = 175 \ pF$

$R_{gb} = 2678 \ \Omega$
$C_{gb} = 5.9 \ nF$

$R_{in} = 807 \ \Omega$
$C_{in} = 562 \ nF$

(b)

(c)

Figure 6-3 (b) and (c). Complex impedance planes of SBT ceramics (with Pt-electrodes) measured at (b) 400°C and (c) 575°C. (Sintering temperature: 1280°C/3 hrs; sample area = 1.1759 cm², sample thickness = 0.1498 cm)

116

upper left corner of Figure 6-3(a). The whole spectrum of the complex impedance at 108°C is shown in the upper right corner of Figure 6-3(a); an inclined spike observed at low frequencies represents the effect of blocking capacitor at the electrode-ferroelectric interface and denoted by C_{bl} in the equivalent circuit. As it was mentioned by Bauerle[105], this spike shown at low frequencies attributes to polarization at electrode-electrolyte interface and it would arise if charge carrier is mobile ions. In this case, the value of R_g obtained at the intersection was then recognized as a resistance corresponding to ionic conduction motion resulted from the mobile species of oxygen vacancies.

However, when temperature increased to above 400°C, the semicircle representing grain boundary effect became visible at low frequencies, e.g., Figure 6-3(b). As temperature increased further, e.g., above 500°C, three semicircles at high, moderate and low frequencies were detected corresponding to the dielectric behaviors arising from the grain interior, grain boundary and the electrode-ferroelectric interface polarization, e.g., Figure 6-3(c). The high temperature representations such as Figure 6-3(b) and (c) can be represented by the equivalent circuit shown in Figure 6-3(c). Three parallel RC circuit elements in series are corresponding to the dielectric behaviors of grain, grain boundary and electrode-ferroelectric interface, respectively. The correlation of these components in the complex impedance was investigated by the temperature dependence resistances obtained from the complex impedance plane as shown in Figure 6-4. It was found that the values of R_g and R_{gb}, obtained from the two semi-circles in high and moderate frequencies, showed a strong similarity in their temperature dependence. This suggests that the resistance R_g and R_{gb} may arise from the same type of physical process. In other words, the two semi-circles in high and moderate frequency regions may represented the dielectric behaviors of SBT arising from grain interior and grain boundaries. Generally, grain boundaries exhibit high resistance in comparison to grain interior. As a result, the
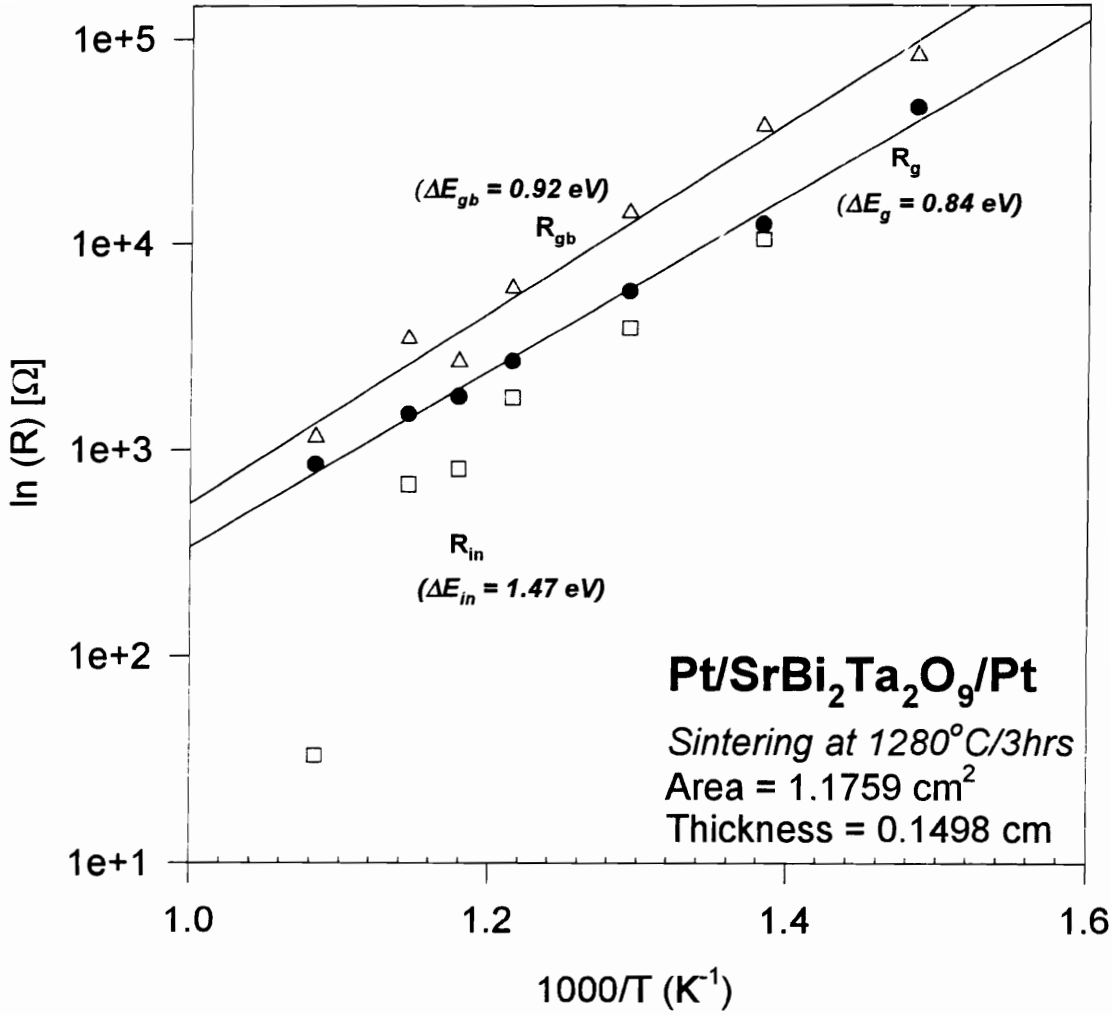
117

Figure 6-4. Temperature dependence resistance of SBT grain interior (R_g), grain boundary (R_{gb}), and electrode-ferroelectric interface (R_{in}).

semi-circle in high frequency region was recognized as the impedance of SBT grain interior (or bulk SBT), while the semi-circle in moderate frequency region was recognized as the impedance of grain boundaries. Thus, the values of R_g and R_{gb} corresponded to the resistances of bulk and grain boundaries, respectively. Consequently, the third semi-circle in low frequency region was then referred to the impedance of electrode-ferroelectric interface. From Figure 6-4, it was also found that the temperature dependence of electrode-ferroelectric interface resistance, R_{in}, corresponded to a thermally activated process with a higher activation energy approximately 1.5 eV. According to the Bauerle's argument, this thermally activated process is possibly resulted from an electron-transfer reaction at the electrode-ferroelectric interface.

6.5.2 Complex Impedance of $SrBi_2Nb_2O_9$

Similar to SBT, the complex impedance of SBN was measured with temperature ranging from room temperature to 700°C, and across a frequency range from 10 Hz to 1 MHz. Figure 6-5 (a) and (b) show the typical examples of complex impedance planes of SBN at 100°C and 600°C, respectively. For temperature below 450°C, similar complex impedance planes were obtained as illustrated in Figure 6-5(a). In this low temperature region, only one semi-circle representing bulk dielectric behavior was observed. The corresponding equivalent circuit is also shown in this figure. A inclined spike shown at low frequencies indicated that the resistance R_g corresponded to the ionic conduction motion resulted from oxygen vacancies movement. The values of R and C are shown in these figures.

When temperature increased above 450°C, a broad second semi-circle began to show in low frequency region. As temperature increased further, e.g., to about 700°C, the
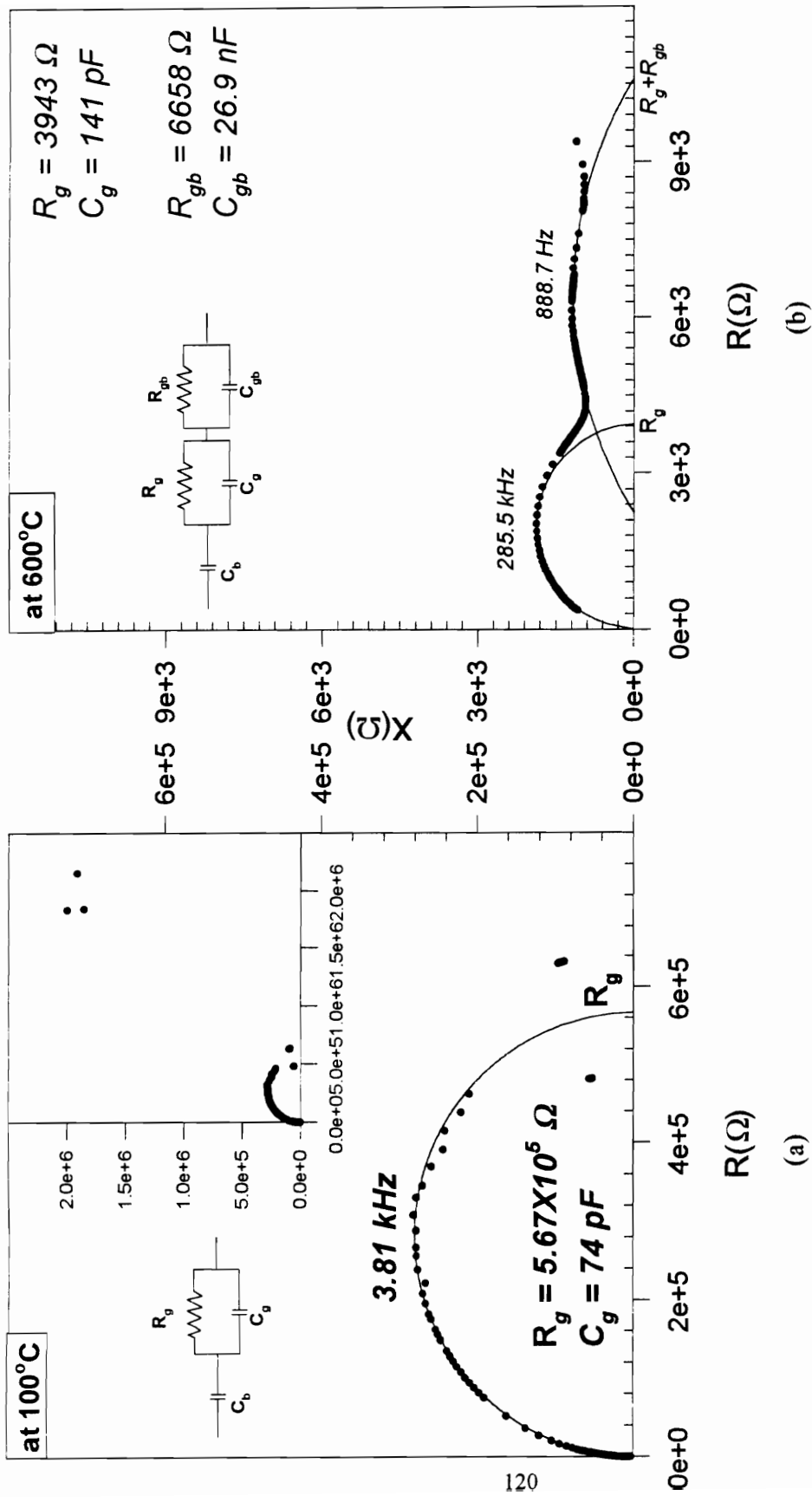
Figure 6-5. Complex impedance planes of SBN ceramics (with Pt-electrode) measured at (a) 100°C and (b) 600°C. (Sintering temperature: 1280°C/3 hrs; sample area = 0.6079 cm², sample thickness = 0.1048 cm)

complex impedance planes were similar to the typical example shown in Figure 6-5(b). In this high temperature region, two semi-circles were shown associated with a small spike in low frequency end. The corresponding equivalent circuit for high temperature representation is also shown in Figure 6-5(b), which has two parallel RC circuit in series in conjunction with a blocking capacitance. How this complex impedance representation correlates to the material properties can be seen from the temperature dependence resistance as shown in Figure 6-6. A very strong similarity of R_g and R_{gb} in temperature dependence was observed. These two parallel lines indicate that the resistances R_g and R_{gb} may be resulted from the same conduction mechanism. This suggests that the two semi-circles observed in high temperature region may represent the dielectric behavior of SBN arising from the grain interior and grain boundaries. Since grain boundaries normally exhibit higher resistance than grain interior; as a result, the first semi-circle in high frequencies region may refer to the bulk behavior while the second semi-circle in low frequencies region may represent the dielectric behavior of grain boundaries. In the case of SBN, the effect of electrode-ferroelectric interface was simply shown by a electrode blocking effect.

6.6 Discussion

By complex impedance study, the effect of ion transport within the bulk (or grain interior) was separated from the whole cell impedance. According to the above results, the bulk ionic conductivity, σ_i, can be derived from the bulk resistance, R_g, by a geometric factor. Figure 6-7 shows the temperature dependence bulk ionic conductivities of SBT and SBN. For both cases, a temperature, T_t, was observed (i.e., 283°C for SBT and 340°C for SBN) at which the conduction mechanism changed. Below this temperature, the σ_i's were
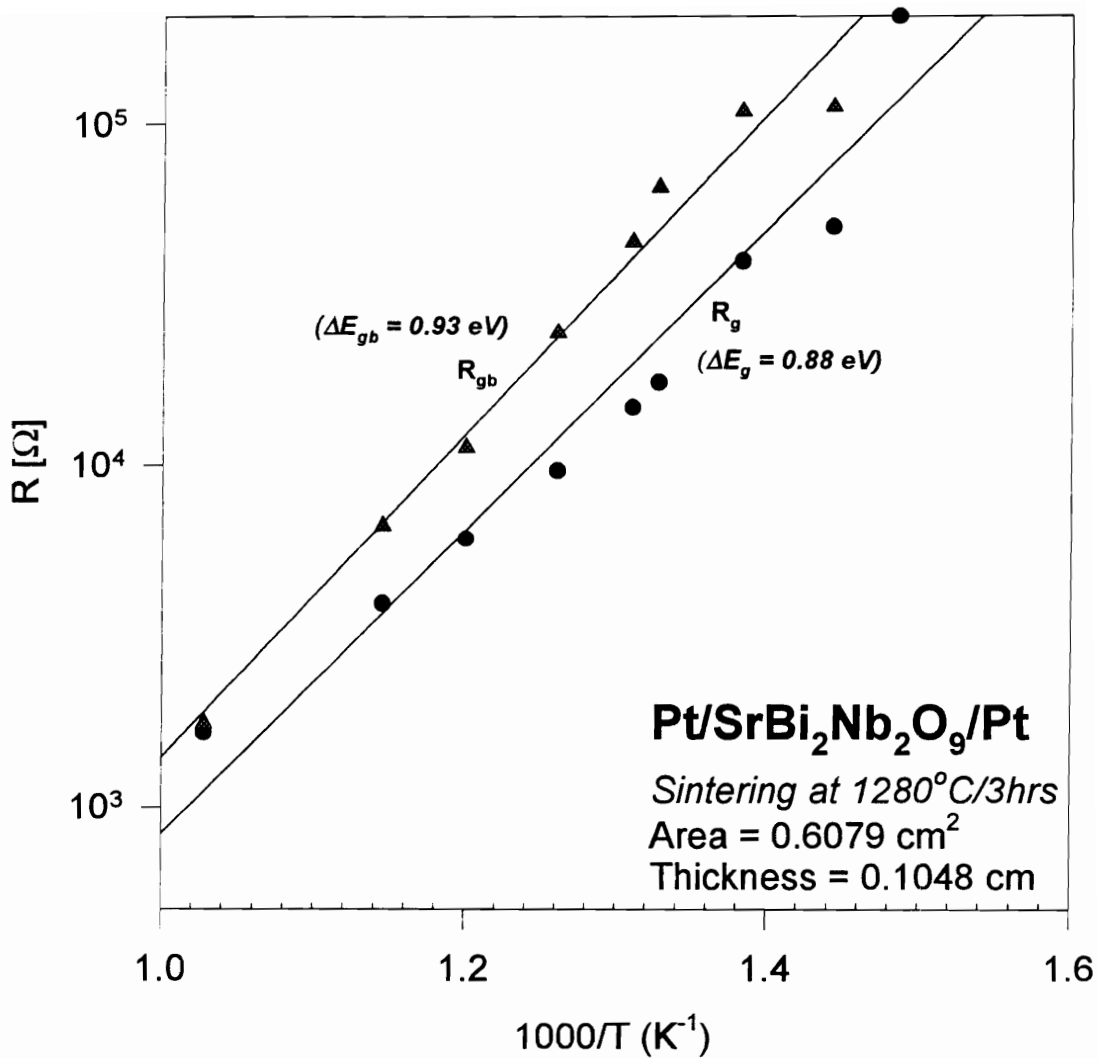
Figure 6-6. Temperature dependence resistances of SBN grain interior (R_g), and grain boundary (R_{gb}).
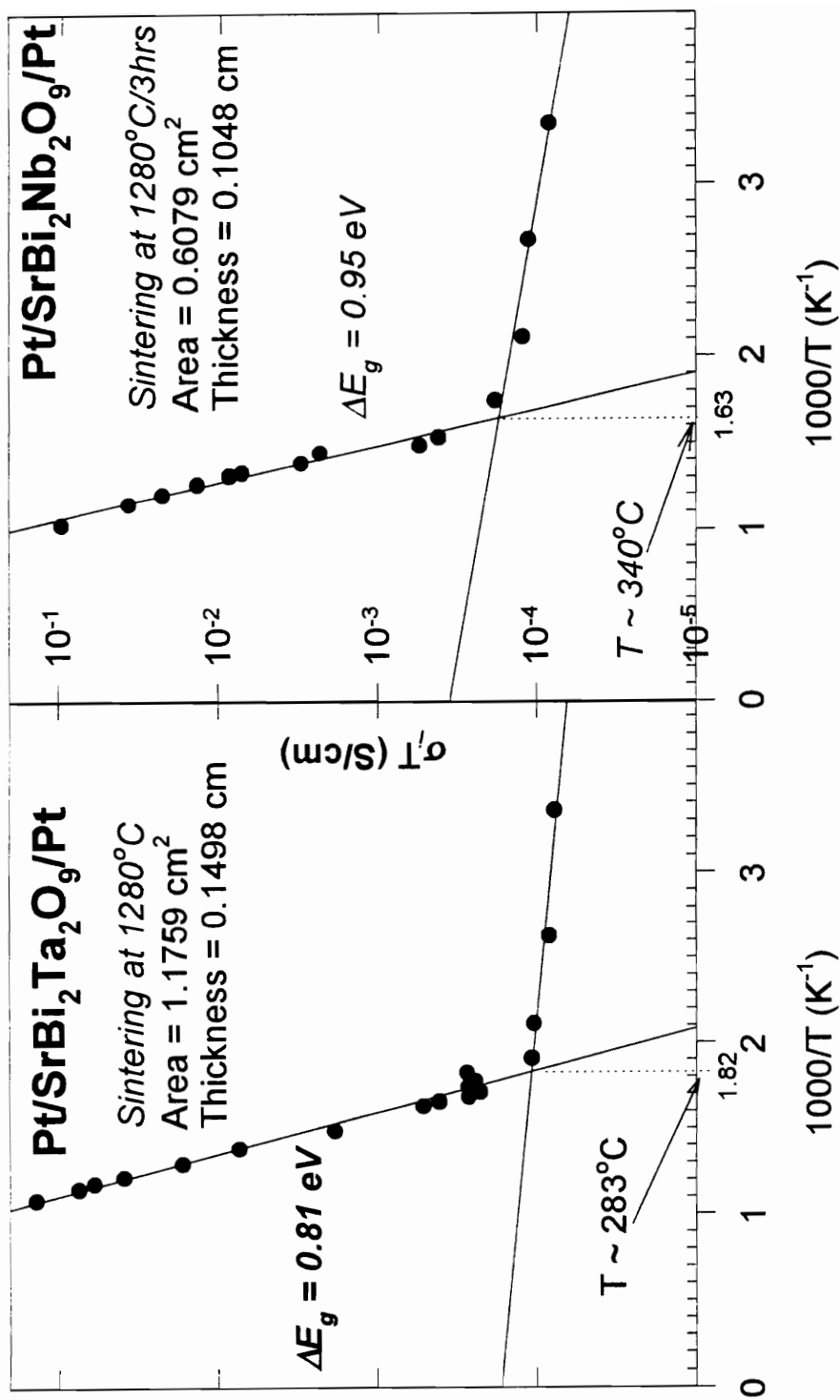
Figure 6-7. Temperature dependence bulk ionic conductivities obtained from complex impedance planes of (a) SBT, and (b) SBN.

found to be not sensitive to the measuring temperatures and with the values of about 10^{-7} S/cm. However, for the temperatures above T_t, the σ_i's were found to be thermally activated with the activation energies about 0.81 eV and 0.95 eV for SBT and SBN, respectively.

It is interesting to note that these T_t's of SBT and SBN were found to be close to the Curie temperatures (T_c) of these materials. As it is shown in Figure 6-8, the Curie temperatures were observed at around 320°C and 420°C for SBT and SBN, respectively. This suggests that the changes in the temperature dependence of bulk ionic conductivity is possibly associated with ferroelectric-paraelectric phase transformation around the T_c. The ionic conductivity of the materials, σ_i, can be expressed by

$$\sigma_i = \sum_j n_j e \mu_j \qquad (6\text{-}3)$$

where μ_j is the mobility of j mobile charges and n_j the number of the mobile charges which corresponds to the defects concentration in the material. It can be seen that the ionic conductivity can be changed by changing either the number of mobile charges or the mobility. However, in the cases of SBT and SBN, abrupt changes of defect concentration at around Curie temperatures should not be expected because, in this temperature region (i.e., around 300-400°C), the temperatures are significantly low for intrinsic defects creation. Consequently, according to the Equation (3), the abrupt changes of conductivities at around Curie temperatures for SBT and SBN is resulted from the mobility changes in the materials. This suggests that the change in conduction mechanism around T_c could be related to the change in mobilities (μ_i) due to ferroelectric to paraelectric phase transformation. However, how the polarization state affects the

124
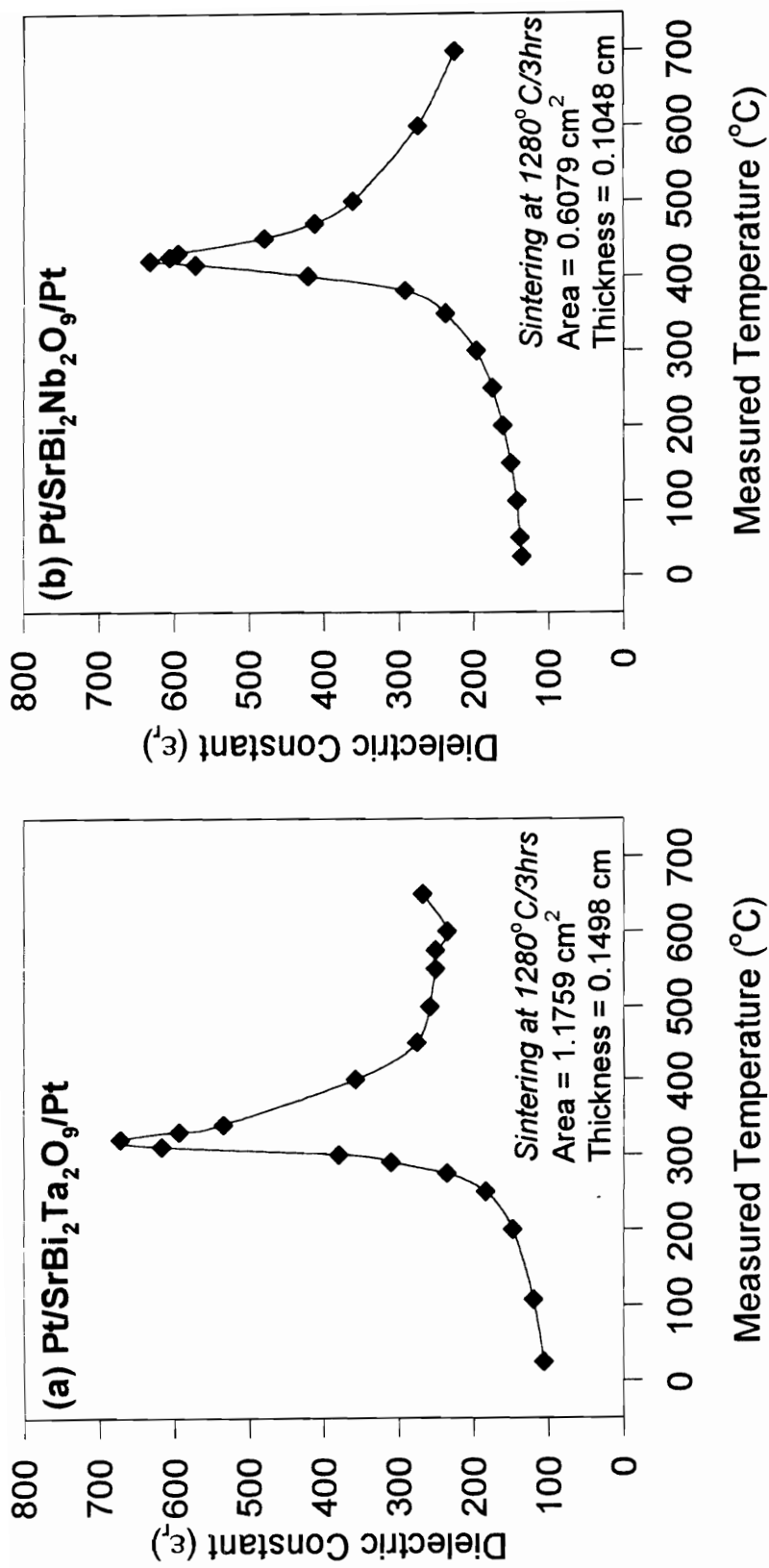
Figure 6-8. Temperature dependence dielectric constants of (a) $SrBi_2Ta_2O_9$, and (b) $SrBi2Nb2O9$, measured at 100 kHz frequency.

125

mobilities in these materials is not clear at this point. Further studies are needed for understanding ferroelectric conduction mechanism.

According to the previous researches [103,110,111], the values of bulk ionic conductivities of perovskite ferroelectric materials (e.g. PZT and BaTiO$_3$, etc.) are approximately 10^{-11} - 10^{-10} S/cm at 100°C and the activation energies are about 1 eV in high temperature region. In comparison, the bulk ionic conductivities of SBT and SBN are much larger (about 10^{-7} S/cm as shown in Figure 6-7)) than those for the perovskite ferroelectric materials at the same temperature. This suggests that high ionic conductivities of these materials in ferroelectric state may be the result of either high defect concentration or high charge mobility in the materials.

According to the fatigue model, the high ionic conductivities and less fatigue lead us to conclude that the reason for fatigue resistance of these materials is possibly due to the easy recovery of these oxygen vacancies from the entrapments. As a result, the oxygen vacancies which reach the interface can easily move back to the bulk ferroelectric when switching the applied field. Consequently, no space charge built up at the interfaces and no fatigue phenomenon is observed.

In the same time, the high temperature complex impedance planes of SBT and SBN also showed that no specific absorption occurred at electrode-ferroelectric interfaces. For SBT, the charge-transfer resistance, R_{in}, at electrode-ferroelectric interface is due to electron-transfer at the interface. This electron-transfer is associated with oxygen dissociation at the electrode-ferroelectric interface caused by highly porosity of Pt-electrodes [105], since the electrodes of SBT sample were simply made by Pt paste. On the other hand, for SBN sample, dense electrodes were made by sputtering method then Pt paste was applied for external connection. Therefore, only simple electrode blocking effect

was observed for SBN. In conclusion, for both SBT and SBN, no specific charge absorption was observed at the electrode-ferroelectric interfaces.

6.7 Conclusion

For the first time, the fatigue model of bismuth layered oxide, SBT and SBN, is proposed. In this model, the reasons for fatigue resistance in SBT and SBN were discussed via the bulk ionic conductivity of the compounds. Complex impedance studies provides an effective method which allows to separate the dielectric behaviors of bulk, grain boundaries and electrode-ferroelectric interfaces from the total cell impedance. In comparison to PZT case, SBT and SBN having perovskite-like layer-type structure showed much higher bulk ionic conductivities. The high ionic conductivities and less fatigue were both observed in these materials, which implies either high defects concentration or mobilities in the materials. Therefore, the model of, which presume low conductivity, low defects concentration is excluded. Consequently, the possible reason to explain high resistance in fatigue for bismuth layered oxides is the easy recovery of these defects from the entrapments at electrode-ferroelectric interfaces. Because of this easy recovery from the entrapments, no space charges can be generated during the polarization reversal process. Additionally, the changes of conduction mechanism around Curie temperatures suggest that ferroelectric polarization may be the key factor that dominates the mobilities in these materials.

In conclusion, although the fatigue model proposed in this research is an empirical result and further studies are needed to ensure the model, the ionic transport phenomenon in bismuth layered oxides, which was studied by impedance spectroscopy study, is shown to be the key factor contributing to the fatigue minimization.

Chapter 7.   Summary

The results of this research are summarized as below:

7.1 Thin Film Characterization

7.1.1 Low Temperature Process Approach

In Chapter 3, we present for the first time the structure development study of SBTN thin films as revealed by spectroscopic ellipsometry. The technique was shown to be a non-destructive, convenience and an effective method to obtain the characteristic temperatures of phase transformation for the films deposited on an opaque substrate, i.e., Pt coated Si-substrate. By this optical method, the temperatures of phase transformation and grain growth were determined by observing the changes in refractive index and films thickness as functions of annealing temperature. The consistent results were obtained from X-ray diffraction measurement. By comparing the results of the structure development study and ferroelectric hysteresis properties investigation, the onset temperature of well-defined hysteresis curves for SBTN films were determined. The critical factor for obtaining well-defined hysteresis properties was found to be the grain size. Even though the nucleation was observed at the temperatures as low as 550°C for SBT films with 50% excess Bi, no ferroelectric properties were detected untill the grain size is grown larger than a critical value, i.e., 0.1 μm in width and 0.27 in length. It was also found that, the additional amount of Bi in SBTN films enhanced the grain growth process and improved the ferroelectric properties dramateically. Without excess Bi, the grain size of SBT films is

far beyoung the critical value and no ferroelectric hysteresis properties were detected below 800°C. However, when the 50% excess Bi was added into SBT film, the grain size was enhanced a lot and the $T_O{}^H$ was observed at about 700°C. Moreover, the onset temperatures for obtaining well-defined hysteresis properties can also be reduced by substituting the Ta ions with Nb ions. By choosing SBN with 50% excess Bi, the $T_O{}^H$ was reduced to about 650°C.

7.1.2 Optimized Process Parameters for SBT Thin Film by MOD Method

1.   For SBT thin films made by MOD method, the compounds with additional amount of bismuth were required to have good ferroelectric properties. The results suggest that the optimized composition for SBT films to have good ferroelectric hysteresis properties is with 30 - 50% excess bismuth in the films with respect to grain size, crystallographic orientation and single phase formation. Within this composition range, the limited solid solution of SBT and Bi_2O_3 was formed. The formation of solid solution enhanced the grain size and the degree of *a-b* plane orientation of SBT films, resulting in improved hysteresis properties of low leakage current density ($\sim 10^{-9}$ A/cm²) and high ramanent polarization ($2P_r \sim 12$ μC/cm²). For the compound with excess bismuth amount more than 50%, highly conductive Bi_2O_3 was observed as a second phase and led to high leakage current and poor ferroelectric properties.

2.   A post-top-electrode-deposition annealing was found to be necessary to obtain the symmetric ferroelectric hysteresis loop as well as improve the ferroelectric properties. The asymmetric hysteresis loop obtained after first annealing could be due to the asymmetry of top and bottom electrode-ferroelectric interfaces. Post-electrode deposition annealing

might change the electrode-ferroelectric interfaces so that improved the ferroelectric hysteresis properties.

7.2 Characterization of SBTN Bulk Ceramics

7.2.1 Optical Properties

The optical dispersion functions of SBTN bulk ceramics shown in Chapter 5 were obtained for the first time. The refractive indices of SBTN were found to vary with Ta/Nb ratio. The variation of refractive indices with composition could be due to the geometric arrangement of atoms. The approximate energy band gaps of the compounds were estimate by $\hbar\omega_0$ using the Lorentz Oscillator model with a surface layer correction. The estimated Eg's for SBTN solid solutions were about 5 eV.

7.2.2 Fatigue Behavior in SBT and SBN

In Chapter 6, the fatigue model of SBT and SBN was proposed for the fist time. The reasons for fatigue resistance of SBT and SBN were discussed via the bulk ionic conductivity of the compounds. To obtain the bulk ionic conductivity, impedance spectroscopy study was employed which provides an effective method allowing to separate the individual contributions of bulk, grain boundaries and electrode-ferroelectric interfaces from the total cell impedance. The impedance spectroscopy study suggested that the conduction mechanism of SBT and SBN was mainly contributed by ion migration. It was found that the bulk ionic conductivities of SBT and SBN ($\sim 10^{-7}$ S/cm) were much higher than for perovskite ferroelectrics, i.e, PZT ($\sim 10^{-11}$ - 10^{-10} S/cm). According to the

130

proposed fatigue model in Chapter 6, the high ionic conductivities and less fatigue led us to the conclude that the reason for fatigue resistance in SBT and SBN was possibly due to easy recovery of defects, i.e., oxygen vacancies, from the entrapments at electrode-ferroelectric interface, because of which, no space charges can be generated during the polarization reversal process. Additionally, the changes of conduction mechanism of SBT/SBN around Curie temperatures suggest that ferroelectric polarization may be the key factor that dominates the charge mobilities in these materials.

Chapter 8. Future Works

The structure and properties interrelationship of SBTN was studied in detail in this research. However, the results of this research are still far from final. The fully characterization of SBTN compounds is not complete yet. In order to achieve the final goal of non-volatile memory device application, further studies on the fundamental understanding of the materials need to be done. The following are the suggestions for future research.

8.1 Thin Film Characterization

It is a challenge to reduce the processing temperature of SBTN thin films fabrication. In other words, not only crystalline layered structure has to be formed at low temperature, but the well-defined ferroelectric hysteresis properties also have to be developed at low temperature. In Chapter 2, we learned the grain size effect on ferroelectric properties. To reduce the onset temperature of well-defined ferroelectric hysteresis properties, we should be able to grow larger grains at lower temperature. It has been shown that larger grain can be obtained at temperature as low as 650°C by choosing SBN compound with 50% excess Bi. At this temperature, a saturated hysteresis curve was developed. However, the values of $2P_r$ are low and E_c are high at such low temperature. This might be due to that the process parameters for SBN were not optimized yet. The results of this research suggest that the SBTN solid solutions have highly potential to develop low temperature processing for the application. Although the properties of SBTN solid solution system were studied in this research, the fully characterization is not

complete. In order to investigate the optimum process parameters, further characterization need to be completed for SBTN solid solution system.

In addition to the optimized process parameters, the results of this research also suggest that combining effect of grain size and crystallographic orientation can improve the ferroelectric hysteresis properties at low temperatures. It has been shown in Chapter 2 and 3 that the grain size and crystallographic orientation are two important factors that affect the ferroelectric hysteresis properties of SBTN films. However, it cannot tell which one is dominant for exhibiting good ferroelectric properties because the effects of grain size and lattice orientation could not be separated in the present work. For the case of SBT with 50% excess Bi, a-b plane preferred orientation and larger grain were observed simultaneously within temperature range of 650 - 700°C. Therefore, we hypothesize that, for the same preferred orientation ratio, larger grain size will give higher P_r values. To show this, the effects of grain size and lattice orientation have to be separated. To approach this, one may fabricate several films with different deposition techniques and different parameters so that it will provide the films with various grain size and lattice orientation. By comparing the ferroelectric properties (i.e., P_r values) with the grain size and orientation, one may be able to separate the contributions from these two factors.

8.2 Bulk Ceramics Characterization

The fatigue model for bismuth layered oxides proposed in this research is the preliminary results from impedance spectroscopy study. The model was built on several assumptions, e.g., oxygen vacancy conducting species and defect entrapment at electrode-ferroelectric interface. According to the model, the behavior of less fatigue for SBT and SBN is possibly due to easy recovery of the defects from the entrapment. One of the

133

possibilities leading to this result is the small energy barrier height at the interface. Therefore, to ensure the proposed fatigue model, the further studies shown below are suggested:

1. Oxygen vacancy conducting mechanism
2. determination of energy barrier height at electrode-ferroelectric interface.

According to the present study, high ionic conductivity indicates high oxygen vacancy concentration. If this is the case, one may detect oxygen vacancy conduction behavior as a function of oxygen partial pressure.

Moreover, the results of impedance spectroscopy studies of SBT/SBN also suggest that the change in conduction mechanism around Curie temperature could be related to the change in charge mobilities due to ferroelectric to paraelectric transformation. However, how the polarization state affects the mobilities in these materials is not clear at this point. Therefore, further studies are also needed for understanding ferroelectric conduction mechanism.

Appendix A

This appendix collects figures not presented in Chapter 5 for the optical dispersion function (i.e., n and k) of SBTN bulk ceramics. They are:

Figure A-1. Wavelength dependence refractive indices of $SrBi_2Ta_2O_9$ bulk and surface layer (EMA) obtained by Cauchy dispersion model.
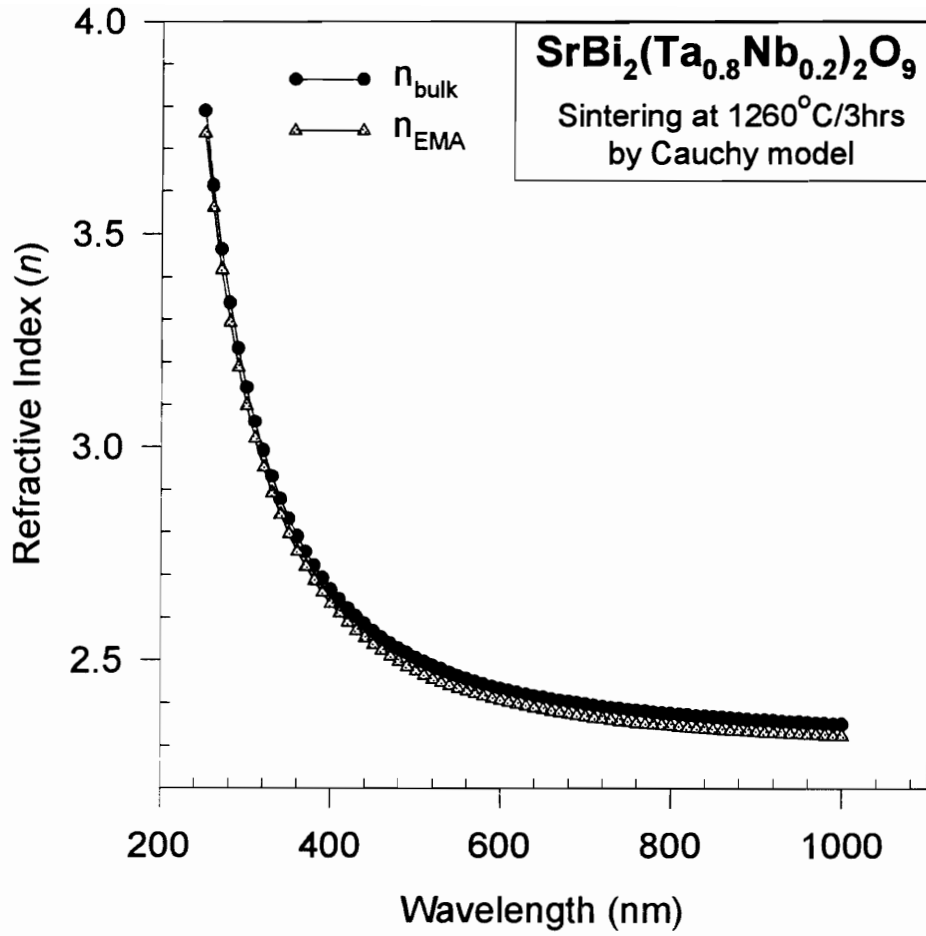
Figure A-2. Wavelength dependence refractive indices of $SrBi_2(Ta_{0.8}Nb_{0.2})_2O_9$ bulk and surface layer (EMA) obtained by Cauchy dispersion model.
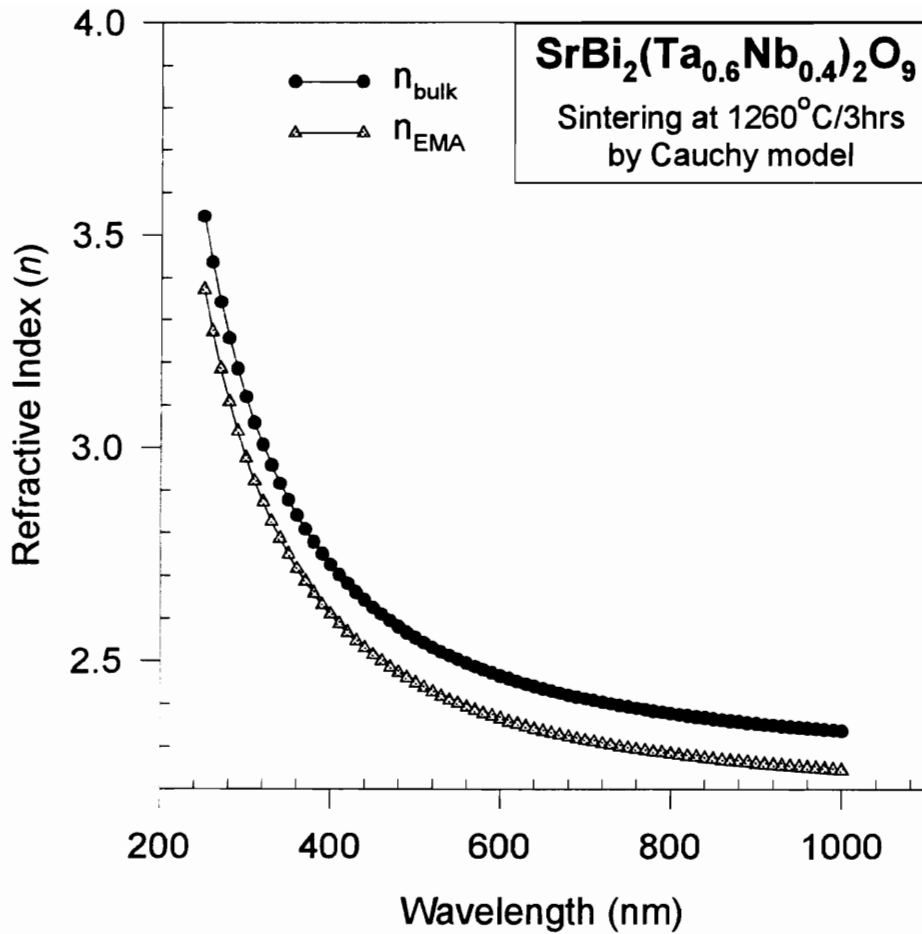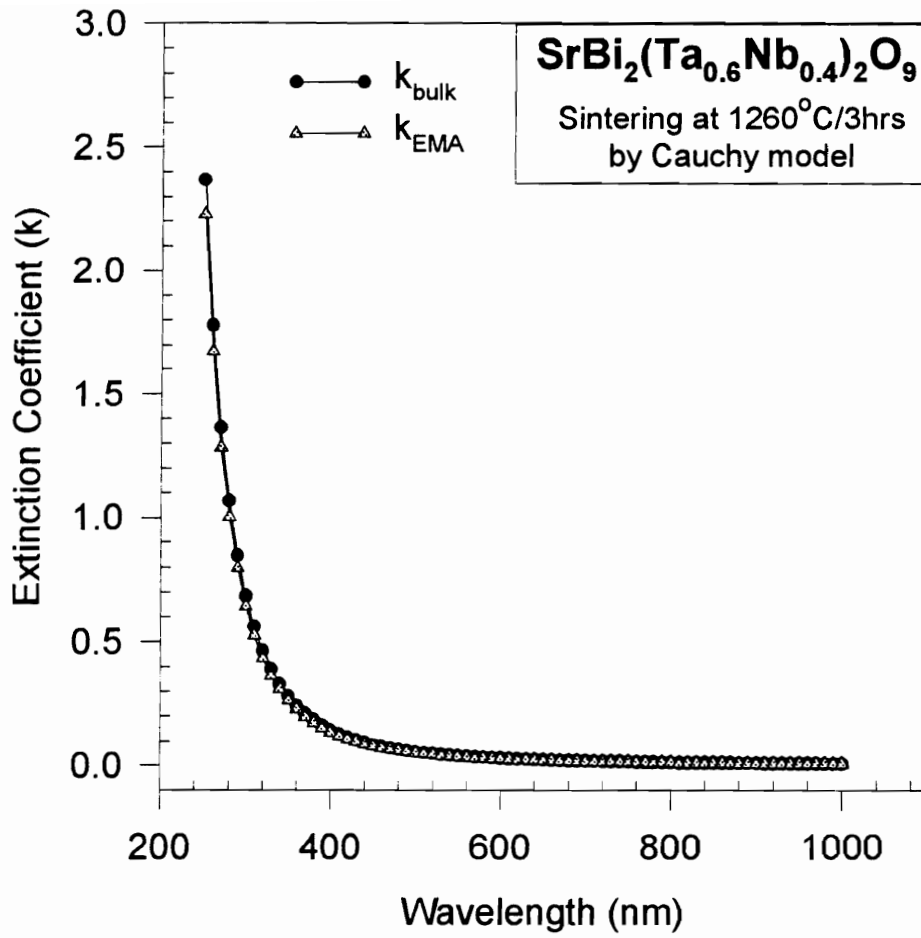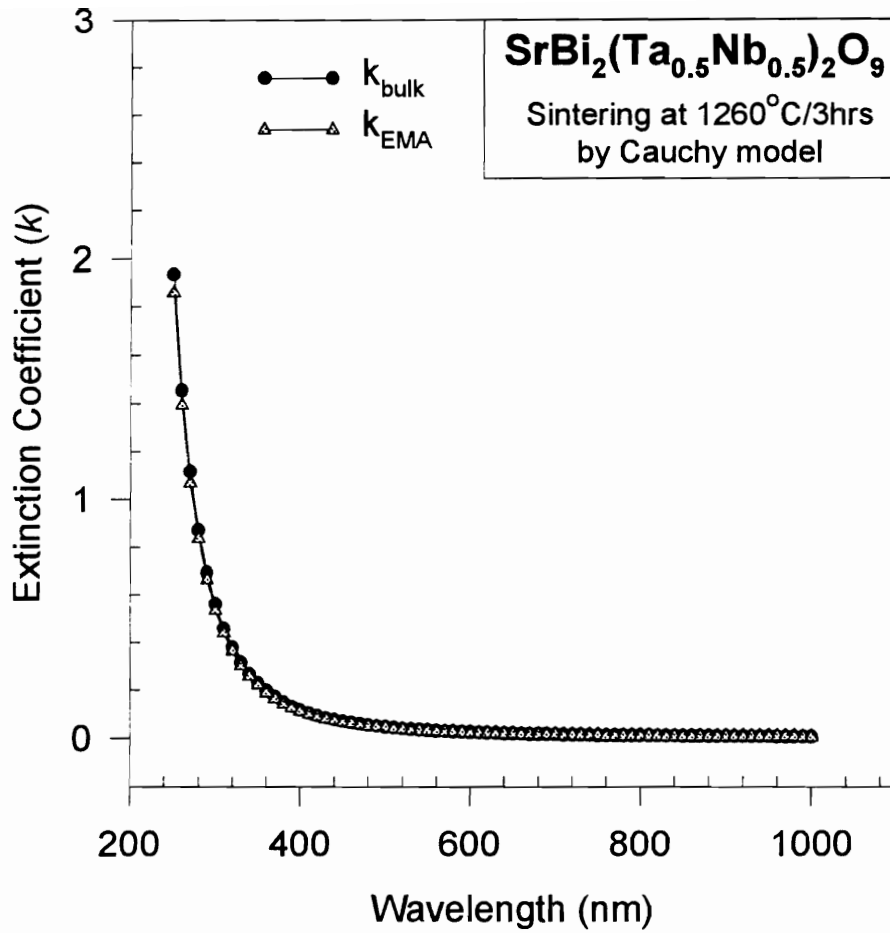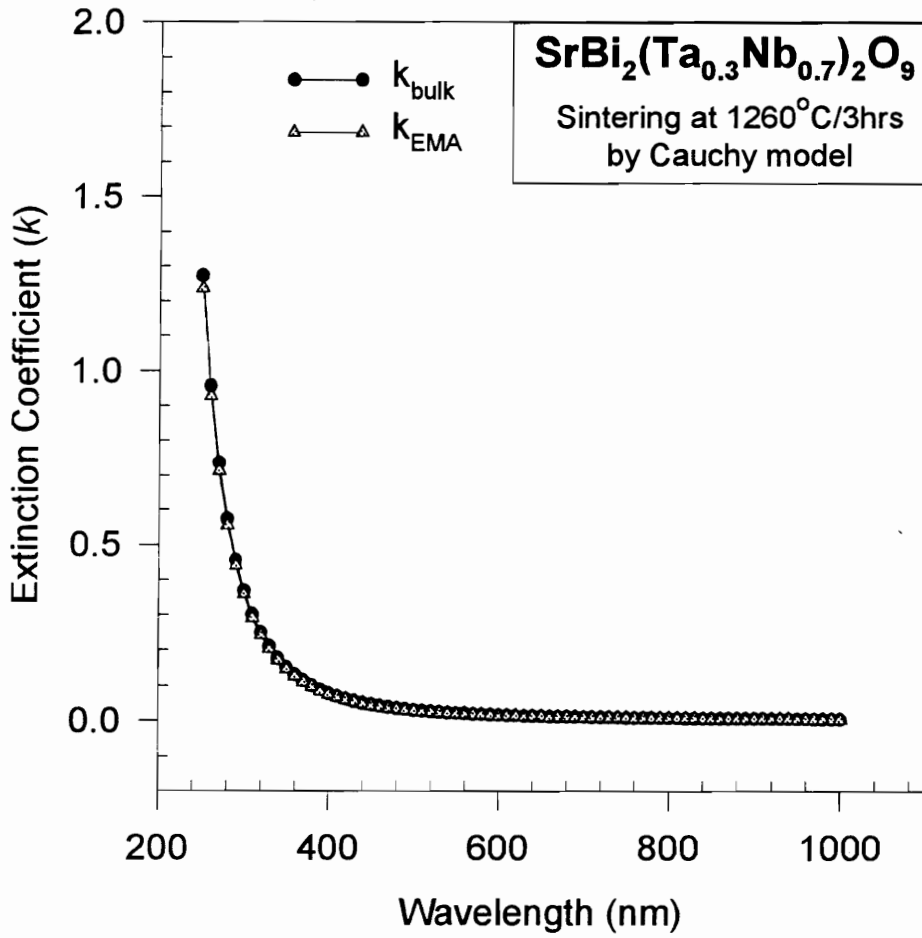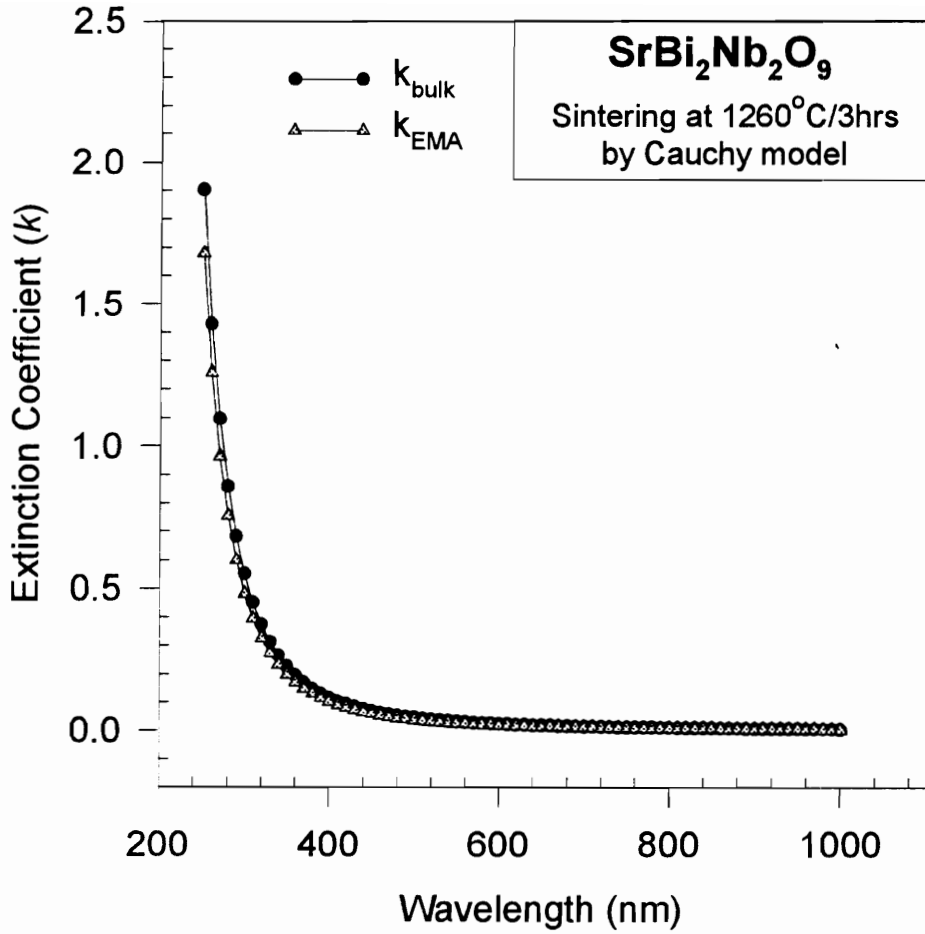
Figure A-3. Wavelength dependence refractive indices of $SrBi_2(Ta_{0.6}Nb_{0.4})_2O_9$ bulk and surface layer (EMA) obtained by Cauchy dispersion model.
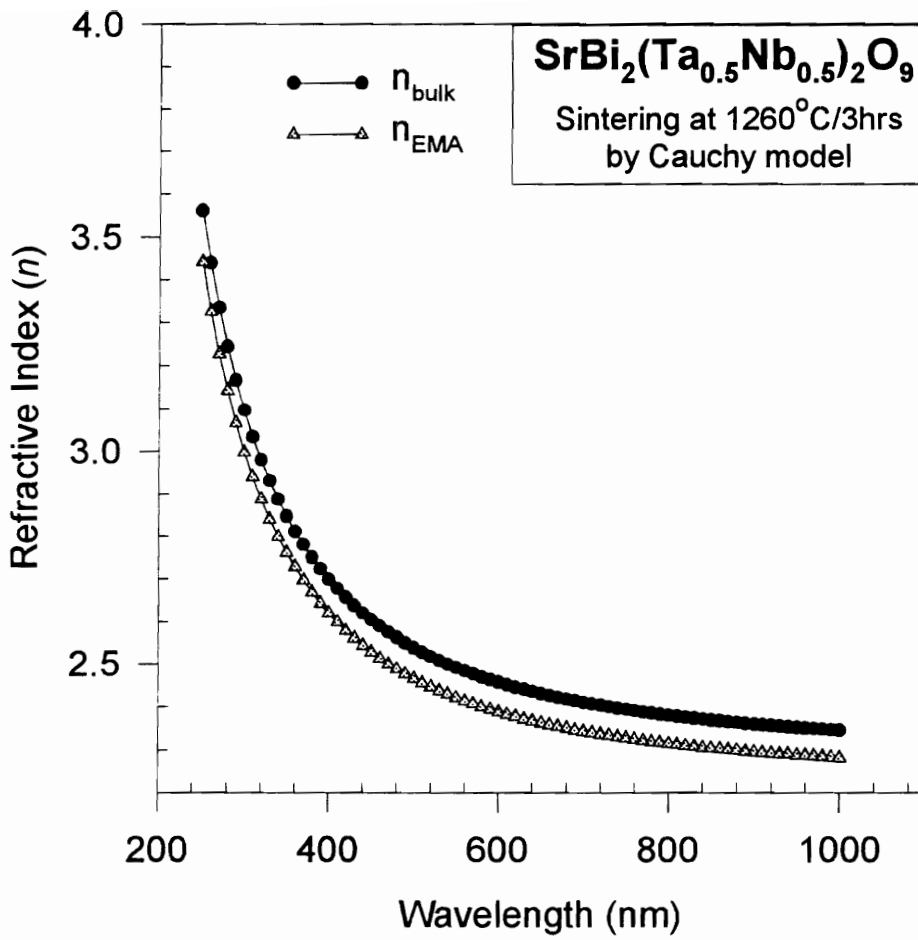
Figure A-4. Wavelength dependence refractive indices of $SrBi_2(Ta_{0.5}Nb_{0.5})_2O_9$ bulk and surface layer (EMA) obtained by Cauchy dispersion model.
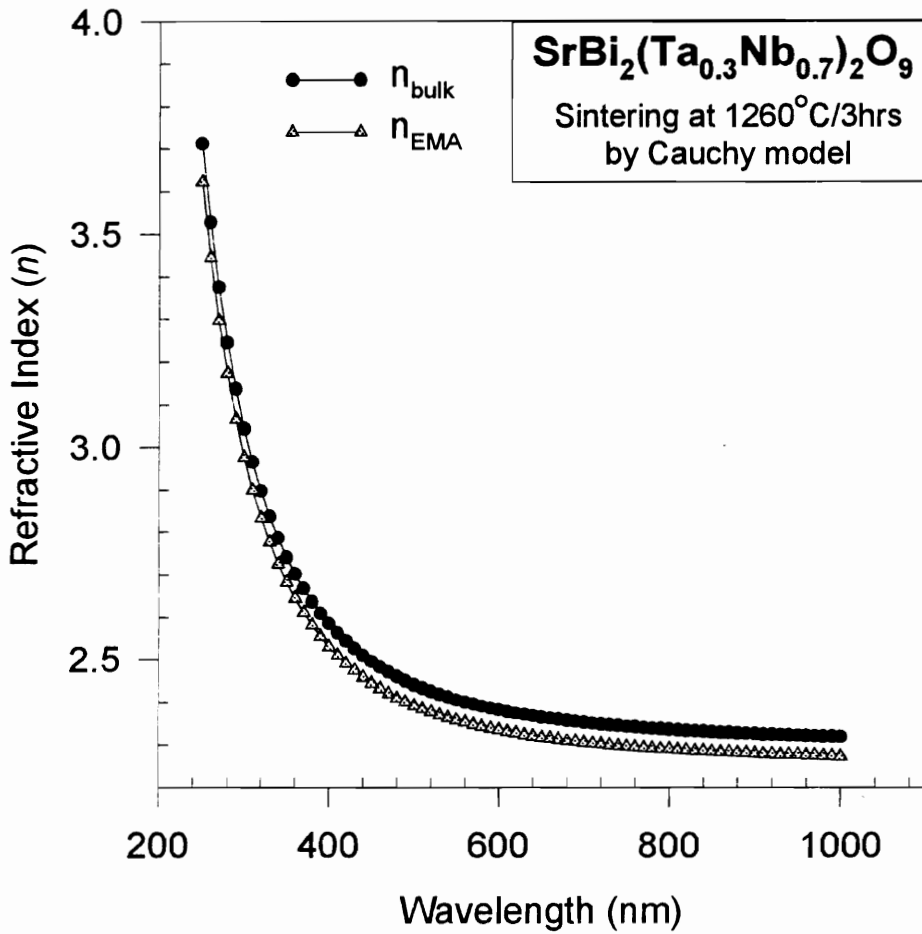
Figure A-5. Wavelength dependence refractive indices of $SrBi_2(Ta_{0.3}Nb_{0.7})_2O_9$ bulk and surface layer (EMA) obtained by Cauchy dispersion model.
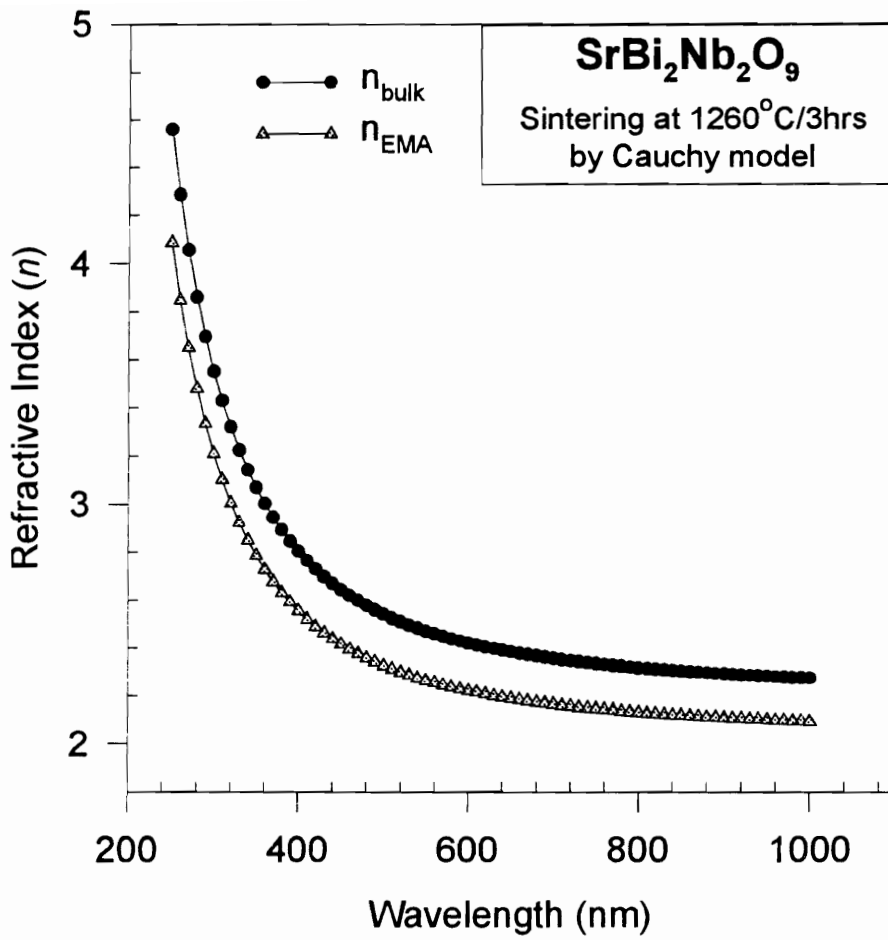
Figure A-6. Wavelength dependence refractive indices of $SrBi_2Nb_2O_9$ bulk
and surface layer (EMA) obtained by Cauchy dispersion model.
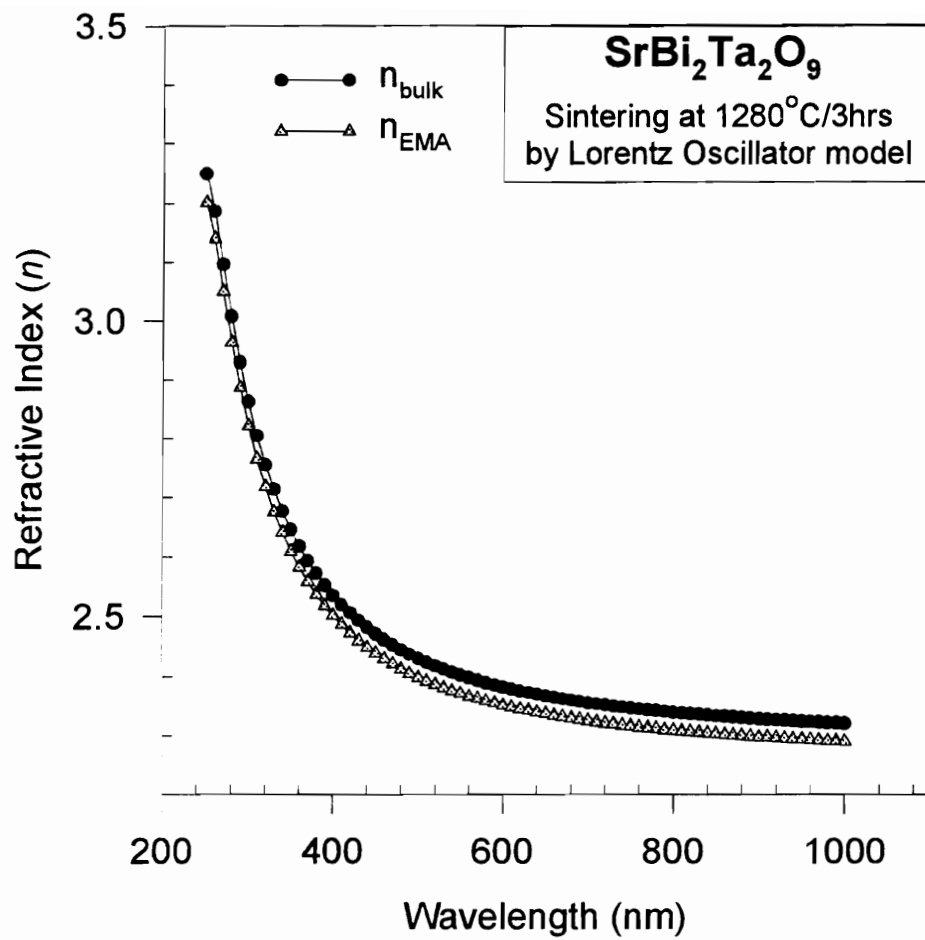
Figure A-7. Wavelength dependence refractive indices of $SrBi_2Ta_2O_9$ bulk and surface layer (EMA) obtained by Lorentz Oscillator model.
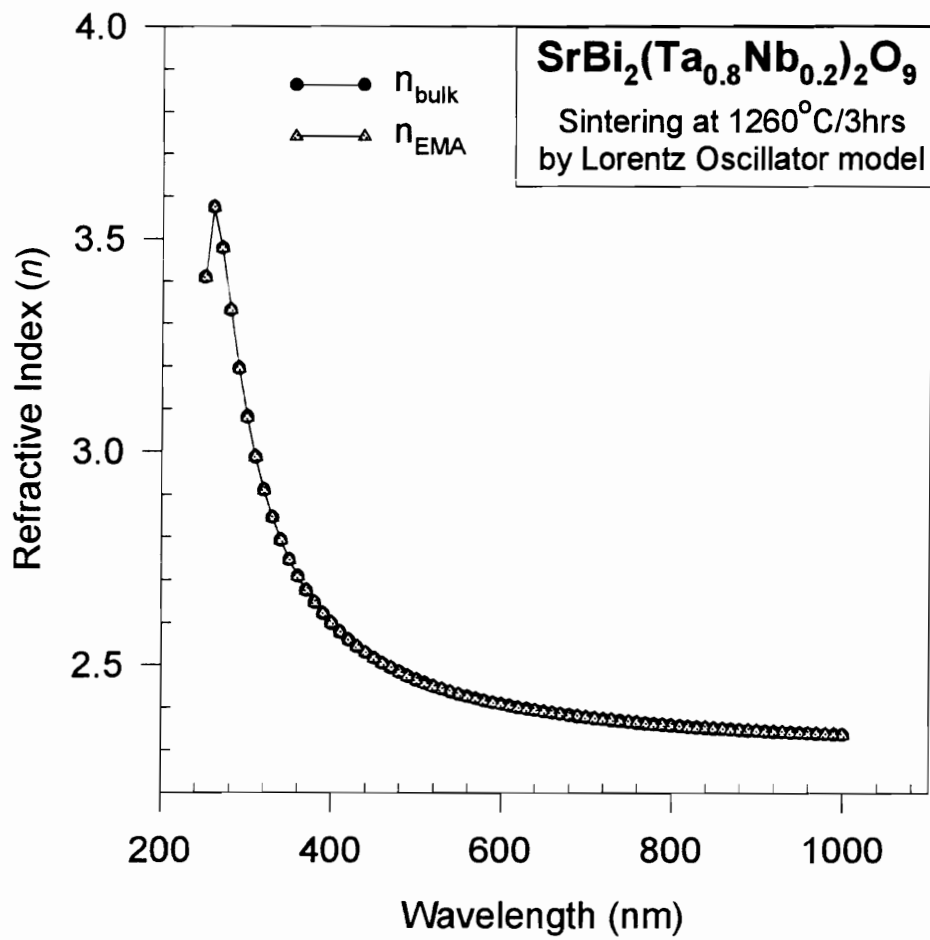
Figure A-8. Wavelength dependence refractive indices of $SrBi_2(Ta_{0.8}Nb_{0.2})_2O_9$ bulk and surface layer (EMA) obtained by Lorentz Oscillator model.
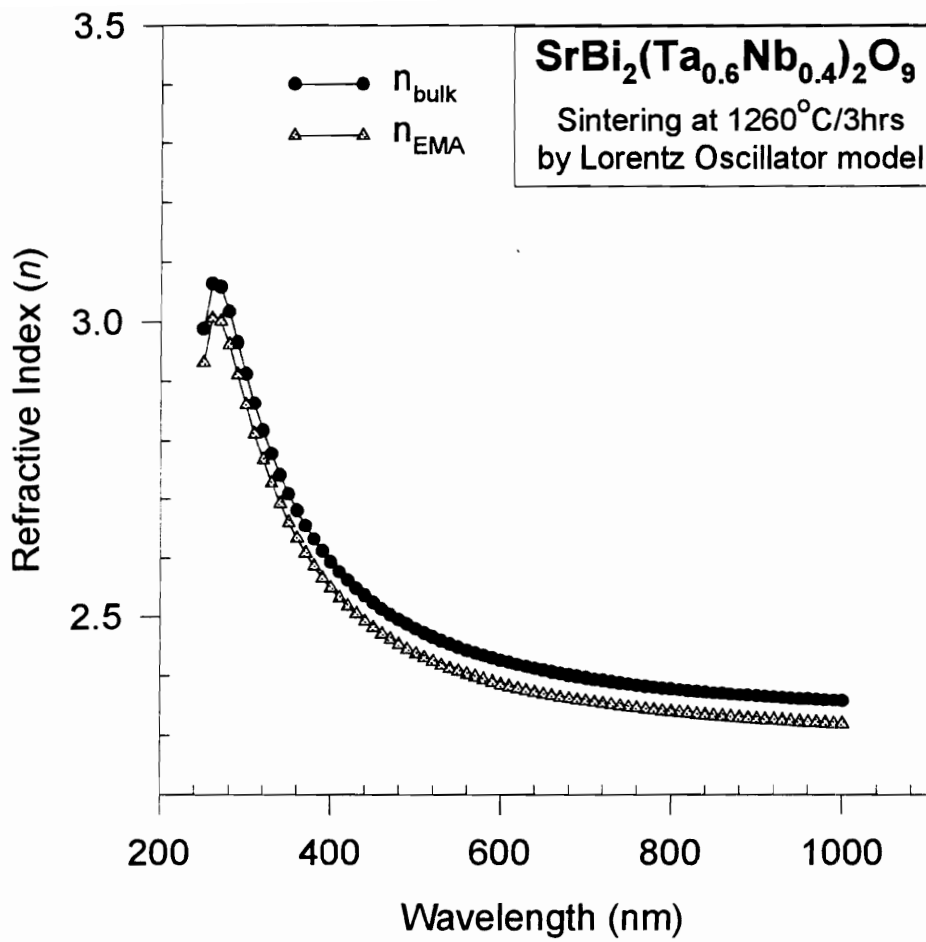
Figure A-9. Wavelength dependence refractive indices of $SrBi_2(Ta_{0.6}Nb_{0.4})_2O_9$ bulk and surface layer (EMA) obtained by Lorentz Oscillator model.
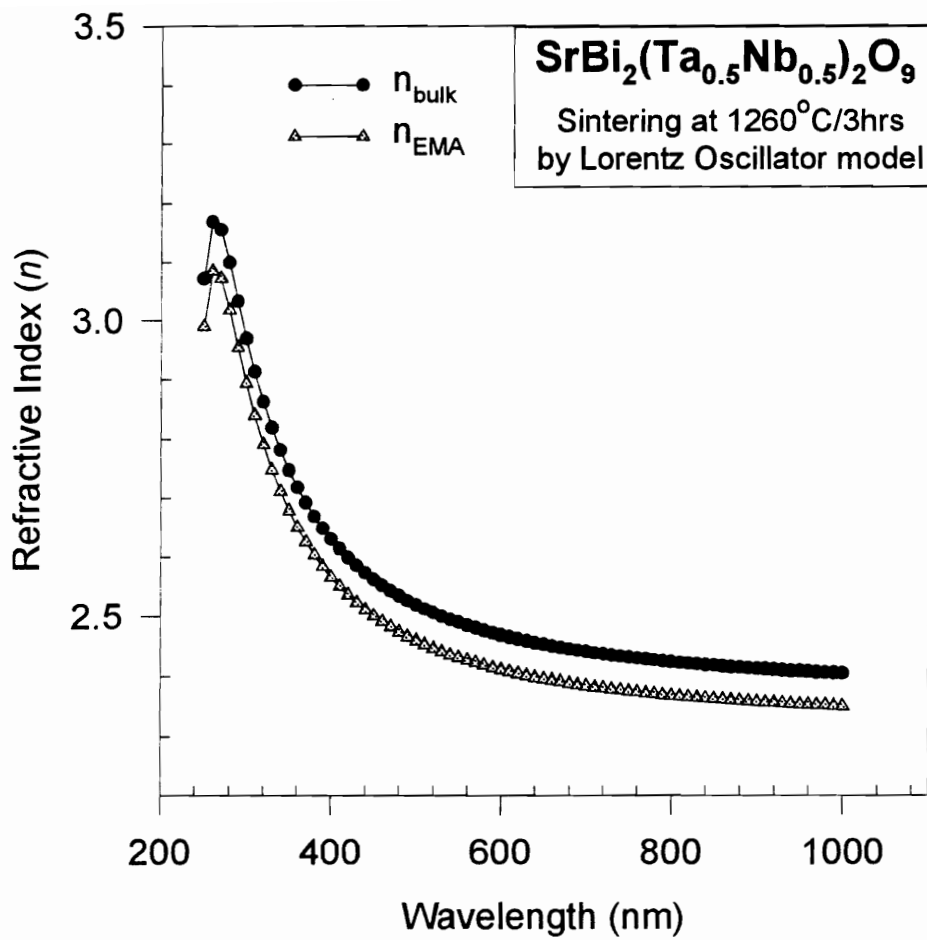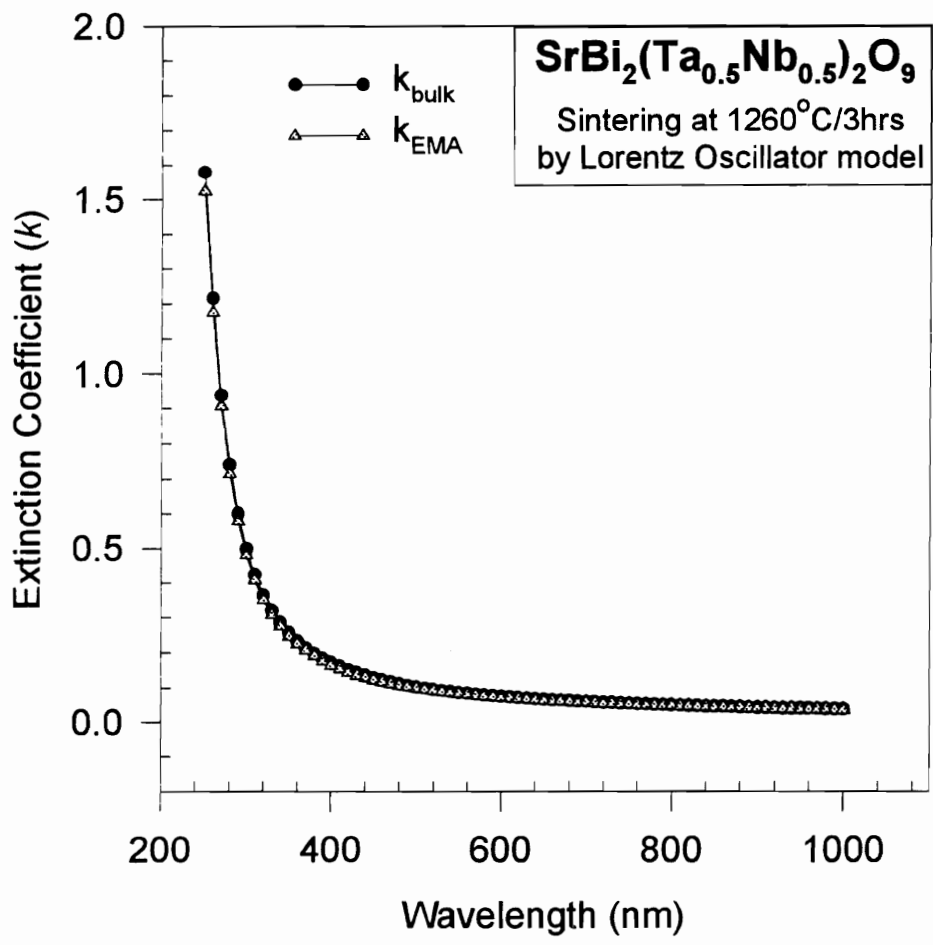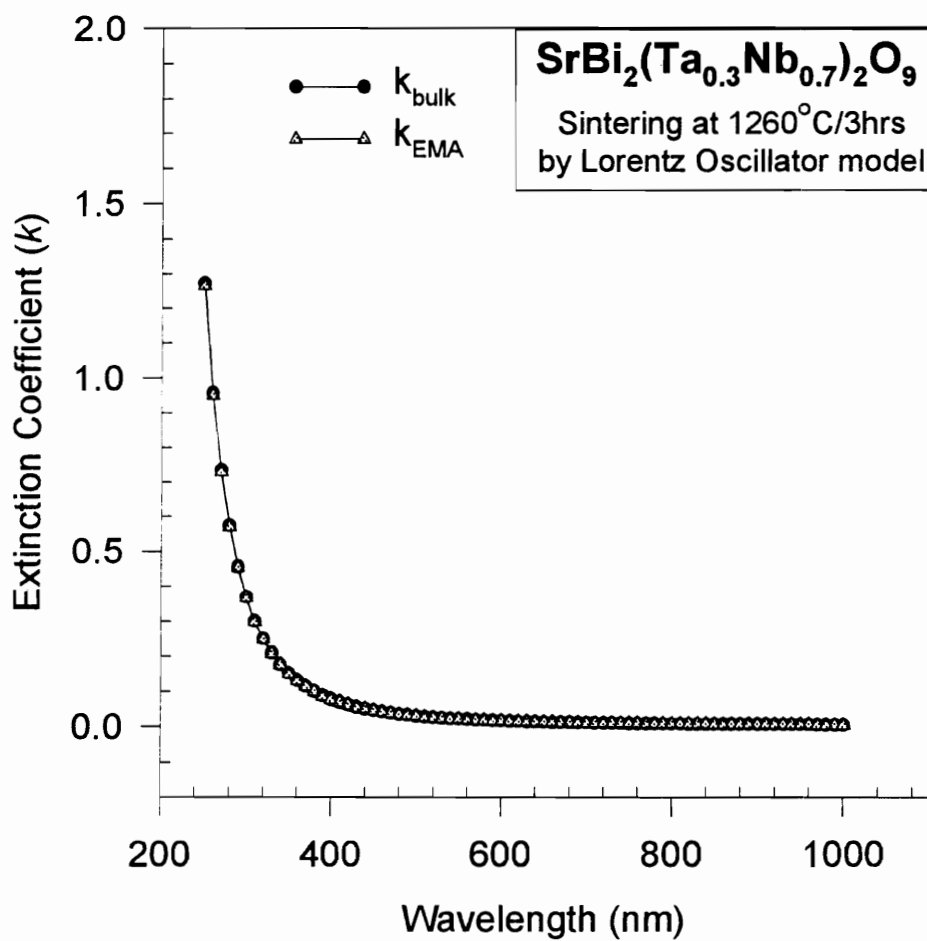
Figure A-10. Wavelength dependence refractive indices of $SrBi_2(Ta_{0.5}Nb_{0.5})_2O_9$ bulk and surface layer (EMA) obtained by Lorentz Oscillator model.
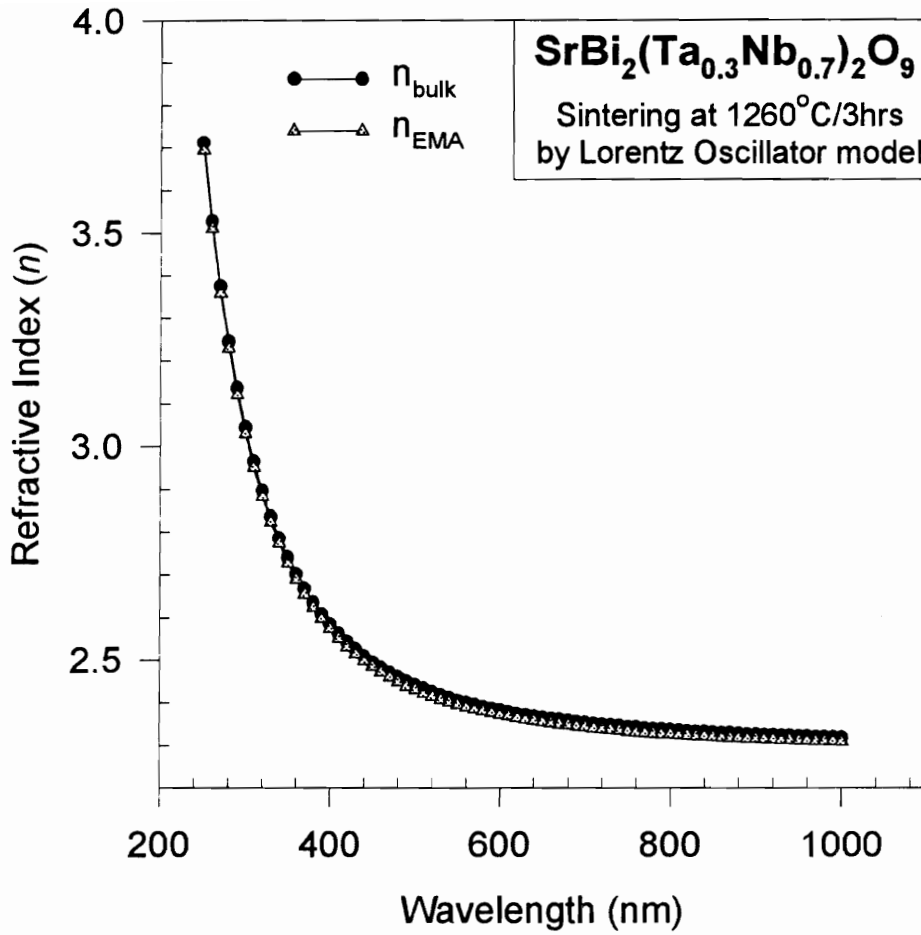
Figure A-11. Wavelength dependence refractive indices of $SrBi_2(Ta_{0.3}Nb_{0.7})_2O_9$ bulk and surface layer (EMA) obtained by Lorentz Oscillator model.
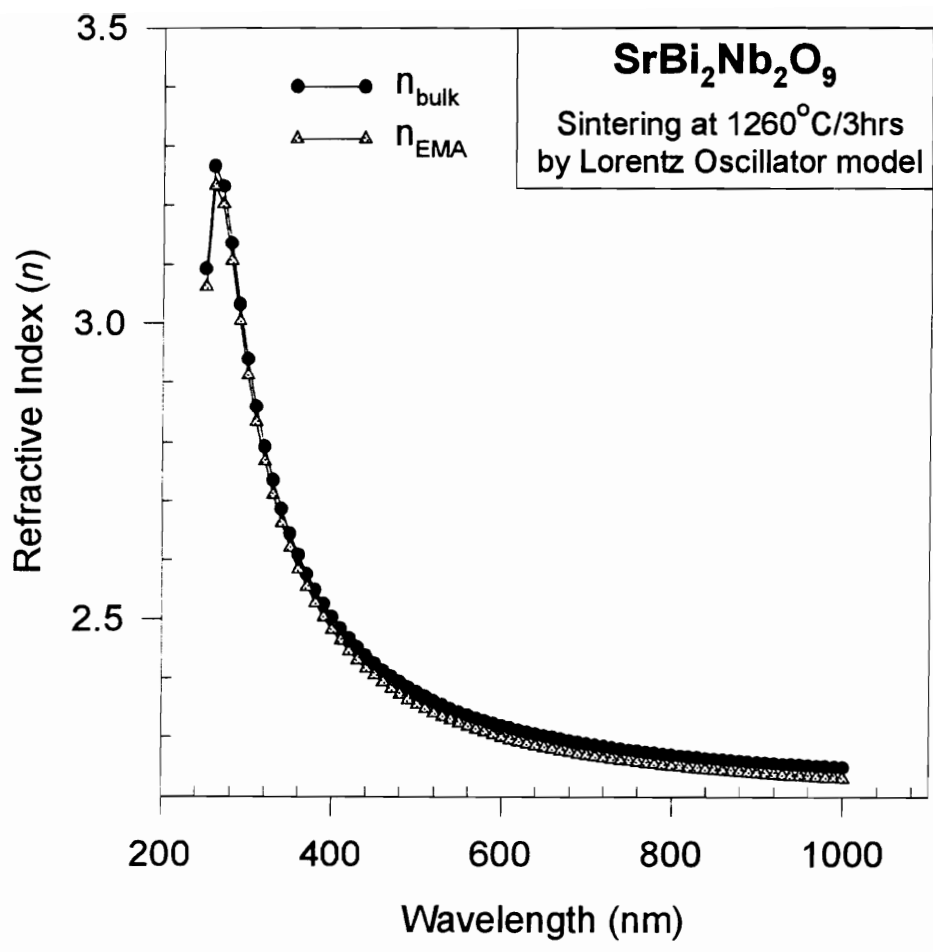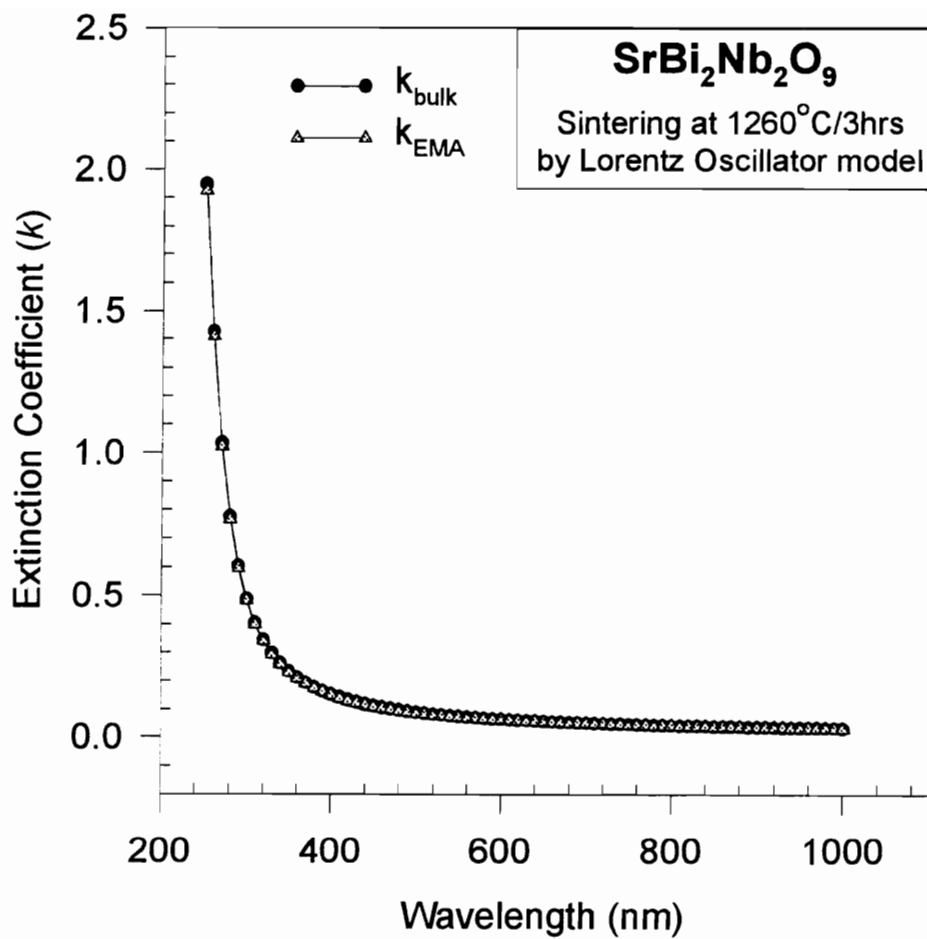
Figure A-12. Wavelength dependence refractive indices of $SrBi_2Nb_2O_9$ bulk and surface layer (EMA) obtained by Lorentz Oscillator model.
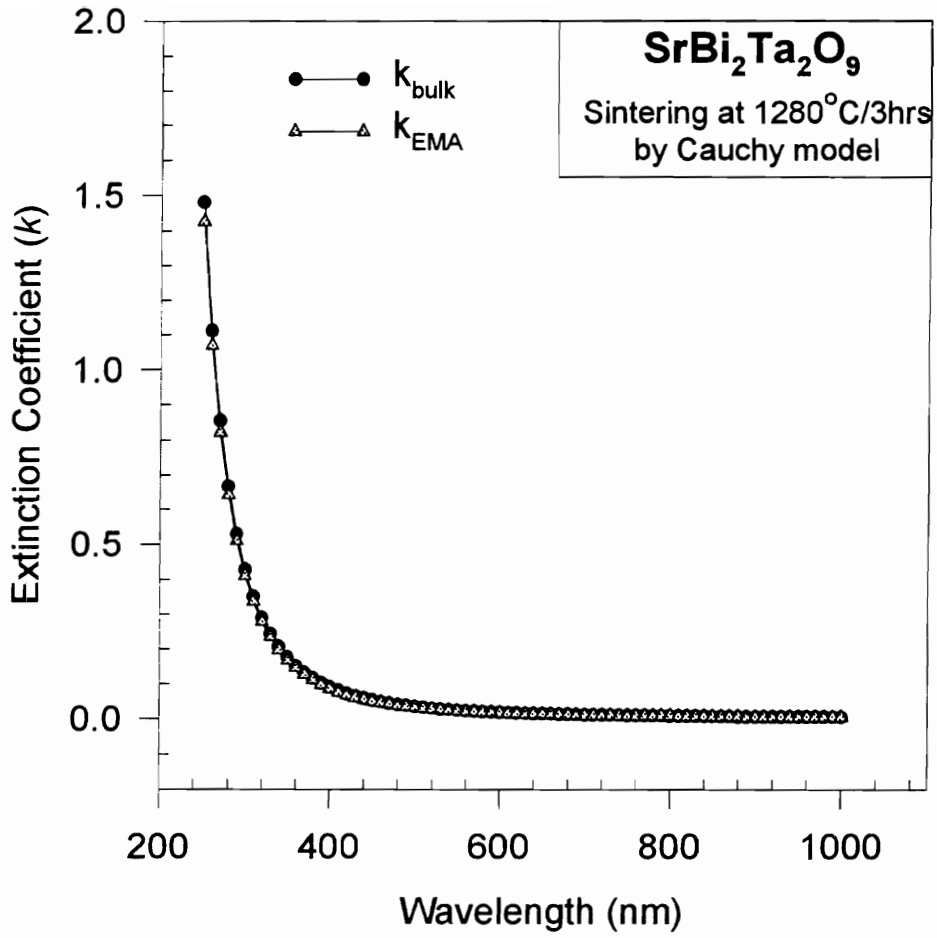
Figure A-13. Wavelength dependence extinction coefficients of $SrBi_2Ta_2O_9$ bulk and surface layer (EMA) obtained by Cauchy dispersion model.
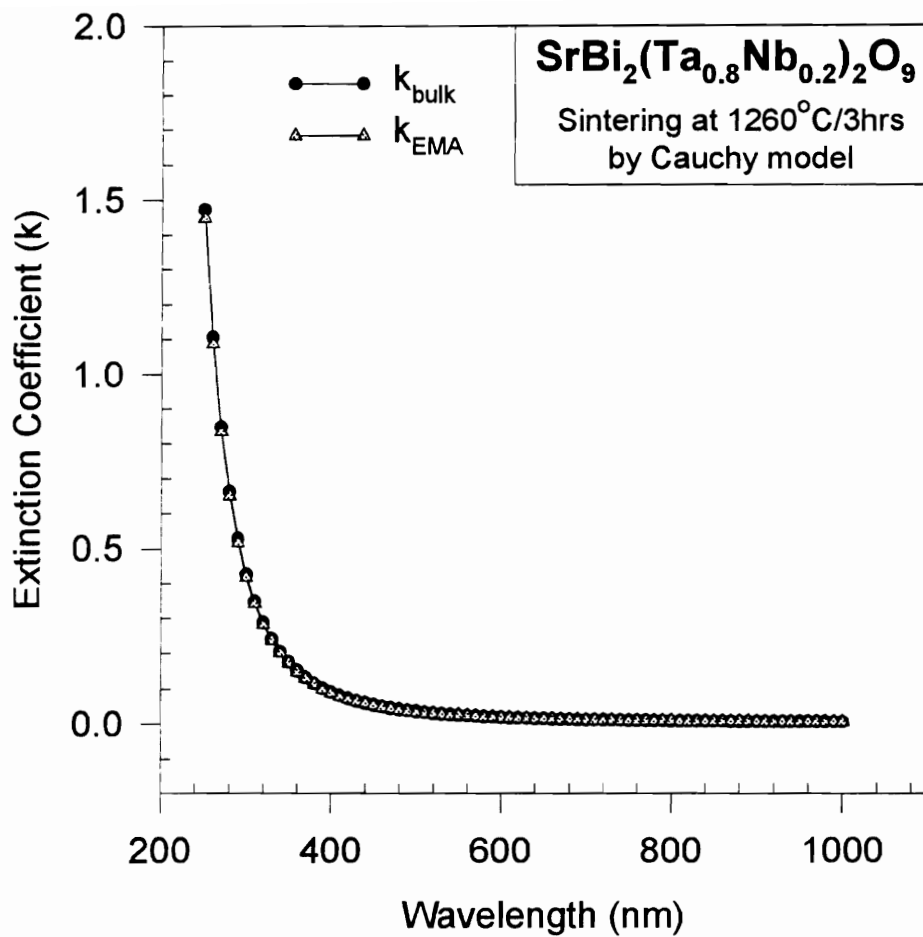
Figure A-14. Wavelength dependence extinction coefficients of $SrBi_2(Ta_{0.8}Nb_{0.2})_2O_9$ bulk and surface layer (EMA) obtained by Cauchy dispersion model.

Figure A-15. Wavelength dependence extinction coefficients of $SrBi_2(Ta_{0.6}Nb_{0.4})_2O_9$ bulk and surface layer (EMA) obtained by Cauchy dispersion model.

Figure A-16. Wavelength dependence extinction coefficients of $SrBi_2(Ta_{0.5}Nb_{0.5})_2O_9$ bulk and surface layer (EMA) obtained by Cauchy dispersion model.

Figure A-17. Wavelength dependence extinction coefficients of $SrBi_2(Ta_{0.3}Nb_{0.7})_2O_9$ bulk and surface layer (EMA) obtained by Cauchy dispersion model.

Figure A-18. Wavelength dependence extinction coefficients of $SrBi_2Nb_2O_9$
bulk and surface layer (EMA) obtained by Cauchy dispersion model.
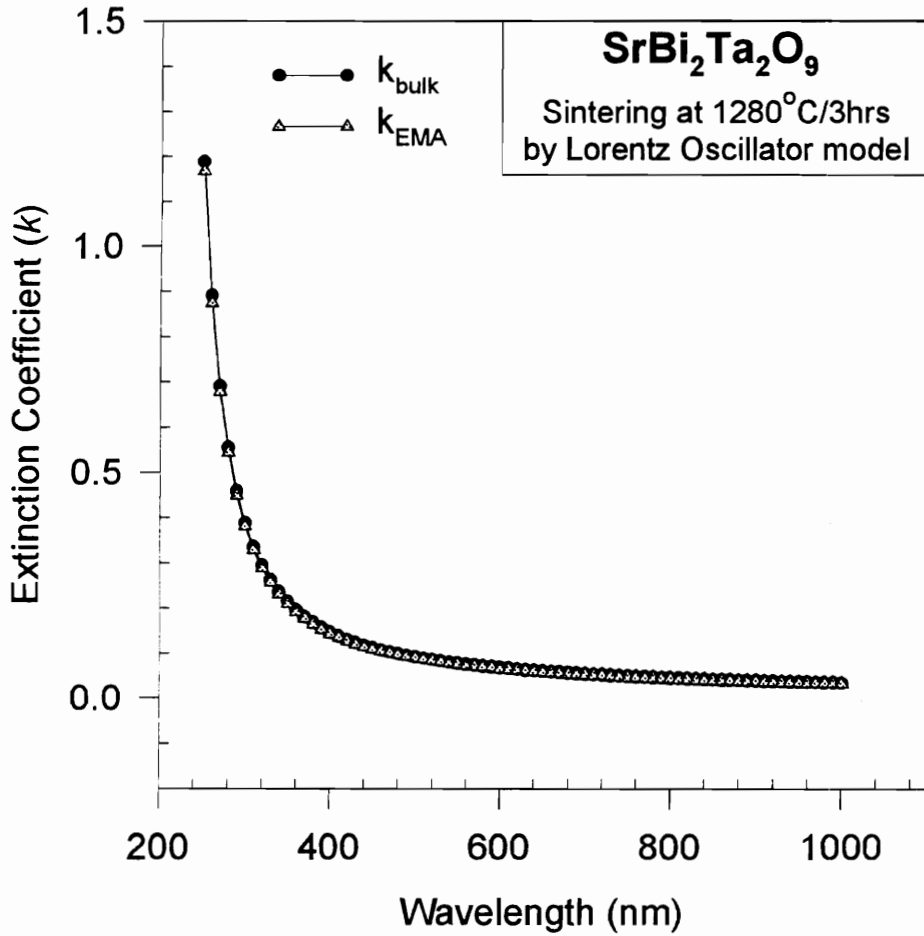
Figure A-19. Wavelength dependence extinction coefficients of $SrBi_2Ta_2O_9$ bulk and surface layer (EMA) obtained by Lorentz Oscillator model.
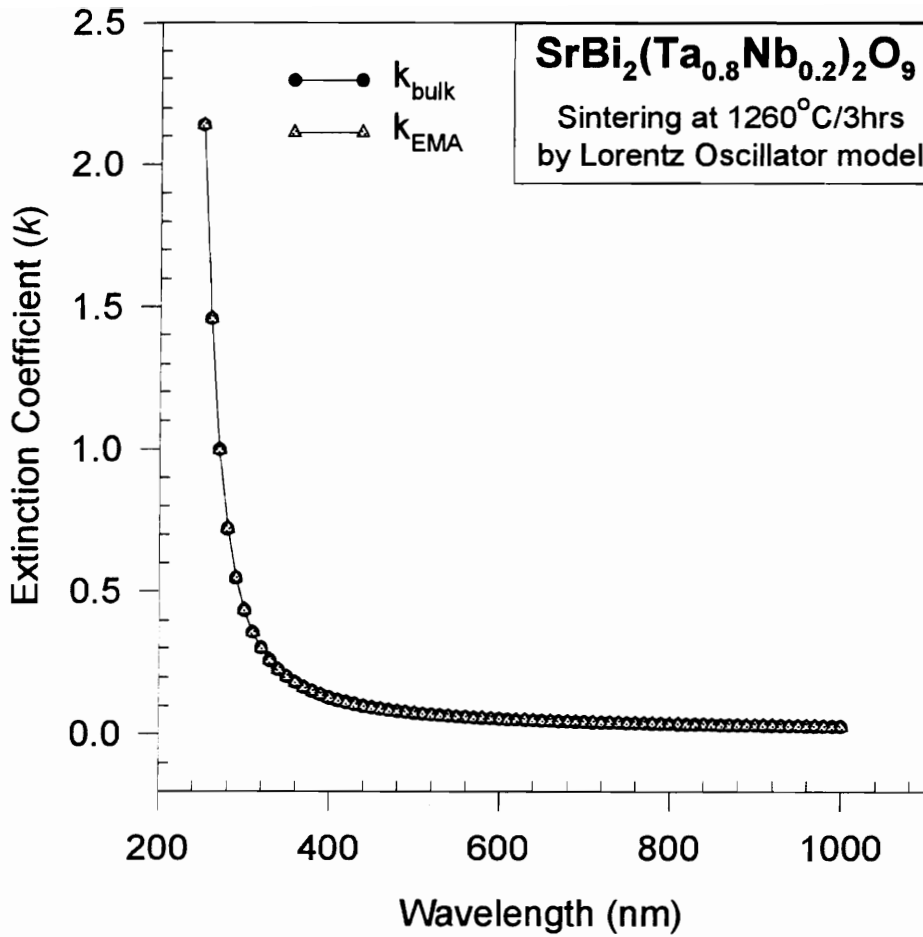
Figure A-20. Wavelength dependence extinction coefficients of $SrBi_2(Ta_{0.8}Nb_{0.2})_2O_9$ bulk and surface layer (EMA) obtained by Lorentz Oscillator model.
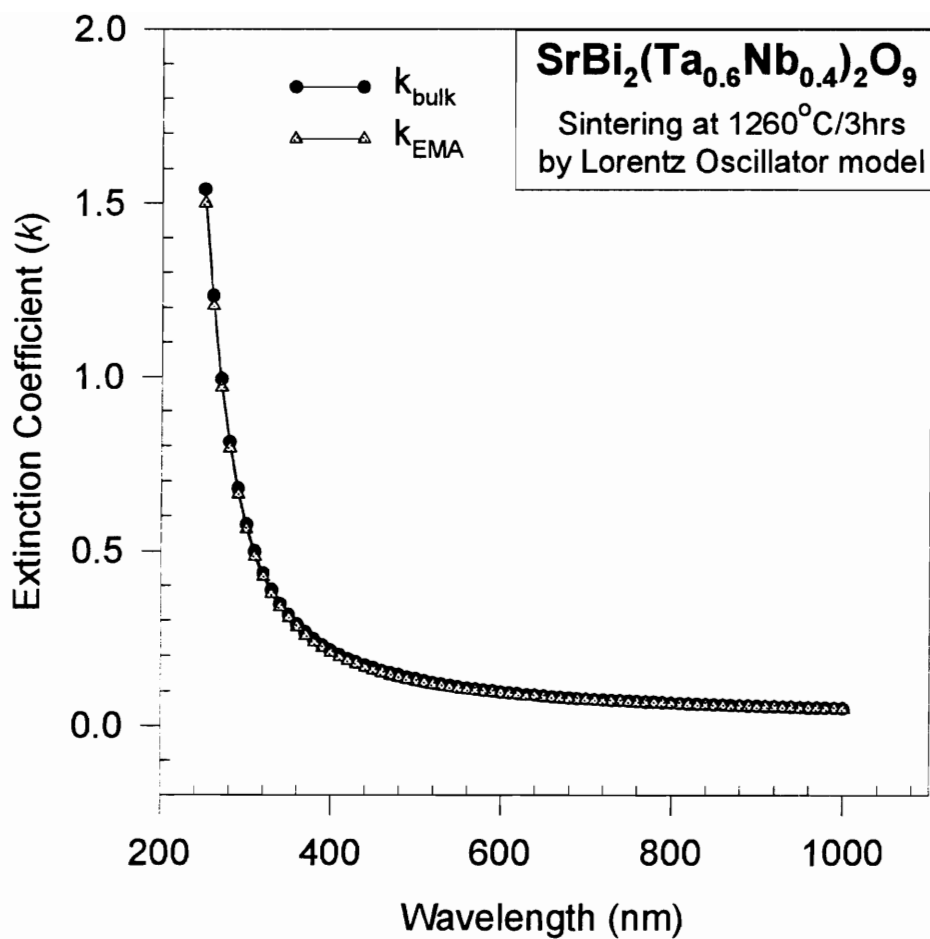
Figure A-21. Wavelength dependence extinction coefficients of $SrBi_2(Ta_{0.6}Nb_{0.4})_2O_9$ bulk and surface layer (EMA) obtained by Lorentz Oscillator model.

Figure A-22. Wavelength dependence extinction coefficients of $SrBi_2(Ta_{0.5}Nb_{0.5})_2O_9$ bulk and surface layer (EMA) obtained by Lorentz Oscillator model.

Figure A-23. Wavelength dependence extinction coefficients of $SrBi_2(Ta_{0.3}Nb_{0.7})_2O_9$ bulk and surface layer (EMA) obtained by Lorentz Oscillator model.

Figure A-24. Wavelength dependence extinction coefficients of $SrBi_2Nb_2O_9$
bulk and surface layer (EMA) obtained by Lorentz Oscillator model.
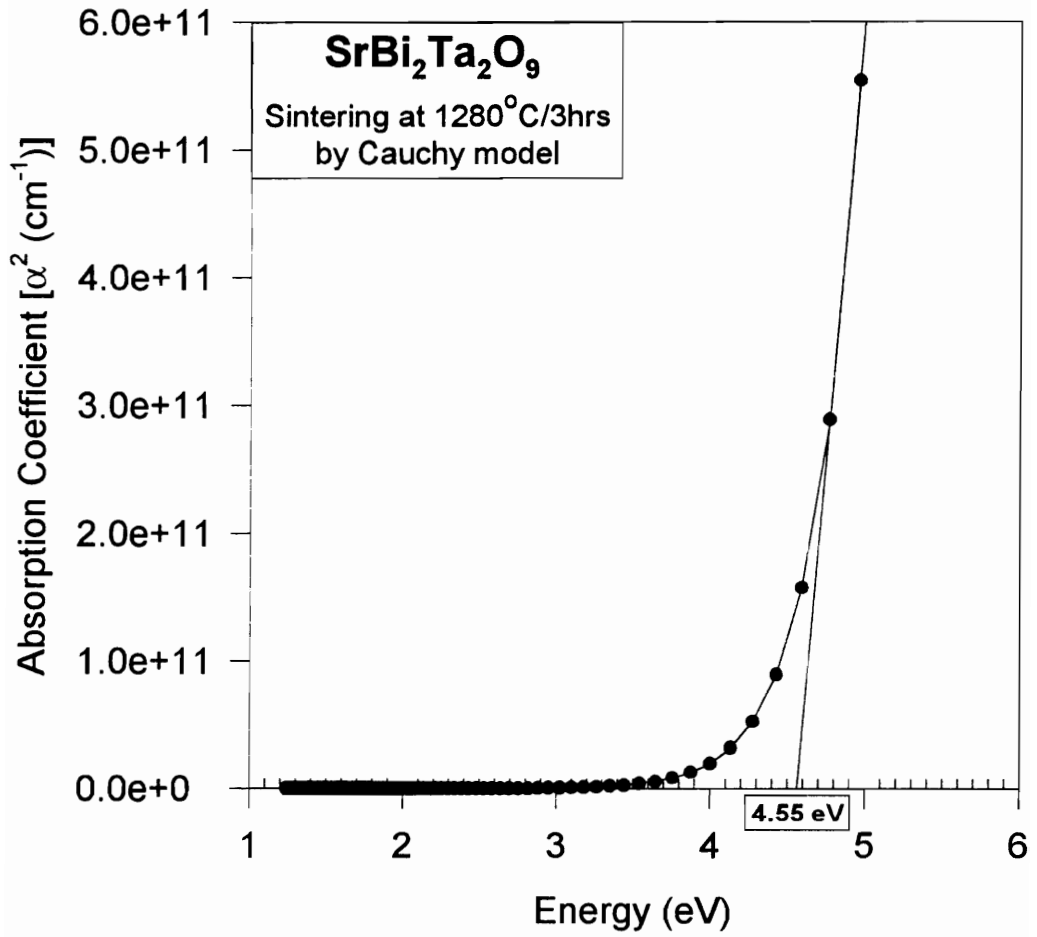
Figure A-25. Dispersion curve of absorption coefficient for $SrBi_2Ta_2O_9$ bulk Ceramics obtained by Cauchy dispersion model.
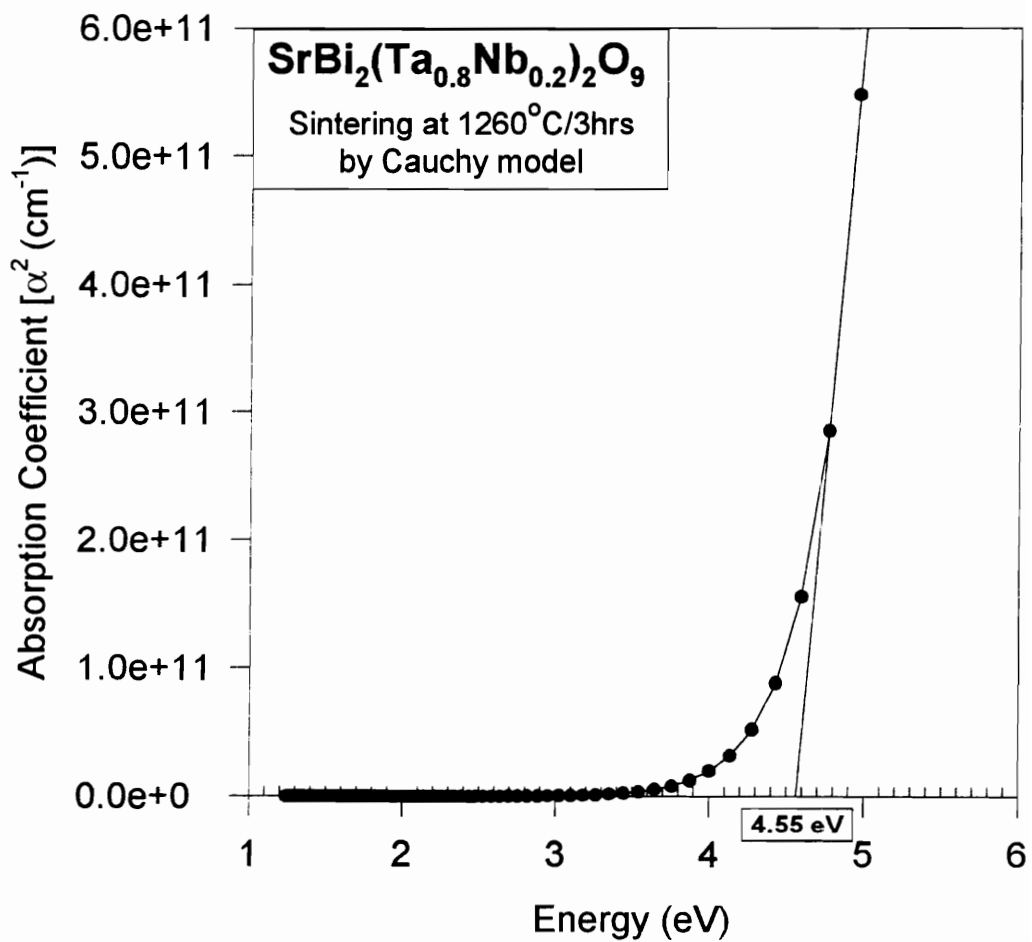
Figure A-26. Dispersion curve of absorption coefficient for $SrBi_2(Ta_{0.8}Nb_{0.2})_2O_9$ bulk Ceramics obtained by Cauchy dispersion model.
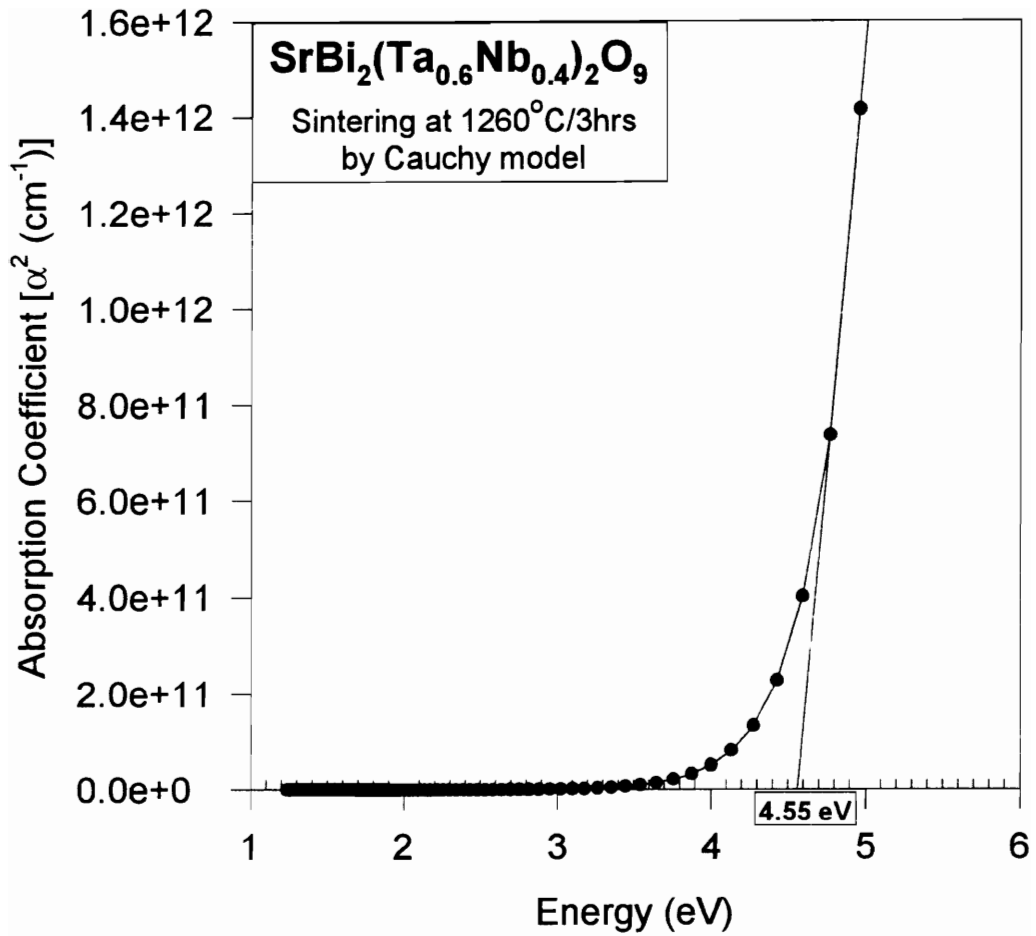
Figure A-27. Dispersion curve of absorption coefficient for $SrBi_2(Ta_{0.6}Nb_{0.4})_2O_9$ bulk Ceramics obtained by Cauchy dispersion model.
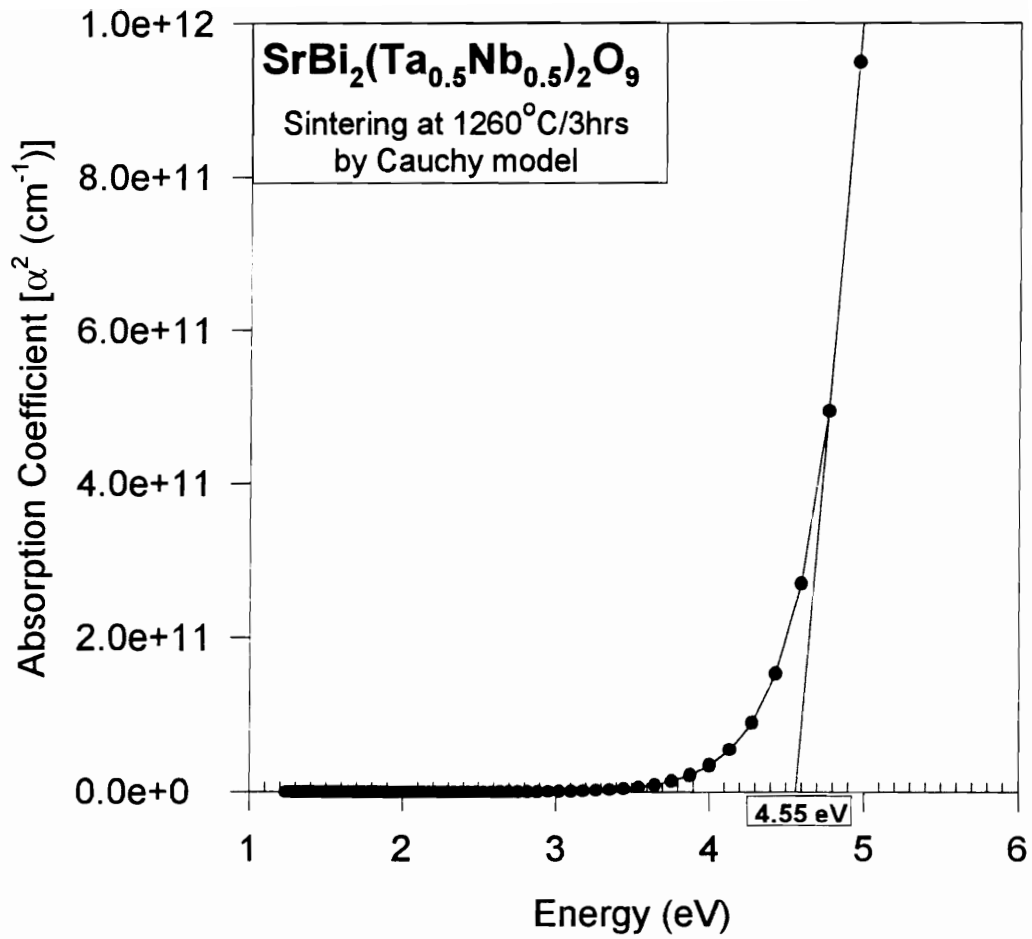
Figure A-28. Dispersion curve of absorption coefficient for $SrBi_2(Ta_{0.5}Nb_{0.5})_2O_9$ bulk Ceramics obtained by Cauchy dispersion model.
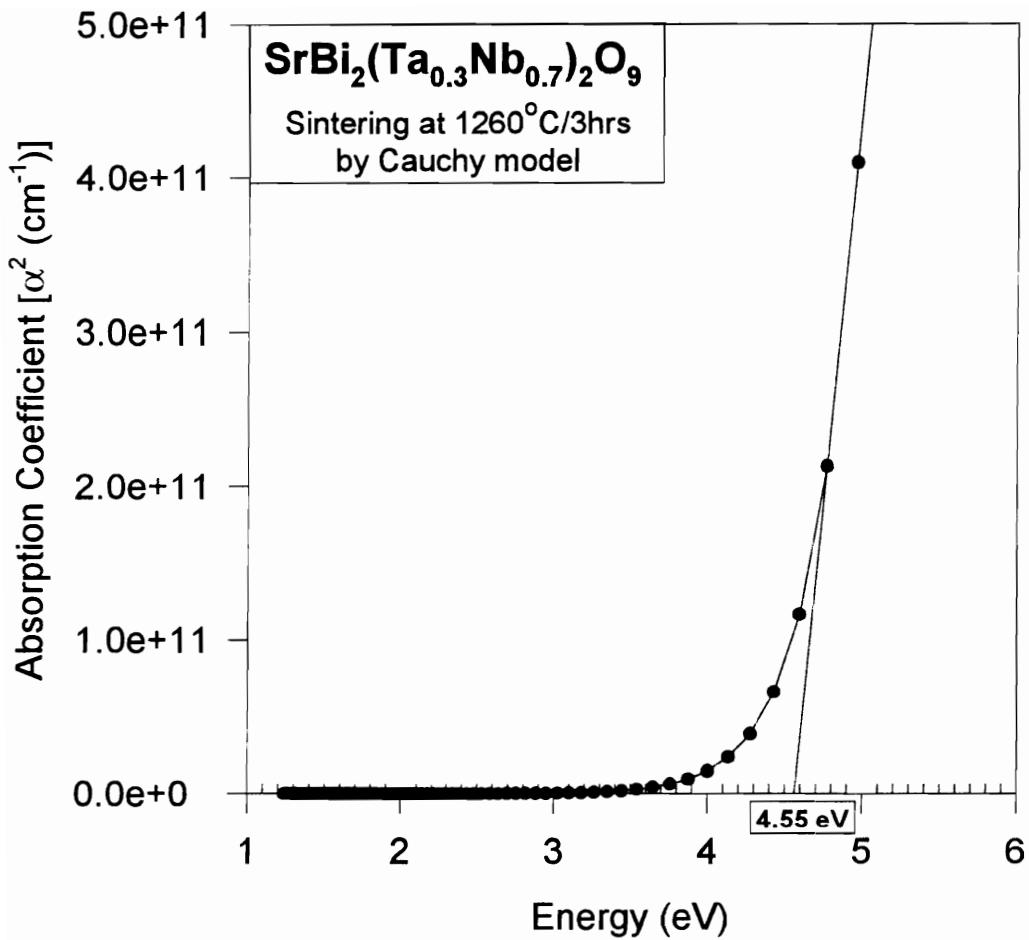
Figure A-29. Dispersion curve of absorption coefficient for $SrBi_2(Ta_{0.3}Nb_{0.7})_2O_9$
bulk Ceramics obtained by Cauchy dispersion model.
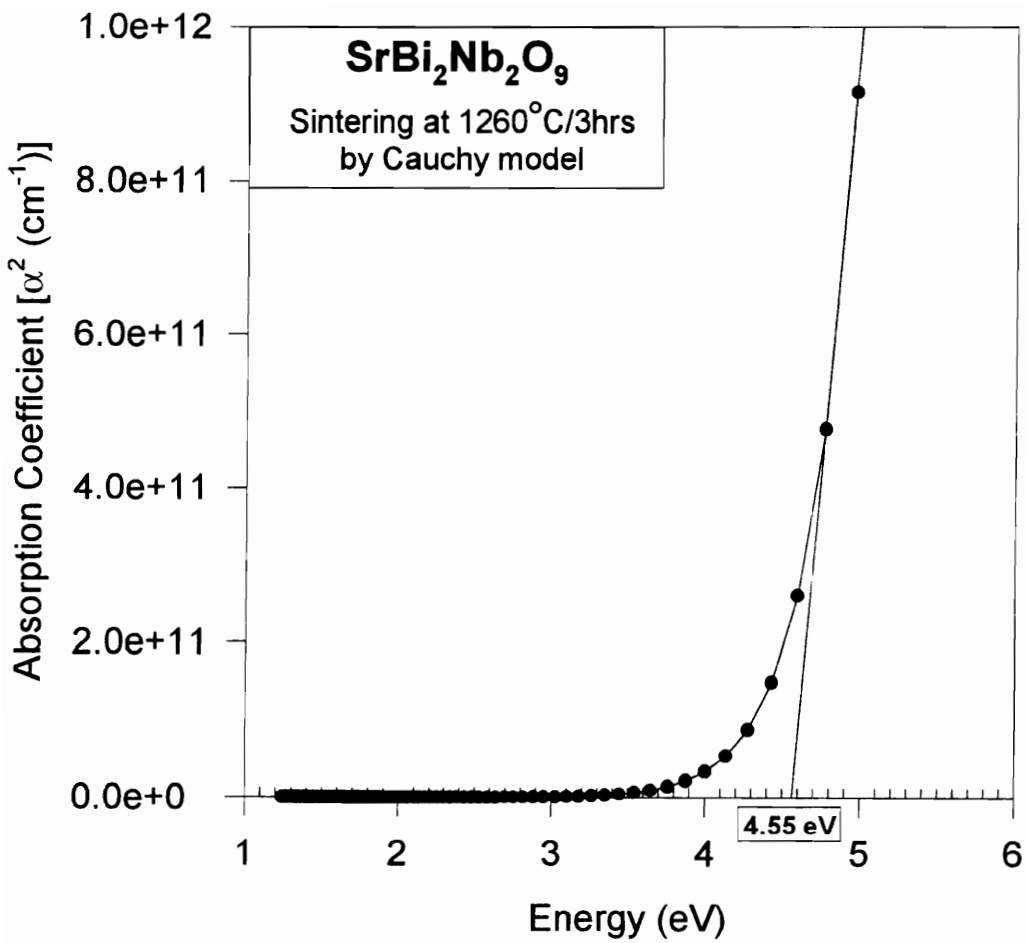
Figure A-30. Dispersion curve of absorption coefficient for $SrBi_2Nb_2O_9$ bulk Ceramics obtained by Cauchy dispersion model.

Appendix B

This appendix collects figures not presented in Chapter 6 for impedance spectroscopy of SBT and SBN bulk ceramics as a function of temperatures. They are:

Figure B-1 ~ B-18   Complex impedance plane of $SrBi_2Ta_2O_9$ bulk ceramics at various temperatures, from room temperature (25^oC) to 650^oC.

Figure B-19 ~ B-31   Complex impedance plane of $SrBi_2Nb_2O_9$ bulk ceramics at various temperatures, from room temperature (25^oC) to 700^oC.
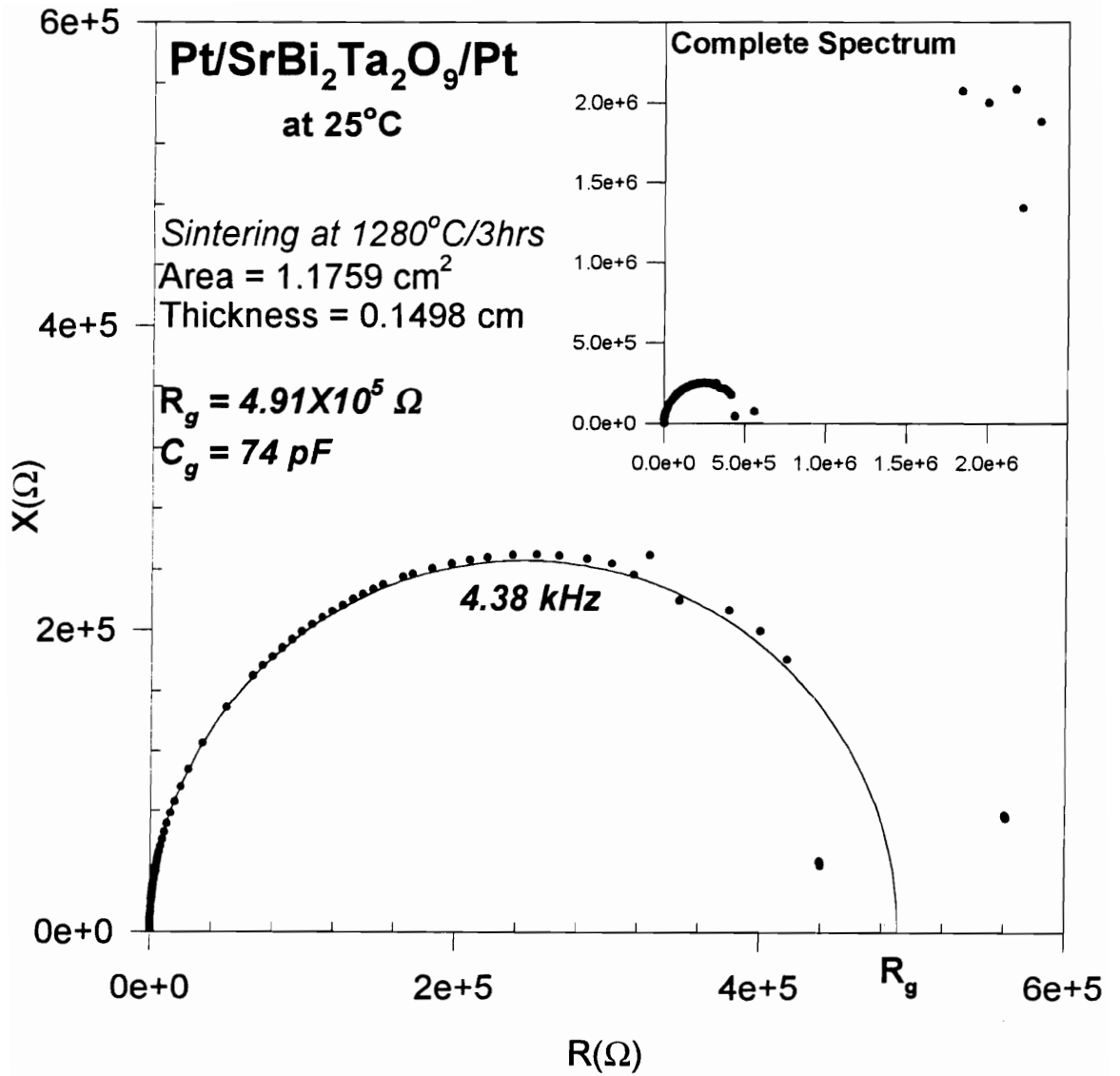
Figure B-1. Complex impedance plane of $SrBi_2Ta_2O_9$ bulk ceramics at 25°C.
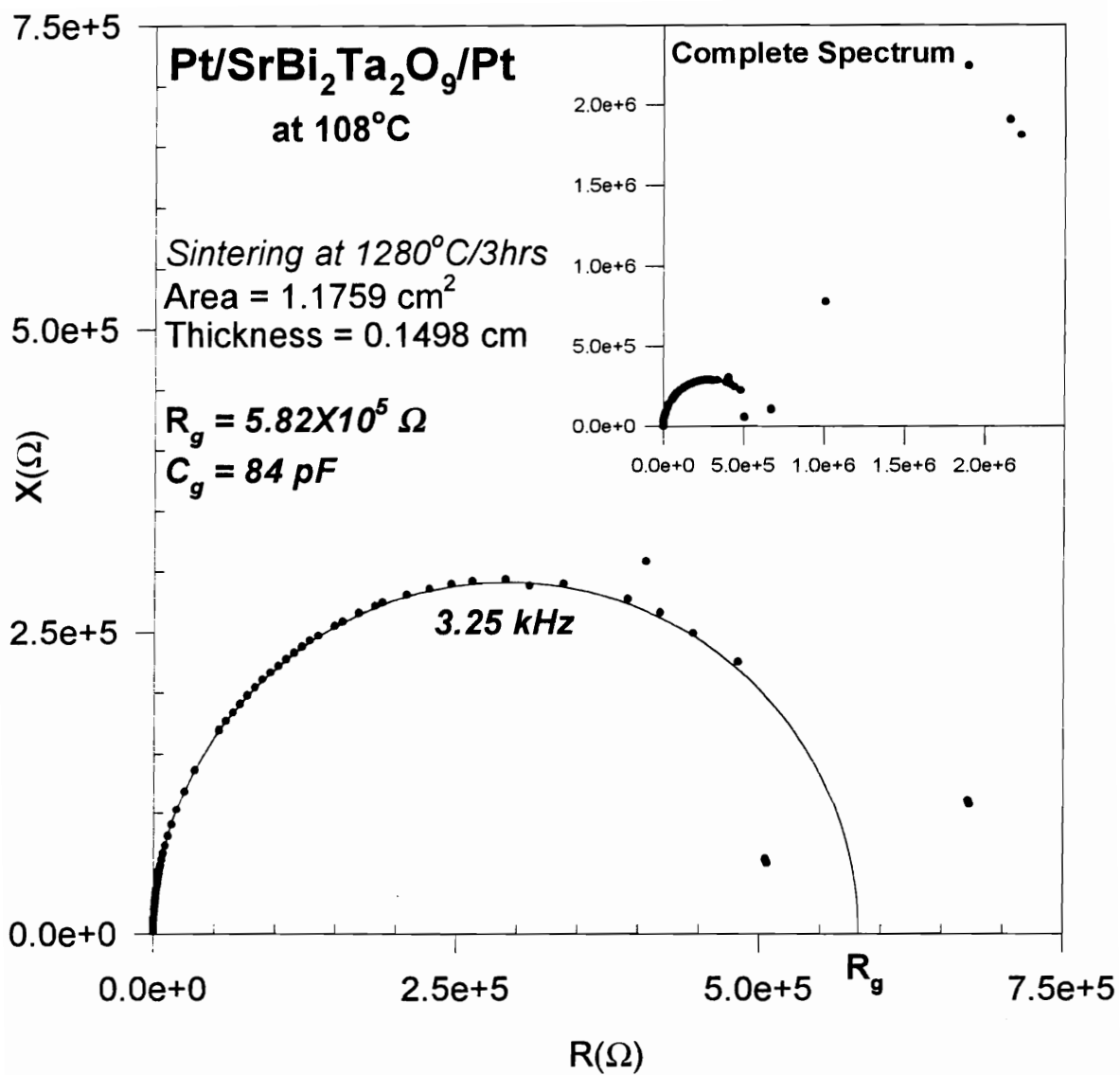
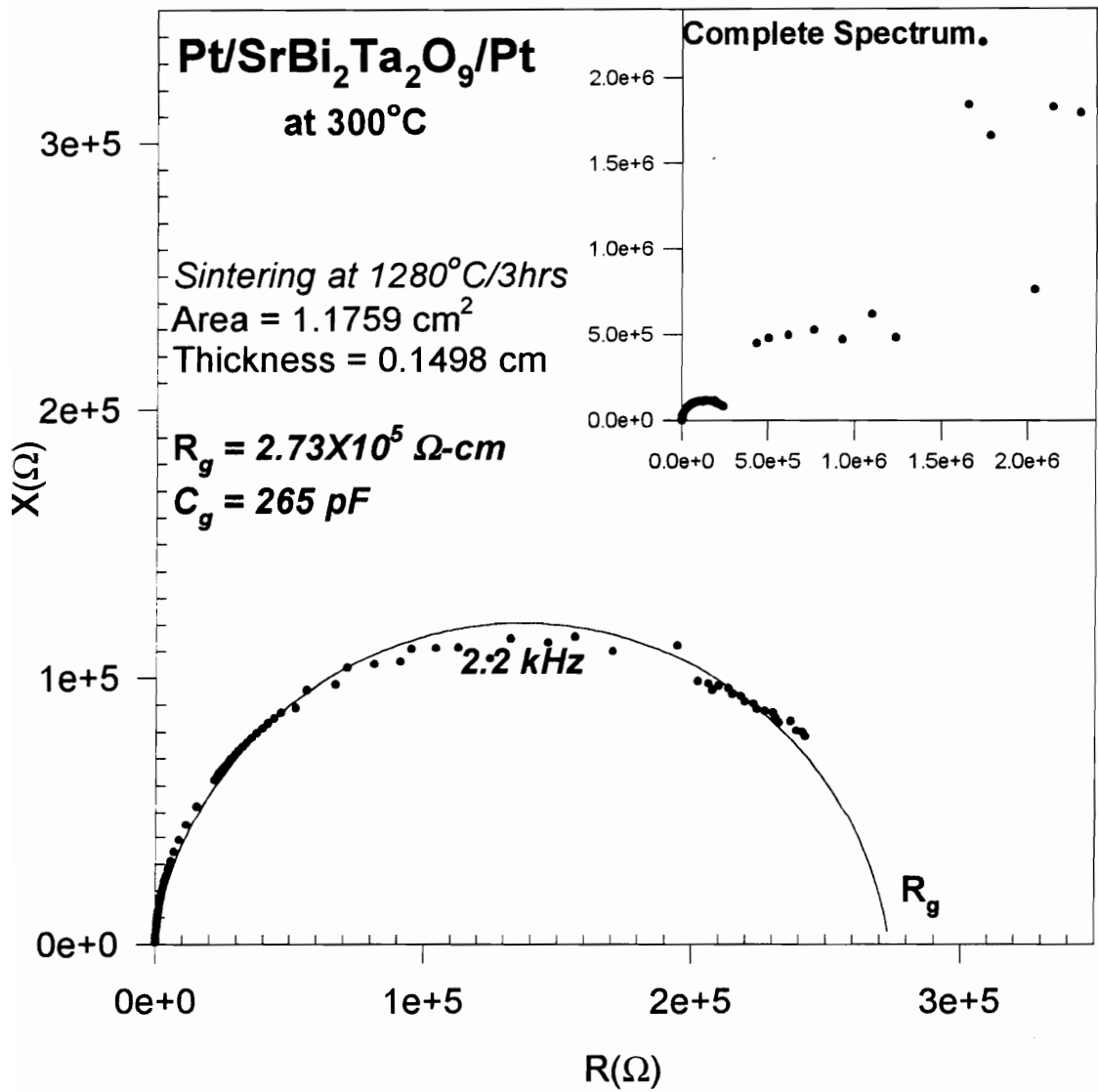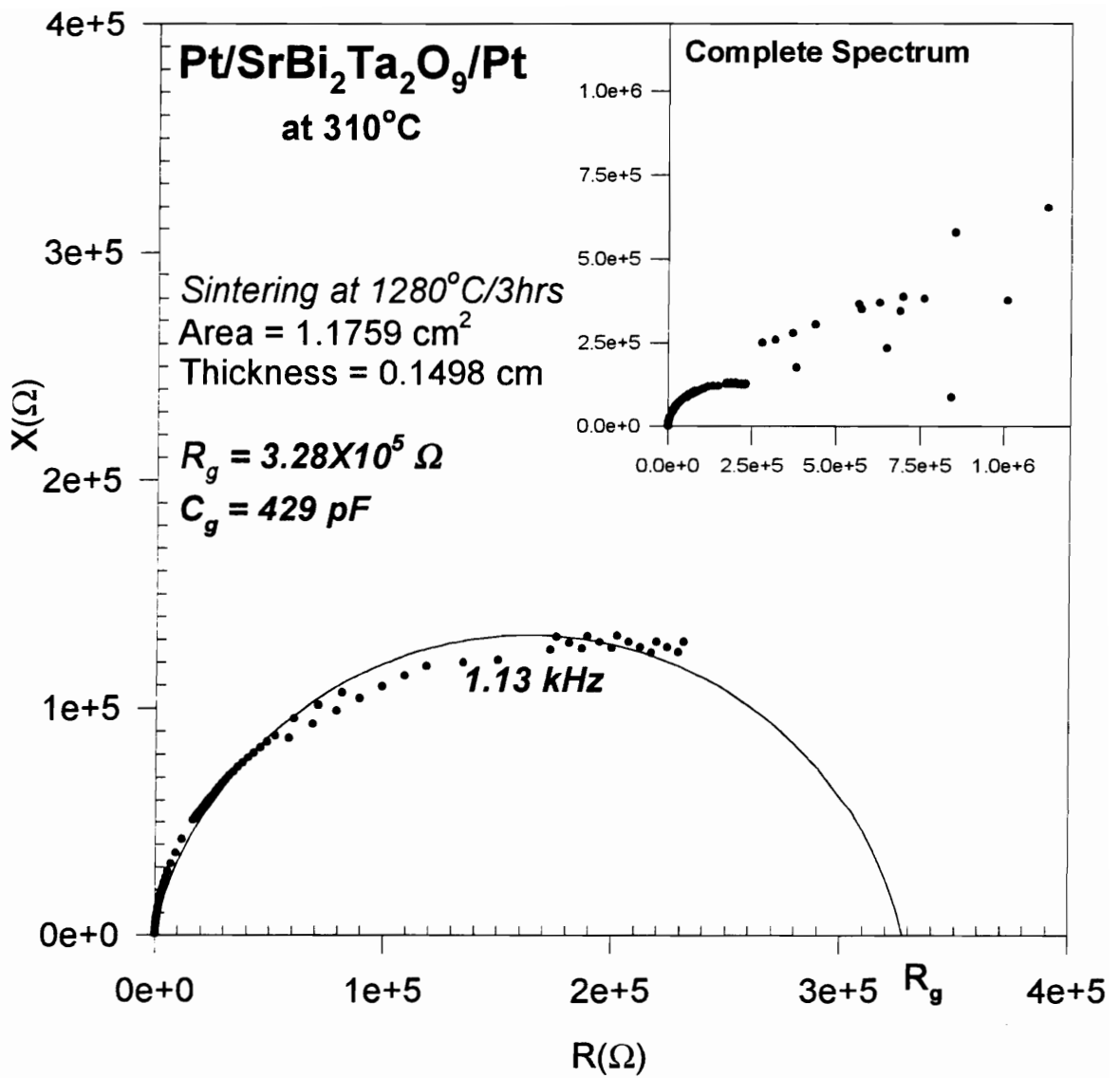Figure B-2. Complex impedance plane of $SrBi_2Ta_2O_9$ bulk ceramics at $108^{\circ}C$.
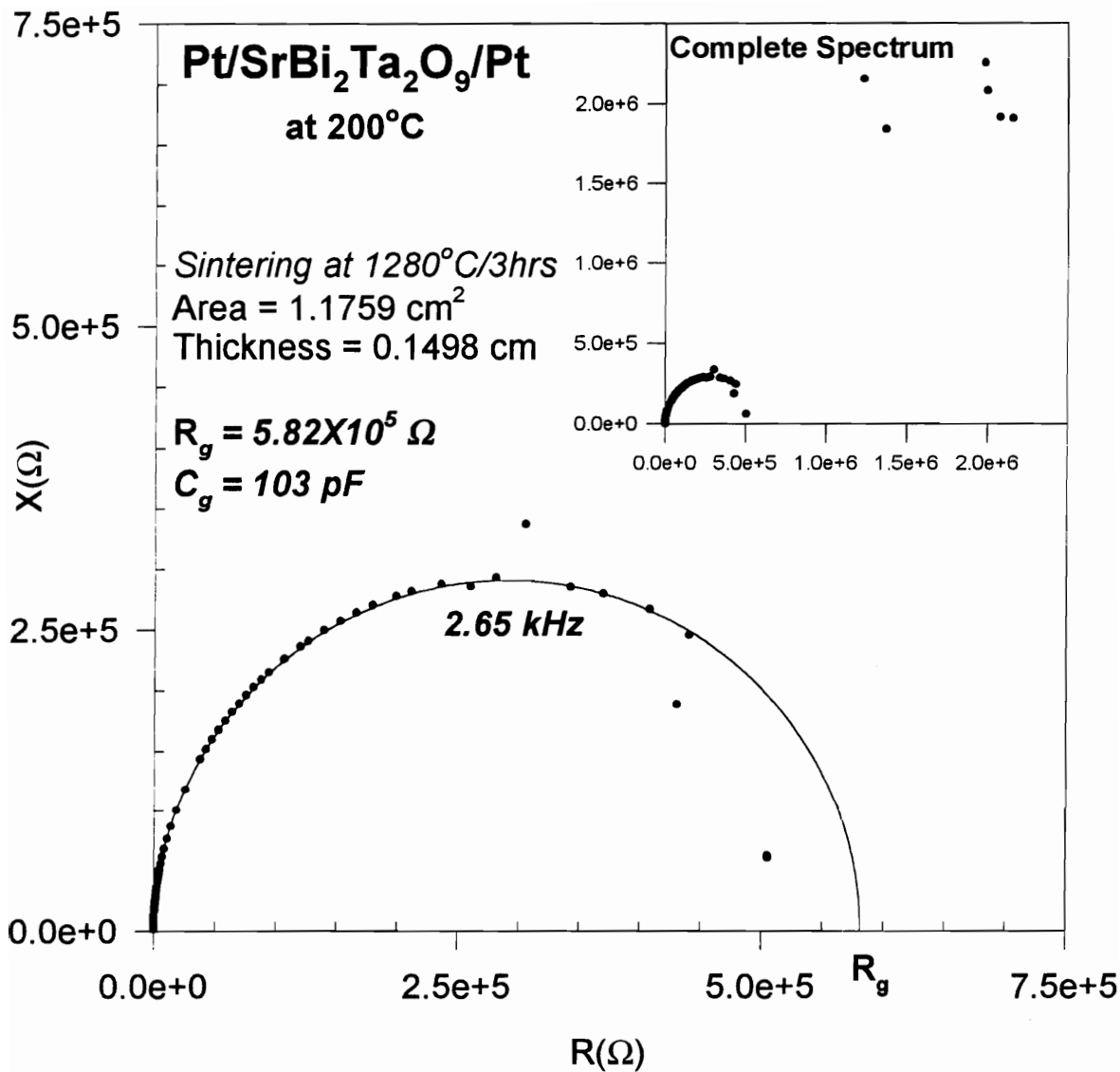
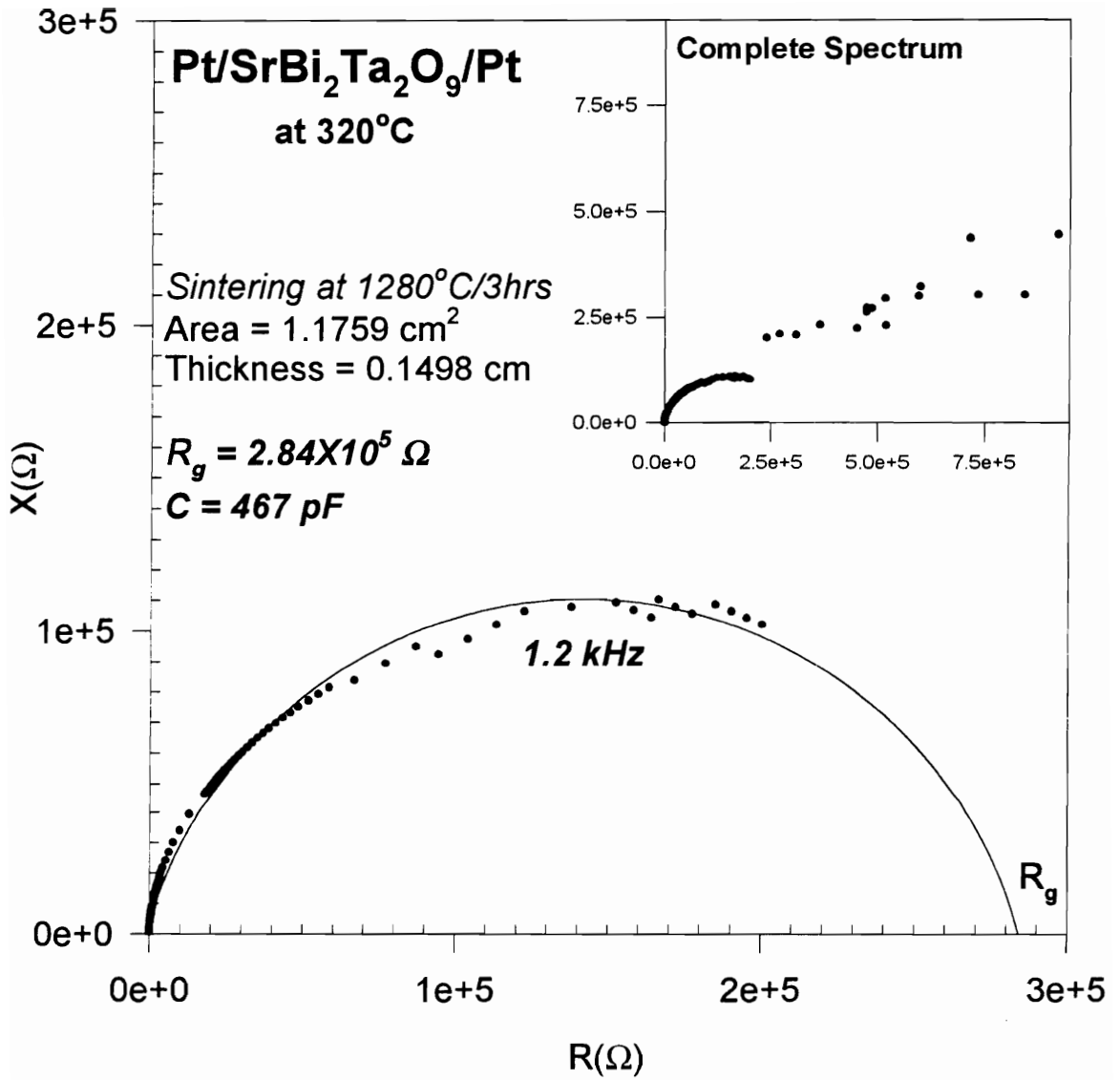Figure B-3. Complex impedance plane of $SrBi_2Ta_2O_9$ bulk ceramics at $200°C$.
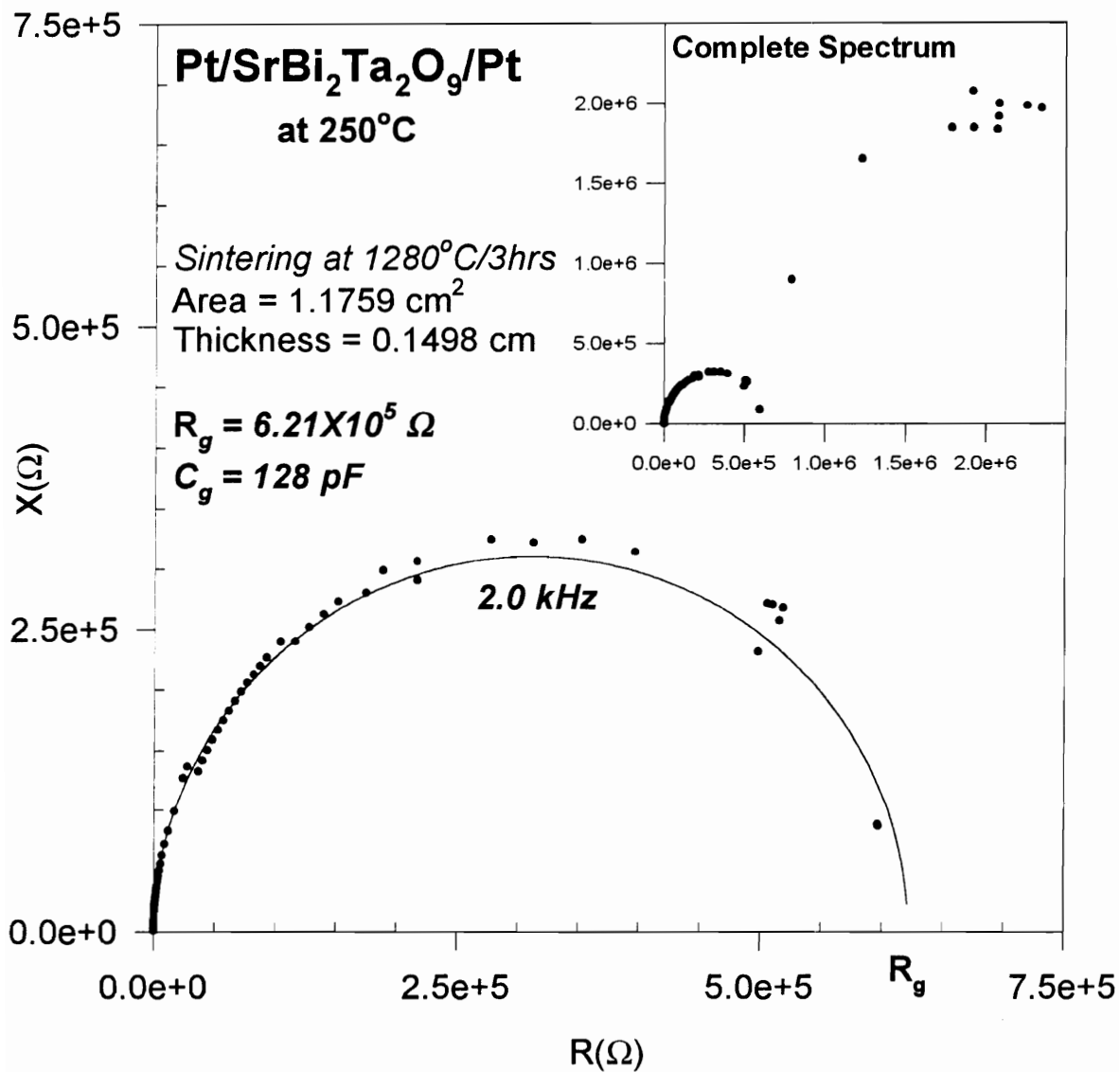
Figure B-4. Complex impedance plane of $SrBi_2Ta_2O_9$ bulk ceramics at 250°C.
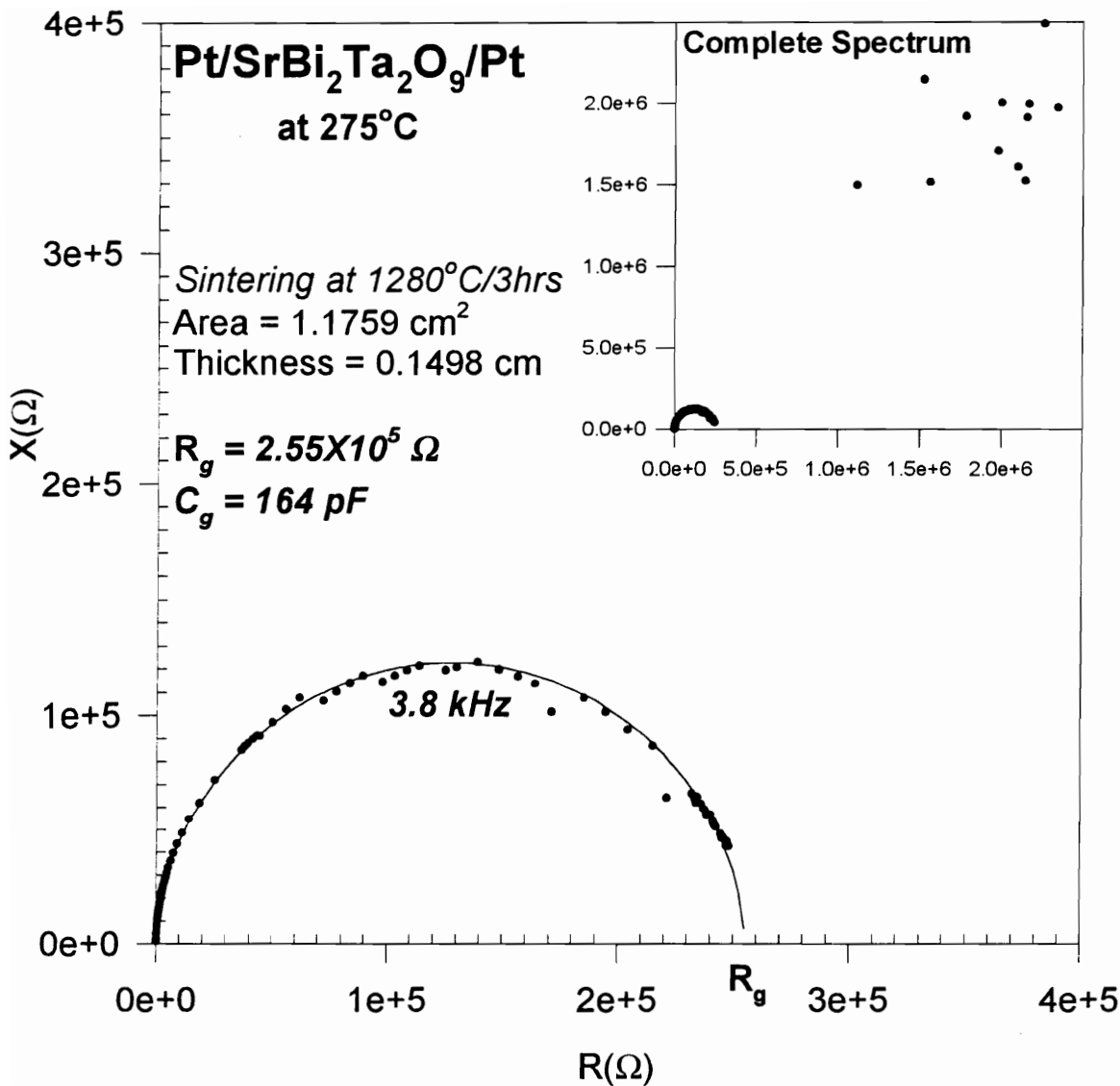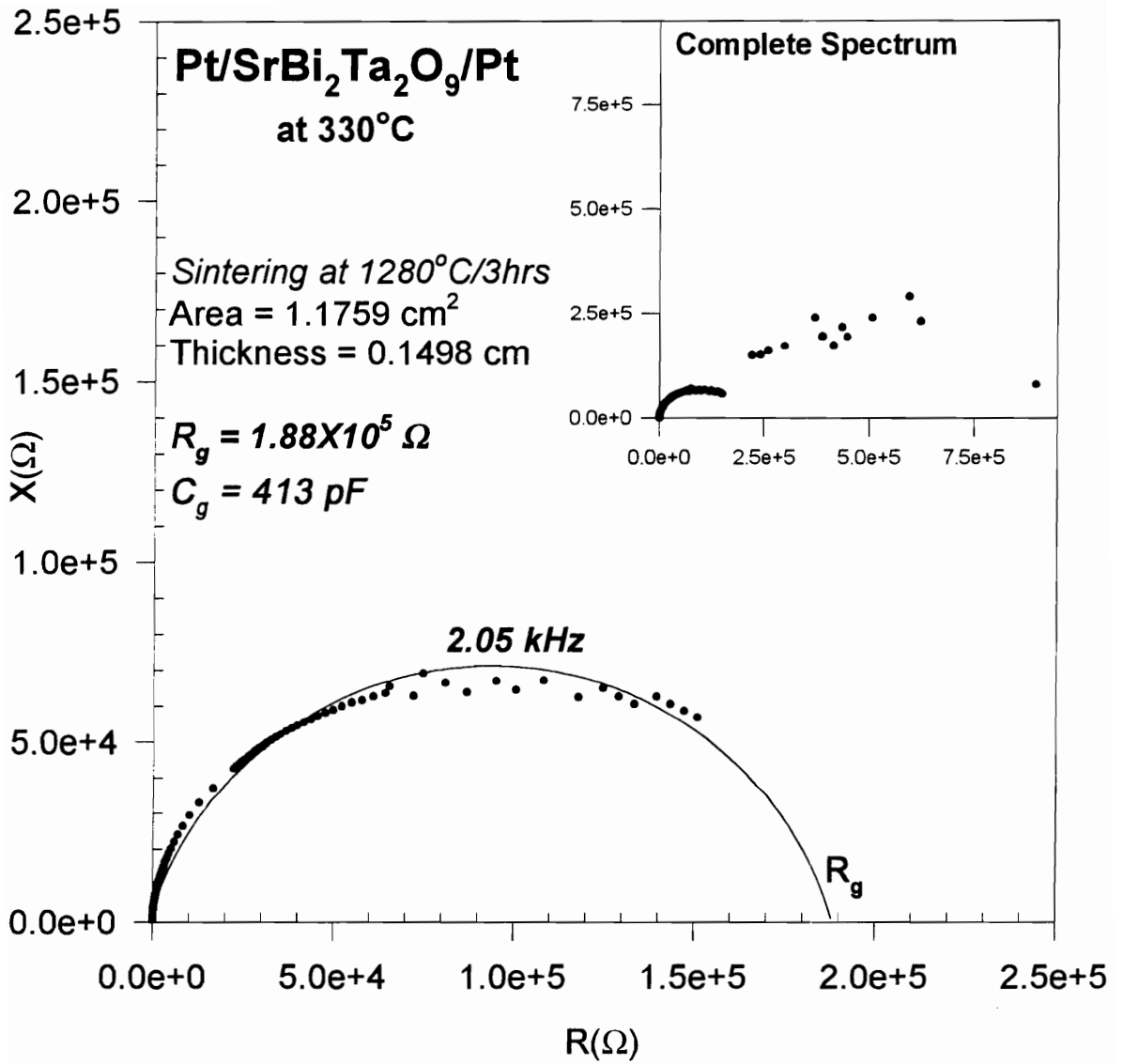
Figure B-5. Complex impedance plane of SrBi$_2$Ta$_2$O$_9$ bulk ceramics at 275°C.
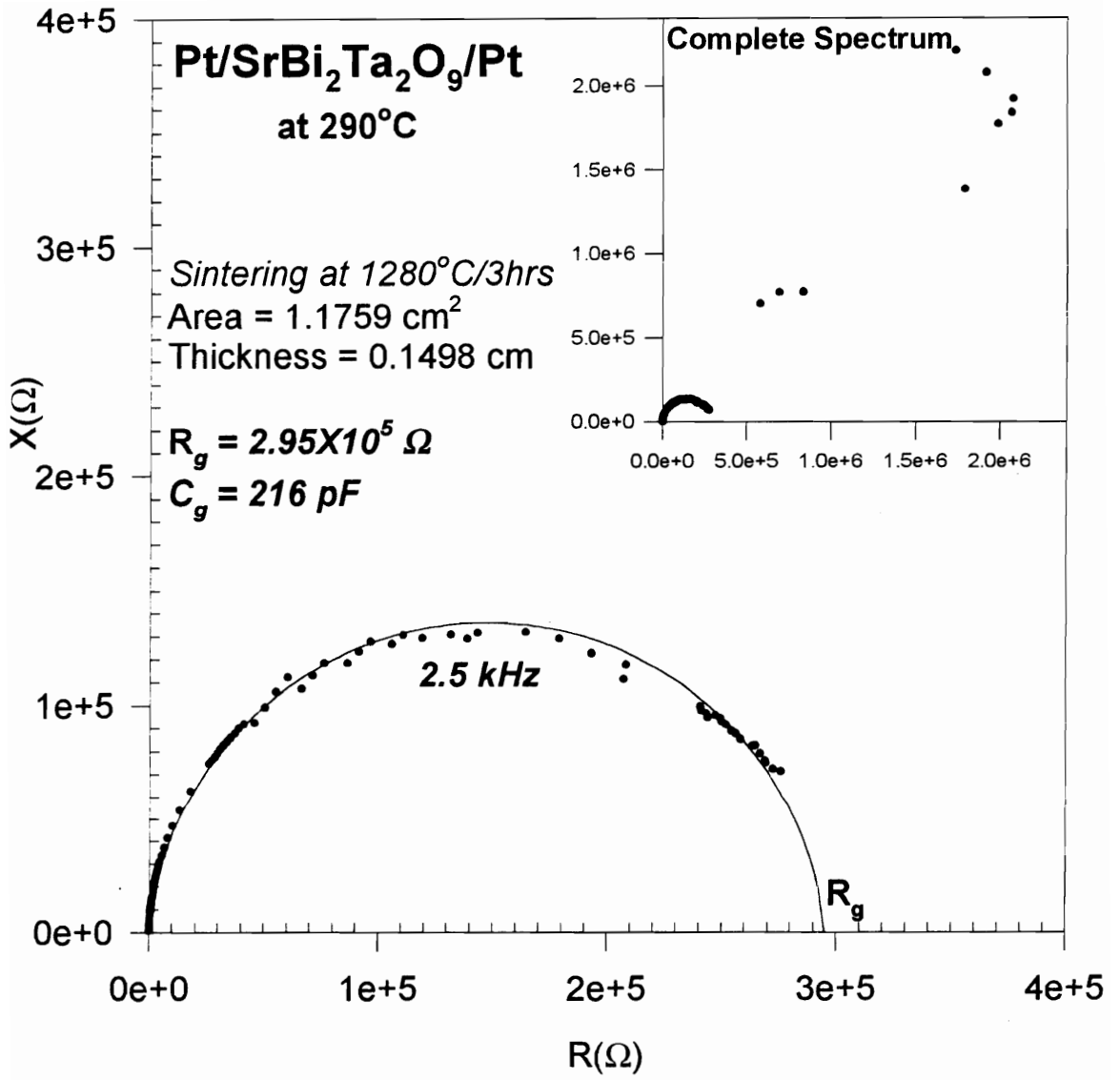
Figure B-6. Complex impedance plane of $SrBi_2Ta_2O_9$ bulk ceramics at $290^\circ C$.

Figure B-7. Complex impedance plane of $SrBi_2Ta_2O_9$ bulk ceramics at $300^\circ C$.

Figure B-8. Complete impedance plane of $SrBi_2Ta_2O_9$ bulk ceramics at $310^\circ C$.

174

Figure B-9. Complete impedance plane of $SrBi_2Ta_2O_9$ bulk ceramics at $320^{o}C$.

Figure B-10. Complex impedance plane of $SrBi_2Ta_2O_9$ bulk ceramics at $330^{\circ}C$.
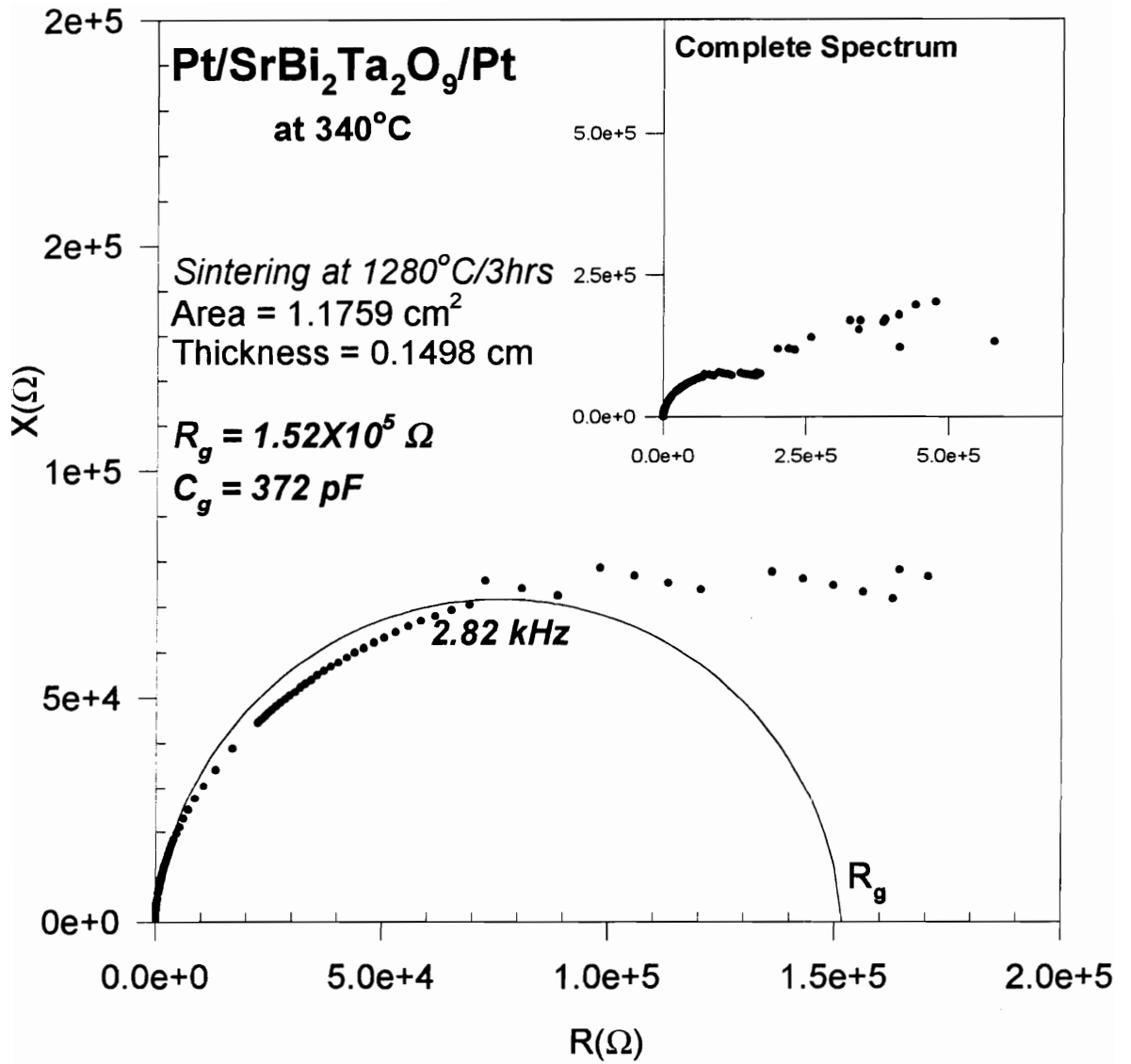
Figure B-11. Complex impedance plane of SrBi$_2$Ta$_2$O$_9$ bulk ceramics at 340°C.
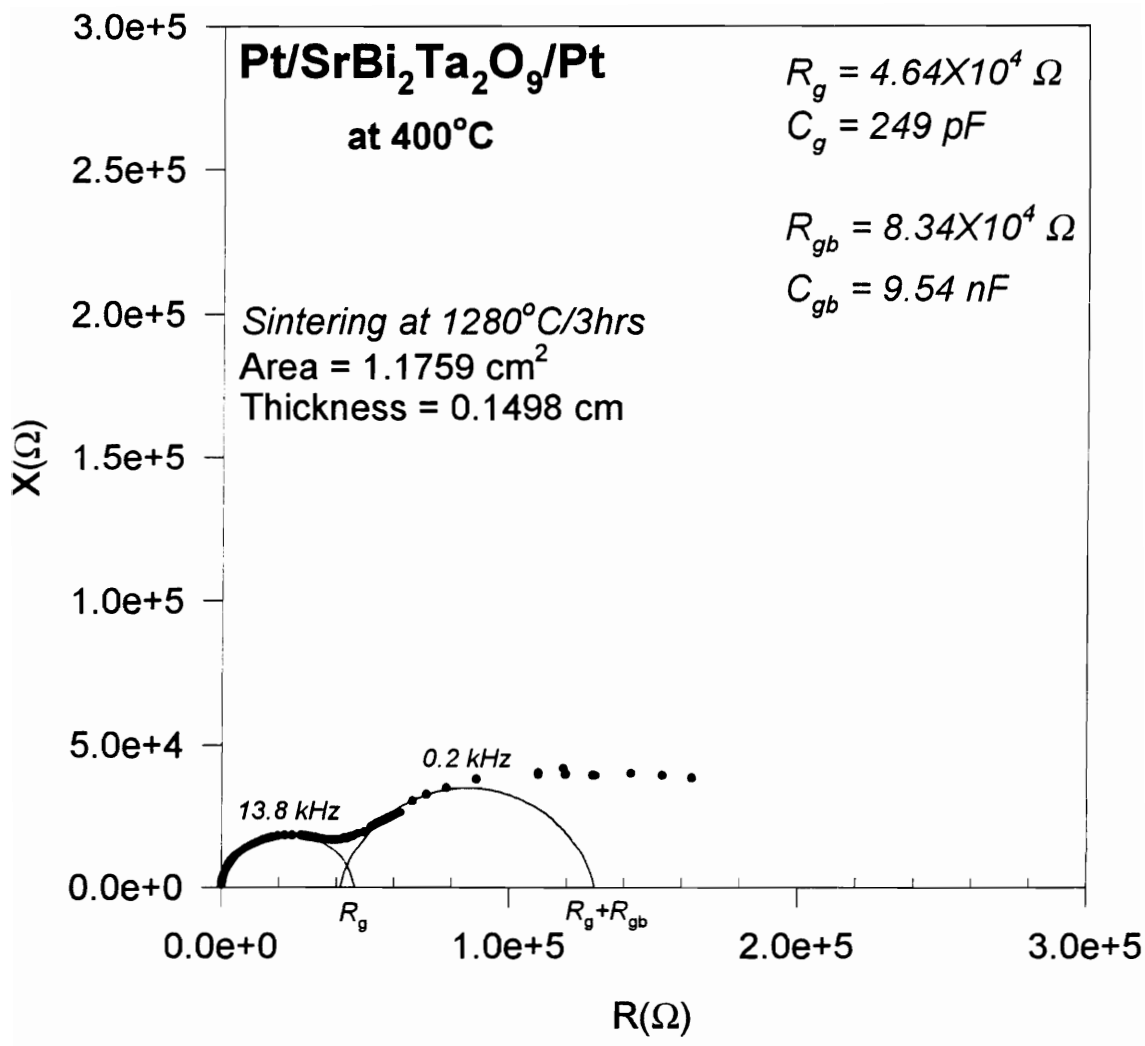
Figure B-12. Complex impedance plane of $SrBi_2Ta_2O_9$ bulk ceramics at $400^\circ C$.
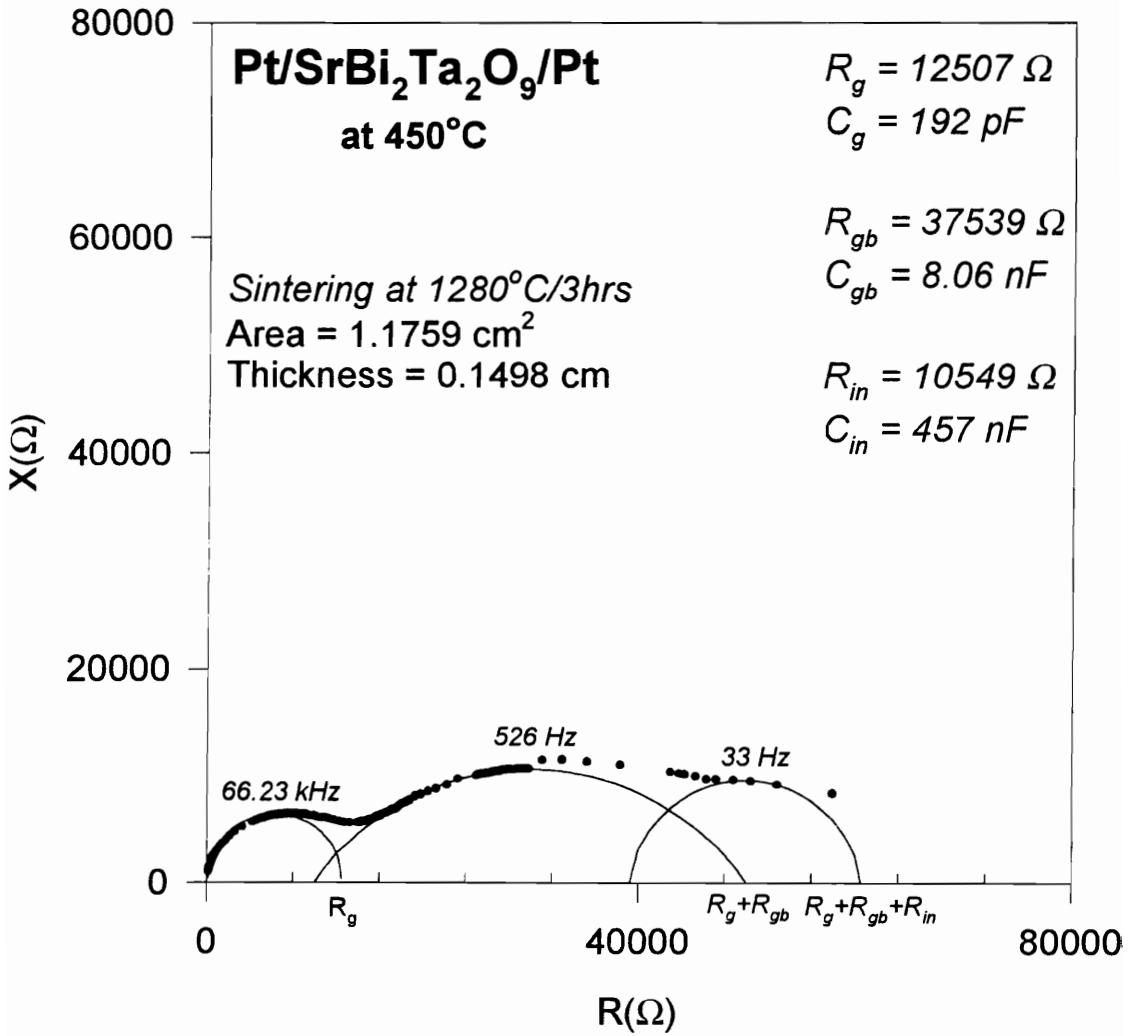
Figure B-13. Complex impedance plane of $SrBi_2Ta_2O_9$ bulk ceramics at 450°C.

Figure B-14. Complex impedance plane of $SrBi_2Ta_2O_9$ bulk ceramics at $500^{\circ}C$.

Figure B-15. Complex impedance plane of SrBi$_2$Ta$_2$O$_9$ bulk ceramics at 550°C.

Figure B-16. Complex impedance plane of SrBi$_2$Ta$_2$O$_9$ bulk ceramics at 575°C.
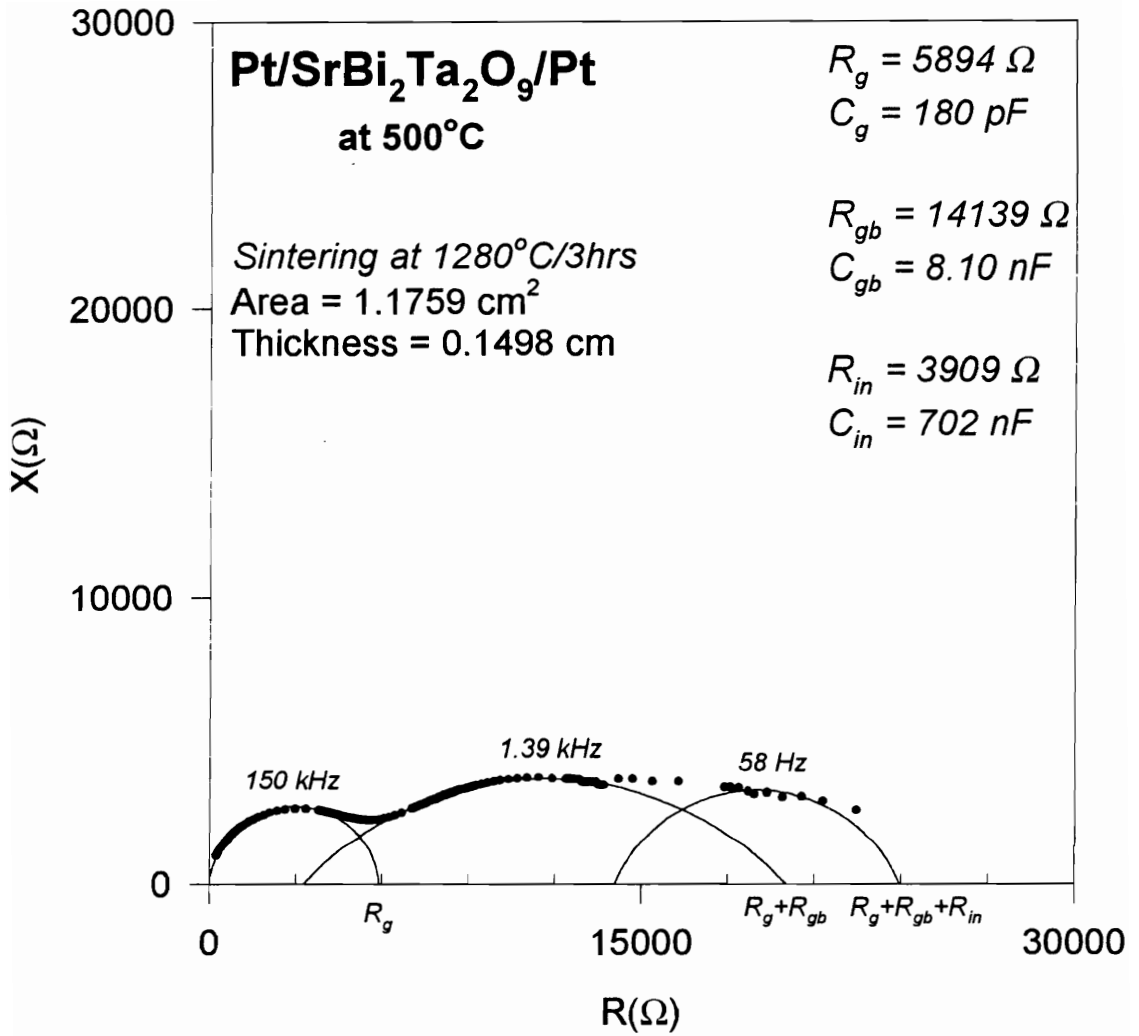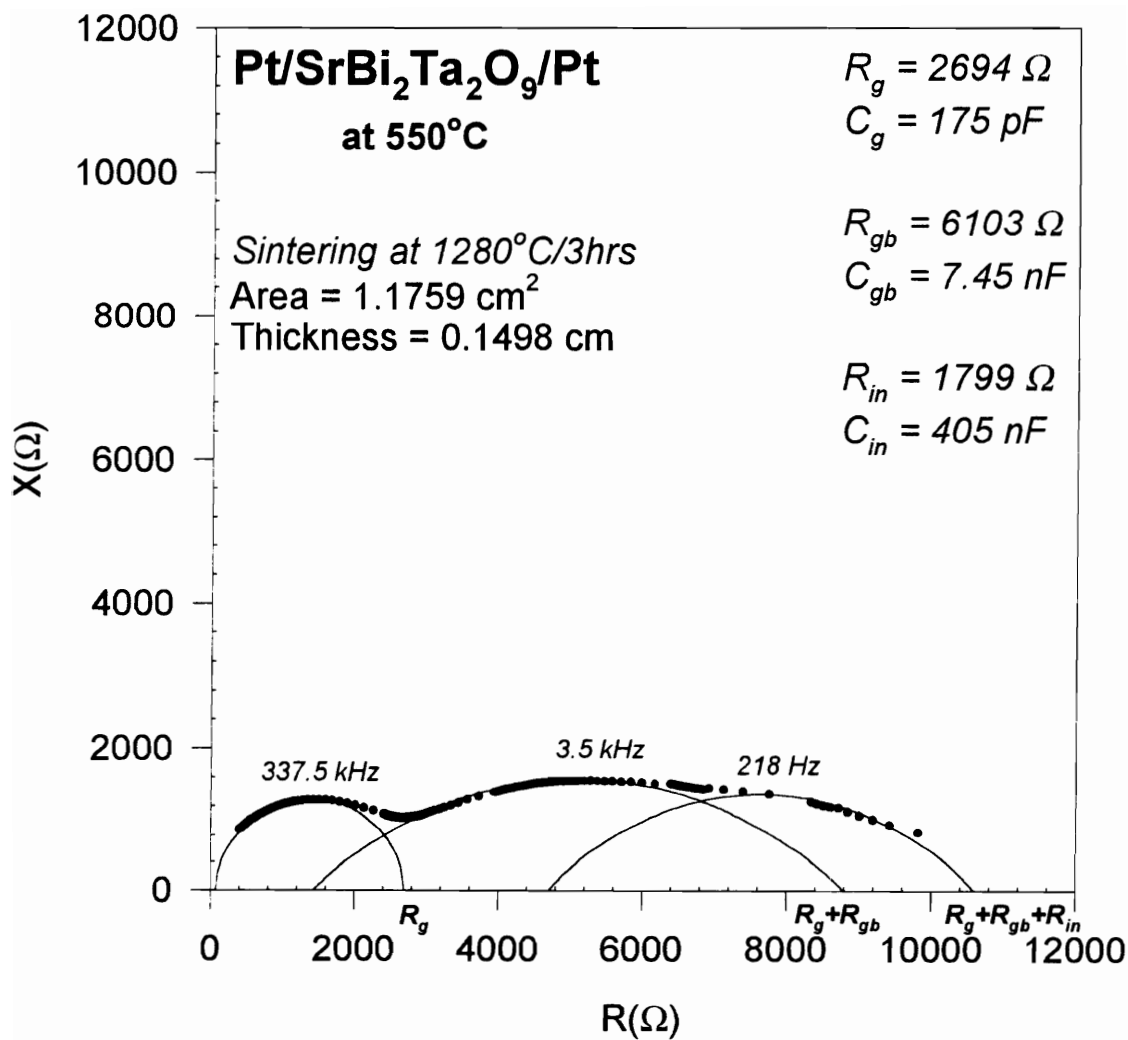
Figure B-17. Complex impedance plane of SrBi₂Ta₂O₉ bulk ceramics at 600°C.

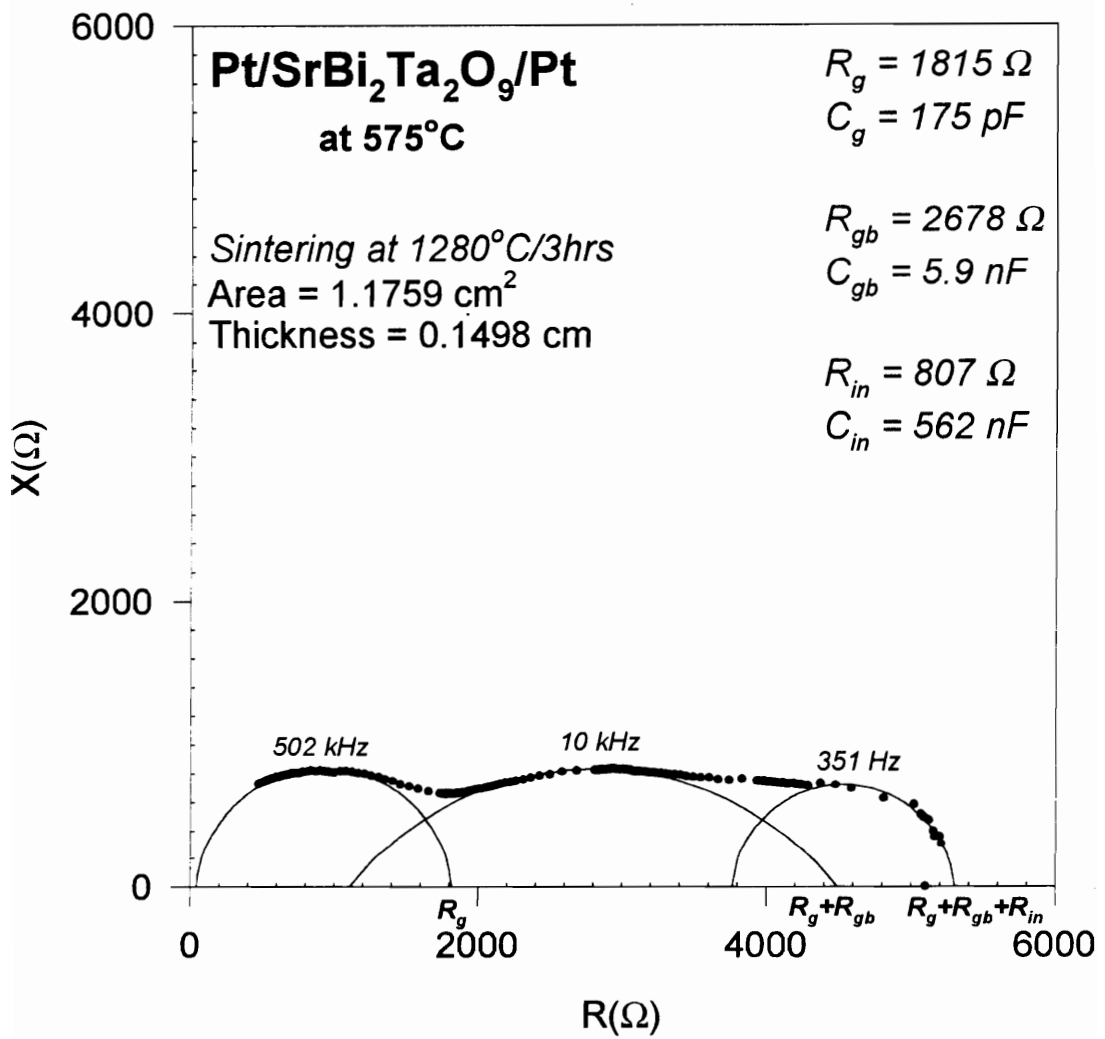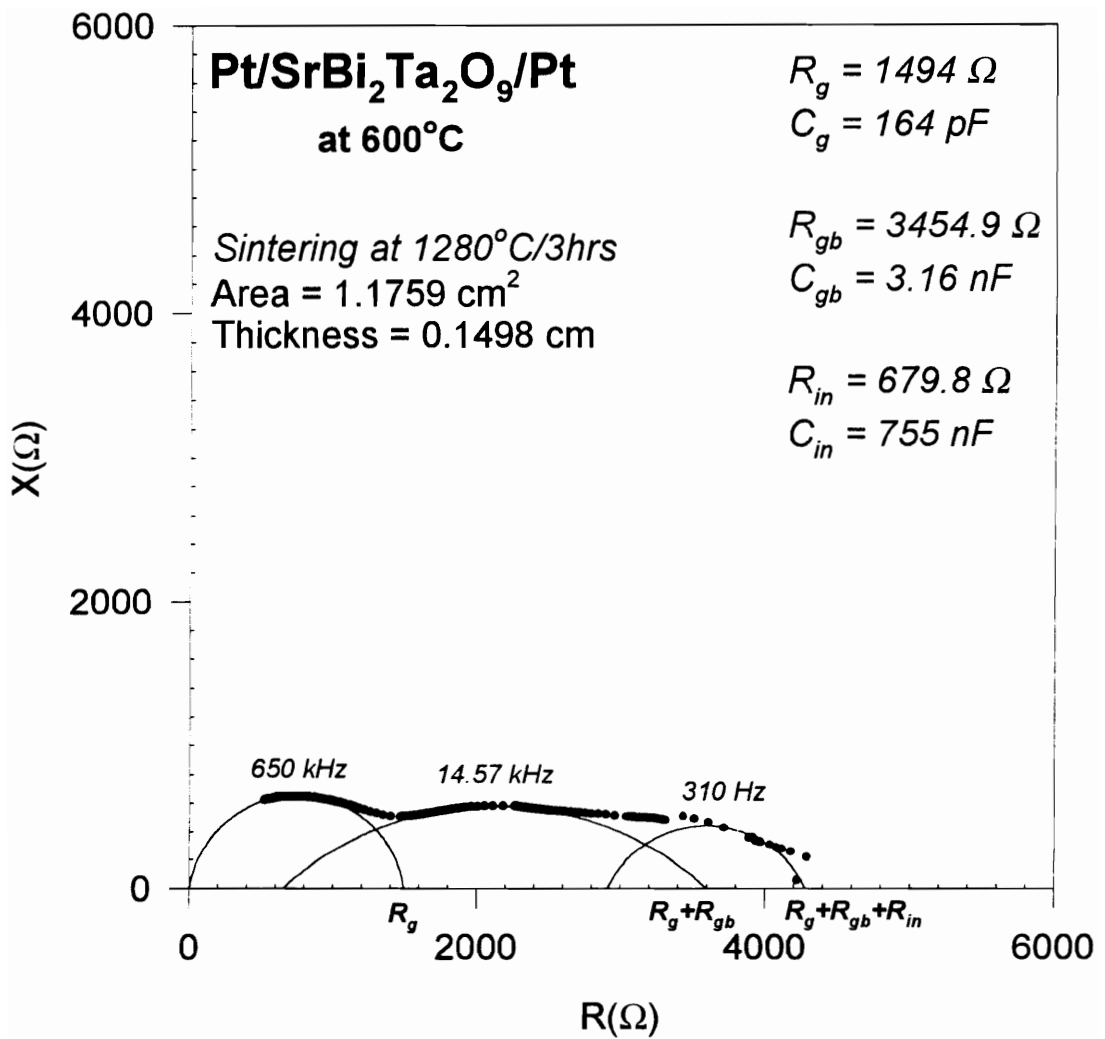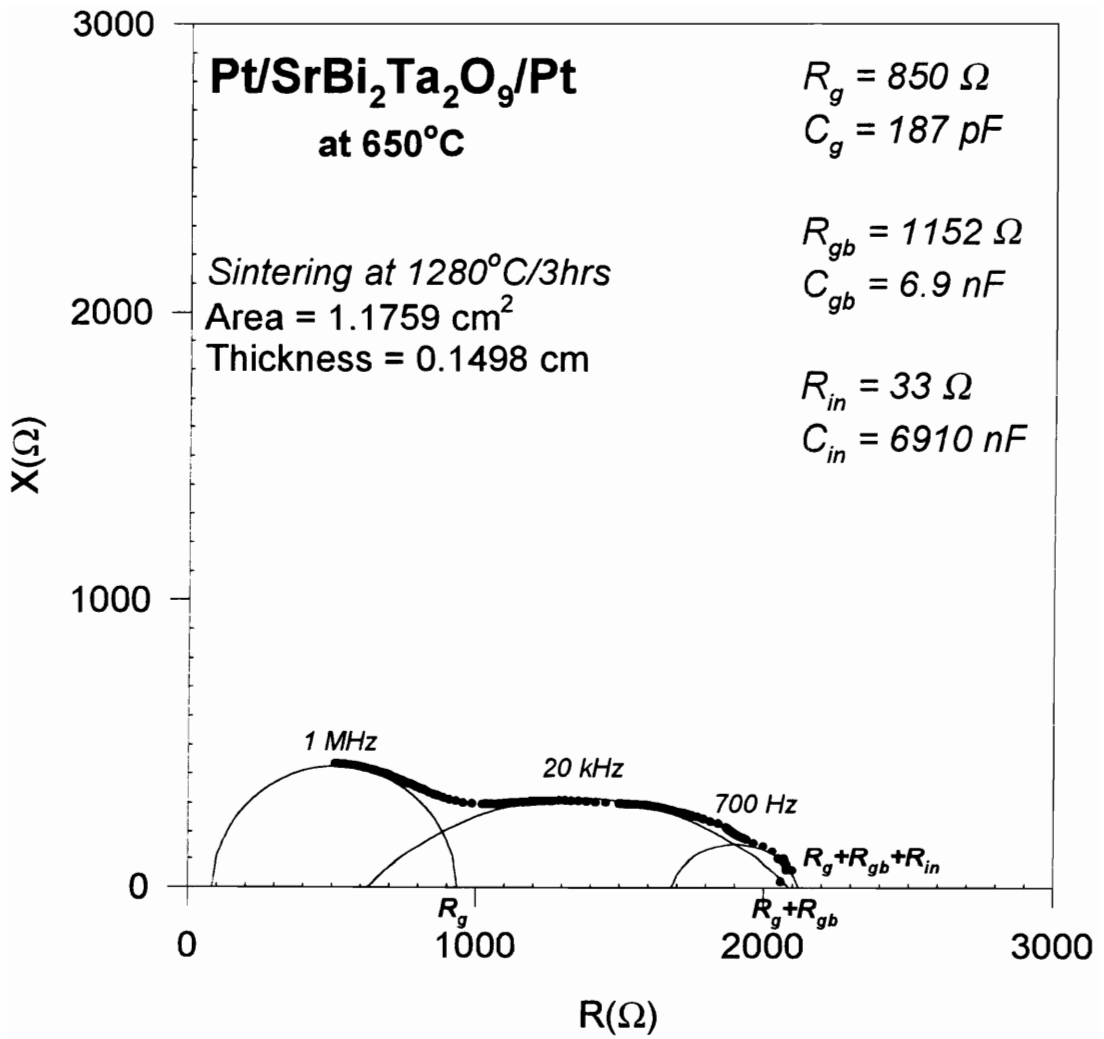Figure B-18. Complex impedance plane of SrBi$_2$Ta$_2$O$_9$ bulk ceramics at 650°C.
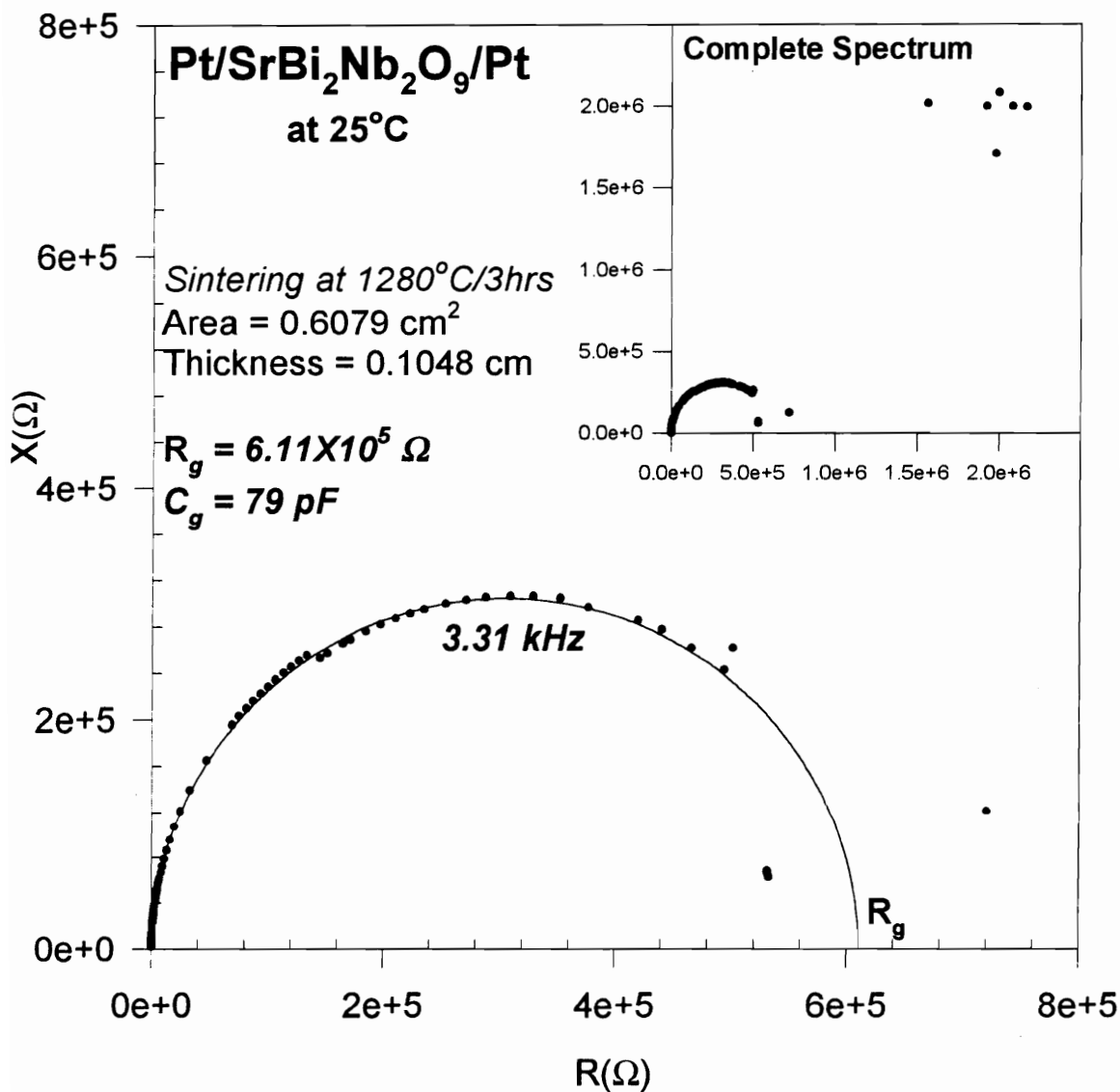
Figure B-19. Complex impedance plane of SrBi$_2$Nb$_2$O$_9$ bulk ceramics at 25°C.
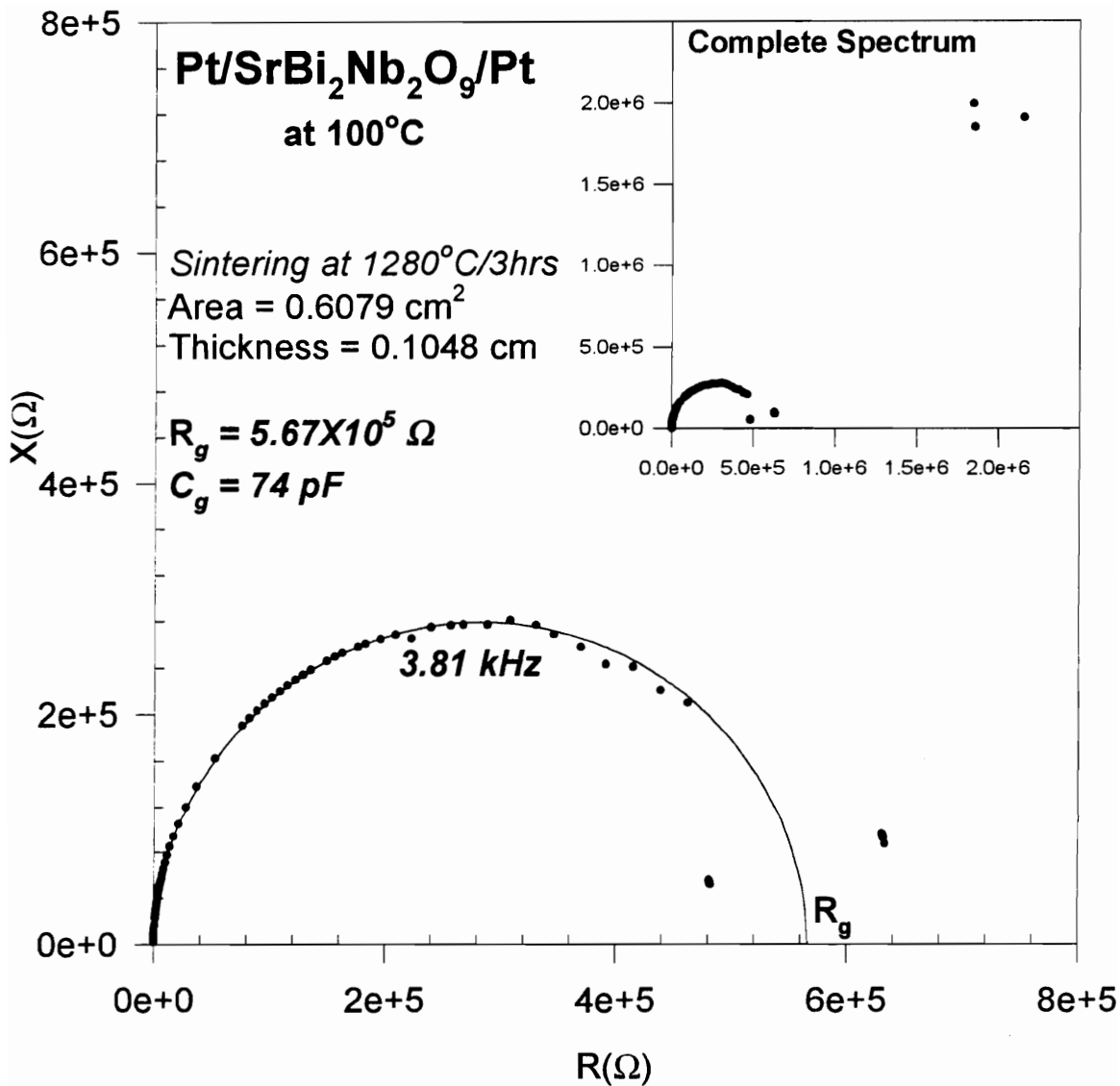
Figure B-20. Complex impedance plane of $SrBi_2Nb_2O_9$ bulk ceramics at $100^\circ C$.

Figure B-21. Complex impedance plane of $SrBi_2Nb_2O_9$ bulk ceramics at $200^\circ C$.

Figure B-22. Complex impedance plane of $SrBi_2Nb_2O_9$ bulk ceramics at $300°C$.

Figure B-23. Complex impedance plane of $SrBi_2Nb_2O_9$ bulk ceramics at $380^{\circ}C$.

Figure B-24. Complex impedance plane of $SrBi_2Nb_2O_9$ bulk ceramics at $420°C$.

Figure B-25. Complex impedance plane of $SrBi_2Nb_2O_9$ bulk ceramics at $450^\circ C$.

Figure B-26. Complex impedance plane of $SrBi_2Nb_2O_9$ bulk ceramics at 480°C.

Figure B-27. Complex impedance plane of SrBi$_2$Nb$_2$O$_9$ bulk ceramics at 490°C.

Figure B-28. Complex impedance plane of $SrBi_2Nb_2O_9$ bulk ceramics at $520^{\circ}C$.

Figure B-29. Complex impedance plane of $SrBi_2Nb_2O_9$ bulk ceramics at $560^\circ C$.
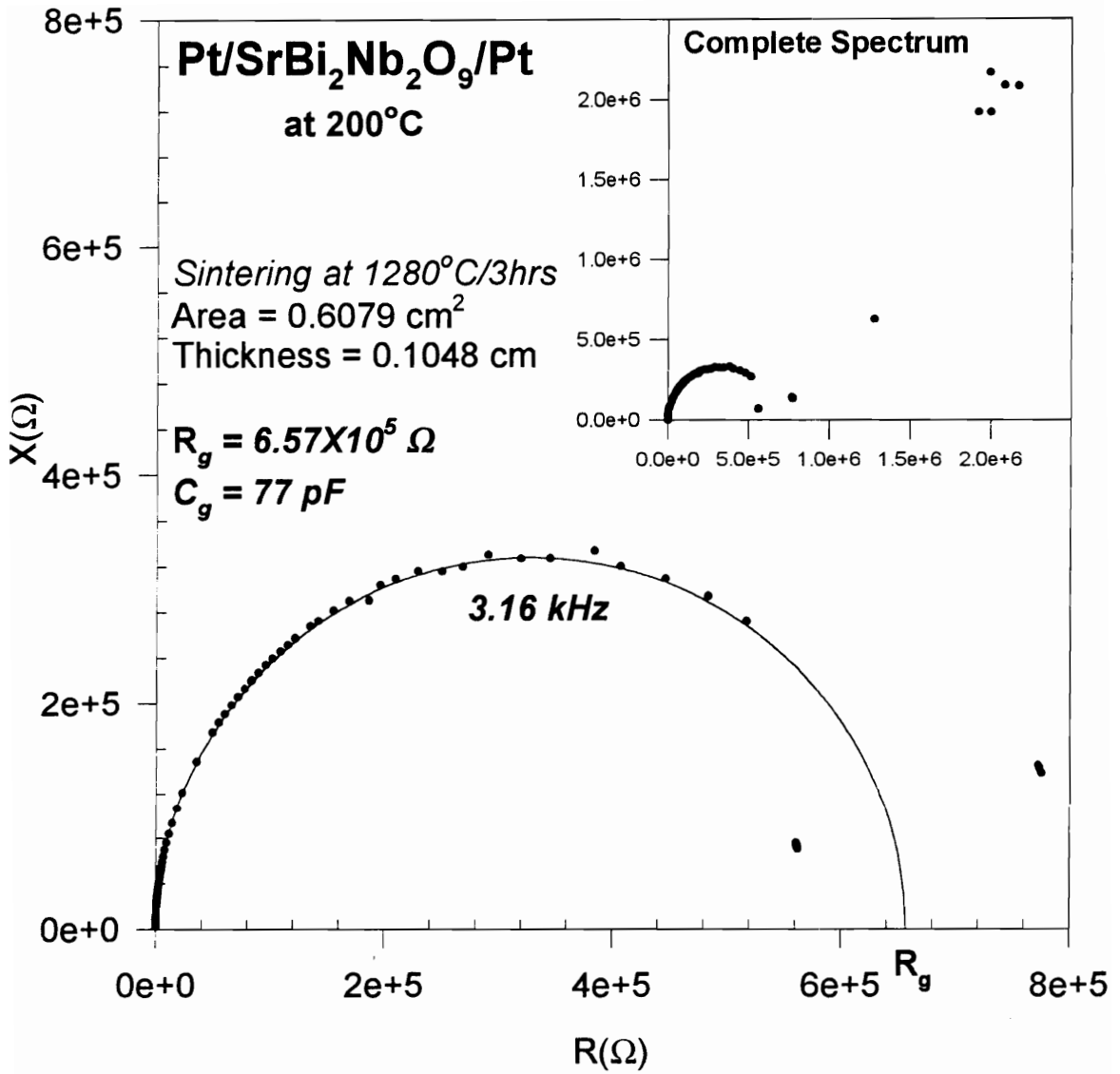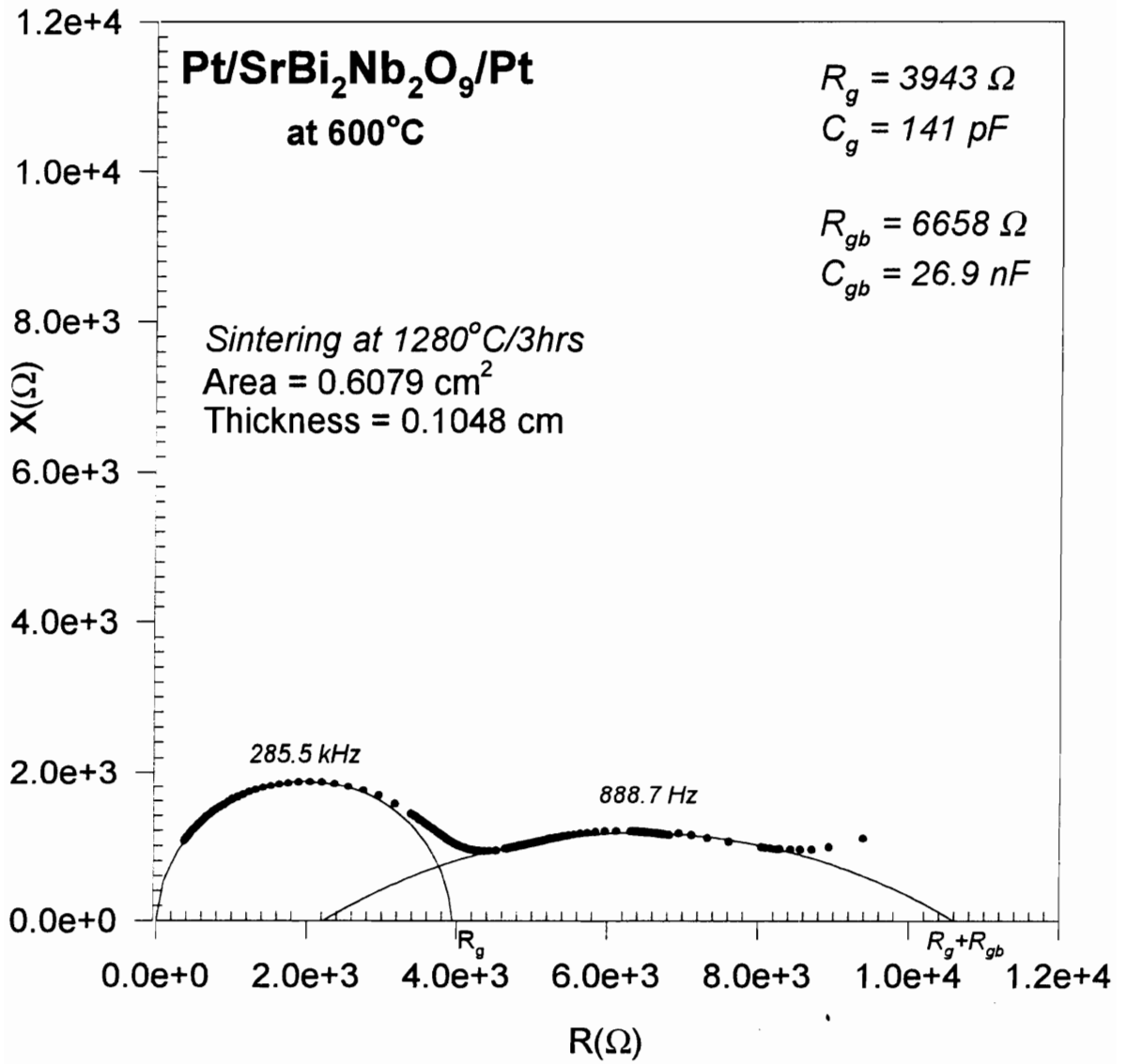
Figure B-30. Complex impedance plane of $SrBi_2Nb_2O_9$ bulk ceramics at 600°C.

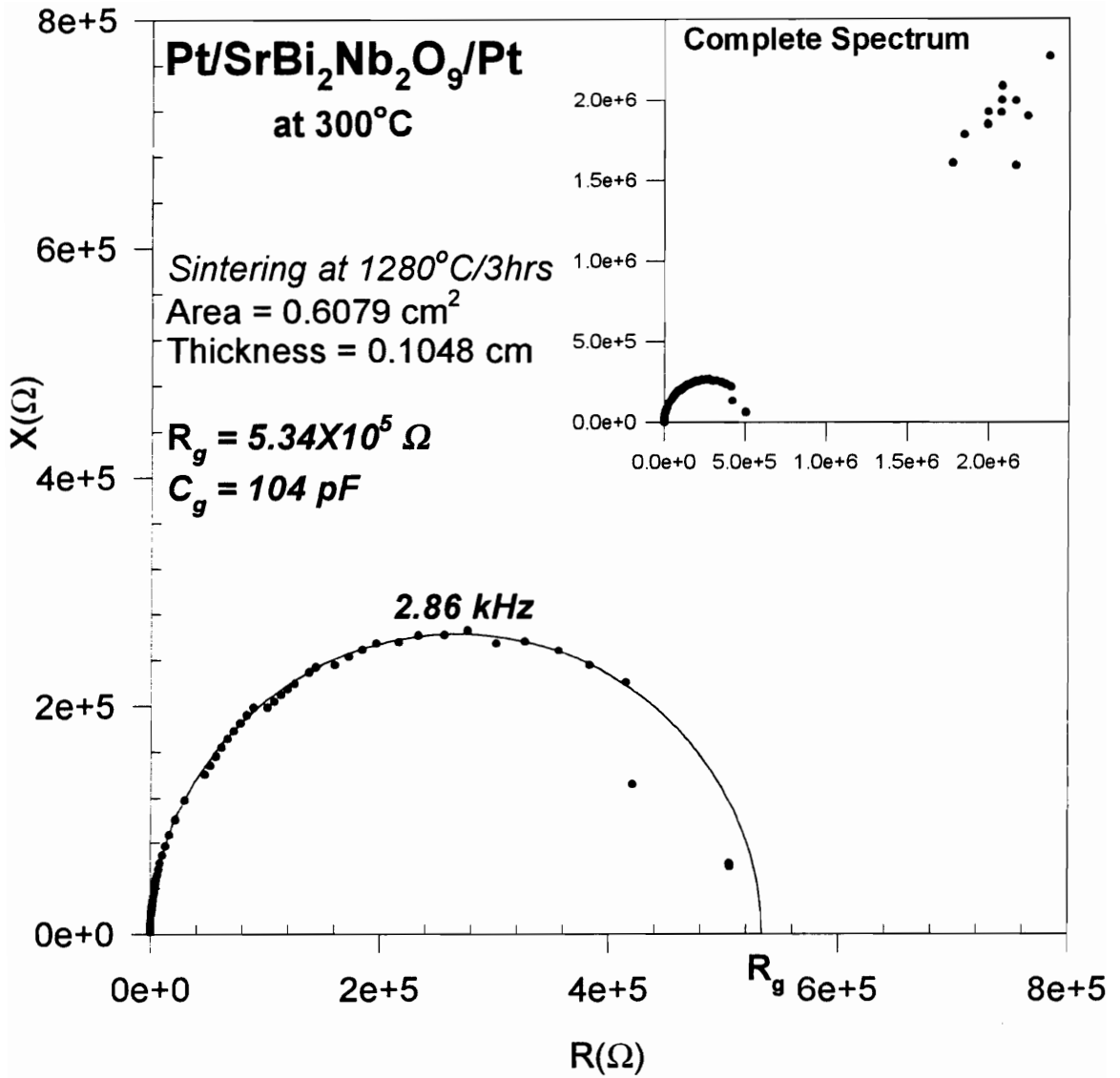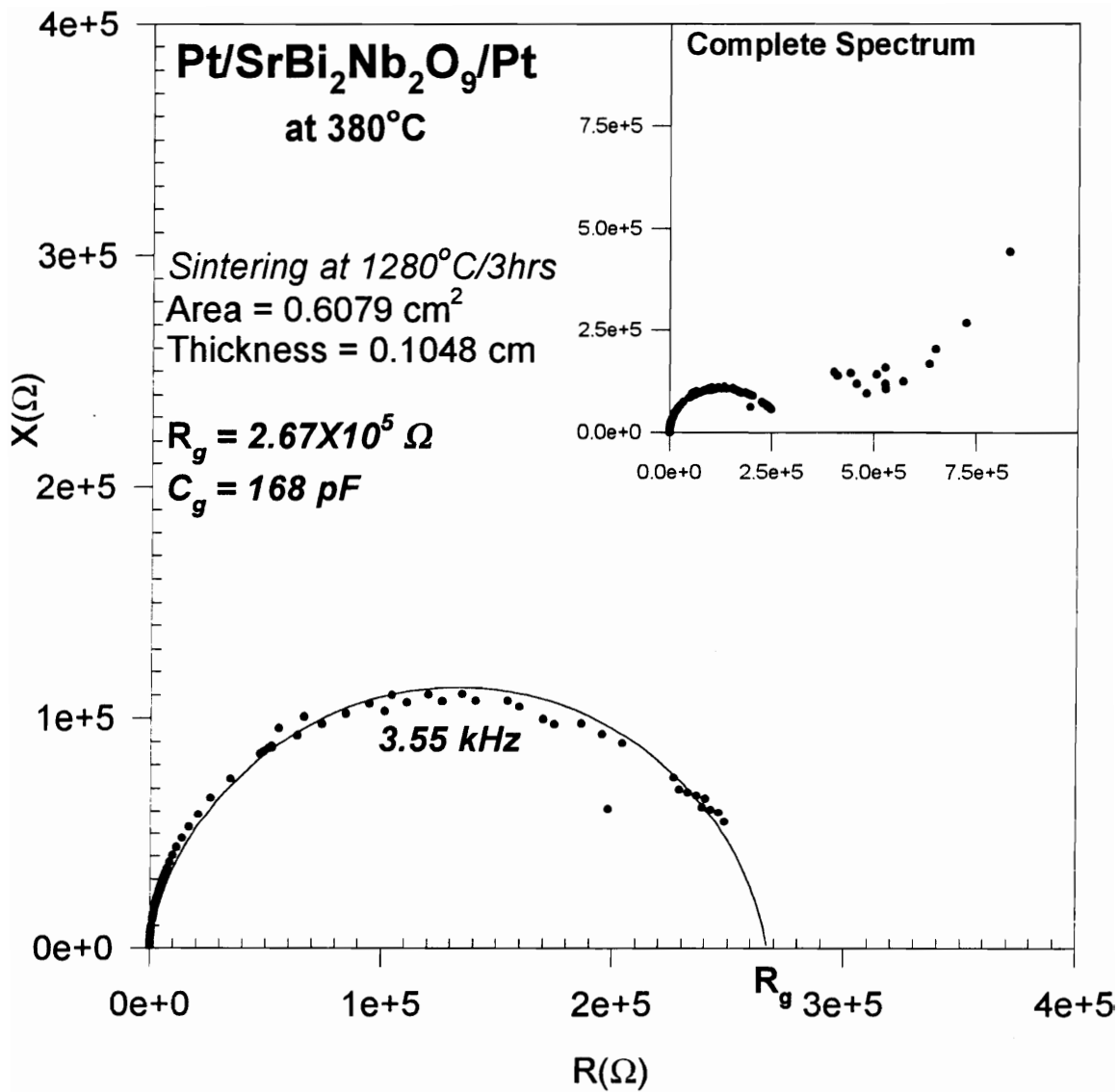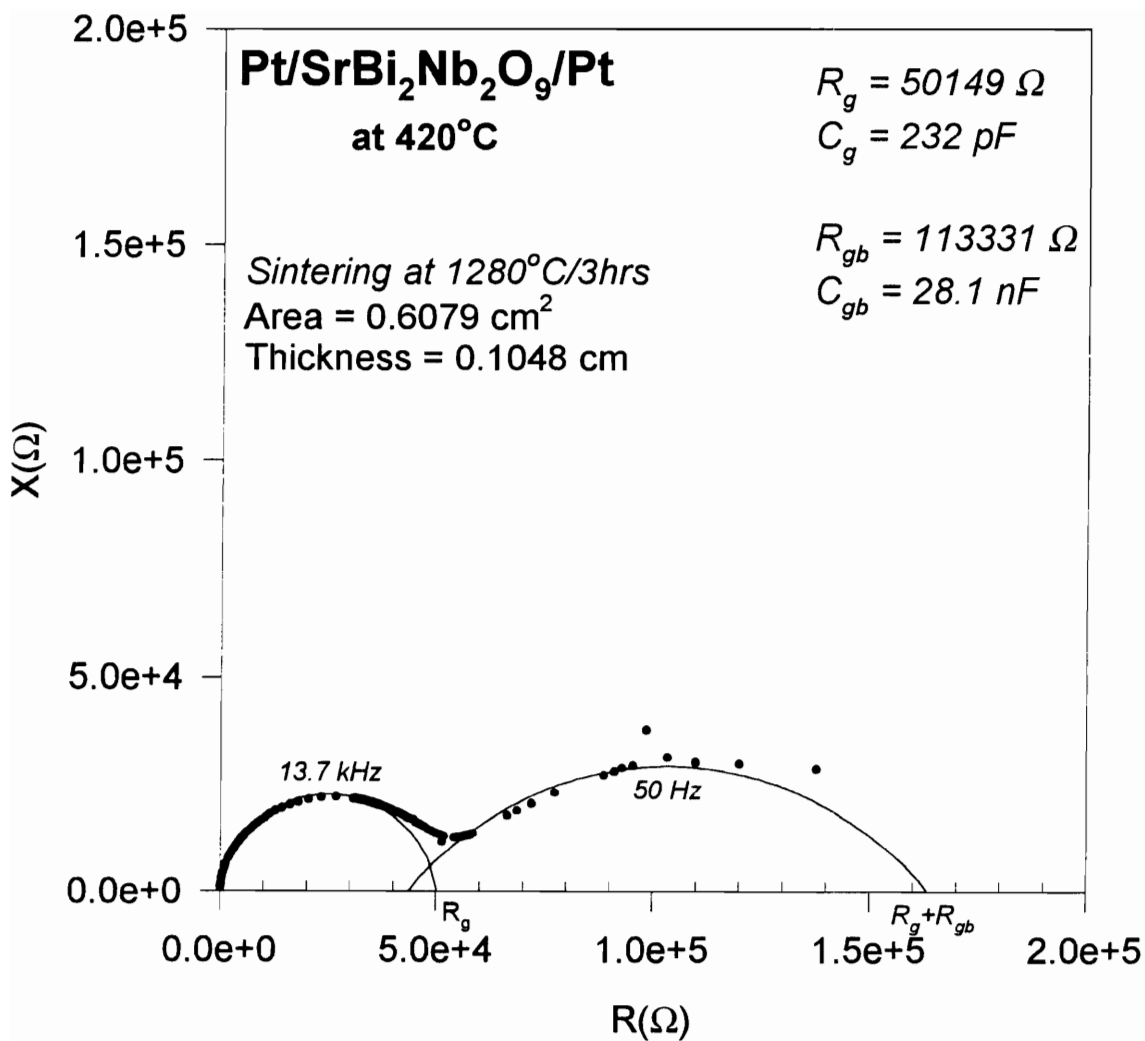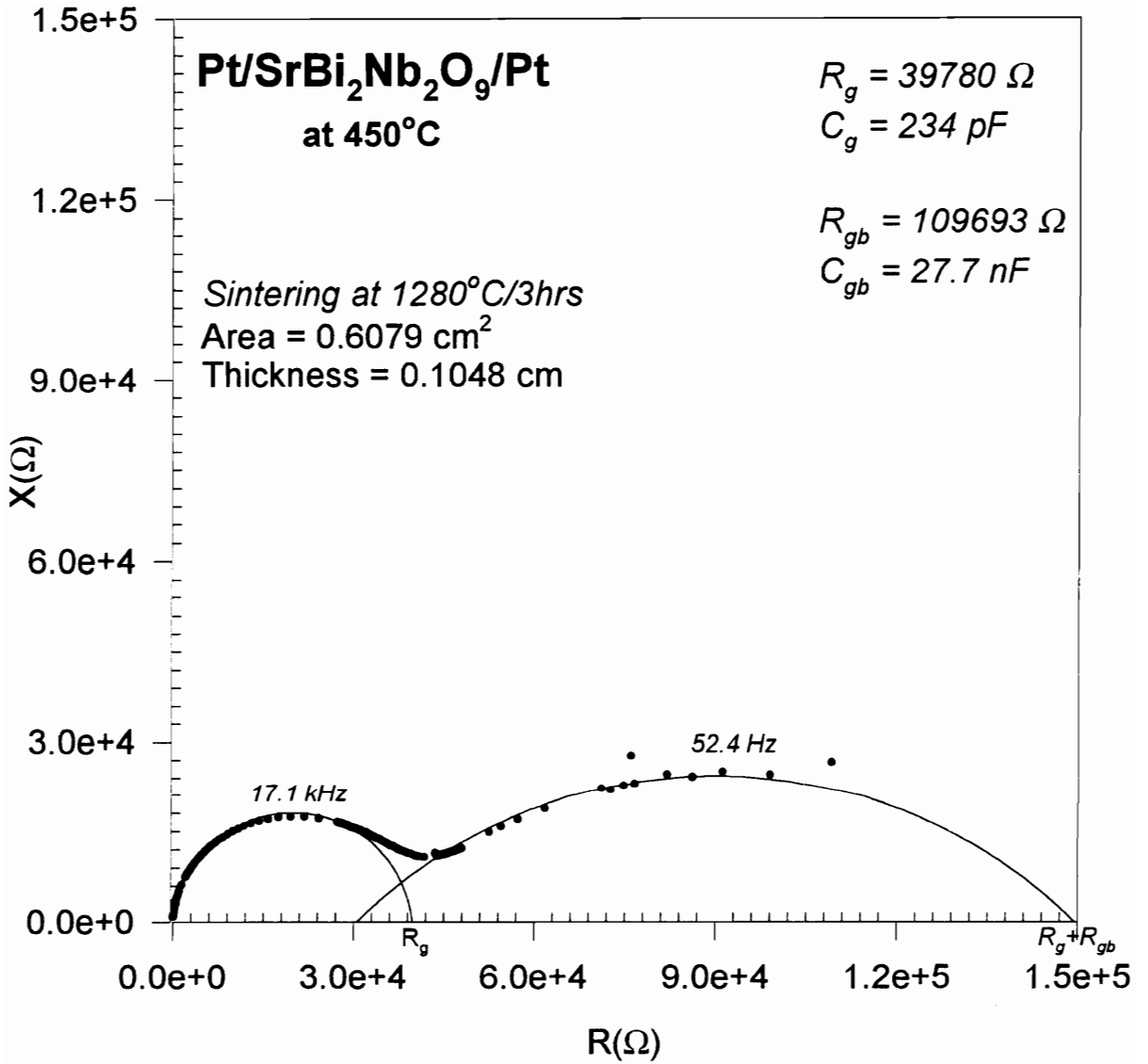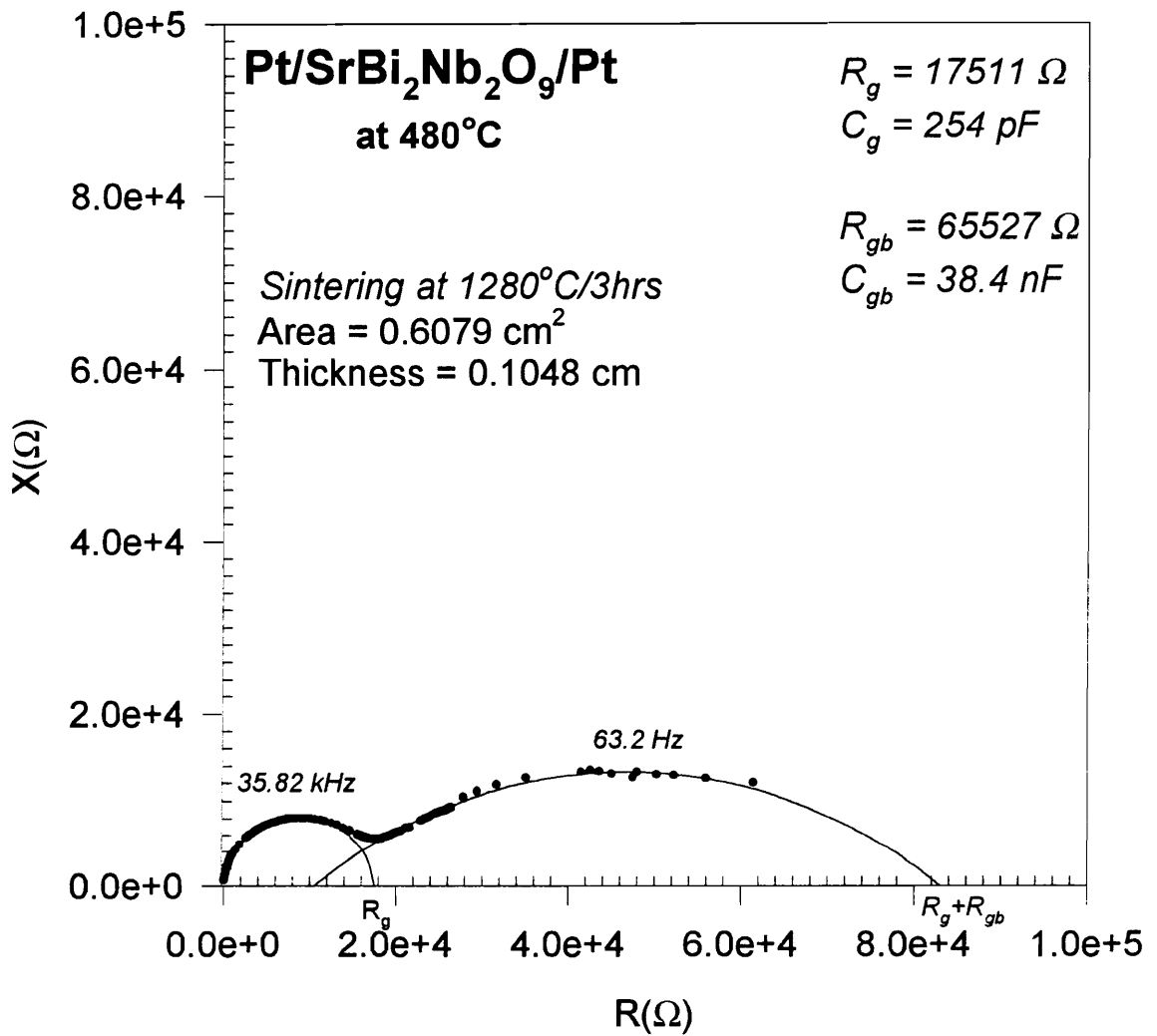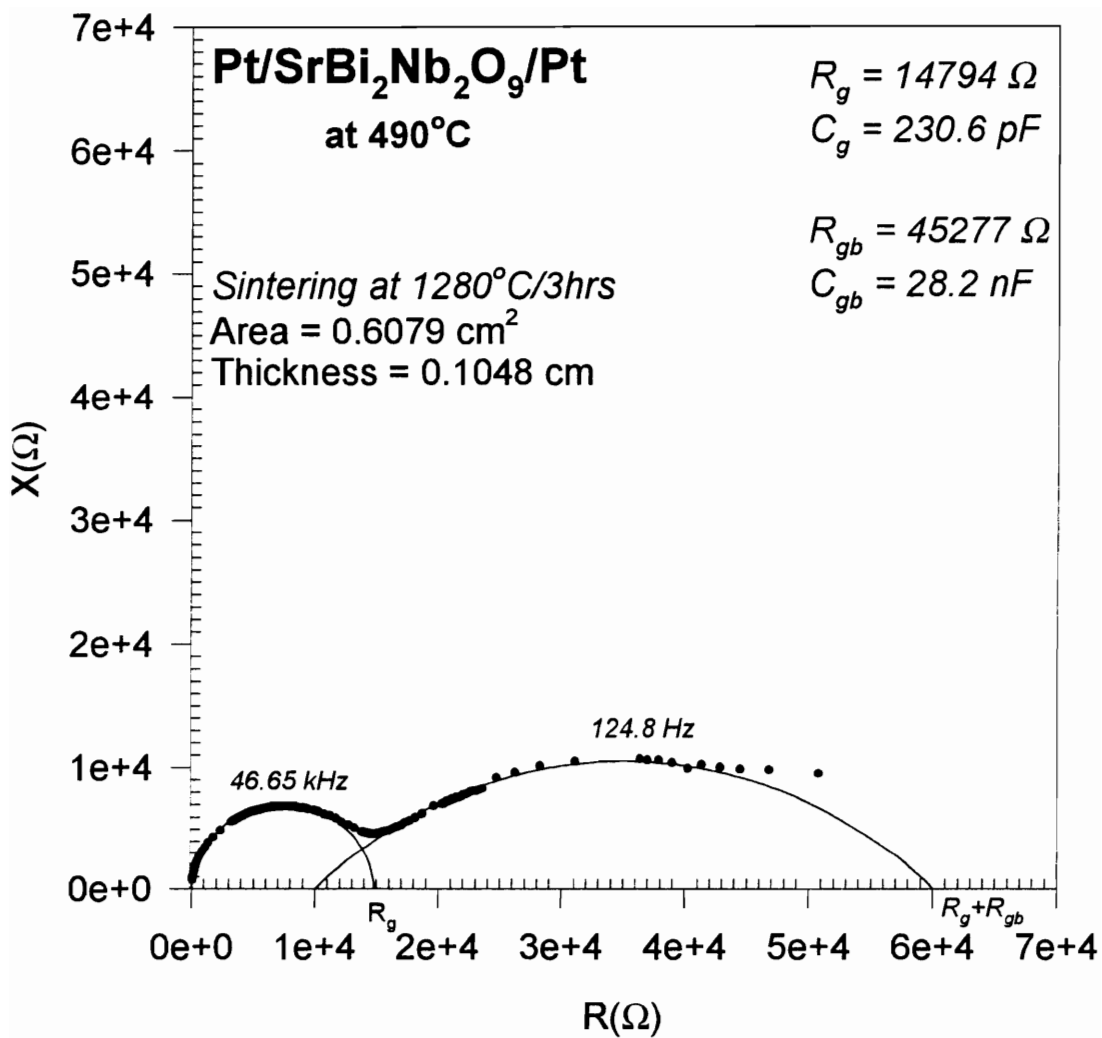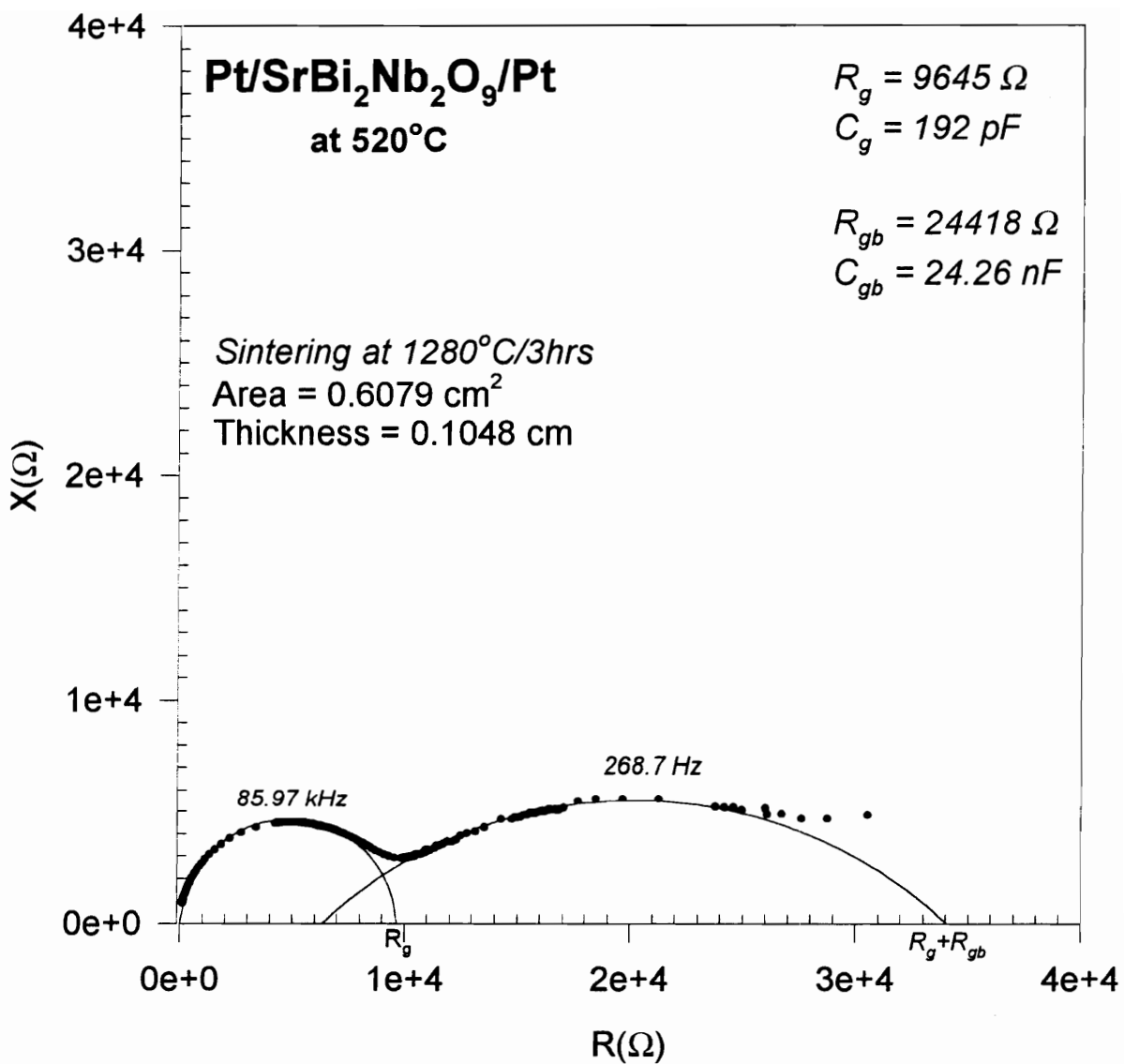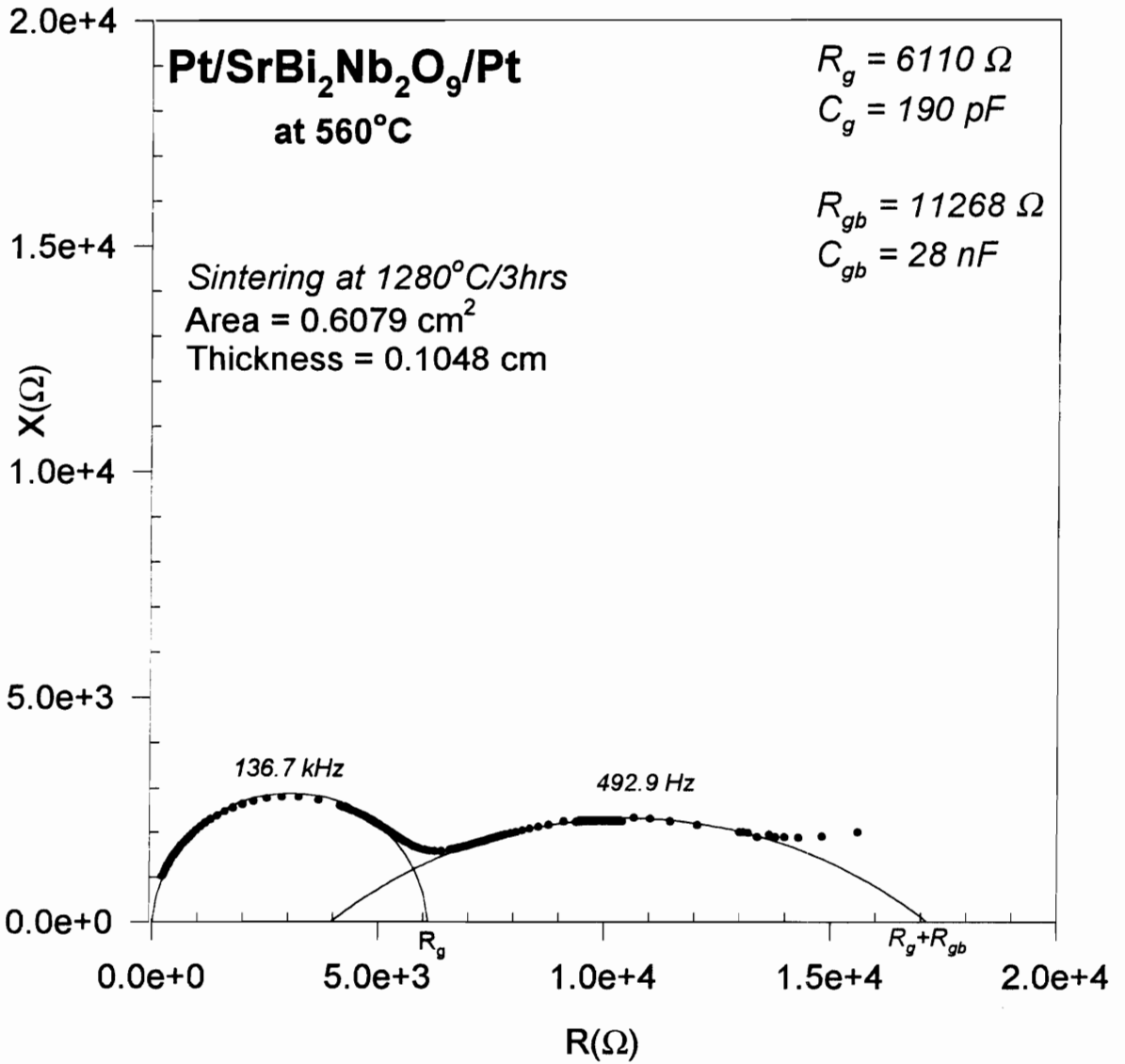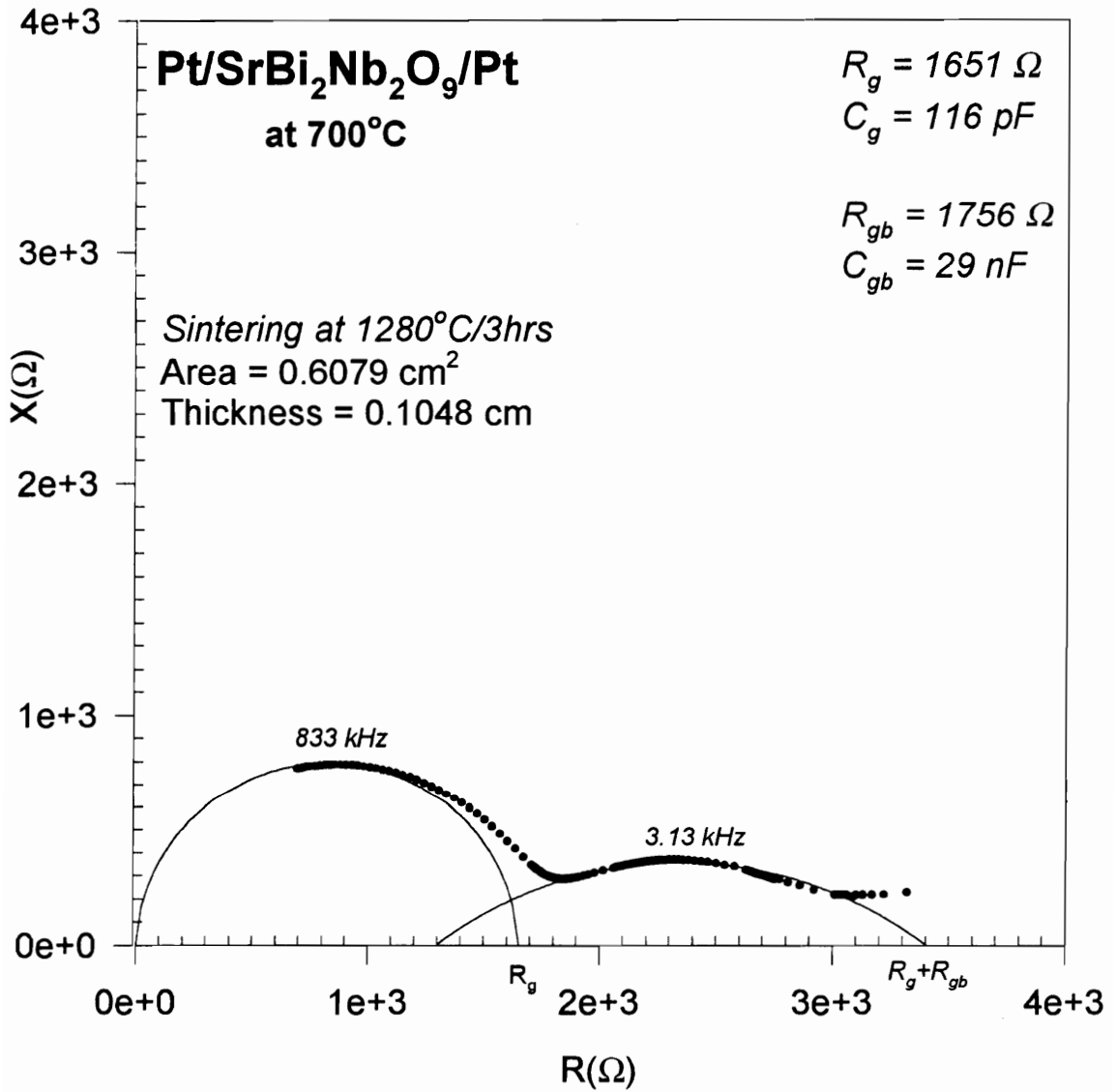Figure B-31. Complex impedance plane of $SrBi_2Nb_2O_9$ bulk ceramics at $700^\circ C$.

References

[1]   J. Valasek, *Phys. Rev*, **15**, 537 (1920), *Phys. Rev.*, **17**, 475 (1921).

[2]   V. Kaushik, P. Maniar, A. Campbell, R. Jones, R. Moazzami, C.J. Mogab, R. Hance and R. Pyle, *Mater. Res. Soc. Symp. Proc.* **310**, 209 (1993).

[3]   J.F. Scott and C.A. Paz de Araujo, *Science*, **246**. 1400 (1989).

[4]   C.A. Araujo, L. McMillan, B. Melnick, J. Cuchiaro, and J.F. Scott, *Ferroelectrics*, **104**, 241 (1990).

[5]   W. Kinney, *Integrated Ferroelectrics*, **4**, 131 (1994).

[6]   R. Moazzami, C. Hu and W.H. Shepherd, *Tech. Digest Sump. on VLSI Technology*, 1990, (Honolulu, HI: IEEE), p. 15.

[7]   K. Torii, T. Kaga, K. Kushida, H. Takeuchi, and E. Takeda, *Japan. J. Appl. Phys.*, **30**, 3562 (1991).

[8]   M. de Keijser, G.J.M. Dormans, J.F.M. Cillessen, D.M. de Leeuw, and H.W. Zandbergen, *Appl. phys. Lett.*, **58**, 2636 (1991).

[9]   H. Miki, Y. Ohji and S. Tachi, *Mater. Res. Soc. Symp. Proc.*, **310**, 210 (1993).

[10]   G. Yi, Z. Wu and M. Sayer, *J. Appl. Phys.*, **64**, 2717 (1988).

[11]   M. Klee, R. Eusemann, R. Waser, W. Brand, and H. van Hal, *J. Appl. Phys.*, **72**, 1566 (1992).

[12]   R. Moazzami, P.D. Maniar, R.E. Jones, A.C. Campbell, and C.J. Mogab, *Tech. Digest Int. Electron Devices Meeting*, 1992 (San Francisco: IEEE), p. 973.

[13]   R. Moazzami, P.D. Maniar, R.E. Jones, and C.J. Mogab, *Tech. Digest Symp. on VLSI Technology*, 1994 (Honolulu, HI: IEEE), p. 55.

[14]   B.T. Matthias, *Science*, **113**, 591 (1951).

[15]   G.A. Smolenskii and N.V. Kozhevnikova, *Dokl. Akad. Nauk., SSSR*, **76**, 519 (1951).

[16]   S. Sinharoy and H. Buhay, *J. Vac. Sci. Technol., A* **10**(4), 1554 (1992).

[17]   P.K. Larsen, G.L.M. Kampschoer, M.J.E. Ulenaers, G.A.C.M. Speirings, and R. Cuppens, *Appl. Phys. Lett.*, **59** (5), 611 (1991).

[18]   R. Moazzami, C. Hu, W.H. Shepherd, *IEEE Electron Device Letter*, **11**(10), 454 (1990).

[19]   L.E. Sanchez, D.T. Dion, S.Y. Wu, and I.K. Naik, *Ferroelectrics*, **116**, 1 (1991).

[20]   S.K. Dey, K.D. Budd and D.A. Payne, *J. Am. Ceram. Soc.*, **7**, C295 (1987), and *IEEE Trans. Ultrason. Ferroelectr. Freq. Control*, **35**, 80 (1988).

[21]   K.D Budd, S.K. Dey and D.A. Payne, *Br. Ceram. Soc. Proc.*, **36**, 107, (1985).

[22]   J. Fukushima, K. Kodaira and I. Matsushita, *J. Mater. Sci.*, **19**, 595 (1984).

[23]   C.K. Kwok and S.B. Desu, *Appl. Phys. Lett.*, **60(12)**, 1430 (1992).

[24]   C.K. Kwok and S.B. Desu, *J. Mat. Res.*, **8(2)**, 339 (1993).

[25]   C.K. Kwok, S.B. Desu, and D.P. Vijay, *Ferroelectric Letters*, **16 (5-6)**, 143 (1994).

[26]   S.B. Krupanidhi, N. Maffei, M. Sayer and K. Dl-Assal, *J. Appl. Phys.*, **54**, 6601 (1983).

[27]   R. Takayama and Y. Tomita, *J. Appl. Phys.*, **65**, 1666 (1989).

[28]   A. Kingon, M. Ameen, O. Auciello, K. Gifford, H. Al-Shareef, T. Graettinger, S-H Rou, and P. Hren, *Ferroelectrics*, **116**, 35 (1991).

[29]   R.W. Vest and W. Zhu, *Ferroelectrics*, **119**, 61 (1991).

[30]   G.A.C.M. Spierings, M.J.E. Ulenaers, G.L.M. Kampschoer, H.A.M. Van Hal, and P.K. Larsen, *J. Appl. Phys.*, **70**, 2290 (1991).

[31]   J.F. Chang and S.B. Desu, *J. Mater. Res.*, **9 (4)**, 955 (1994).

[32] J.F. Chang and S.B. Desu, *Ceramic Transactions*, **25**, 155 (1992).

[33] C.H. Peng and S.B. Desu, *Appl. Phys. Lett.*, **61(1)**, 16 (1992).

[34] S.B. Desu, C.H. Peng, T. Shi, and P.A. Agaskar, *J. Electrochem. Soc.*, **139(9)**, 2682 (1992).

[35] C.H. Peng and S.B. Desu, *J. Am. Ceram. Soc.*, **77 (7)**, 1799 (1994).

[36] W. Tao, S.B. Desu and T.K. Li, *Mater. Lett.*, **23**, 177 (1995).

[37] D.P. Vijay and S.B. Desu, *J. Electrochem. Soc.*, **140** (9), 2640 (1993).

[38] H.M. Duiker et. al., *J. Appl. Phys.*, **68** (11), 5783 (1990).

[39] A.R. Khan and S.B. Desu, *J. Mater. Sci.*, **10(11)**, 2777 (1995).

[40] D.P. Vijay and S.B. Desu, *J. Electrochem. Soc.*, **140(9)**, 2640 (1993).

[41] L.A. Bursill, I.M. Reaney, D.P. Vijay, and S.B. Desu, *J. Appl. Phys.*, **75(3)**, 1521 (1994).

[42] D.P. Vijay, C.K. Kwok, W. Pan and S.B. Desu, *ISAF 1992 Proceedings*, 408 (1992)

[43] R. Ramesh, W.K. Chan, B. Wilkens, H. Gilchrist, T. Sands, J.M. Tarascon, V.G. Keramida, D.K. Fork, J. Lee and A. Safari, *Appl. Phys. Lett.*, **61**, 1537 (1992)

[44] S.D. Bernstein, T.Y. Wong, Y. Kisler and R.W. Tustison, *J. Mater. Res.*, **8**, 12 (1992)

[45] K.R. Bellur, H.N. Al-Shareef, S.H. Rou, K.D. Gifford, O. Auciello and A.I. Kingon, *ISAF 1992 Proceedings*, 448 (1992)

[46] H. Watanabe, T. Mihara, H. Yoshimori and C.A. Paz de Araujo, *ISIF 1992 Proceedings*, 346 (1992)

[47] J. Carrano, C. Sudhama, V. Chikarmane, J. Lee, A. Tasch, W. Shepherd, and N. Abt, *IEEE*, 690 (1991).

[48]   C. A-Paz de Araujo, J.D. Cuchlaro, M.C. Scott, L.D. McMillan, and J.F. Scott, *Natural*, **374**, 627 (1995).

[49]   T. Ito, S. Hiraide, H. Yoshimori, H. Watanabe, T. Mihara, C.P. de Araujo, M.C. Scott, and L.D. McMillan, *Proc. 6th Int. Symp. on Integrated Ferroelectrics*, 1994 (Monterey, CA: Gordon and Breach).

[50]   S.B. Desu and D.P. Vijay, *Mat. Sci. and Eng.*, **B32**, 75 (1994).

[51]   S.B. Desu and D.P. Vijay, *Materials Science and Engineering*, **B32**, 83 (1995).

[52]   J.J. Lee, C.L. Thio and S.B. Desu, *J. Appl. Phys.*, **78(8)**, 5073 (1995).

[53]   S.B. Desu and T.K. Li, *Materials Science and Engineering*, **B34**, L4 (1995).

[54]   S.B. Desu and W. Pan, *Appl. Phys. Lett.*, (1995) in press.

[55]   T.K. Li, Y. Zhu, S.B. Desu, C. Peng, and M. Nagata, *Appl. Phys. Lett.*, (1996) in press.

[56]   D.P. Vijay, S.B. Desu, M. Nagata, X. Zhang, and T.C. Chen, *Mat. Res. Soc. Symp. Proc.*, **361**, 3 (1995).

[57]   G.A. Smolenskii, V.A. Isupov and A.I. Agranovskaya, *Soviet Phys. Solid State*, **1**, 149 (1959).

[58]   G.A. Smolenskii, V.A. Isupov and A.I. Agranovskaya, *Soviet Phys. Solid State*, **3**, 651 (1961).

[59]   E.C. Subbarao, *J. Chem. Phys.*, **34**, 695 (1961).

[60]   E.C. Subbarao, *J. Am. Ceram. Soc.*, **45**, 166 (1962).

[61]   S. Ikegami and E. Ueda, *Jap. J. Appl. Phys.*, **13**, 1572 (1974).

[62]   E.C. Subbarao, *J. Phys. Chem. Solids*, **23**, 665 (1962).

[63]   W. Kanzig, *Phys. Rev.*, **98**, 549, (1955).

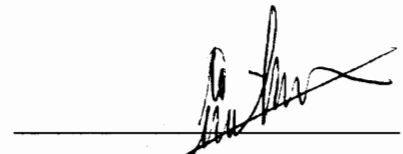[64]   J.F. Scott, C.A. Araujo, B.M. Melnick, L.D. McMillan and R. Zuleeg, *J. Appl. Phys.*, **70**, 382 (1991).

[65]   J.M. Duker, P.D. Beal, J.F. Scott, C.A. Araujo, B.M. Melnick, J.D. Cuchiaro and L.D. McMillan, *J. Appl. Phys.*, **68**, 5783 (1990).

[66]   I.P. Batra, P. Wurfel and B.D. Silverman, *J. Vac. Sci. Technol.*, **10**, 687 (1973).

[67]   R. Moazzami, *Semicond. Sci. Technol.*, **10**, 375 (1995).

[68]   T.K. Li, T.C. Chen, S.B. Desu, and C.H. Peng, *J. Integrated Ferroelectrics*, (1995), in press.

[69]   S.B. Desu and W. Pan, *Appl. Phys. Lett.*, (1995), in press.

[70]   C.K. Kwok and S.B. Desu, *Ceramic Transactions*, **25**, 85 (1992).

[71]   C.K. Kwok and S.B. Desu, *J. Mat. Res.*, **9(7)**, 1729 (1994).

[72]   C.H. Peng and S.B. Desu, *J. Am. Ceram. Soc.*, **77(6)**, 1486 (1994).

[73]   C.H. Peng and S.B. Desu, *J. Am. Ceram. Soc.*, **77(4)**, 929 (1994).

[74]   D.G.A. Bruggeman, *Ann Phys. (Leip.)*, **24**, 636 (1935).

[75]   K. Amanuma, T. Hase and Y. Miyasaka, *Appl. Phys. Letter*, **66** (2), 221 (1995).

[76]   Chapter 3.

[77]   P. Drude, *Wied. Ann.*, **43**, 126(1891).

[78]   P.D. Thacher, *J. Appl. Phys.*, **41**, 4790 (1970).

[79]   C.E. Land and P.D. Thacher, *The Physics of Opto-Electronic Materials*, W.A. Albers, Jr., Ed. (Plenum, New York, 1971), p. 169.

[80]   P.D. Thacher, *Applied Optics*, **16** (12), 3210 (1977).

[81]   D.E. Aspnes, *SPIE Proc.*, **276**, 188 (1981).

[82]   D.E. Aspnes and A.A. Studna, *SPIE Proc.*, **276**, 227 (1981).

[83]   P. Rouard and A. Meessen, in "*Progress in Optics*" (E. Wolf ed.), Vol. 15, p. 77, North-Holland, Publ., Amsterdam, 1977.

[84]   D.E. Aspnes, *Thin Solid Films*, **89**, 249 (1982).

[85]   L. Cauchy, *Bull. Sc. Math.*, **14**, 9 (1830).

[86] E.B. Brown, *Modern Optics*, Reinhold, New York (1965).

[87] F.A. Jenkins and H.E. White, *Fundamentals of Optics*, McGraw-Hill, Inc., 4th edition (1976).

[88] F. Wooten, *Optical Properties of Solids*, Academic press, Inc., New York., 1972.

[89] H.A. Lorentz, The Theory of Electrons, Dover Publications, Inc., New York, 1952.

[90] Chapter 6.

[91] I.K. Yoo and S.B. Desu, *Mater. Sci. Eng.*, **B13**, 319 (1992).

[92] I.K. Yoo and S.B. Desu, *Phys. Stat. Sol. (a)*, **133**, 565 (1992).

[93] I.K. Yoo and S.B. Desu, *J. Electrochem. Soc.*, **140**, L133 (1993).

[94] I.K. Yoo and S.B. Desu, *J. Intell. Mater. Syst. and Struct.*, **4**, 490 (1993).

[95] C. Karan, IBM Tech. Rep., 1955.

[96] I.S. Zheludev, *Physcis of Crystalline Dielectrics, Electrical Properties*, Vol. 2, Plenum Press, New York 1971, pp. 474.

[97] A.Y. Kudzin, T.U. Panchenko, and S.P. Yudin, *Soviet Phys. - Solid State*, **16**, 1589 (1975).

[98] J.M. Duiker, P.D. Beale, J.F. Scott, C.A. Paz de Araujo, B.M. Melnik, J.D. Cuchtaro and L.D. McMillan, *J. Appl. Phys.*, **68**, 5783 (1990).

[99] J.F. Scott, C.A. Araujo, B.M. Melnik, L.D. McMillan and R. Zuleeg, *J. Appl. Phys.*, **70**, 382 (1991).

[100] C.K. Kwok and S.B. Desu, *Mater. Res. Soc. Symp. Proc.*, **243**, 393 (1992).

[101] J.J. Lee and S.B. Desu, *Mater. Res. Soc. Symp. Proc.*, Fall Meeting, 1994.

[102] T.H. Etsell and S.N. Flengas, *Chem. Rev.*, **70**, 339 (1970).

[103] R. Waser, *J. Am. Ceram. Soc.*, **74** (8), 1934 (1991).

[104] J.H. Sluyters, *Recl. Trav. Chim. Pays-Bas*, **79**, 1092 (1960).

[105] J.E. Bauerle, *J. Phys. Chem. Solids*, **30**, 2657 (1969).

[106] R.W. Powers and S.W. Mitoff, *J. Electrochem. Soc.*, **122**, 226 (1975).

[107] R.D. Armstrong, T. Dickinson and P.M. Willis, *J. Electroanal. Chem.*, **53**, 389 (1974).

[108] T.K. Li, T.C. Chen, S.B. Desu, and C.S. Peng, *J. Integrated Ferroelectrics*, (1995) in press.

[109] Chapter 3.

[110] D.M. Smyth, *Ferroelectrics*, **151**, 115 (1994).

[111] Y.Y. Lee, L. Wu, C.K. Liang and T.S. Wu, *Ferroelectrics*, **138**, 11 (1993).

[112] G.A. Smolenskii, V.A. Isupov and A.I. Agranovskaya, *Soviet Phys. Solid State*, **3**, 651 (1961).

VITA

Tze-Chiun Claire Chen was born on December 4, 1964 in Kaohsiung, Taiwan. In 1987, she received the Bachelor of Science degree in Materials Science and Engineering at Feng-Chia University, Taichung, Taiwan. After four years of working in semiconductor industry, she pursued further academic education in September 1991 to attend George Washington University, Washington DC, where she studied Materials Science and Engineering. In January 1992 she transferred her graduate study to Virginia Polytechnic Institute and State University, Blacksburg. She then completed her research and received the Ph.D. of Materials Engineering Science on December 1995. During her Ph.D. research, she joined the thin film group in Materials Science and Engineering department and worked under guidance of Dr. S. B. Desu.

Tze-Chiun C. Chen